Fall 2023

Investigations of a Surrogate Fuel Based on Fischer-Tropsch GTL and CTL in CVCC, IDI and DI Compression Ignition Engines

Amanda C. Weaver

Recommended Citation
Weaver, Amanda C., "Investigations of a Surrogate Fuel Based on Fischer-Tropsch GTL and CTL in CVCC, IDI and DI Compression Ignition Engines" (2023). *Electronic Theses and Dissertations*. 2669.
https://digitalcommons.georgiasouthern.edu/etd/2669

INVESTIGATIONS OF A SURROGATE FUEL BASED ON FISCHER-TROPSCH GTL AND CTL IN CVCC, IDI AND DI COMPRESSION IGNITION ENGINES

by

AMANDA C. WEAVER

(Under the Direction of Valentin Soloiu)

ABSTRACT

With the increase in availability, feedstocks, and properties of alternative fuels, compatibility issues emerge between current engine platforms often requiring a limit on the blend percentage of alternative fuel in conventional fuel or alteration to the engine platform. Two key metrics were identified, autoignition quality and lubrication characteristics, as vital for the proper function of a compression ignition engine, and if the blend of alternative fuels matches these two criteria for the diesel standard, then the resulting blend percentage can be considered as a viable alternative for complete replacement of conventional petroleum ULSD. Autoignition quality was matched using blends S-8, DCN 62, and IPK, DCN 26, with three blends labeled as B1, B2, and B3. A modified DCN equation was then derived for the F-T fuels based on measured ID, CD, and DCN. The results of which determined that a 60% S-8 and 40% IPK blend percentage match the DCN set point of 50 and denoted in the text as S1. The lubricity investigation found that a 3% of a biodiesel compound, methyl oleate, improved average friction force and wear scar depth to within 1% of ULSD. This final surrogate blend is denoted as S2 for the duration of this study. All researched neat fuels and blends were investigated in the CVCC for LTHR, NTC, HTHR, peak pressure ringing, and energy released and duration of each combustion region. The analysis of peak pressure ringing indicated an increase in combustion stability for S2 when compared to ULSD. The LTHR analysis revealed that S2 has a much longer NTC region when compared to ULSD despite its increase in DCN. Three representative fuels were chosen for further investigation in both dual combustion chamber indirect injection and common rail direct injection engine platforms: ULSD (baseline), S2, and IPK. In both engines, the combustion of S2 resulted in a reduction in ringing intensity, BSFC, NOx emissions, CO_2 emissions. No significant differences were found in peak pressure, peak pressure rise rate, or combustion phasing between the combustion of S2 and the combustion of ULSD indicating its high viability as a functional drop-in fuel replacement.

INDEX WORDS: Alternative fuels, Fischer-tropsch fuels, Drop-in fuel replacement, Compression ignition engines, Diesel surrogate, Autoignition characteristics, Low temperature heat release, Negative temperature coefficient region, Emissions characteristics

INVESTIGATIONS OF A SURROGATE BASED ON FISCHER-TROPSCH GTL AND CTL IN CVCC, IDI AND DI COMPRESSION IGNITION ENGINES

by

AMANDA C. WEAVER

B.S., Georgia Southern University, 2021

A thesis Submitted to the Graduate Faculty of Georgia Southern University

in Partial Fulfillment of the Requirements for the Degree

MASTER OF SCIENCE

ALLEN E PAULSON COLLEGE OF ENGINEERING AND COMPUTING

STATESBORO, GEORGIA

INVESTIGATIONS OF A SURROGATE FUEL BASED ON FISCHER-TROPSCH GTL AND CTL IN CVCC, IDI AND DI COMPRESSION IGNITION ENGINES

by

AMANDA C. WEAVER

Major Professor:	Valentin Soloiu
Committee:	Marcel Ilie
	Mosfequr Rahman

Electronic Version Approved:
December 2023

DEDICATION

This work is dedicated to all the times I felt like giving up and didn't, the countless hours sacrificed, the pieces of me I've lost, and most importantly the people around me whose help was irreplaceable. I am proud of the person I was and the person I am today for choosing to continue down this path which led me to this field I love.

Furthermore, I cannot accurately express the enormity of my gratitude for the family and friends who supported me and my work through these difficult years. My sister, Alex, my mother, Elizabeth, my father, Mike, and my brother Zach were and are the most amazing and supportive family and this work would not have been possible without them.

ACKNOWLEDGEMENTS

Nothing more can be said without first giving acknowledgement and credit to my research mentor, Dr. Valentin Soloiu, for his contribution to this work. The space and equipment utilized in my research was made available through the extraordinary efforts of Dr. Soloiu and previous student researchers. My experience working with him over the past 4 years has taught me more about leadership, professionalism, and integrity than I had anticipated. Furthermore, I would like to acknowledge the contributions of my fellow student researchers in the Automotive and Aerospace laboratory for motivating me to achieve greater heights and providing my invaluable experience and insight into team dynamics and the variety of ways to approach a research or team dilemma. Special thanks go out to my fellow lab members Brad Willis, Nick Dillon, and Kody Pierce for their contribution to this research. I would like to further acknowledge the contribution of the Airforce Research Laboratory for providing the fuels used in this investigation as well as the National Science Foundation research grant number 1950207.

TABLE OF CONTENTS

LIST OF TABLES

LIST OF FIGURES

LIST OF EQUATIONS

LIST OF ABBREVIATIONS

A	Area
A_{res}	Resonance Chamber Cross Sectional Area
AFR	Air Fuel Ratio
AHRR	Apparent Heat Release Rate
AIT	Autoignition Temperature
ATDC	After Top Dead Center
B1	Fuel Blend: 75% IPK, 25% S-8
B2	Fuel Blend: 50% IPK, 50% S-8
B3	Fuel Blend: 25% IPK, 75% S-8
B_{abs}	Absorption Coefficient
BEV	Battery Electric Vehicle
BTDC	Before Top Dead Center
BMEP	Break Mean Effective Pressure
CAD	Crank Angle Degree
CA10	Crank Angle Degree @ 10% mass burned
CA50	Crank Angle Degree @ 50% mass burned
CA90	Crank Angle Degree @ 90% mass burned
C_D	Coefficient of Drag
CD	Combustion Delay
CDC	Conventional Diesel Combustion
CI	Compression Ignition
CO	Carbon Monoxide
CO_2	Carbon Dioxide
CoV	Coefficient of Variation
CRDI	Common Rail Direct Injection
CVCC	Constant Volume Combustion Chamber
DCN	Derived Cetane Number
DI	Direct Injection
DTA	Differential Thermal Analysis
Dv10	Largest Droplet size in μm at 10% of the Total Fuel Spray

Dv50	Largest Droplet Size in μm at 50% of the Total Fuel Spray
Dv90	Largest Droplet Size in μm at 90% of the Total Fuel Spray
EOC	End of Combustion
f_0	Resonance Frequency
F-T	Fischer-Tropsch
FCEV	Fuel Cell Electric Vehicle
FID	Flame Ionization Detection
$\dot{\gamma}$	Fluidic Shear Rate
γ	Specific Heat Ratio
HEV	Hybrid Electric Vehicle
HHV	Higher Heating Value
HTI	High Temperature Ignition
IC	Internal Combustion
ICE	Internal Combustion Engine
ID	Ignition Delay
IDI	Indirect Injection
IMEP	Indicated Mean Effective Pressure
IPK	Iso-paraffinic Kerosene
L	Characteristic Spindle Length
l	Characteristic Droplet Length
LHV	Lower Heating Value
LTC	Low Temperature Combustion
LTI	Low Temperature Ignition
LTHR	Low Temperature Heat Release
M	Motor Torque
MFB	Mass Fraction Burned
MO	Methyl Oleate
η	Dynamic Viscosity
N	Engine Speed
NOx	Nitrogen Oxides
NTC	Negative Temperature Coefficient

NVH	Noise Vibration Harshness
Oh	Ohnesorge Number
ρ	Fluidic Density
ρ_A	In-Cylinder Gas Density
PHEV	Plug-in Hybrid Electric Vehicle
P_L	Laser Intensity
P_m	Sound Intensity
PPRR	Peak Pressure Rise Rate
PRR	Pressure Rise Rate
R_c	Container Radius
Re	Reynold’s Number
R_s	Spindle Radius
RI	Ringing Intensity
S	Stroke
σ	Surface Tension
S1	Surrogate Fuel Blend: 40% IPK, 60% S-8
S2	Surrogate Fuel Blend: 38.5% IPK, 58.5% S-8, 3% Methyl Oleate
SMD	Sauter Mean Diameter
SOC	Start of Combustion
SOI	Start of Injection
τ	Shear Stress
TA10	Temperature @ 10% mass vaporized
TA50	Temperature @ 10% mass vaporized
TA90	Temperature @ 90% mass vaporized
TGA	Thermogravimetric Analysis
T_W	Wall Temperature
λ_A	Thermal Conductivity
μ_A	Viscosity In-cylinder Gases
ULSD	Ultra-Low Sulfur Diesel
v	Velocity

ω	Rotational Velocity
We	Weber Number

CHAPTER 1

INTRODUCTION

1.1 PURPOSE OF STUDY

As the world continues to progress, global energy demands across all economic sectors rapidly increase and although great strides have been made in the field of renewable energy, heavy dependance on fossil fuels is needed to fulfill the current and rising worldwide energy needs. The pathway by which energy is extracted from fossil fuels is through their combustion producing emissions whose negative impact on human health, the environment, and global climate is both well-known and well understood. Additionally, fossil fuels are considered non-renewable resources indicating that the pathways necessary for generation of additional resources are very specific and time consuming on a geological scale. This means that there is a guaranteed point in time where there will be an inevitable depletion in the supply of fossil fuels should our reliance on energy from their combustion go unchanged. Some alternatives to this form of energy and transportation are beginning to develop and show promise in alleviating some of this dependance. The drawbacks to these alternatives are that they don't mesh well with our current infrastructure. All modern internal combustion engines and turbojet engines use petroleum fuels to create power and replacing them with electric motors is currently not feasible and requires a large quantity of difficult to find rare earth metals such as lithium and cobalt. An area which shows promise is the drop-in fuel replacement.

This is a term which describes an alternative fuel that will cause no decrease in performance or integrity to an engine when run in the engine. This study seeks to create a drop-in fuel replacement from three alternative fuels. Two of these fuels are Fischer-Tropsch synthetic kerosene and the other is the biodiesel methyl oleate. Fischer-Tropsch fuels are those which are derived from coal, natural gas, or biomass using the Fischer-Tropsch process to create a fuel which is more refined with fewer components which produce harmful emissions. Iso-paraffinic kerosene is a Fischer-Tropsch synthetic kerosene which has low autoignition characteristics compared to its counterpart, S-8, another F-T kerosene. Methyl oleate, a primary component of a wide variety of different biodiesels, is added as the previous kerosenes do not have a high enough lubricity to function in a common IC engine.

1.2 HOW THIS STUDY IS ORIGINAL

Currently, there are caps to the maximum amount of alternative fuel which can be blended with conventional petroleum fuel varying based on the type of engine and the alternative fuel. This is due to the discrepancy in thermophysical and combustion properties of alternative fuels when compared to conventional fuels. As mentioned in the following chapters, much of the alternative fuel research either upholds current engine design through blending alternative fuels with petroleum fuels or creates a new engine design dedicate to one of the many currently available alternative fuels. This study seeks to apply blending techniques to meet compression ignition fuel standards using only alternative fuels. The ASTM standard D975 outlines the properties that various grades of diesel fuels must meet to achieve acceptability including flash point, cloud point, water and sediment, carbon residue, ash, distillation, viscosity, sulfur, copper corrosion, cetane number, cetane index, aromaticity, lubricity, and conductivity. Previous studies research the effects of blending synthetic fuels with petroleum fuels to determine their effect on combustion (S.S. Gill et al. 2011; Alleman et al. 2005; Soloiu et al. 2023). For this study, three alternative fuels are chosen whose properties negate equivalency to conventional Ultra-Low Sulfur Diesel (ULSD), but through blending these fuels a drop-in replacement for ULSD will be created. Two main parameters will be used as a guide for determining the fuel blend's viability as a drop-in replacement. These parameters are the Derived Cetane Number (DCN) and the lubricity.

1.3 HISTORY OF INTERNAL COMBUSTION (IC) ENGINES

Internal combustion engines were created to convert chemical energy to mechanical power. This style of engine was an improvement on the previous external combustion engine. These changes improved engine efficiency by containing the combustion reaction within the engine. External combustion engines and the first piston engines used steam as the fuel source. It was not until the 1860's that internal combustion engines really became commonly functional (Newell 1953). These early engines ran on coal and did not contain a compression stroke. The first marketable engines were spark ignition and used gasoline as the fuel source. This engine combined the intake and expansion phases of the otto cycle into one stroke and expelled exhaust gasses on the second stroke (Heywood, 2018).

The next development in the internal combustion engine was the atmospheric engine developed by Nicolaus Otto and Eugen Langen. This engine used the pressure rise created from combustion of the fuel-air charge. The resulting momentum would then create a vacuum in the cylinder such that atmospheric pressure would then push the piston back to its original location. After this initial engine, Otto created the four-stroke engine and the model for the four-stroke piston cycle referred to now as the Otto cycle (Newell 1953). These strokes consist of the intake, compression, expansion, and exhaust. Otto's patent was then brought into question by a French patent issued to Alphonse Beau de Rochas prior to Otto's. Beau de Rochas outlined the conditions for which a four-stroke engine would operate at maximum efficiency. Heat losses from the charge must be kept to a minimum. The greatest possible expansion for post combustion gases as well as highest possible in cylinder pressures (Heywood 2018).

Further developments on the internal combustion engine moved quickly following the works of Otto and Beau de Rochas. The two-stroke engine was successfully developed as well as an increased expansion and compression stroke. In was not until 1892, however, that Rudolph Diesel created the patent for the compression ignition engine. This engine doubled efficiency over previous models with very high compression ratios (Newell 1953). By the 1900's two main fuel types were in use: diesel (compression ignition) and gasoline (spark ignition). Gasoline is the lighter of the two crude oil fuels used in spark ignition engines. Its high volatility makes starting the engine easy and creating more homogeneous fuel-air mixtures easier (Heywood 2018).

It was not until the 1940's that the issue of emissions became apparent. Through the 1950's and 1960's the issue of smog in the cities caused the introduction of emissions standards. Since then, there has been a significant reduction in the emissions caused by both spark ignition and compression ignition engines. Some of these advancements include the use of catalysts in spark ignition engines as well as the exclusion of lead as an anti-knock additive. Noise played a role in the pollution caused by engines as well. Legislation on the regulation of vehicle noise was introduced in the 1970's (Heywood 2018).

It was also in the 70's that a shortage of crude oil caused a sharp increase in fuel prices. This sparked the conversation of long-term sustainability of crude oil. The combination of fuel consumption requirements as well as the emissions standards led to the investigations into the use of alternative fuels. Initial advancements in alternative fuels were made with the introduction of methanol and ethanol. These alcohols can currently be blended with gasoline in quantities of up to 85% alcohol (Heywood 2018).

Though there is continued development toward alternative sources of power and energy, the internal combustion engine remains a vital part of our modern society. The concept seems complete, however, there is ongoing research into ways to improve the engine in terms of power and efficiency. As new manufacturing techniques, engine designs, and alternative fuels are researched and developed, both spark ignition and compression ignition engines improve in efficiency, power, and emissions production (Heywood 2018).

1.4 INTRODUCTION TO THE PROBLEM: ENVIRONMENTAL AND SUPPLY CONCERNS

The impact of the combustion of fossil fuels has long contributed to the degradation of air quality. Coal, for example, has been one of the most widely used fuels for power generation for over 100 years because of its widespread availability and accessibility (de Lorenzi 1957). While the industrial revolution opened vast possibilities for the development of civilization and began the technological advancements make life better for millions of people, the price for that advancement was the environmental pollution brought on by the combustion of fossil fuels. Despite the fluctuations in global temperatures through the course of earth’s history, the rate at which temperatures are rising with the majority of the warming occurring in the 20th century. The primary fuel at that time was coal for the production of steam power which covered cities and nearby forests in soot and particulate matter in addition to the NOx and CO_2 sent into the atmosphere (EIA 2022). As technology progressed in the field of power generation and transportation grew, increasing reliance on the internal combustion engine increased both the demand for fossil fuels and the emissions produced from their combustion. Figure 1 shows the sources of global greenhouse gas emissions by economic sector.

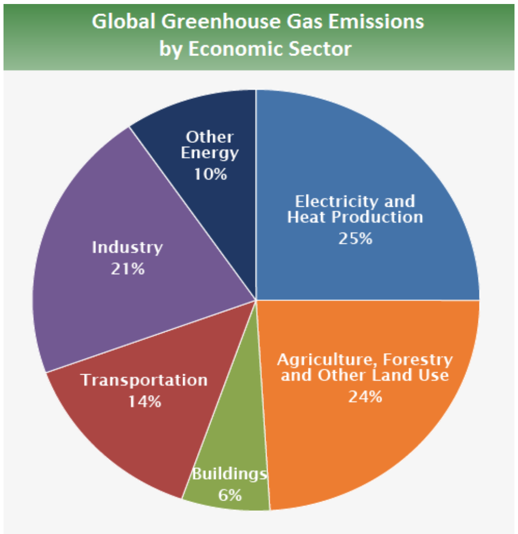

Figure 1: Global Greenhouse Gas Emissions by Economic Sector (Gilfillan et al. 2020; EPA 2023)

Internal combustion engines, and more specifically compression ignition engines, have a strong foothold in every sector listed in Figure 1. This provides a significant opportunity for the reduction of harmful emissions as continued development puts increasing pressure on the environment and on human health. The combustion of hydrocarbon fuels produces several different emissions species which have adverse effects on the breathability of air or on global climate and the atmosphere. Gaseous emissions species are divided by the percentage of total emissions which can be attributed to that species in Figure 2.

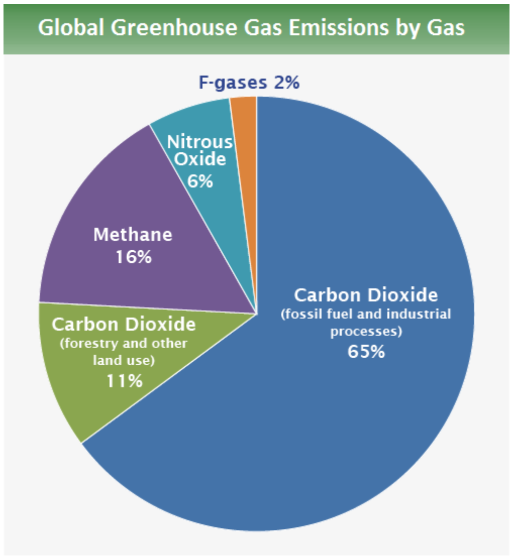

Figure 2: Greenhouse Gas Emissions by Species (EPA 2023)

Carbon dioxide makes up the vast majority of global greenhouse gas emissions consisting of over 75% of global greenhouse gas emissions between the combustion of fossil fuels and other industrial processes and the emissions produced from forestry and agriculture. Globally, internal combustion engines contribute to about 20% of the CO_2 emissions contributing to the increase in global temperatures due to the greenhouse effect of carbon dioxide. Over the last 200 years, atmospheric carbon has increased from 278 ppm to 417 ppm (Anandan 2023).

While the primary emission from the combustion of hydrocarbon fuels is CO_2, there are a few other emissions that can cause damage to both people and the environment. A breakdown of typical diesel combustion exhaust composition can be found in Table 1. Nitrogen oxides are a by-product of high temperature combustion as the atmospheric nitrogen breaks its double bond and reacts with free oxygen to form nitrogen oxides (Hamid R. Rahai 2011). The three primary nitrogen oxides are Nitrogen Dioxide (NO_2), Nitric Oxide (NO), and Nitrous Oxide (N_2O) (Pani 2020). Falls in the same grouping as carbon dioxide as it acts as a greenhouse gas in the atmosphere contributing to the increase in global temperatures. Nitric oxide is an odorless and colorless gas which makes up the majority of the NOx emissions from combustion. When it gets into the atmosphere, however, it reacts to form the much more hazardous nitrogen dioxide. It's yellowish-brown in color and is a strong oxidant contributing to photochemical pollution and the formation of excess ozone (Aste et al. 2013).

Table 1: Typical Diesel Exhaust Composition (Jelles 1999)

Component Species	Concentration
CO	100-10000 ppm
HC	50-500 ppm (C_1, CH_4, Methane)
NOx	30-1000 ppm
SOx	Proportional to fuel sulfur
Diesel Particulate Matter	20-200 mg/m^3
CO_2	2-12 vol%
Ammonia	2.0 mg/mile
Cyanides	1.0 mg/mile
Benzene	6.0 mg/mile
Toluene	2.0 mg/mile
PAH	0.3 mg/mile

Another major component of hydrocarbon combustion exhaust, primarily diesel exhaust, is soot which can have hugely detrimental effect on human health and the environment. Small soot particles, also known as smoke, can infiltrate lung tissue when inhaled causing damage to the lung tissue having a severe impact on primary bronchial epithelial cells (Rahman et al. 2023). This can lead to the development of cancer, cardiovascular, and respiratory issues as well as secondary immune and hormonal issues (Kodavanti et al. 2011; Sydbom et al. 2001). The environmental issues associated with excessive soot are the pollution of soil, water, and air. The wide range of chemical composition of particulate matter emissions causes a range of issues when it infiltrates soil, air, and water supply. Accumulation of particulate matter in soil can cause heavy metal toxicity affecting vegetation growth and ecosystem stability. Secondary effects of particulate matter contamination are the acidification and nitrogen saturation of the soil due to the disruption of the life cycle of microorganisms which participate in the natural nitrogen cycle (Grantz, Garner, and Johnson 2003).

In addition to the emissions produced from combustion, the extraction process for fossil fuels can have a significant impact on the environment. As with all large industrial projects, there is ecosystem destruction caused by the clearance of land to make way for extraction which not only impacts the local wildlife but also disrupts the soil layers contributing to water table and topsoil degradation. This poses a threat to local municipal water supplies through limitation and potential drought. Crude oil drilling and gas drilling can result in leakages from machinery failures causing extreme levels of soil contamination and, if the leak is at sea either at the well or in transport, cause the widespread death of sea life and damage coastal communities (Nayak et al. 2019).

1.5 CURRENT SOLUTIONS AND LIMITATIONS

There are several solutions to the problems associated with the pollutant emissions produced from the IC engine involving the implementation of electrical drive systems and the development of novel fuels for use in IC engine systems. These options can be split into two primary categories: whether it keeps or discards the IC engine. For the category that scraps the IC engine in favor of transportation driven by electric motors, the differences arise in the power source where modern vehicle options include Battery Electric Vehicles (BEV), Hybrid Electric Vehicles (HEV), Plug-in Hybrid Electric Vehicles (PHEV), and Fuel Cell Electric Vehicles (FCEV). On the other hand, there is one primary pathway for reducing the environmental impact for IC engines and that is alternative fuels. Not only do alternative fuels offer the opportunity for the reduction of harmful emissions in the cylinder, but also the opportunity to eliminate the reliance on fossil fuels and the destructive methods used to extract them. In the following section, each of these alternatives is discussed as well as the potential limitations of their use.

1.5.1 BATTERY ELECTRIC VEHICLES (BEV'S)

Battery Electric Vehicles are the "all in" proposed technology to alleviate the reliance on fossil fuels as the impact of their emissions. BEV's have can have up to four electric motors to provide power to the wheels coupled to the on board battery bank through a DC/DC converter used to reduce the high voltage output of the batteries to the lower voltage range required for the motor/s. Batteries are recharged through an external charging port as a conventional ICE driven vehicle would fill the fuel tank. On board computer systems manage the electronics controls with some BEV's equipped with a mechanical transmission like those found in conventional ICE vehicles(AFDC 2023d). A schematic of a typical BEV can be seen in Figure 3.

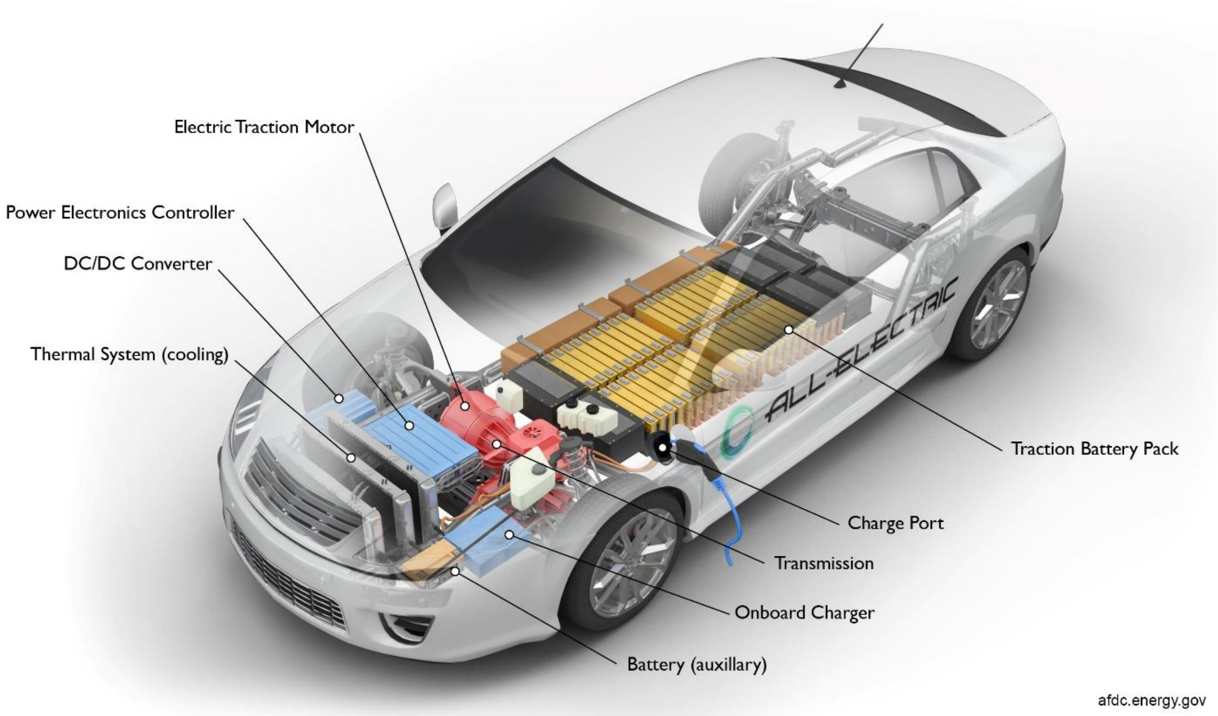

Figure 3: Schematic of a Typical BEV(AFDC 2023d)

There are several advantages supporting further development of BEV's. Most notably is the reduction of tail-pipe emissions to zero, giving it a distinct advantage in more confined environments where there is a high volume of vehicles such as cities or other high-traffic, populated areas. Furthermore, the development of renewable energy sources exemplifies the environmental benefits from the use of BEV’s. Renewable energy now contributes 13% of the total energy consumption of the United States coming from a combination of geothermal, solar, hydroelectric, wind , and biomass (biomass waste, biofuels, and wood) (EIA 2023). Projections for the increase in renewable power generations show in increase in fractional contribution to the U.S. electrical supply to increase to 44% by 2050 with solar energy leading the way providing 51% of that energy (EIA 2023).

From a performance perspective, BEV’s have an advantage over IC engines as torque can be applied to the wheels immediately by an electric motor whereas IC engines have a great deal more rotational inertia to overcome before maximum torque can make it to the wheels. This in combination with the lack of a functional speed limitation for electric motors means that BEV’s can accelerate much faster than ICE vehicles.

1.5.2 Hybrid Electric Vehicles (HEVs) and Plug-in Hybrid Electric Vehicles (PHEVs)

A modification to BEVs is the hybrid and plug-in hybrid electric vehicles which bridge the gap between eliminating the IC engine completely and electrifying the vehicle drive train. Both configurations use one or multiple electric motors to drive the wheels while an IC engine provides the power to charge the batteries to run the motors. This connection is referred to as a series connection where a parallel connection enables either the IC engine or the electric motors to provide direct power to the wheels. Standard HEVs still use liquid fuel as the only source of input power while PHEVs have the option to directly charge the batteries as in a BEV. Some designs offer the option to switch between series operation and parallel operation (Mi and Masrur 2018). A schematic of a typical HEV vehicle configuration can be found in Figure 4.

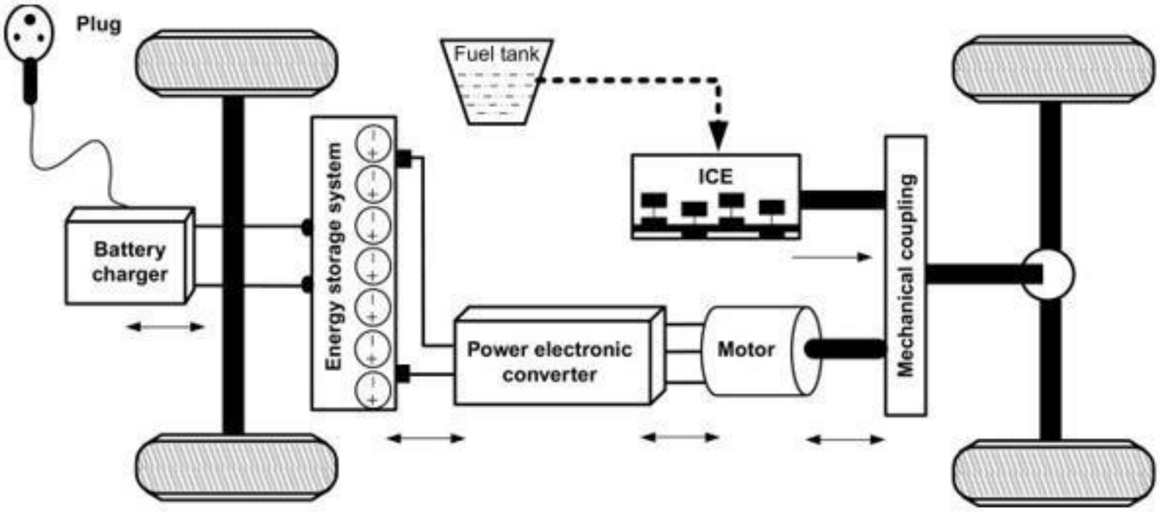

Figure 4: Block Diagram of an HEV(Upadhyay et al. 2021)

This solution eliminates one of the bigger fuel economy costs in vehicles driven solely off the IC engine with the intermediary system between the engine and vehicle speed. In a conventional ICE vehicles, the engine speed has to follow the vehicle speed where changes in engine speed incur substantial losses from the energy requirements to overcome inertial forces. This variation is quantified by drive cycle data where speed and load over time can be observed and analyzed. For HEVs and PHEVs, load can be taken off the IC engine and the speed can remain constant as the primary demand on the IC engine is power to the batteries (Mi and Masrur 2018).

1.5.3 FUEL CELL ELECTRIC VEHICLES (FCEVS)

The Fuel Cell Electric Vehicle (FCEV) is another modification to the BEV and the HEV/PHEV wherein the main drive power comes from electric motors. In FCEVs, the battery packs found in BEVs are replaced by fuel cell stacks and a tank of hydrogen. A schematic of a typical FCEV can be found in Figure 5. The primary components of this configuration are the fuel cell, motor drive, electric motor, and optional auxiliary energy generation units. FCEVs are very similar to HEVs/PHEVs in that there is an internal source of power generation which requires fuel where the IC engine is replaced with a fuel cell (İnci et al. 2021). Fuel cells can be hybridized with a variety of other systems for power storage including batteries, ultra capacitors, photovoltaic panels, flywheel, and superconducting magnetic energy storage providing several opportunities for further technological development.

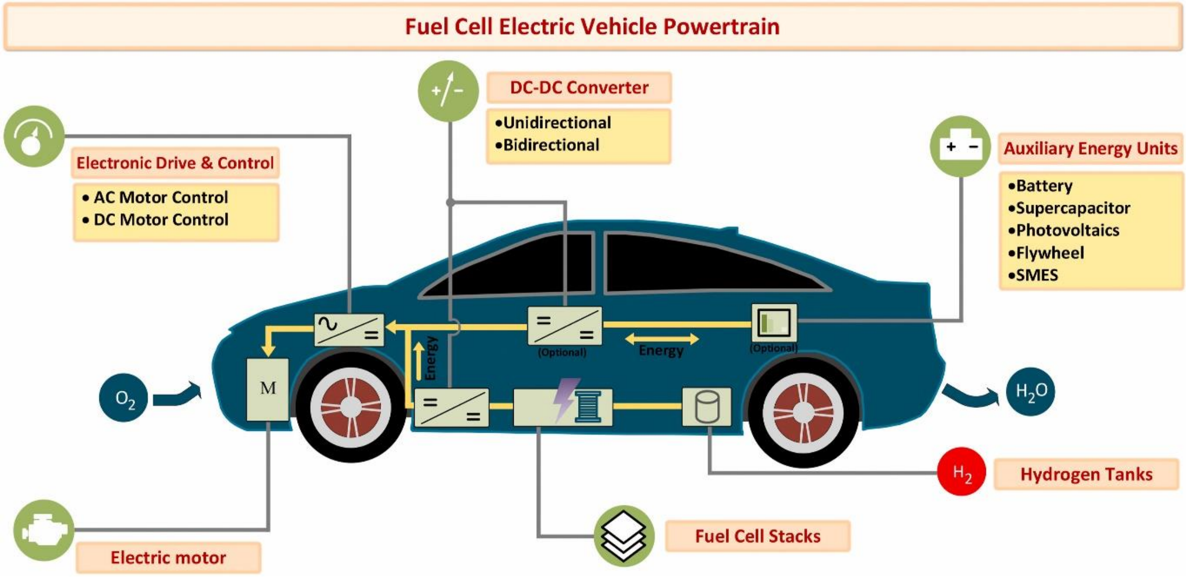

Figure 5: Design of a FCEV (İnci et al. 2021)

The current fuel cell design operates off hydrogen and oxygen fuel sources with the production outputs of water and electrical energy. The design uses a cathode, anode, and electrolyte where the cathode and anode plates are separated by the electrolyte mixture. Hydrogen is applied to the anode side and oxygen is applied to the cathode side. Hydrogen then decomposes on the anode side with the positive proton particles traveling to the cathode through the electrolyte. The electrolyte allows the protons to pass and rejects the negative electrons. The electrons then reunite at the cathode through a resistive bridge to the cathode side where the hydrogen protons react with the oxygen to create water and heat. The forced movement of the electrons created by the charge imbalance induces an electron flow that generates electricity (İnci et al. 2021). This combination of electric vehicle design and fuel cell technology provides a low-emission solution with greater versatility than the BEVs in terms of variability of energy storage methods. There are still several factors limiting their widespread use including longevity of the fuel cells, hydrogen supply, and durability (İnci et al. 2021).

1.5.4 Disadvantages to Electric Vehicles

There are several disadvantages to electric vehicles from inconveniences of daily ownership to costly nationwide infrastructure changes and material requirements that have a significant negative impact both from a humanitarian and environmental perspective. From a consumer standpoint, electric vehicles pose a few issues that give many people hesitation when looking to purchase one. First and foremost is the initial cost of the vehicle with EVs costing on average more than an ICE vehicle. Additionally, charging times are significantly longer when compared to the time it takes to fill a gas tank with minimum charge times at for DC fast charging compared to the few minutes it takes to fill the gas tank. Range is another issue of key concern as the availability of charging stations is currently limited to more populated areas. Climate also has a significant effect on EV range.

Cold temperatures greatly influence the functionality of Lithium-ion batteries reducing range capacity by approximately 40% in temperatures below freezing (Mohan et al. 2019). This poses a considerable issue for EVs of any type but especially BEVs whose sole power source is its battery bank as the vast majority of the U.S. experiences temperatures below freezing at some point in the year. For BEVs, this contributes to current concerns regarding vehicle range with studies being conducted on the range requirements necessary for both daily and distance driving for EVs when compared to ICE vehicles (Dalla Chiara, Deflorio, and Eid 2019). The full electrification of all on-road cars and trucks would require significant changes to both the U.S. power grid and to the infrastructure of power deliver, household charging capability, and nationwide charging stations.

The average U.S. household consumes 10, 632 kWh annually (Bastawrose 2023). This number would increase by up to 50% with the addition of an electric vehicle with the average yearly consumption of power by an EV at 4,310 kWh assuming the average American yearly driving distance of 13,476 miles per year (OHPI 2022; EVBox 2022). As such, for all current on road vehicles to convert to BEVs, the U.S. would have to increase its power generation by a minimum of 22% (Harto 2023). This metric covers just the energy requirements, and although important, doesn’t account for the infrastructure necessary for power delivery. BEVs and PHEVs require charging stations and cabling completely different from the current infrastructure for liquid fuel powered vehicles. Not only do these stations need to be built across the US, but household residences with these vehicles would need to have the capacity to fully charge the vehicle (AFDC

2023c). Given an estimated 2.6 million new electric vehicles, cost estimates indicate that home charging costs would total $1.3 billion with an additional $940 million for new workplace, public level 2, and DC fast charging infrastructure from an analysis of major metropolitan areas (Nicholas 2019).

Furthermore, as more and more people get EVs, the end of life management for these vehicles becomes increasingly important. Life Cycle Assessment (LCA) is a methodology established by the ISO in 2006 to analyze the complete life cycle of different products and systems for their environmental impacts. From previous LCAs of EVs, the largest drivers of the environmental impacts of EVs are in the electricity production and the battery production (Marmiroli et al. 2018; Peters et al. 2017). The batteries in EVs are a significant limitation to the longevity of the vehicle where battery capacity and efficiency degrade over time and with the number of charge/discharge cycles (Birkl et al. 2017). Well-to-wheel assessments of BEVs show a strong correlation between the method of energy production and the quantity of total carbon dioxide emissions from their use (Nordelöf et al. 2014).

The production cost of BEVs can be significant and environmentally damaging as well. Both the disposal of batteries and their production can have issues regarding greenhouse gas emissions and other pollutants. From a production standpoint, ICE vehicles produce less emissions than EVs considering sources raw materials, manufacturing, and disposal. Almost all batteries end up in landfills leaching toxic chemicals into the soil. Additionally, the high flammability of batteries has led to a significant increase in battery related fires. The wide variety of batteries creates barriers to the development of effective recycling techniques. These battery types consist of lead-acid, Nickel-Metal hydride, and lithium-ion batteries with some systems implementing ultracapacitors for power storage with lithium-ion being the most common in EVs (Dawes 1956; AFDC 2023a). Much of the lead that is produced goes toward the production of lead-acid batteries for vehicles with a large portion of the lead in global commerce sourced through recycling(Singh and Li 2014). Mining the necessary materials for the production of batteries, Lithium-ion batteries in particular, requires either open-pit mining or brine extraction (IER 2023). In 2021, global production of raw materials required for battery production was 4.3 million metric tons of lead, 100,000 metric tons of lithium, and 170,000 metric tons of cobalt (USGS 2022).

1.5.5 ALTERNATIVE FUELS FOR IC ENGINES

With the current energy demand, the U.S. uses Alternative fuels reduce emissions and reliance on fossil fuels while maintaining the platforms that we as a society have grown accustomed and adapted to. The IC engine, as outlined in Section 1.2, has a very long history of research and development and the technology is very well understood by the engineering and scientific community. Furthermore, the IC engine has a recyclability that is just not currently possible for electric vehicles. While electronics still require rare metals, the continued use of IC engines for transportation and power generation leaves the small supply we have here for other technologies and does not increase the demand such that poor extraction practices are the only way to meet the increasing demand.

One of the options for the development of an alternative fuel is to redesign the engine platform in order to accommodate the differing properties of that alternative fuel. This approach encounters a similar problem to that of electric vehicles in that the existing platforms will have to be phased out while new models are introduced. While possible, the resources required to shift the industry would become expensive given its size. This problem is eliminated with drop-in fuel replacements as no changes would be necessary to the established automotive industry.

1.5.6 CURRENT ALTERNATIVE FUELS

In the market right now are several different alternative fuels which can either be run as blends with traditional petroleum fuels or in dedicated engines whose design changes to accommodate the changes in the fuel properties of that particular alternative fuel. The following section is an overview of the alternative fuels that are currently in the consumer market and those still in development for use in internal combustion engines.

Compressed natural gas (CNG) has been used for a long time in stationary applications but is now developed for on road applications in diesel trucking. This development can be attributed to the advancement of the fuel storage and delivery system that is lightweight with high pressure capacity. Spark Ignition (SI) engines can run a blend of CNG with gasoline or by using an SI engine which exclusively runs CNG. In compression ignition, a similar strategy is implemented where two primary fuels are used, diesel and CNG, or with dedicated engines. The primary changes to these dedicated engines are the fuel and intake system and the use of ignition enhancement. This can be through a small diesel injection in a separate combustion chamber to initiate flame or through the replacement of the diesel injector with a spark plug. CNG is advantageous in its cost when compared to diesel and gasoline, reduction in GHG emissions, and widespread availability (Semin 2008).

Propane is another gaseous fuel currently on the market for use in on-road vehicles that is mined in conjunction with natural gas. Propane gas, or Liquified Petroleum Gas (LPG), has been in development as a fuel for combustion engines since 1910 with 13 million propane-fueled vehicles on the road by 2009. It remains more expensive than diesel, gasoline, and natural gas but has a greater energy storage capacity in its liquid form when compared to CNG. EPA evaluation of LPG indicated its potential to reduce carbon monoxide emissions and non-methane hydrocarbons. Like CNG, however, LPG can only run in dual fuel modes or in dedicated engines due to the considerable differences in thermophysical properties from standard petroleum fuels (Werpy, Bertram, and Burnham 2010).

Biodiesel is a common way to reduce reliance on petroleum diesel through blending. As the production of biodiesel uses carbon sources from recently sequestered carbon with feedstocks including cotton seed oil, livestock fat and manure, agricultural waste, etc (Selim and Amano 2021). More modern developments in the production of biodiesels have grown to include microalgae, cyanobacteria, water hyacinth, waste cooking oil, and waste plastic (Jain, Bora, and Kumar 2023). Biodiesel is currently used in moderate to heavy duty compression ignition engines in blend percentages with petroleum diesel of up to 100% biodiesel. The most common use being in large commercial trucks in a 20% biodiesel blend (AFDC 2023b). Other applications for biodiesel include construction and agriculture, diesel locomotives, inland waterways and oceanic vessels, residential heating, and power generation. Some of the drawbacks for biodiesel include are due to its increased viscosity and density and higher freeze point, cloud point, and pour point leading to potential clogs in the fuel system and reduced combustion efficiency (McCormick and Moriarty 2023).

Although it’s primarily used in SI engines, ethanol is an alternative fuel derived from biomass feedstocks, usually corn, most commonly used in blends with gasoline with 100% ethanol used in specific engine designs. It is widely regarded as a renewable fuel for blending with gasoline in SI engines as it has favorable physiochemical properties and is produced from renewable sources. The current maximum blend percentage for use in non-specific SI engines is 10% ethanol with flex fuel engines increasing to 85% ethanol. The oxygen content in ethanol increases combustion efficiency reducing the impact of fuel rich zones in the combustion chamber. In current on-road blend percentages, the effect of the increase in oxygen content with the addition of ethanol is apparent in the decrease in carbon monoxide and unburned hydrocarbon emissions (Iodice and Cardone 2021). Ethanol continues to be researched for use in internal combustion engines with development of injection strategies for use in compression ignition engines for expanding the potential for emissions reduction through the use of ethanol (Gainey et al. 2022).

Along the lines of alcohol alternative fuels in development is methanol for use in compression ignition engines. Methanol has similar advantages to ethanol as both can be sources from processing biomass and produce little to no soot from their combustion. Both alcohols face issues in regard to their fuel characteristics and use in compression ignition engines. To overcome both thermophysical and autoignition differences, design changes and new strategies must be implemented on the conventional diesel engine. As density, viscosity, lubricity, and heat of vaporization are vastly different between ULSD and methanol, the injection and fuel delivery system for the alcohol requires total augmentation from the fuel system used for ULSD. Additionally, methanol has a much higher autoignition temperature of 450°C when compared to 250°C for ULSD due to its high resistance to autoignition. The most common method of compensating for the property of methanol is using a dual fuel method with a smaller injection of diesel to act as a chemical spark to initiate combustion (B. Wang et al. 2019; Honecker et al. 2023).

Though it has been in development for compression ignition engines since the 80’s, hydrogen, in recent years, has gained more traction in the field of combustion science for its prospects as a zero carbon fuel in compression ignition engines (Ikegami, Miwa, and Shioji 1982). For implementation in compression ignition engines, hydrogen faces similar issues to that of CNG and LPG but emphasized as its density is one tenth that of natural gas and an autoignition temperature 45°C higher than natural gas. The primary advantages of hydrogen as a fuel are its high energy content per unit mass and the absence of carbon resulting in no CO_2 or CO emissions from its combustion. Hydrogen is sourced through natural gas reforming, gasification, or electrolysis. While gasification and natural gas reforming are methods that still rely heavily on fossil fuels for production, electrolysis provides the opportunity for hydrogen to be stored as a liquid fuel in the form of water or ammonia and separated using electricity for combustion. Hydrogen is used in dual fuel operations with diesel or with methane for reduction of combustion instabilities due to its high resistance to autoignition. For 100% hydrogen operations, initiated ignition must be implemented in the form of a glow plug or spark plug (Dimitriou and Tsujimura 2017). Emissions from hydrogen combustion while completely eliminating carbon emissions, face issues with a sharp increase in NOx emissions which must be removed through catalytic conversion (Onorati et al. 2022).

Ammonia is mentioned in the previous paragraph as a potential storage mechanism for hydrogen combustion, but it has surfaced in recent years as another potential alternative fuel for zero carbon combustion. Ammonia can be produced through the reaction of renewably produced hydrogen and nitrogen from the air and has been used as fertilizer, chemical raw material, and refrigerant for the past 100 years. Unlike hydrogen, CNG, and LPG, it is liquid at standard temperature and pressure although its thermal properties in terms of boiling point and condensation pressure are very similar to those of propane. Ammonia combustion, as with previously mentioned fuels, faces several combustion challenges with its low flammability and high NOx emissions (Kobayashi et al. 2019). In spark ignition engines, low research into the accurate combustion modeling of ammonia is taking place to better understand the flame mechanisms and potential areas for in-cylinder reduction of NOx emissions (Duynslaegher et al. 2012).

1.6 FISCHER-TROPSCH SYNTHESIS

The Fischer-Tropsch process was invented in Germany in the 1920's. This process is a method of producing liquid fuels from coal, natural gas, or biomass. Fuels derived from coal are known as coal-to-liquid (CTL) and fuels derived from natural gas are referred to as gas-to-liquid (GTL). Gasification is the first process of syngas production. Clean syngas exits the gasification process to be taken to the second process known as Fischer-Tropsch synthesis. The syngas is converted to wax, hydrocarbon condensate, tail gas, and reaction water. These products are then broken down into lighter weight hydrocarbon liquids through the use of hydrocracking in the presence of hydrogen. The tail gas is sent to the hydrogen recovery unit which is used to extract the required quantity of hydrogen for the was hydrocracking. The complete reaction process produces different liquids of different hydrocarbon weights which can be used in a variety of applications (Crocker, 2010). A schematic of this process is shown in Figure 5.

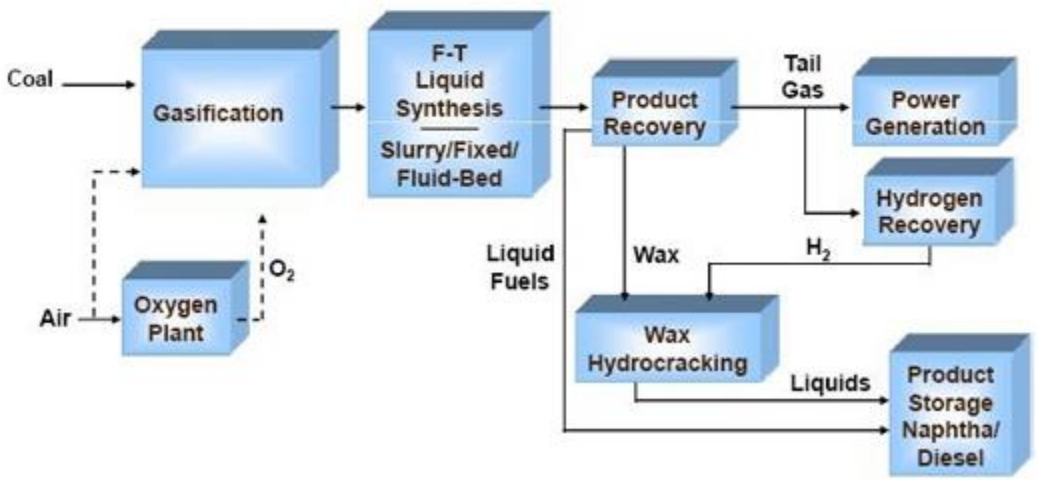

Figure 6: Fischer-Tropsch Synthesis Diagram (Crocker 2010)

1.6.1 Fischer-Tropsch Synthetic Fuels: Gas-to-Liquid (GTL) and Coal-to-Liquid (CTL)

Natural gas and coal are in abundant supply in the US and the extraction methods pose less danger to the ecosystem than oil extraction, especially offshore drilling. Additionally, sources of methane gas can be shifted to alternative, renewable sources with the extraction of methane from the decomposition of agricultural and farming waste improving the environmental impact of fuel production when compared to conventional petroleum fuel. Both coal and natural gas are prime candidates for the application of the Fischer-Tropsch process for the production of synthetic fuel. The change in feedstock, however, causes significant differences in the properties of the resulting fuel. Applying the Fischer-Tropsch prosses to gaseous methane/natural gas produces a liquid fuel referred to as Gas-to-Liquid with a very high affinity for autoignition composed primarily of iso-paraffins and normal paraffins while applying the same method to coal The Gas Chromatographic distribution for the hydrocarbons in Fischer-Tropsch GTL and CTL can be seen in Figure 6. Hydrocarbon content for each fuel is then further grouped into paraffin structure in Figure 7.

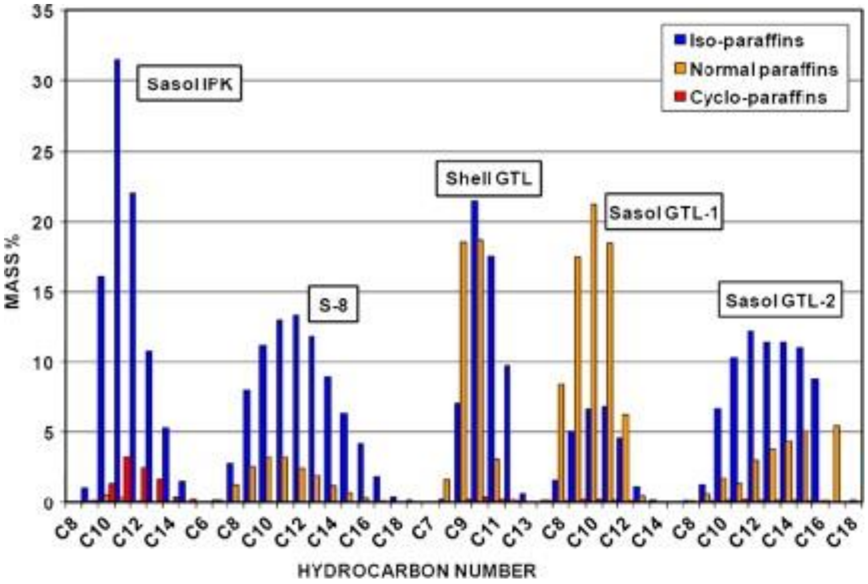

Figure 7: Comparative Hydrocarbon Distributions of Various Synthetic Aviation Fuels(Moses 2008)

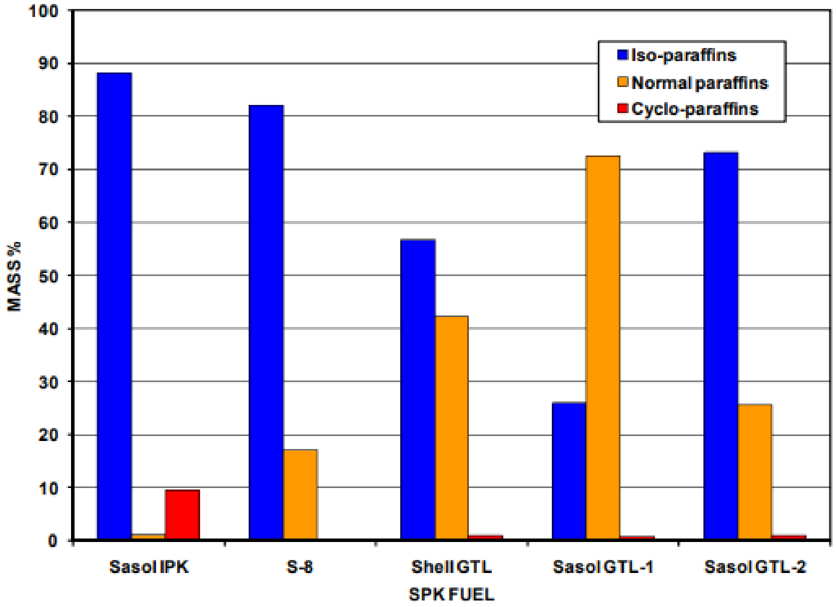

Figure 8: Structural Paraffin Content of Various Synthetic Aviation Fuels(Moses 2008)

1.7 STATEMENT OF HYPOTHESIS AND CRITERIA FOR SUCCESS

Properties of ULSD vital for engine performance can be matched through the implementation of fuel blending of the alternative fuels, Gas-to-Liquid (S-8) and Coal-to-Liquid (IPK). The final blend would then function as a drop-in fuel replacement for ULSD in multiple engine platforms with no alterations to any of the subsystems within the configuration. This would be achieved through the application of careful analysis methods for the characterization of the thermophysical, combustion, and autoignition properties of alternative fuels, accurate comparisons can be made between the alternative fuels and the conventional petroleum fuel, ULSD.

CHAPTER 2

LITERATURE REVIEW

2.1 COMBUSTION AND PERFORMANCE OF ALTERNATIVE FUELS

Charitha et. al. carried out a study on reactivity-controlled charge compression ignition on a conventional compression ignition diesel engine. For the low reactivity fuel, cotton seed biodiesel (COME) was injected into a modified intake manifold using a port fuel injector. The high reactivity direct injection used conventional diesel. The study then looked at the smoke and NOx emissions from the test. Results saw the reduction in smoke and NOx emissions with the addition of port fuel injected COME. Decreasing at a lower percentage of COME PFI, were CO_2 and HC emissions. This trend shifted with increasing percentages of PFI COME increasing the CO_2 and HC. An observed increase in the brake thermal efficiency was recorded for all loads. For RCCI as compared to CDC, lower exhaust gas temperatures and brake specific fuel consumption was reduced. The results indicate a drop in NOx emissions with the introduction of COME. At 30% COME, smoke concentration decreased as well as an increase in the brake thermal efficiency. Further improving the performance of the engine was the observed reduction in ignition delay with the addition of COME in RCCI (Charitha et al. 2019).

Santos et. al. studied the debate and the mechanisms for Fischer-Tropsch synthesis in terms of the main catalysts, industrial process requirements, and chemical reaction kinetics. The methods of obtaining synthetics fuels from synthetic gas are known as Fischer-Tropsch synthesis. FT is a synthesis method which uses a metallic catalyst to convert syngas into hydrocarbons and the chemical precursors to hydrocarbons. Biosyngas is recognized as a potential substitute for other nonrenewable resources such as conventional fossil fuels. It is through the continuing study on the FT process that aids in the development of purer and more economically viable resultant fuels. Gasification and the production of synthetic fuels are directly coupled to the FT process (Santos and Alencar 2020).

Marchese et. al. studied the conversion of carbon dioxide to use in power to liquid applications. For conversion of carbon dioxide into synthetic value-added products, a possible solution is the power-to-liquid pathways. Studied in this paper are the different options for synthesis of Fischer-Tropsch fuels. This study looks at the potential for various processing variables to produce the most efficiency out of the FT synthesis method. Ideal parameters were determined for the FT process. Determinations on the efficacy of two different processes were conducted to determine the ideal application for the power to liquid process. The first case was used at RWGS reactor while the second case used a SOEC electrolysis operation. Both reaction processes were found to have different ideal operating parameters with a few parameters used to increase performance in both cases. This expands the applications for which these operations can be conducted (Marchese et al. 2020).

Dooley et. al studied the combustion kinetics of synthetic paraffinic kerosene SPK jet fuel to a known, experimentally validated surrogate fuel. The surrogate fuel was formed such that the combustion properties were matched to emulated gas phase chemical kinetics of the SPK fuel S-8. S-8 is a Fischer-Tropsch kerosene derived from natural gas and is used as an aviation fuel. Surrogate compounds for this fuel were identified to be iso-octane and n-dodecane. Combustion phenomena used to determine the surrogate fuel’s viability are oxidative reactivity, autoignition behavior, and strained extinction limits of diffusion flame. Derived cetane number is used as a determination for autoignition characteristics. The DCN of iso-octane, n-dodecane, and S-8 were found to be 17, 78, and 58.7. By blending 51.9% n-dodecane and 48.1% iso-octane a fuel surrogate can be created which has a DCN of 58.7 for use in modeling S-8 (Dooley et al. 2012).

Ryder et. al. performed a computational analysis of aerospace S-8 and JP-8 in combustor sector performance. This research is relevant to modern aircraft as fuel blends of up to 50% synthetic fuels such as S-8 are currently used in civil and military flights. These fuels are considered fully compatible with aircraft in use in terms of performance, emissions, and fueling system. It is these properties which this study aims to investigate using computational analysis. Two baseline fuels that are used in the experiment are JP-8 and Jet-A. Computational analyses of synthetic paraffinic kerosene are compared to these baseline numbers. Computational analysis of flow structure and thermal profiles were conducted on JP-8, S-8 and a blend of 50% S-8 and 50%

JP-8. Rake temperature differences showed enough disparity to warrant further investigation into the applicability of S-8 in turbine fueling schemes (Ryder et al. 2010).

2.2 AUTOIGNITION CHARACTERISTICS AND THE REGIONS OF COMBUSTION

Low temperature combustion is the region of fuel combustion which includes the area of low temperature heat release (LTHR) and negative temperature coefficient (NTC) region. This region is associated with the formation of cool flames (Nayagam 2012). These cool flames are described as areas in which only a small portion of the reactants combust before being quenched. These flames emit a faint light blue light and can happen multiple times during low temperature combustion (Heywood 2018). These cool flames are then followed by hot flames associated with high temperature heat release. These two areas of combustion are known as two-stage ignition (Heywood 2018). Derived cetane number is a value which relies on the duration of low temperature combustion. Additionally, this region of low temperature combustion plays a role in the emission output (Ju 2019). LTC region and low temperature ignition (LTI) have been found to have a strong connection to the functional equivalence ratio of combustion. This was determined in a low temperature combustion study by Colket et. al. correlating the lean burnout limit to derived cetane number (Colket et al. 2012).

2.3 COOL FLAME FORMATION AND LOW TEMPERATURE HEAT RELEASE

One of the most pressing issues facing the world today is the increase in greenhouse gas (GHG) emissions causing irreversible changes to the atmosphere. The primary cause of these emissions is from the use of fossil fuels in compression ignition and turbine engines for use in transportation, power generation, and agriculture. A study by Grigoratos et. al looked at the GHG's and regulated emissions produced from a prototype compression ignition engine. This engine was designed to run on natural gas. The engine was tested in comparison to conventional compression ignition engine which was used as a base to design the new natural gas engine. The new design saw a marked reduction in CO_2 emissions as well as NOx and CO emissions. Total hydrocarbon (THC) and CH_4 emissions increased with the new design. It was concluded that the new concept would require additional aftertreatment systems before it was road capable (Grigoratos et al. 2016).

Another study involving the use of alternative fuels and their GHG emissions was conducted by Gokalp et. al. on the performance and emissions of a compression ignition engine fueled by marine diesel and soybean methyl ester. The feasibility of biodiesel as a replacement has to do with the fuel properties as well as the emissions produced. A constant engine torque and load was used at various engine speeds. Marine fuel was compared to biodiesel for its emissions profile as well as three blends between the two fuels. Peak thermal efficiency was achieved at 5% biodiesel in marine fuel. The addition of biodiesel reduced the particulate matter, CO, and NO_x emissions (Gokalp, Buyukkaya, and Soyhan 2011).

Morita et. al. studied the variation of densities and viscosities in diesel fuel and their effect on exhaust emissions. A range of 9 different fuel types were investigated, six of which were commercially available diesel fuel. The other three fuels included a kerosene fuel, a high-density diesel fuel, and an automotive diesel from Singapore. The lowest viscosity was measured to be 1.52 (mm^2/s) and maxed out at 5.44 (mm^2/s). Density ranged from 0.796 (g/cm^3) to 0.856 (g/cm^3). A strong correlation was found between particulate matter emissions and fuel density. The greater the fuel's density, the greater the PM emissions. A spray analysis was performed and found a correlation between an increase in the fuel's viscosity and an increase in the Sauter Mean Diameter (SMD) of the researched fuel. Total Hydrocarbon (THC) and CO emissions were found to have a much closer link to the cetane number of the fuel than to either the density or viscosity (Morita and Sugiyama 2003).

2.4 Fuel Characteristics and Chemical Composition

One of the primary factors which affect the autoignition characteristics of a fuel is the chemical composition. The difference between the combustion of n-paraffins, iso-paraffins, cycloparaffins, naphthalenes, and aromatics as well as the variations between the different branch chain iso-paraffins greatly influences the chemical properties of the fuel. A study conducted by Wang et. al. looked at the variations in the chemical composition of a variety of different conventional and synthetic aviation fuels and their effect on the autoignition behavior of that fuel. This study concluded that the fuels which contained a higher weight percent of linear n-paraffin and light, branched chain iso-paraffin hydrocarbons displayed more significant low temperature combustion regions (X. Wang et al. 2020).

A study conducted by Elmalik et. al. quantified the role of hydrocarbons on Gas-to-Liquid (GTL) fuel characteristics. The study focused on the primary hydrocarbon building blocks of n-, iso-, and cyclo- paraffins. The researched properties included density, freezing point, flash point, and create content. The study also found that aromatics are of primary concern when looking at the emissions output of the researched fuel. Cyclo-paraffins were found to cause a significant increase in the fuel's density. Cyclo-paraffins were also found to have a negative relationship to the heat of combustion (Elmalik et al. 2013).

Nabi et. al. studied the effects of oxygenated fuels on the energy and exergy parameters in the context of the first and second law of thermodynamics. The base fuel used was a Fischer-Tropsch fuel as its properties are very similar to those of diesel. Diesel blends were then created to test the changes in energy and exergy parameters. These blends were also oxygenated and contained different ratios of oxygen. Results showed very little change in the parameters based on the fuel blend and oxygen ratio (Nabi, Hustad, and Arefin 2020).

2.5 INJECTION SYSTEM DYNAMICS

2.5.1 LUBRICITY

Diesel fuel pumps and injection systems are designed to be lubricated by the fuel itself. Traditional measurements of the fuel's lubricity were done through rough estimate based on the fuel's viscosity. As fuel progresses, this assumption does not remain true as certain fuels, such as ultra-low sulfur diesel, have a higher viscosity but lower lubricity and less wear protection.

Barbour et. al. studied the lubricative properties of diesel and its effect on the injection system and fuel components of a standard compression ignition engine. It was found that diesel lubricity is largely provided by trace amounts of polar compounds which form a protective layer on the surface of the metal. Sulfur compounds do not correlate with these compounds but rather the nitrogen and oxygen containing hetero compounds which are most important. The process which reduces the sulfur content of the fuel also destroys these polar compounds. Lubricity additives help maintain the standard of lubricity (Barbour, Rickeard, and Elliott 2000).

Lacey et. al. reviewed the effect of the fuel's lubricity on component systems, the definitions for which lubricity can be measured, and the mechanisms and categorization of various lubricative properties. These systems were reviewed as they correlate to time as these models and methods of measurement changed through history. Properties were also compared between different countries as fuels developed in different locations maintain different fuel properties. The primary focus for lubricity research is aimed toward diesel fuel and much less so toward gasoline. This is due to the heavy reliance of compression ignition engines on the lubrication provided by the fuel (Lacey and Howell 1998).

Sukjit et. al. studied the effect of blending biodiesel with Ultra Low Sulfur Diesel (ULSD) on the lubricative properties of the resulting fuel. The biodiesels used in the investigation include fatty acid methyl esters derived from RME and gas-to-liquid (GTL). The blends were researched in a high-frequency reciprocating rig and the mating surfaces analyzed at the microscopic level using a scanning electron microscope (SEM) to determine the wear scar diameter and profile. With the reduction in the sulfur content of diesel, the lubricity is reduced.

This leads to the need to include a lubricity additive to meet the requirements for diesel engines. GTL fuel needs this additive as well to function as a standalone fuel. The lubricity of each of the fuels saw significant improvement with the addition of the RME biodiesel with only a 10% addition. The addition of RME, however, increased the formation of residue as observed by topographical analysis. This residue did not appear in mixture which contained a large quantity of GTL fuel. This is despite having a similar percentage of hydrocarbons when compared to RME and ULSD. It is important to note there is a tradeoff between the increase in the fuel's lubricity and the reduction of carbonaceous deposits (Sukjit, Dearn, and Tsolakis 2011).

2.5.2 OHNESORGE NUMBER AND MIXTURE FORMATION

Ohnesorge number is a dimensionless value which associates the viscous forces in a fluid and is described below in Equation 1. Low Oh numbers ($Oh<0.1$), indicate a higher affinity for that droplet to break apart. In this equation μ is the dynamic viscosity, ρ is the density, σ is the surface tension, L is the characteristic length, Re is the Reynold's number, and We is the weber number. An illustration of a breaking droplet as gas is passed over the droplet resting on a surface is shown in Figure 9.

$$Oh = \frac{\mu}{\sqrt{\rho\sigma L}} = \frac{\sqrt{We}}{Re} \quad \text{Eq.1}$$

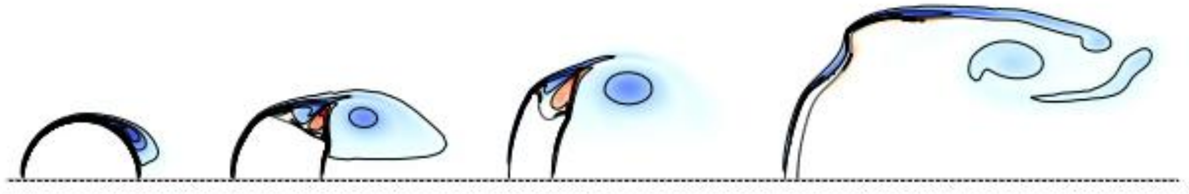

Figure 9: Representation of a Breaking Droplet in a Fluid-to-Fluid Interaction (Marcotte and Zaleski 2019)

Weber number is the association of drag force and cohesion force and is described in Equation 2. Further variables in this equation include C_D for the coefficient of drag, v representing the velocity, and l for the characteristic length. This number is used in cases where the interaction and interference between two fluids is analyzed. As We increases, drag forces overcome cohesive forces and the droplet breaks more rapidly.

$$We = \frac{Drag\ Force}{Cohesion\ Force} = \left(\frac{8}{C_D}\right)\frac{\left(\left(\frac{\rho v^2}{2}\right)C_D \pi \frac{t^2}{4}\right)}{(\pi\ l\ \sigma)} = \frac{\rho v^2 l}{\sigma} \qquad \text{Eq. 2}$$

Radhakrishna et. al. studied the secondary atomization characteristics of fluids with high Ohnesorge numbers. This study identifies an Oh less than 0.1 as low and aims to investigate droplet breakup at Oh numbers between 0.5 and 1 with a We of 30-120. Fluid droplets were quantified using Particle Image Velocimetry (PIV) and Digital in-line Holography (DIH). Blends of glycerin and water were used to create fluids of increasing We and Oh numbers. It was found that, unlike in fluids with an Oh number less than 0.1, the fluid tends toward shapes with a smaller surface area to volume ratio where despite the observed droplet deformation, no breakage is observed. This is in contrast to fluids of Oh<0.1 which tend to form sheets the fragment at the periphery (Radhakrishna et al. 2021).

Contrasting this study is a study by Marcotte et. al. on the density dependence of fragmentation at low Oh numbers. Single liquid drops were studied for fragmentation dynamics when subjected impulse exerted by a unidirectional gas stream for the effect of fluid-to-fluid interaction with high density contrast. Two primary regimes were analyzed which characterized the method and form by which droplets within the stream broke. Additionally, there was found to be significant differences in fragmentation threshold despite small changes in the ratio between liquid and gas densities (Marcotte and Zaleski 2019).

As it depends on density, viscosity, and surface tension, Ohnesorge number is a good determination of the fuel's atomization and spray distribution characteristics in an internal combustion engine. A study conducted by Shah et. al. studied the effect of preheating fuel on the spray atomization and droplet distribution by calculating the Ohnesorge number. Though the primary focus of this study was to determine the influence of preheating on the spray pattern, Ohnesorge number was used as a metric to compare temperature to spray pattern as it relates all the values which influence it. Each value changes with an increasing temperature though not all at the same rate giving merit to the reliance on Ohnesorge number. The study found that the increase in temperature from room temperature to 90°C decreased the SMD by upwards of 50%. Additionally, from the Ohnesorge determination, it was found that preheating the biodiesel karanj oil changed the fuel properties such that it was comparable to diesel fuel (Shah and Ganesh 2018).

Properties which affect the spray atomization and therefore combustion characteristics of a fuel are the viscosity, density, and surface tension (Lefebvre and McDonnell 2017). Fuels with a higher density, while they may contain more energy per unit volume, do not atomize as well in the combustion chamber. Alpetkin et. al. studied the two different commercially available diesel fuels and their blends with biodiesels produced from six different vegetable oils (sunflower, canola, soybean, cottonseed, corn oils, and waste palm oil). Blends were prepared by volume of B2, B5, B10, B20, B50, and B75. Fuel lubricity and density were measured via ASTM standards. Generalized equations could be used to predict the density, and viscosity of each blend as proposed by Arrhenius and described by Grunberg and Nissan. There was found to be an acceptable agreement between the measured and estimated values for density and viscosity. Both values increased with the increase in the volumetric percentage of biodiesel present in the blend.

Density equation used: $D = Ax + B$ where D is density, A and B are coefficients, and x is the percentage of biodiesel.The density of biodiesel was found to range between 0.9 and 0.86 g/cm3. Waste palm oil had the lowest density among the trial group with soybean oil biodiesel having the highest. Though biodiesel has a consistently higher density than diesel, it has a lower energy content. The viscosity of the researched fuels ranged from 3.97-4.34 mm2/s which were also consistently higher than the viscosity of diesel. Both the density and viscosity of the blended fuels increased with the volumetric percentage of biodiesel (Alptekin and Canakci 2008).

The surface tension of a fuel is a property of the fuel which is a factor characterizing the spray atomization of that fuel. While the density of the fuel resists fuel atomization, the surface tension of the fuel adversely affects droplet formation. Fuels which have a higher surface tension are less likely to form smaller droplets (Lefebvre and McDonnell 2017). Ejim at. Al. studied the atomization of biodiesel and biodiesel blends as it relates to a direct injection diesel injector. Several biodiesels as well as their blends for analyzed at 80°C. It was found that fuel which had a similar surface tension and density atomized with an equivalent droplet size and distribution. Of the fuel properties which affect the atomization of fuel, viscosity was found to have the largest effect on Sauter Mean Diameter (SMD) and density had the smallest effect on SMD with surface tension in between (Ejim, Fleck, and Amirfazli 2007).

Another study by Mousavi et. al. focused on predicting the surface tension of fatty acid ethyl esters and biodiesel fuel for use in predicting spray pattern. This prediction method uses the equality of chemical potentials between the vapor-liquid interface and liquid bulk to determine the surface tension. Surface tension was predicted from 303.15K to353.15K for a series of 31 different biodiesels. The use of this method produced results which closely matched the experimental values for surface tension. For each of the fuels, surface tension decreases with the increase in temperature indicating fuels at a higher temperature (Mousavi, Romero-Martínez, and Ramírez-Verduzco 2020).

CHAPTER 3

EXPERIMENTAL METHODOLOGY AND INSTRUMENTATION

3.1 OVERVIEW

In this section, a series of fuel analysis investigations were performed to determine the thermophysical properties of each of the neat fuels and the final blend. The rotational viscometer determines the viscosity of the fuel based on the torque applied to the spindle caused by the shear rate of the fuel. Lubricity was determined using a pin-on-disk tribometer to verify the blend adquitely met the lubrication criteria outlined in the criteria for success. A calorimetry analysis was conducted to determine the lower heating value of each of the neat fuels and the final fuel blend. A thermogravimetric (TGA) and differential thermal analysis (DTA) will be performed to determine the volatility as well as the exothermic and endothermic reactions of the oxidation of the fuel as temperature is increased to 600°C. A Constant Volume Combustion Chamber will be used to determine the DCN of the neat fuels as well as the different blends to determine the ideal mixture of S-8 and IPK that will create the desired DCN. If these fuel tests conclude that the fuel blend meets acceptable parameters for proper engine function, a dynamic engine test will be performed using two different single cylinder, compression ignition research engines. As this blend is intended as a drop-in replacement for ULSD, two engine platforms were chosen for verification of performance across different engine designs and configurations. The performance and emissions characteristics of combustion using this fuel blend will be determined for this investigation and compared to conventional ULSD and neat alternative fuels.

3.2 FUEL ANALYSIS

3.2.1 CONSTANT VOLUME CALORIMETRY

The determination of the lower heating value of the research fuel is a representation of the energy content within the fuel from combustion. This value was measured for the neat fuels as well as the final blend using a constant volume calorimeter. The Parr 1341 constant volume calorimeter was the instrument used to determine the heat of combustion. In this analysis, approximately 0.5 g of fuel was placed in a crucible and placed in a pressurized container. This container was pressurized to 25 atm with pure O_2 and submerged in 2kg of water.

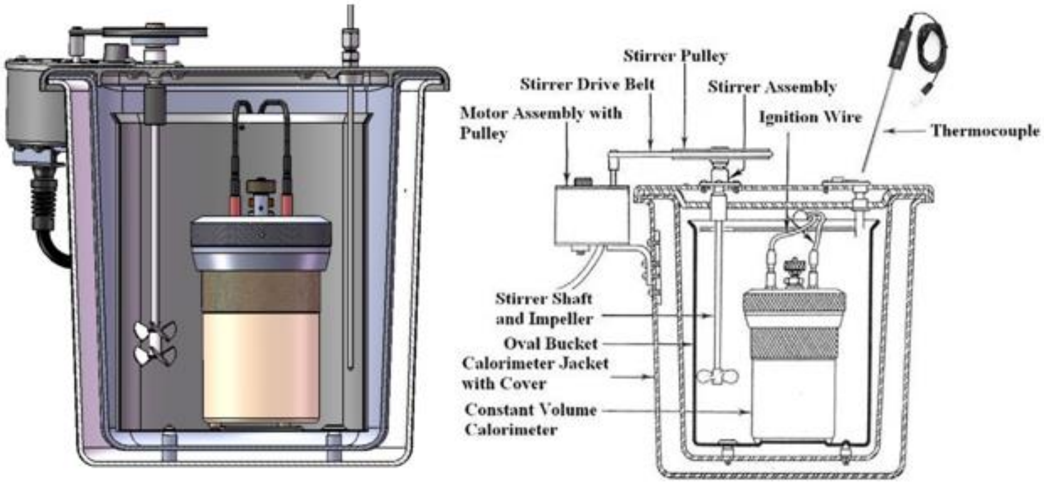

Figure 10: Parr 1341 Plain Jacket Constant Volume Calorimeter (Parr 2023)

The water was agitated with a small impeller and the change in temperature due to the combustion of the fuel is used to determine the net heat of combustion. The pressure vessel is also equipped with two fuse wire connections to ignite the sample fuel. These connections are used to supply a current to the fuse wire strung directly above the fuel between the two connections. This fuse wire transferred power between the instrument and the fuel and burns as a result of the combustion of the fuel. The weight of the wire was measured before testing then and after testing to identify the quantity of the wire which was consumed during experimentation. This is used as another measurement to determine the heat of combustion of the researched fuel. An image of the apparatus as well as a cross sectional view in Figure 10.

3.2.2 Differential Thermal Analysis and Thermogravimetric Analysis

The Shimadzu DTG-60 was used for two determinations which indicate the volatility of the fuel. The Differential Thermal Analysis (DTA) and the Thermogravimetric Analysis (TGA) are both conducted during the course of experimentation using the instrument pictures in Figure 11. The DTA is a measurement of the exothermic and endothermic reactions the fuel undergoes as the temperature rises. This measurement was taken in terms of µV/mg and is displayed over temperature. The TGA is a measurement of the percent of the original mass of the fuel that is left in the pan as the temperature rises. These values indicate the transition temperature, melting point, temperature of reaction, boiling point, and vaporization rate of each of the researched fuels (Shimadzu 2018).

Figure 11: Shimadzu DTG-60 Measurement Apparatus(Shimadzu 2018)

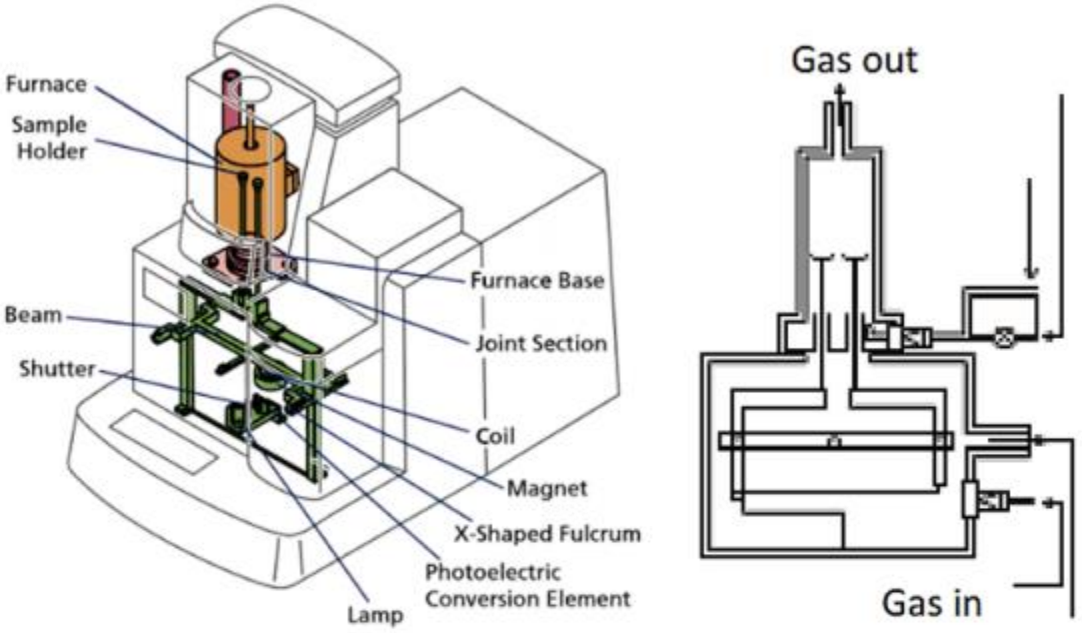

Figure 12: Schematic of the Internal Components of the DTG-60 (Selim and Amano 2021)

The test was conducted within a constant volume oxidation chamber. This chamber was purged with air at a rate of 5ml/min and increased in temperature from 23°C to 600°C at a rate of 20°C/min to simulate the environment in an IC engine. Two spindle scales within the chamber are sensitive to the µg level and measure the change in mass of the fuel sample. One of these pans was used for the fuel in question while the other was used to contain the baseline alumina powder. This baseline was used as a constant value reference for testing as the alumina powder loses little to no mass as it was heated. A schematic of the internal components can be seen in Figure 12.

3.2.3 BROOKFIELD DV-II +PRO ROTATIONAL VISCOMETER

The viscosity of each of the fuels as well as the blends play a vital role in the proper function of the engine. It affects the injection timing, fuel rail pressure, and the spray atomization of the fuel. This value was measured using a Brookfield DV-II +Pro rotational viscometer pictured in Figure 13. Viscosity was determined by measuring the torque applied to the spindle, SC-18, of the viscometer as the temperature if the fuel increases.

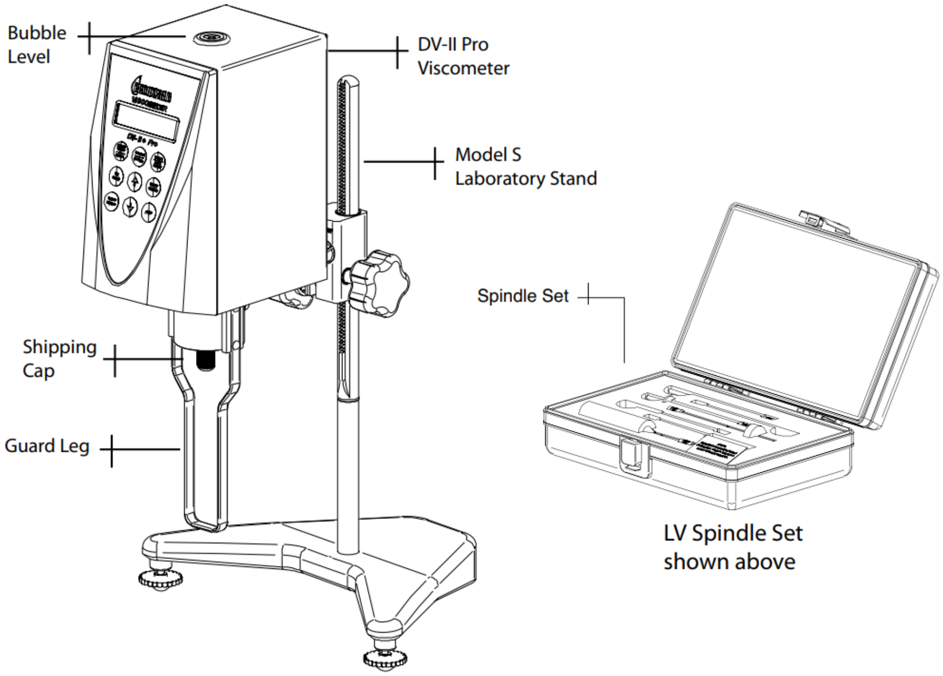

Figure 13: Schematic of the Brookfield DV-II +Pro Rotational Viscometer (Brookfield 2015)

The viscometer spindle was submerged in 7.0 mL of the given fuel such that the fluidic shear rate between the spindle and the wall can be accurately measured. The fuel was heated from 23°C to 90°C in increments of 2°C by a circulated coolant jacket. This coolant was externally heated by an Omega temperature controller with the flow surrounding the fuel in a separated coolant jacket. An image of the viscometer as well as a schematic of the spindle and coolant jacket can be seen in Figure 14.

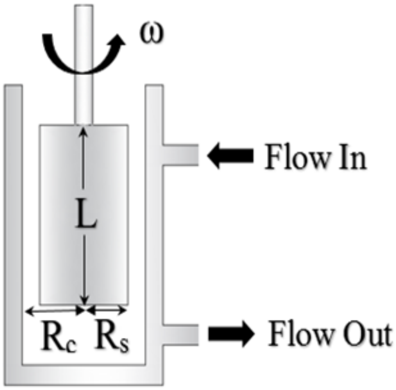

Figure 14: Schematic of the Spindle, Coolant Flow, and Descriptive Variables (Soloiu, Weaver, Parker, Brant, et al. 2022)

$$\eta = \frac{\tau}{\dot{\gamma}} \qquad \text{Eq. 3}$$

The dynamic viscosity is represented as η in units of $Pa * s$, shear stress is measured in N/m^2 represented by τ, and the shear rate is $\dot{\gamma}$ measured in s^{-1}. The SC-18 spindle was submerged in approximately 7.0 mL of fuel and rotated at a speed of 200 rpm. This spindle was chosen for its compatibility with kerosene-type fuels. The fuel was then heated by a double wall jacket of coolant to determine the drop in viscosity with the increase in temperature. Viscosity was measured from 26°C to 90 °C in increments of 2 °C. Figure 14 displays the variables for the calculation of the shear rate and shear stress. These values were determined using Eq. 4 and Eq. 5. R_c and R_s are the radii of the container and spindle and are represented in meters; and ω is the rotational velocity of the spindle rad/sec. M represents the motor torque in Nm, and L is the length of the SC-18 spindle in contact with the fuel.

$$\dot{\gamma} = \frac{2\omega {R_c}^2}{{R_c}^2 - {R_s}^2} \qquad \text{Eq. 4}$$

$$\tau = \frac{M}{2\pi {R_s}^2 L} \qquad \text{Eq. 5}$$

3.2.4 AUTOIGNITION AND COMBUSTION CHARACTERISTICS IN CONSTANT VOLUME

The PAC CID 510 Constant Volume Combustion Chamber was used to determine the apparent heat release rate, low temperature combustion properties, and the derived cetane number of each of the given research fuels. Measurements were taken by the apparatus on the pressure in the combustion chamber as well as the ignition delay and the combustion delay. These values were then used to determine the DCN using Equation 6 (ASTM 2022).

$$DCN = 13.028 + \left(-\frac{5.3378}{ID}\right) + \left(\frac{300.18}{CD}\right) + \left(-\frac{12567.90}{CD^2}\right) + \left(\frac{3415.32}{CD^2}\right) \qquad \text{Eq. 6}$$

As seen in Equation 6, the ignition delay and combustion delay have an inverse relationship to the DCN. The longer the ID and CD, the lower the DCN. This is a representation of the autoignition quality of the fuel or how readily it combusts at a given temperature and pressure. For this experimentation, A LAUDA Alpha RA chiller maintained a line of coolant at 50°C to cool the combustion chamber after each combustion event. Ultra-high purity (UHP) N_2 and O_2 were routed through the back of the apparatus. These gases were used as the air surrogate in the combustion chamber. The combustion chamber was filled with this air mixture with a volume of 0.000473 m^3. The mass of the fuel injected into the chamber stays around the same at approximately 62 mg. The method of DCN determination follows the ASTM standard D7668-14a as shown in Table 2.

Table 2: ASTM Standard D7668-14a for DCN Determination (ASTM 2022)

Wall Temp.	Fuel Injection Pressure	Coolant Temperature	Injection Pulse Width	Chamber Pressure
595.5 °C	1000 Bar	50 °C	2.5 ms	20 Bar

The pressure values were determined as an average of 15 injection and combustion cycles following 5 priming cycles. This pressure data was then used to determine temperature, Apparent Heat Release Rate (AHRR), energy released, and each of the combustion duration values. Energy released is used alongside lower heating value to determine the percent mass burned of the fuel as a function of time during combustion.

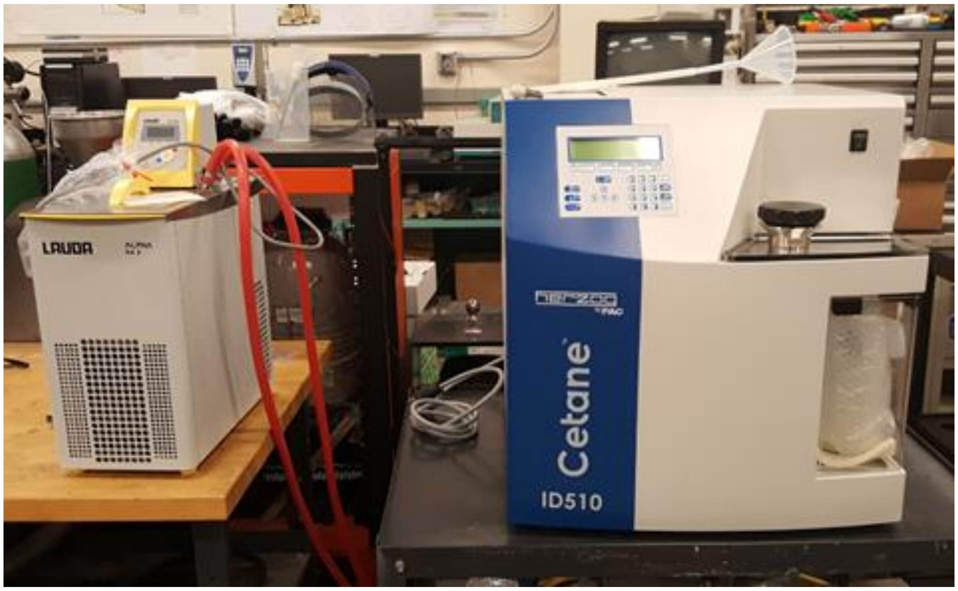

Figure 15: PAC CID 510 Experimental Setup

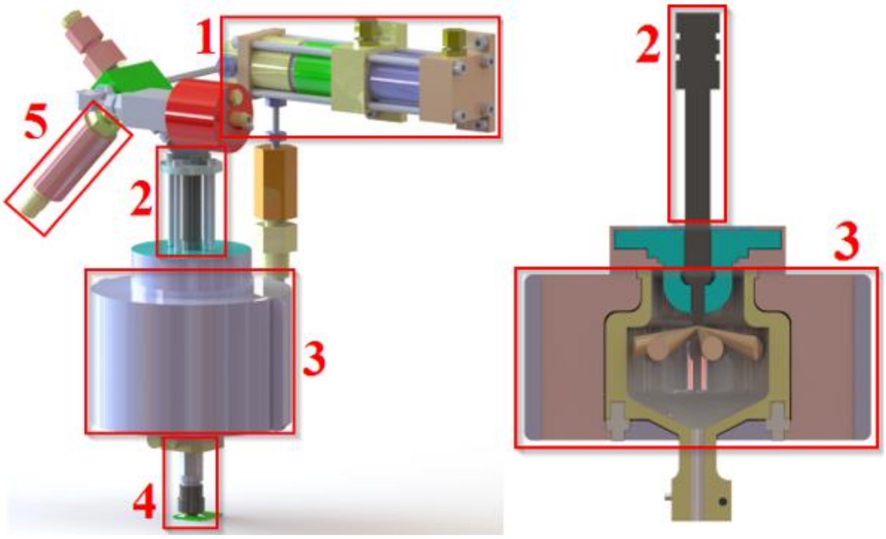

Figure 16: CAD Model of the Internal Components of the PAC CID 510

Table 3: Component Descriptions for the PAC CID 510

Component	**Description**
1	High Pressure Common Rail
2	6-Orifice Bosch High Pressure Fuel Injector
3	Insulated Combustion Chamber
4	Combustion Chamber Pressure Transducer
5	Fuel Line Pressure Sensor

3.2.5 MALVERN MIE SCATTERING HE-NE LASER

Spray profile and atomization characteristics were determined using a Malvern Spraytec He-Ne laser as displayed in Figure 17. This system was used to determine the spray and droplet distribution for each fuel injection. The laser was shown through the spray as sensors on the other side detect the changes in the laser due to the refraction from the fuel droplets. Mie scattering or Fraunhofer Diffraction theory was then used to determine the droplet pattern and distribution. The injector was set 100mm away from the laser with the spray atmosphere at standard temperature and pressure. Data collection begins at 0.1 ms before the triggered injection and continuously samples data at 10 kHz for 5 ms. The Sauter Mean Diameter (SMD) and the droplet size distribution for the fuel spray.

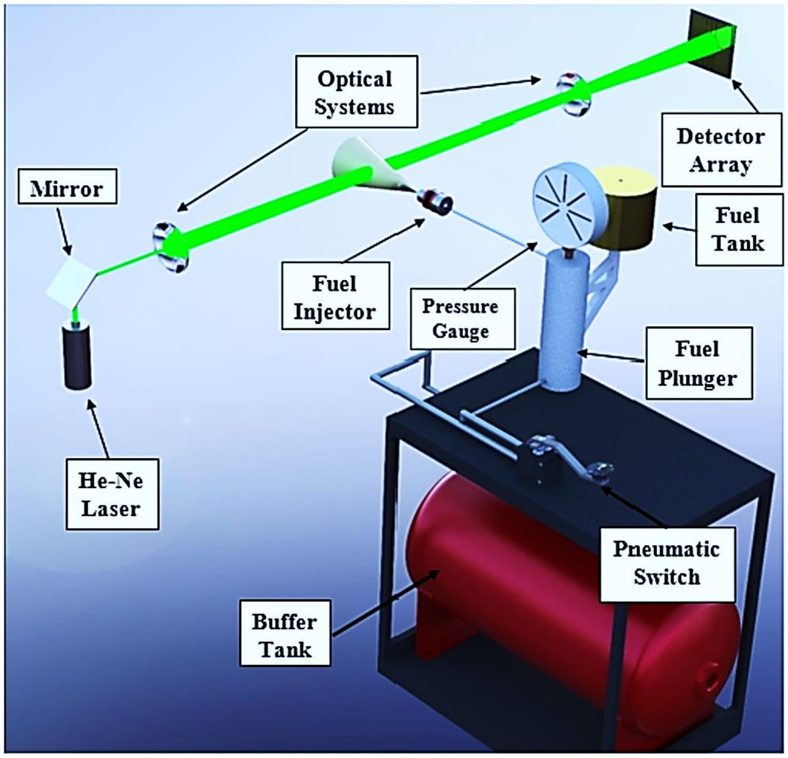

Figure 17: Schematic of the Mie Scattering Helium-Neon Laser (Soloiu, Weaver, Parker, Brant, et al. 2022)

The spray atomization, droplet formation, and mixture formation characteristics were found used Mie scattering and Fraunhofer diffraction theories. The mathematical correlation used to describe the scattering of unpolarized light by a single spherical droplet is described in Equation 7 (Sympatec 2023).

$$I(\theta) = \frac{I_0}{2k^2a^2}([S_1(\theta)]^2 + [S_2(\theta)]^2) \qquad \text{Eq. 7}$$

Here the scattering intensity, I(θ), is described as a function of its angle (θ), illuminating intensity (I_0), wavenumber (k), and distance between the detector and the scatterer (a). The angle θ describes the angle made from the centerline of the beam to the line formed from the refracted beams which occur tangent to the spherical droplet. The wavenumber, k, of the laser before interaction with the droplets is given by 2π/λ. S1(θ) and S2(θ) are dimensionless, complex functions describing the change of amplitude in the perpendicular and the parallel polarized light (Sympatec 2023).

Fraunhofer diffraction theory was used primarily for measurement of mixtures of varying materials and shapes as this theory omits the optical properties of the droplet only taking into account the refractivity index of each fuel with an assumed linear correlation between refractivity and mass percent for blended fuels. This correlation shown in Equation 8 is a simplification of the equation for I(θ). The equation includes the addition of the dimensionless parameter $\alpha=\pi x/\lambda$ with x representing droplet size.

$$I(\theta) = \frac{I_0}{2k^2a^2}\alpha^4\left(\frac{J_I(\alpha\sin(\theta))}{\alpha\sin\theta}\right) \qquad \text{Eq. 8}$$

3.3 LUBRICITY: PIN-ON-DISK TRIBOMETER

For the lubricity analysis conducted in this investigation, all neat, researched fuels and the surrogate fuel blends were investigated for the tribological differences between alternative and conventional fuel and the effect of blend additives. It is a vital metric for any system with interacting surfaces (Lyu, Bergseth, and Olofsson 2016). A series of 5 measurement points were taken for ULSD, IPK, S-8, and Methyl Oleate with additional testing conducted on the DCN optimized alternative fuel blend with the addition of a methyl oleate lubricity additive. A T-11 pin-on-disk tribometer was used with each test run for 300s per test with a 2kg applied normal force and a data sampling rate of 0.02s.

The pin-on-disk tribometer was used to determine the lubricity of the fuel blend as an indicator of its viability in an internal combustion engine. This device works by applying pressure to a spindle on a rotating disk submerged in a small amount of the test fuel. This was then left for the given amount of time to allow for the spindle to form a wear scar on the disk. The disk was weighed before testing and after testing to determine the material lost as a result of the spindle's motion. The wear scar was then viewed at a microscopic level to determine the width and depth of the wear scar. A mass percentage of biodiesel was added to proposed fuel blend until with lubricity measurement is equivalent to current on-road ULSD.

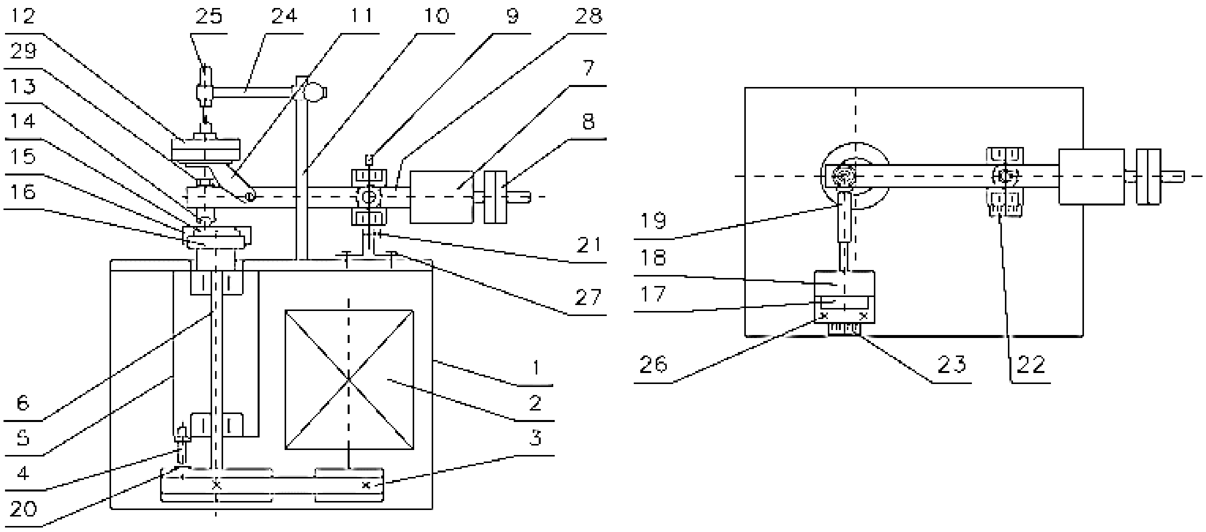

Figure 18: Pin-on-Disk Tribometer Schematic and Labeled Components (Jozwik et al. 2019)

Table 4: Component List for the Pin-on-Disk Tribometer

Label	**Component**	**Label**	**Component**
1	Frame	**14**	Sample disk
2	Motor	**15**	Disk clamping screw
3	Belt-drive gear	**16**	Keep plate
4	Impulse Sensor	**17**	Force sensor base
5	Spindle sleeve	**18**	Friction force sensor
6	Spindle	**19**	Pusher
7	Counterweight	**20**	RPM sensor pin
8	Balancing weights	**21**	Clamping screw - 1
9	Rotational Axis	**22**	Clamping screw - 2
10	Bracket	**23**	Friction radius variation scale
11	Weighing arm	**24**	Wear sensor arm
12	Weights	**25**	Inductive wear sensor
13	Sample Pin	**26**	Force sensor base clamping screw

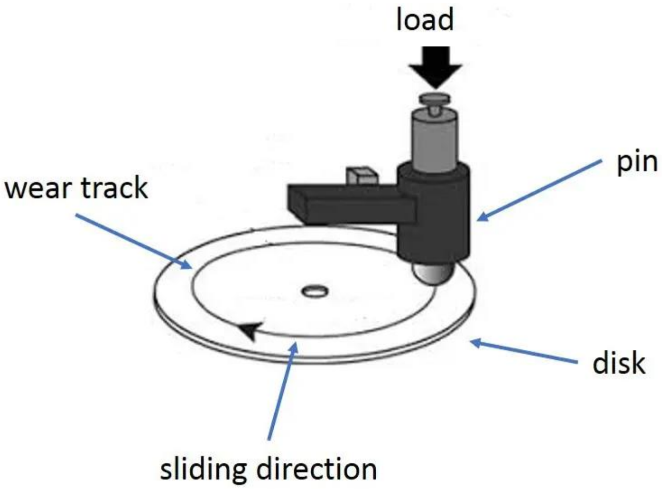

Figure 19: Diagram of Force and Load Application for the Tribometer (TriboNet 2022)

The tribometer, shown in Figures 18 and 19, is an internal belt driven by a DC motor at a constant rpm with the desired normal force load placed over the pin on the weighing arm. The sample disk is composed of AINSI 1018 steel, and the pin is made of stainless steel AINSI 316. Disks were weighed before and after testing to determine the eroded mass and measured for surface roughness using a Mitutoyo Surftest SJ 210 as shown in Figure 20. Additionally, friction force was acquired for the duration of each test using a NI 9205 DAQ (Figure 21) as measured from point 18 on the diagram in Figure 18. Additional specifications for the tribometer, surface roughness assessment tool, friction force transducer and NI DAQ can be found in Tables 5 and 6.

Figure 20: Mitutoyo Surfest 210 Surface Roughness Assessment Tool (Mitutoyo 2016)

Figure 21: NI 9205 Data Acquisition Unit (NI 2023)

Table 5: Specifications for the NI DAQ 9205(NI 2023)

Specifications	**Type 9205**
Number of Channels	16 dual-end/32 single-end
ADC resolution	16 bits
Resolution	10 bits, 1 in 1,024
Accuracy	±1% of full scales
Maximum Voltage	±30 V DC Channel-to-COM
Range	**Sensitivity**
±10 V	96.0 µV
±5 V	46.4 µV
±1 V	10.4 µV
±0.2 V	4.0 µV

Figure 22: HBM Force Transducer Type U1A (HBM 2005)

Table 6: Specifications for the HBM Force Transducer Type U1A (HBM 2005)

Type			**U1A**		
Accuracy class			0.1		
Nominal force		N	10	20	50
Nominal sensitivity	C_{nom}	mV/V	2		
Linearity deviation	d_{lin}	%	0.1		
Temperature effect on the sensitivity/10 K	TK_C	%	0.1		
Temperature effect on the zero signal/10 K	TK_0	%	0.05		
Effect of eccentricity / mm	d_E	%	0.1		
Rel. creep over 30 min	d_{crF+E}	%	0.06		
Input resistance	R_e	Ω	>345		
Output resistance	R_a	Ω	300 −400		
Isolation resistance	R_{is}	Ω	$5 \text{ x } 10^9$		
Reference excitation voltage	U_{ref}	V	5		
Operating range of the excitation voltage	$B_{U,G}$	V	0.5 ... 6		
Nominal temperature range	$B_{t,nom}$	oC	−10 ... +50		
Operating temperature range	$B_{t,G}$	oC	−20 ... +50		
Reference temperature	t_{ref}	oC	+23		
Max. operational force	(F_G)	%	120		
Limit force	(F_L)	%	1000	500	200
Breaking force	(F_B)	%	2000	1000	400
Static lateral limit force	(F_Q)	%	200	100	40
Nominal displacement	S_{nom} f_G	mm	0.28	0.21	0.2
Fundamental resonance frequency		Hz	300	450	**700**
Weight		kg	0.3		
Rel. permissible vibrational stress	$\mathbf{F_{rb}}$	**%**	70		

Friction force for each fuel test was taken as a function of time with mass and surface roughness taken before and after testing. Each disk was cleaned with degreaser before weighing and measuring surface roughness and before running the test. The disk was again cleaned with degreaser before it was remeasured after testing. The wear disks after cleaning were then taken for imaging and depth analysis of the wear scar using a Keyence VHX-1000E digital microscope as pictured in Figure 23. Each sample disk marked with its associated fuel was placed on the microscope platform and imaged for surface topography. The “depth up” setting was used to determine the wear scar depth and width for each sample scar.

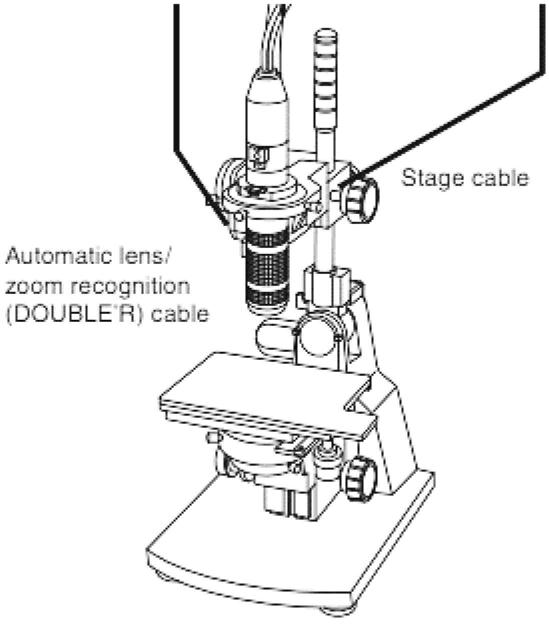

Figure 23: Keyence VHX-1000E Digital Microscope (Keyence 2012)

3.4 FUEL BLENDING

3.4.1 AUTOIGNITION CHARACTERISTICS: S-8/IPK FUEL BLENDS AND OPTIMIZATION

For the determination of the ideal fuel blend ratio, each of the neat fuels was investigated in the CVCC for baseline measurements of DCN, ID, and CD. As was established in previous investigations and further verified in this study, the synthetic GTL kerosene, S-8, has a DCN significantly higher than the standard for both CN and DCN for on-road ULSD in the United States and Europe while synthetic CTL kerosene, IPK, has a DCN far below diesel standards (Soloiu et al. 2020). Given this baseline determination, blends of IPK and S-8 were investigated in the CVCC to determine the effect of blending on DCN, ID, and CD and to approximate the percentage necessary to match a specified DCN. The F-T blends were based on the concentration of IPK in the blend and included 25%, 50%, and 75% by mass with S-8. With sufficient data points on the ID, CD, and DCN of the F-T fuels, linear regression modeling was used to determine with a higher degree of accuracy the DCN of these synthetic fuels and subsequent blends. The DCN equation for Ignition Quality Testing as outlined by ASTM standard D6890-18 was used in the linear regression modeling to determine the coefficients in each term specific to the F-T fuel testing. Using the resulting equation, a blend percentage of 40% IPK and 60% S-8 was determined as the optimum blend percentage to achieve a predicted DCN of 50. This DCN matched surrogate blend, consisting of IPK and S-8, will be referred to as S1 for all of the following investigations, determinations, and discussions.

3.4.2 BIODIESEL ADDITION

As confirmed in Section 4.1.1, one of the major concerns regarding the use of F-T fuels in current engine platforms is their lack of lubricity. To maintain the objective of creating a drop-in replacement using strictly alternative fuels, the most promising method of improving the lubricity of the surrogate is through the addition of biodiesel or a biodiesel component. As established in (Sukjit, Dearn, and Tsolakis 2011), biodiesel has been shown in previous research to increase fuel lubricity when used as an additive. Methyl oleate was selected to act as the lubricity additive as it is a FAME with consistent and well researched fuel properties, high viscosity (Section 4.1.1), and high lubricity (Section 4.1.2). A blend percentage of 3% by mass was chosen as this percentage is low enough to have very little to no effect on combustion while providing the greatest benefit to the lubricity of the resulting fuel blend. This final surrogate blend will be referred to as S2 for all of the following investigations, determinations, and discussions.

3.4.3 FINAL BLEND TESTING

Once the final blend amounts are determined, the final fuel blend was run through all of the fuel tests outlined previously in Chapter 3. This testing was vital as it will determine whether the fuel meets the standard necessary for proper engine function. Should the results of the blend testing conclude that the fuel blend meets the proper fuel property standards, research on this drop-in fuel replacement will continue to the dynamic engine setting for further investigation into the performance, emissions, and efficiencies of the created fuel.

3.5 DYNAMIC COMBUSTION ANALYSIS: IDI AND CRDI

As discussed in the introduction, there is an increasingly wide variety of alternative fuels whose fuel properties require changes to the engine configuration in order to effectively perform in an internal combustion engine. The purpose of the surrogate fuel blend investigated in this study is to perform as a drop-in replacement for ULSD in the same conditions and configurations as

ULSD. For this reason, test points were taken on two different research engine platforms of different displacement, operating speed, compression ratio, internal geometry, injectors, and injection pumps. The differentiating parameter used to reference one engine or the other for the duration of this paper is the injection strategy. The first research engine is Indirect Injection (IDI) into a Ricardo-Commet (P.W. Gill, Smith Jr., and Ziurys 1954) separate combustion chamber and will be designated as the IDI engine. The second research engine uses Common Rail Direct Injection (CRDI) into a single combustion chamber with an omega bowl piston geometry and will be referred to as the CRDI engine for the remainder of this study.

3.5.1 OVERVIEW: IDI

For the IDI dynamic engine testing, a single-cylinder compression ignition mechanically injected research engine was operated at 2400 rpm and 4 bar BMEP. This IDI engine, a Kubota EA330-E3-NB1, is naturally aspirated and liquid cooled. The engine has two valves per cylinder and a separate combustion chamber which houses three vortices to mix fuel and air in this precombustion chamber. The speed of the engine is capped at 3000 rpm with a continuous power output of 6 HP. Fuel injection for this engine is done using a plunger type pump actuating a 1×1.200mm pintle tip needle injector. Three pressure sensors were used on the engine: one for the prechamber, one for the main chamber, and one for fuel line pressure. The main chamber pressure sensor was a Kistler type 6053C, and the prechamber pressure was measured using a Kistler 6056A. The fuel line pressure was measured with the last transducer, Kistler type 6229A, in conjunction with a Kistler clamp adapter. For engine timing and crank angle position measurements, an Omron 2000 pulse/rev rotary encoder was implemented on the engine. Data for the three pressure sensors and the rotary encoder was captured on a Yokogawa DL850 high speed data acquisition system capable of recording 1MS/s. Engine output torque was measured using an Omega TQ513 torque cell. Intake air flow rate was measured by mass using a Merriam Z50MC2-2 laminar flow meter and integral flow meter. This flowmeter was equipped with a probe that automatically adjusts air density based on the test cell ambient temperature and pressure. For measurement of the emissions, an AVL 483 Micro Soot Sensor, a Horiba MEXA-720NOx analyzer, and an MKS Multigas 2030 FTIR were used to measure a broad spectrum of different emissions species. The IDI engine Specifications are outlined in Table 7 and a schematic of the complete experimental setup can be seen in Figure 24.

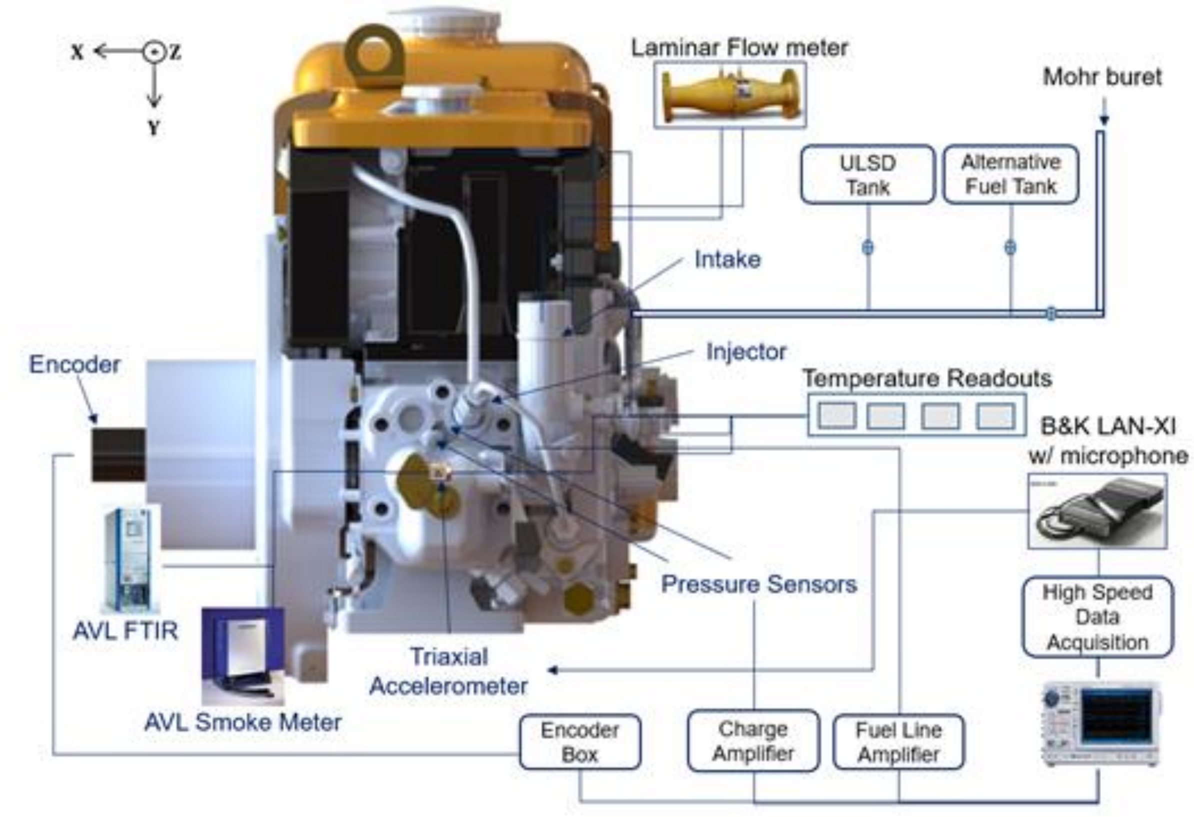

Figure 24: Experimental IDI Engine Configuration Schematic (Soloiu, Weaver, Parker, Smith III, et al. 2022)

Table 7: Specifications for the IDI Engine used in this Investigation

Model	EA330-E3-NB1
Emissions Regulation	Tier 4
Type	Horizontal 4-cycle liquid cooled diesel
Number of Cylinders	1
Bore (mm)	77
Stroke (mm)	70
Displacement (L)	0.325
Connecting Rod Length (mm)	111
Compression Ratio	23.5:1
Injection Nozzle	1 Orifice x 0.20 mm
Nominal Injection Pressure (bar)	150
Combustion System	IDI (TVCS)
Aspiration	Naturally Aspirated
Operating Speed (rpm)	2400
Effective Power (kW)	5.2 @ 3000 rpm
Effective Torque (Nm)	18 @ 2400 rpm
Injection Timing	24.75 to 26.25° BTDC

3.5.3 OVERVIEW: CRDI ENGINE

The fuel was further investigated in a Common Rail Direct Injection (CRDI) compression ignition research engine. This engine was a naturally aspirated and liquid cooled Yanmar single cylinder model TS190 . Measurements were taken for ULSD, IPK, and S2 at 1500 rpm and 4 bar BMEP with an injection timing of 15° BTDC. The complete diagram of the experimental set-up can be found in Figure 25 with additional specifications for this engine platform can be found in Table 8. A Cummins common rail and BOSCH fuel injector were used along with a Compact Rio 9076 Drivven ECU for control of injection timing, pulse width, and rail pressure. Crank angle was captured using an Omron 3600 pulse rotary encoder for both crank initiated signal clocking and measurement initiation trigger using the B channel pulses and the Z channel TDC pulse respectively. Data from the intake pressure, exhaust pressure, in-cylinder pressure, boost pressure, and TDC signal were taken using a Yokogawa DL850 oscilloscope for data recording and AVL Indicom for real-time engine monitoring and TDC offset determination. Values for IMEP, PRR, Coefficient of Variability (CoV), CA50, and Peak AHRR were all used to monitor the condition of the engine during testing and recorded for future evaluation of the collected data. Fuel flow rate was captured using an NI DAQ for both flow in and flow out using two Maxx Flow meters type 213. In-cylinder combustion pressure was measured using a Kistler pressure sensor type 6053cc and accompanying Kistler type 5010B dual mode amplifier. Intake pressure was measured using a Kulite pressure transducer and intake mass air flow measured using a Meriam Z50MC2-2 laminar flow meter. Soot emissions were measured using an AVL model 483 Micro Soot Sensor (MSS), and gaseous emissions were measured using an MKS FTIR gas species analyzer to analyze NO_x, THC, CO, UHC, Formaldehyde, and CO_2.

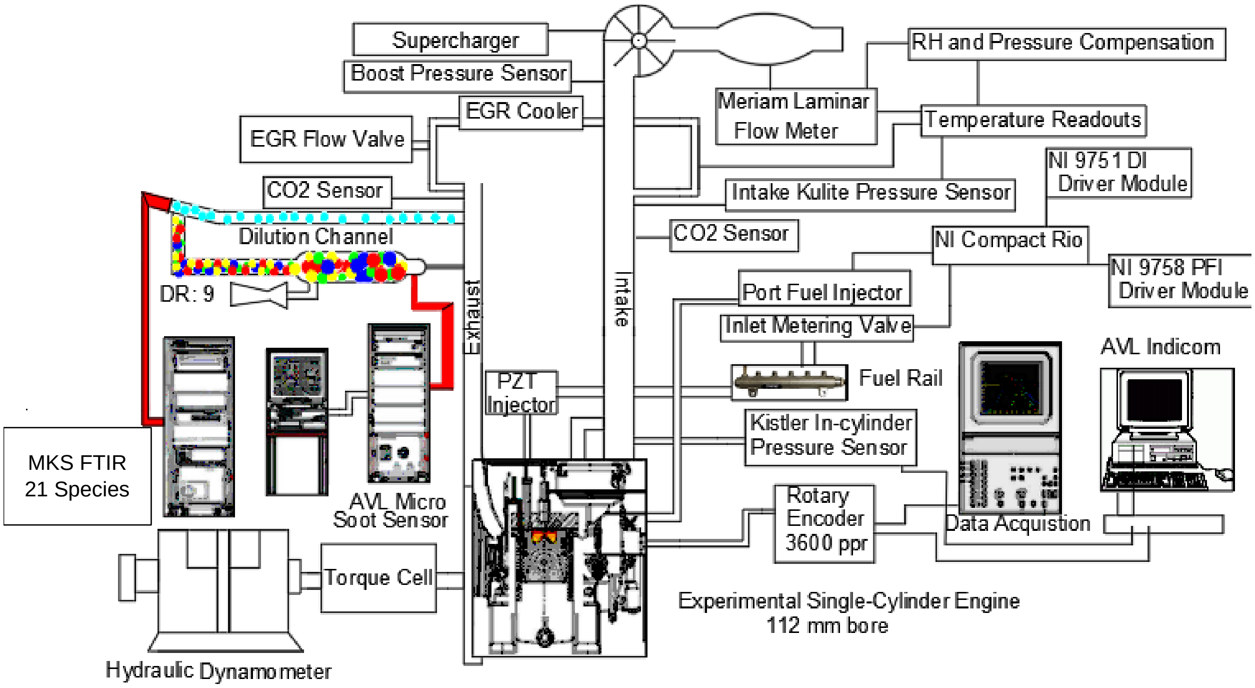

Figure 25: Experimental CRDI Engine Configuration (Soloiu, Smith III, et al. 2022)

Table 8: Specifications for the CRDI Engine used in this Investigation

Parameter	**Value**
Type	Horizontal 4-cycle liquid cooled diesel
Number of Cylinders	1
Bore (mm)	112
Stroke (mm)	115
Compression Ratio	16:1
Displacement (L)	1.12
Combustion System	CR DI
Aspiration	Naturally Aspirated
Operating Speed (rpm)	1500
Output (kW)	5.15
Oil Pan Capacity (L)	1.3
Starter Capacity (V-kW)	12-0.8
Alternator Capacity V-A	12-3.5
Length (mm)	566
Width (mm)	411
Height (mm)	457
Injection Timing	15° BTDC

3.5.3 Pressure Transducers: Sensors and Instrumentation

The CAD model in Figure 26 depicts the instrumented cylinder head on the IDI engine. The main chamber pressure was measured through a machined hole in the cylinder head while the pre-chamber sensor was mounted using an adapter to fit in the glow plug port. The adapter, pre-chamber, and main chamber pressure sensors can be found in Figures 27, 28, and 29 with their operating specifications listed in Tables 9 and 10.

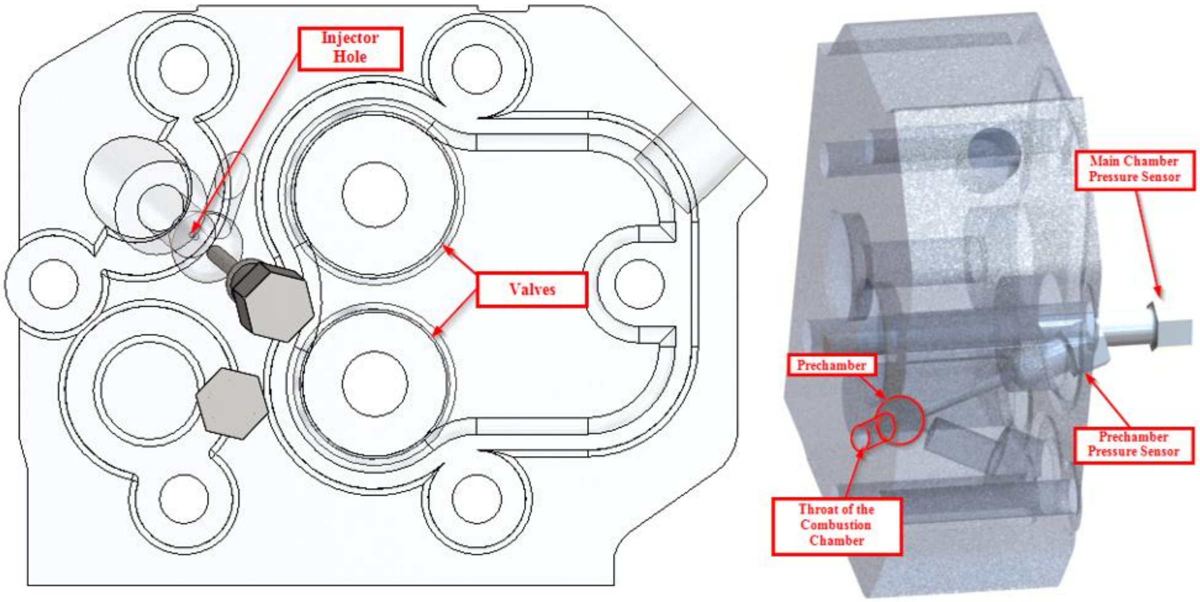

Figure 26: CAD Model of the Pressure Sensor Placement for the Main Chamber and the Pre-Chamber on the Head of the IDI Engine

For combustion pressure, two pressure transducers were used to measure the pressure both in the main chamber and the pre-chamber in the IDI engine. As the CRDI engine does not have a pre-chamber, the pressure sensor used to measure its cylinder pressure is identical to the one used for main chamber pressure measurement in the IDI engine. The pressure transducers are contained within a stainless-steel case to protect the sensor. The pre-chamber pressure sensor was implemented using a glow plug adapter for mounting on the swirl chamber. Data gathered from these sensors was compared to the crank angle degree measurement obtained from the rotary encoder to align pressure data to the combustion cycle for both IDI and CRDI. The pressure sensor used for the main chamber pressure was a Kistler type 6053CC (Figure 27).

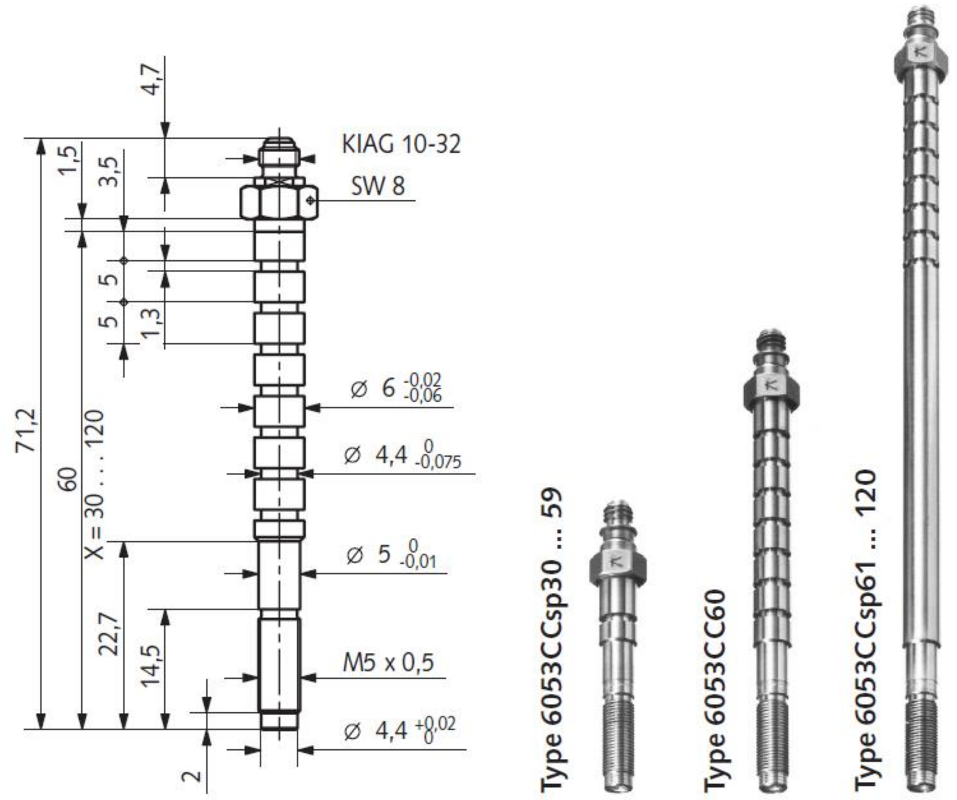

Figure 27: Kistler Main Chamber Transducer Type 6053CC (Kistler 2020b)

Table 9: Kistler Type 6053CC Specifications (Kistler 2020b)

Measuring Range (bar)	0-250	**Sensitivity (%)**	≤±2
Calibrated sub-ranges (bar)	0-50, 0-100, 0-150, 0-250	**Thermal Shock Error (bar)**	≤±0.5
Overload (bar)	300	**Δp_{min}**	≤±2
Sensitivity (pC/bar)	≈ -20	**Δp_{max}**	≤±1
Natural Frequency, Nominal (kHz)	≈ 160	**Insulation Resistance at 23°C (Ω)**	< 1013
Linearity at 23 ℃ (%FSO)	≤ ± 0.03	**Shock resistance (g)**	2000
Acceleration Sensitivity (bar/g)	< 0 .0002 < 0.0005	**Tightening torque (Nm)**	1.5
Operating temperature range (°C)	- 20 – 360	**Weight (g)**	10
Connector (°C)	200	**Connecter (PTFE)**	KIAG 10-32

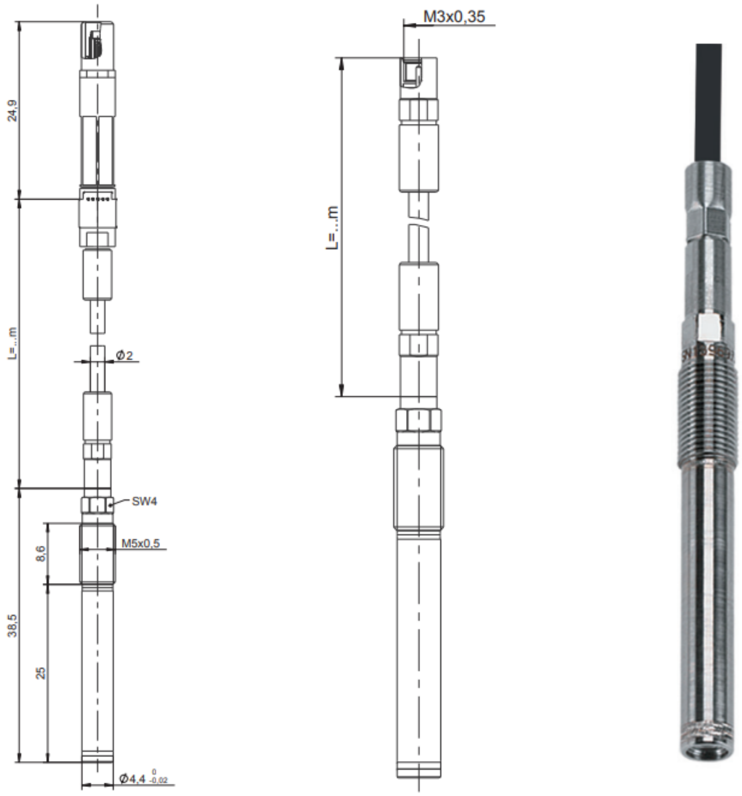

Figure 28: Kistler Swirl Chamber Transducer Type 6056 (Kistler 2011b)

Table 10: Kistler Type 6056A Specifications (Kistler 2011b)

Range (bar)	0 – 250
Calibrated Ranges (bar)	0 – 50, 0 – 100, 0 – 150, 0 – 250
Overload (bar	300
Sensitivity (pC/bar)	-20
Natural Frequency (kHz)	≈ 160
Linearity %FSO	≤ ± 0.03
Acceleration Sensitivity (bar/g)	< 0.0005
Shick Resistance (g)	2,000
Thermal Shock Error Δp (bar)	≤ ± 0.7
Operating Temperature rance (°C)	-20 - 350
Capacitance (pF)	5
Insulation Resistance @ 23°C (TΩ)	$\geq 10^{13}$
Tightening Torque (Nm)	1.5
Weight (g)	30

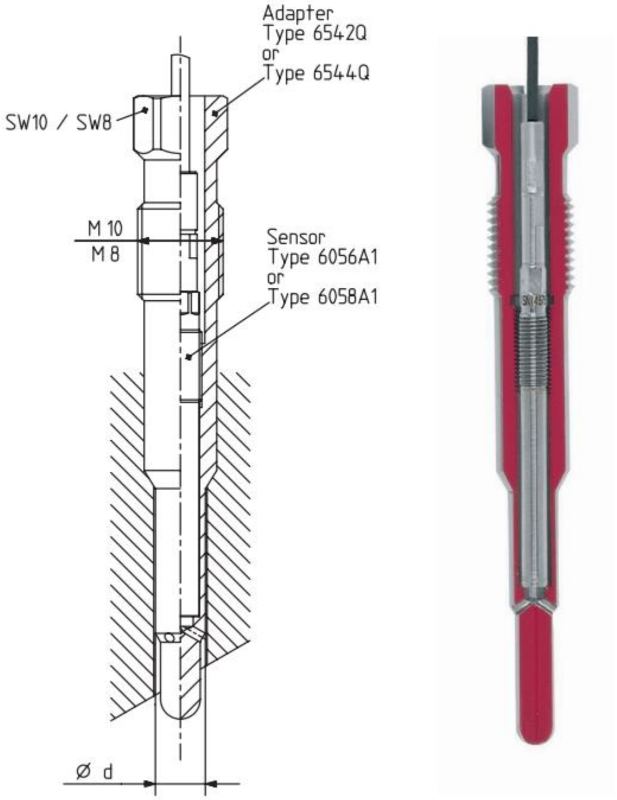

Figure 29: Glow Plug Adapter (Kistler 2020a)

Pre-chamber pressure was measured using a Kistler type 6053A mounted with a Kistler glow plug adapter. These can be seen in Figures 28 and 29 respectively. Specifications for the pressure sensor can be found in Table 10. For each of the sensors, a stainless-steel diaphragm covers the sensitive piezoelectric crystal. This element causes changes in voltage when it experiences deformation. Pressure from the cylinder causes this deformation and the voltage measurement is used to determine pressure. Since this voltage change for these sensors is too low for raw measurement, a Kistler 5010B was the charge amplifier used to increase the signal intensity.

Fuel line pressure is measured using a Kistler type 6229A pressure transducer (Figure 30) and mounted to the fuel line using a Kistler clamp adapter (Figure 31). Specifications for the pressure transducer can be found in Table 11. The signal for the fuel line pressure transducer was amplified using a Kistler type 4618A2 piezoresistive amplifier pictured in Figure 33.

Figure 30: Kistler Type 6229A Fuel Line Pressure Transducer (Kistler 1997)

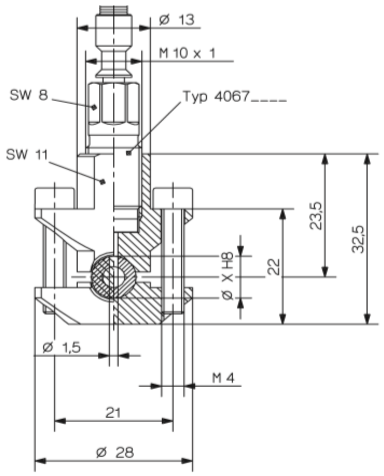

Figure 31: Kistler Clamp on Adapter (Kistler 1997)

Table 11: Kistler Type 6229A Transducer Specifications

Range (bar)	0-5000
Calibrated Partial Range (bar)	0-500
Overload (bar	6000
Sensitivity (pC/bar)	-2.5
Natural Frequency (kHz)	≥200
Rise Time (µs)	1
Linearity (%FSO)	≤±1
Acceleration Sensitivity (bar/g)	≤0.004, ≤0.01
Shock Resistance (g)	10,000, 5,000
Temperature Coefficient of Sensitivity(%/°C)	+0.02
Operating Temperature Range (°C)	-50-200
Capacitance (pF)	≈8
Insulation Resistance (TΩ)	50
Tightening Torque (Nm)	20
Weight (g)	12
Service Life (number of cycles from 0-3000 bar)	$\geq 10^7$

3.4.4 PRESSURE SENSOR AMPLIFIERS

For the amplification of weak voltage signals from the pressure transducers, a Kistler Dual Mode Amplifier is used for signal amplification and conditioning. Since the piezoelectric transducers have a high impedance, the amplifier was run using its charge amplifier mode for the combustion chamber pressure transducers. The fuel line pressure sensor is a piezoresistive pressure transducer requiring constant current excitation with the use of a piezoresistive amplifier. An image of the charge amplifier for the combustion pressure sensors and the piezoresistive amplifier used for the fuel line pressure can be seen in Figure 32 and Figure 33.

Figure 32: Kistler 5010 Dual Mode Charge Amplifier (Kistler 2009)

Figure 33: Fuel Line Pressure Transducer Piezoresistive Amplifier (Kistler 2011a)

For signal conditioning and amplification, the small input voltage is converted to a 0-10 V power output. The amplifier uses a measurement scale defined by Measuring Units per Volts (MU/V) with a sensitivity measured in pC/MU. It is defined this way as this amplifier can be used in a variety of different settings to amplify transducers that measure force, strain, acceleration, etc. and the MU is a nonspecific method of notation. Specifications on this component can be found in Table 12.

Table 12: Kistler Type 5010B Amplifier Specifications (Kistler 2009)

Specifications	**Type 5010B**	**Time Constant (sec)**	**Type 5010B**
Measurement range (pC)	±10-999000	Long	0 - 100000
Scale settings 1,2,3,4,5 Sequence (MU/V)	0.0002 - 10000000	Medium	1 - 10000
Sensor sensitivity (pC/MUmV/MU)	0.01 -9990	Short	0.01 - 100
Input		**Time constant resistor** (Ω)	
Connector charge, voltage	BNC neg.	Long	$\geq 10^{14}$
Impedance charge mode (Ω)	70	Medium	10^{11}
Impedance voltage mode (Ω)	100K	Short	10^{9}
Voltage max. (V)	50	**Noise**	
Insulation resistance at input (Ω)	10^{14}	Referred to with input shield (pCrms)	0.0035
Sensor power voltage mode	4	1 pC/V max (μVrm)	500
Frequency response (kHz)	180	Drift MOSFET leakage current (pC/s)	≤ ± 0.03
Accuracy (%)	≤ ± 0.050	Zero offset (mV)	0.50

3.5.5 ROTARY ENCODER

Engine position sensing is vital to accurate integration of sensor data. This measurement was taken in this configuration using an Omron E6C2-CWZ3E incremental rotary encoder as seen in Figure 34. This instrument measures the crank angle position based on the flywheel of the engine. It was mounted behind the engine on the flywheel using a flex coupling. This configuration directly measures the Top Dead Center (TDC) of the engine.

Figure 34: Omron E6C2 Rotary Encoder (Omron 2015)

The rotary encoder used three channels (A, B, and Z) at 2000 (IDI engine) and 3600 (CRDI engine) pules per revolution (ppr) for the A and B channels with the Z channel outputs 1 ppr. This single pulse was aligned at TDC such that signals from the other sensors can be properly timed. In this scenario, the B channel was to account for changes of direction and this engine always spins counterclockwise when facing the flywheel in place of direct signal measurement.

3.5.6 TEMPERATURE MEASUREMENT

During the course of testing, multiple temperatures are monitored to allow for repeatability as well as to safeguard against engine failure. Changes in operating temperatures have a direct effect on the performance, combustion properties, pressure, and emissions. Temperatures were measured using K-type thermocouples for the exhaust gas, engine oil, cooling water, and dyno oil. These thermocouples are then wired to an Omron E5CS temperature controller. This controller has the capability to measure temperature with a ±0.3% accuracy. An image of this controller is displayed in Figure 35.

Figure 35: Omron Thermocouple Controllers (Omron 2015)

K-type thermocouples were chosen for this instrumentation as they have a very large temperature range and can be implemented in a variety of settings without damaging the probe. The temperature range for K-type thermocouples is -200°C to 1250°C. Exhaust gas temperature measures the highest temperatures of the recorded values and was never found to exceed these parameters.

3.5.7 INTAKE AIR FLOW METERS

Intake air flow was measured by mass using a Merriam series 50 MC2 laminar flow meter in conjunction to a Merriam integral flow computer. These measurement tools can be seen in Figures 36 and 37 respectively. The flow computer is used to provide more accurate results as it adjusts the output value based on test cell pressure, static pressure, temperature, and relative humidity. Measurements are determined using differential pressure.

Figure 36: Meriam 50 MC2 Series Laminar Flowmeter (Meriam 2018)

Figure 37: Meriam Integral Flow Computer (Meriam 2018)

3.5.8 EMISSIONS ANALYZERS

The emissions analysis was conducted using Fourier-Transform infrared spectroscopy with an MKS MultiGas 2030 (Figure 38) to determine the gaseous emissions produced from combustion and photoacoustic chamber resonance with an AVL 483 for soot measurement. The MKS FTIR measures with a sensitivity of 10-100 parts per billion of each of the 30 different emissions species from the engine exhaust at a sampling rate of 1Hz. The measured species and their calibration ranges are displayed in Table 13.

Table 13: MKS Main Measured Species and Calibration Ranges (MKS 2023)

Nitrogen Monoxide (NO) 0 -3000 ppm	Carbon Monoxide (CO) 0 – 500 ppm	Ethane (C2H6) 0 - 1000
Nitrogen Dioxide (NO2) 0 -2000 ppm	Carbon Dioxide (CO2) 0 – 20 %	Ethylene (C2H4) 0 – 3000 ppm
Acetylene (C2H2) 0 – 1000 ppm	Isocyanic Acid (HNCO) 0 – 400 ppm	Ammonia (NH3) 0 – 3000 ppm
Methanol (MeOH) 0 – 1000 ppm	Formic Acid (HCOOH) 0 – 100 ppm	Propylene (C3H6) 0 – 1000 ppm
Water (H2O) 0 – 25 %	Nitrous Acid (HNO2) 0 – 20 ppm	Sulfur Dioxide (SO2) 0 – 300 ppm
Ethanol (C2H6O) 0 – 10000 ppm	Hydrogen Cyanide (HCN) 0 – 100 ppm	Benzene (C6H6) 0 – 1000 ppm

Figure 38: MKS MultiGas 2030 FTR (MKS 2023)

The MKS Multigas 2030 FTIR uses an infrared beam passed through the gas sample to determine the chemical species based on the frequency and intensity of the beam after it passes through the gas sample. These values change depending on the atoms and chemical bonds of the emissions species. This makes the changes in the laser unique to each species. This instrument can also detect ions during the combustion of organic compounds in a hydrogen flame using a Flame Ionization Detection (FID). This ion formation is an indicator of the organic compound in the sampled gases as it has a proportional relationship to these compounds. It is in this way that the MKS can measure unburned hydrocarbons in the exhaust.

For operation, the MKS is purged with gaseous nitrogen for a minimum of 8 hours after which the analyzer chamber is filled with approximately 800 ml of liquid nitrogen. After this, the MKS and its component systems can be turned on. The operating temperature for the MKS is 191°C and heating the system takes approximately 2 hours. Before an analysis, the MKS must undergo a health check where the ambient temperature, pressure, and humidity must be within certain parameters in order to pass the check. The device must be run in 20-60% humidity, and between 50°F-75°F.

Figure 39: AVL Micro Soot Sensor 483 (BOSMAL 2018)

To measure soot emissions, an AVL Micro Soot Sensor 483 (Figure 39) was used for soot analysis of exhaust gas. This sensor operates on the principles of photo acoustics wherein a laser is used to transfer radiation energy to the particles. The particle heat rapidly causing thermal expansion of the air surrounding the particle and a pressure differential. With cyclic application of the laser beam, the heat induced heat cycling of the particle creates periodic sound waves within the measurement chamber. The frequency of the sound waves is equal to the laser's frequency, and in transient analysis of soot particles in exhaust gas, the frequency is tuned to match the resonance frequency of the measurement chamber or resonance chamber. This means that while the laser is active, there is a standing sound wave which amplifies the pressure waves created from the soot particles. A microphone is then used to measure the intensity of the sound within the chamber which increases with the increase in exhaust gas soot. Response magnitude is also directly related to the absorption coefficient of the particle calculated using Equation 9 (Arnott et al. 2006).

$$B_{abs} = P_m \frac{1}{P_L} \frac{A_{res}}{\gamma - 1} \frac{\pi^2 f_0}{Q} \qquad \text{Eq. 9}$$

In this equation, B_{abs} represents the light absorption coefficient of the measured particles, P_m is the sound intensity, and P_L is the laser intensity. The other variables describe properties of the chamber where A_{res} is the cross-sectional area, γ and Q are the specific heat ratio and the quality of the chamber gas, and f_0 is the resonant frequency of the chamber walls. Specific heat ratio, γ, is assumed to be that of air at standard temperature and pressure (STP) at constant 1.4. A schematic of the measurement chamber is shown in Figure 40.

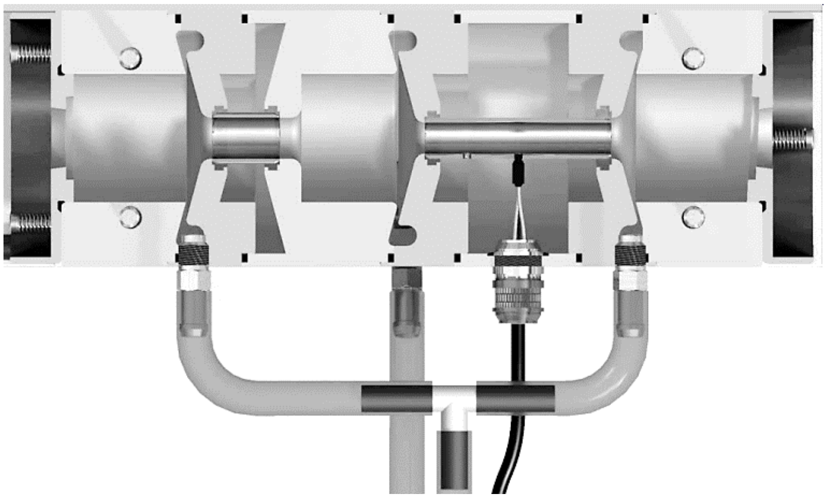

Figure 40: Microsoot Sensor Internal Geometry (AVL 2008)

CHAPTER 4

RESULTS

4.1 FUEL ANALYSIS

Analysis of the thermophysical properties of each fuel was conducted using the procedures outlined in Section 3.2-3.3. A summary of the final values for the determined thermophysical properties can be found in Table 14. It should be noted that S1 and S2 refer to fuel blends determined from the investigations into the lubricity and autoignition characteristics used to match the previously outlined criteria for a drop-in fuel replacement. S1 is a blend of 40% IPK and 60% S-8 as determined from the investigations conducted for DCN in the CVCC in Section 4.2. S2 is considered the final surrogate blend as it includes 3% methyl oleate lubricity additive with the remining 97% comprised of the S1 fuel blend. Further analysis for the determination of this fuel blend is outlined in Section 3.4.

Table 14: Thermophysical Properties of the Neat Researched Fuels and Fuel Surrogate Blends

Property	**Fuel**					
-	**ULSD**	**S-8**	**IPK**	**S1**	**S2**	**Methyl Oleate**
Lot/POSF	N/A	5109	7629	N/A	N/A	A0436822
Formula	$C_{12}H_{23}$	$C_{10.82}H_{23.7}$	$C_{10.5}H_{23}$	$C_{10.7}H_{23.4}$	$C_{10.9}H_{23.8}O_{0.06}$	$C_{19}H_{36}O_2$
H/C**	1.92	2.2	2.17	2.19	2.17	1.89
LHV [MJ/kg]	42.84	42.04	44.25	43.97	43.31	37.3
Viscosity @ 40°C [cP]	2.46	1.30	1.06	1.35	1.41	4.54
SMD [μm]	20.94	19.19	15.097	17.67	17.77	30.84
Density @ 26°C [g/cm^3]	0.85	0.755	0.74	0.744	0.748	0.862
Surface Tension [N/m]**	28.02	22.30	20.30	21.50	21.68	27.40
Oh	0.1102	0.0723	0.0704	0.0801	0.0833	0.1682
TA10	122.68	100.24	84	-	90.16	210.88
TA50	184.42	150.34	122.06	-	133.7	254.68
TA90	238.1	182.59	144.56	-	165.71	273.08
Chemical Composition**						
% n-Paraffins	13.6	17.7	2.1	11.46	11.16	-
%iso-Paraffins	11.8	82	88	84.4	81.85	-
%Cycloparaffins	43.5	<0.4	9	3.84	3.7	-
%Aromatics	23.5	<0.1	<0.5	0.26	0.351	-
%Sulfur	0.00144	<0.001	<0.001	<0.001	<0.00097	-

***Derived from researched data with all other properties determined using equipment in the Automotive and Aerospace Combustion Laboratory at Georgia Southern University**

****Found from Literature: (Valco et al. 2015; Mousavi, Romero-Martínez, and Ramírez-Verduzco 2020; X. Wang et al. 2020; Zhang et al. 2016; Mueller et al. 2012)**

4.1.1 FLUIDIC SHEAR RATE AND THERMAL RESPONSE

The viscosity of the fuel has an impact on a wide variety of different engine parameters and combustion metrics. It is a key factor in the spray penetration, droplet size, and mixture formation within the cylinder. In the fuel pumps, filters, injectors, and lines, it gives an indication of the lubrication characteristics and its fluidic characteristics. Additionally, viscosity is an indication of a fuel's lubricity characteristics as, in general, fuels with a higher viscosity also have a higher lubricity (Maleev 1954). Viscosity was measured for ULSD, S-8, IPK, S1, and methyl oleate using the procedures outlined in Section 3.2.3, and the resulting graphs are then displayed in Figures 40 and 41. Figure 40 includes the trace viscosity curve for methyl oleate, and Figure 41 omits it so as to better illustrate the differences between the fuels of lower viscosity.

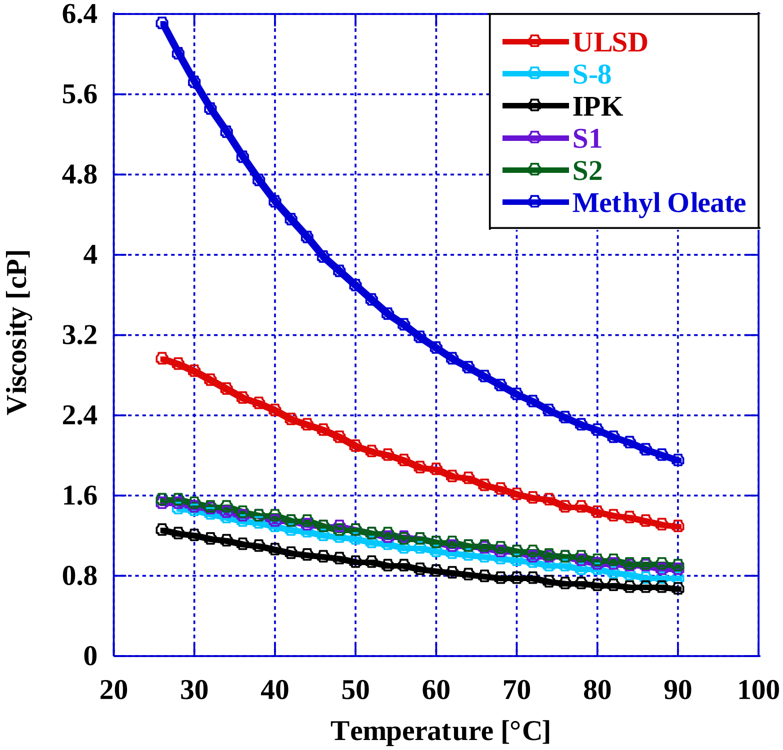

Figure 41: Viscosity Determination for ULSD, S-8, IPK, S1, S2, and Methyl Oleate

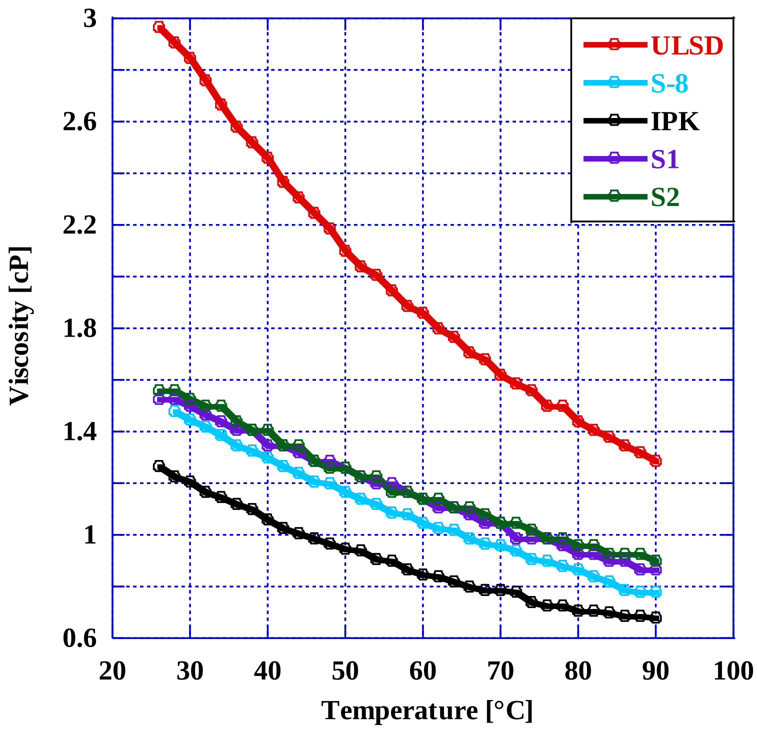

Figure 42: Viscosity of ULSD, S-8, IPK, S1, and S2

Dynamic viscosity values at 40°C were identified for each of the fuels and are displayed in Table 15. IPK was found to have the lowest viscosity throughout the measured temperature range and methyl oleate to an extent that the graph range which excludes its trace needed to be made for further analysis of the other researched fuels. At 40°C, the viscosity of IPK was measured to be 1.04 cP compared to 4.54 cP for methyl oleate at that same temperature Additionally, it was found that as the room temperature viscosity of the fuel decreased, the reduction in viscosity as temperature increased from 0-90°C decreased as well. Methyl oleate dropped by 4.35 cP while the viscosity of IPK dropped by only 0.58 cP.

The surrogate blends exhibited a viscosity closer to the F-T fuels than to ULSD with a 45% reduction in viscosity for S1 and a 43% reduction in viscosity for S2 when compared to ULSD. Comparing the two surrogate blends revealed that the addition of 3% by mass of methyl oleate to the blend increased the viscosity at 40°C by 4.44%. While this is not a significant difference in comparison with the difference in viscosity between the F-T fuels and the diesel/biodiesel, this difference could cause an increase in spray droplet size resulting in a reduction in combustion efficiency in the IC engine.

Table 15: Viscosity for S-8, IPK, and ULSD at 40°C

Fuel	Viscosity @ 40°C (cP)	% Diff from ULSD
ULSD	2.46	-
S-8	1.30	-47.15%
IPK	1.06	-56.91%
S1	1.35	-45.12%
S2	1.41	-42.68%
Methyl Oleate	4.54	84.55%

4.1.2 FRICTION FORCE AND WEAR SCAR DEPTH

For the investigation into the lubrication characteristics, the procedure outlined in Section 3.3 was conducted for each of the researched fuels. The results of the friction force vs time are shown in Figure 42 for ULSD, S-8, IPK, S2, and Methyl Oleate. The fuel blend, S2, is comprised of 97% F-T fuel with a methyl oleate additive concentration of 3%. Although conventional additives for improving lubricity are added in much lower concentrations, it was considered that methyl oleate is a single component of biodiesel and not a deigned lubricity improver indicating the necessity of much higher concentrations. As blend concentrations exceeding 5% can no longer be considered as additives, the blend percentage estimated to yield the most improvement to lubricity while remaining an additive was 3%. It was found that the difference in fuel lubricity became apparent only after around 50 seconds of run-time. This can be attributed to the transition between static and dynamic loading as the sample disk begins to rotate. Additionally, the initial friction force response is due to the sudden drop in friction coefficient as the pin track removes enough material that the track forms a semi-circular wear pattern. While more of the pin surface is in contact with the wear material, the normal force is distributed more evenly along the contact surface thus reducing total friction force. Over time, however, it becomes clear that methyl oleate is the most lubricating of the researched fuels as the friction force remains under 0.2 N for the duration of the test. Following methyl oleate, it was found that the S2 surrogate, which contains 3% methyl oleate, maintains a lower friction force during the initial phase of the experimentation and maintains a comparable friction force to that of ULSD from 100 seconds to 300 seconds. The F-T performed the worst resulting in the highest overall friction force which continued to increase after the initial 50 seconds.

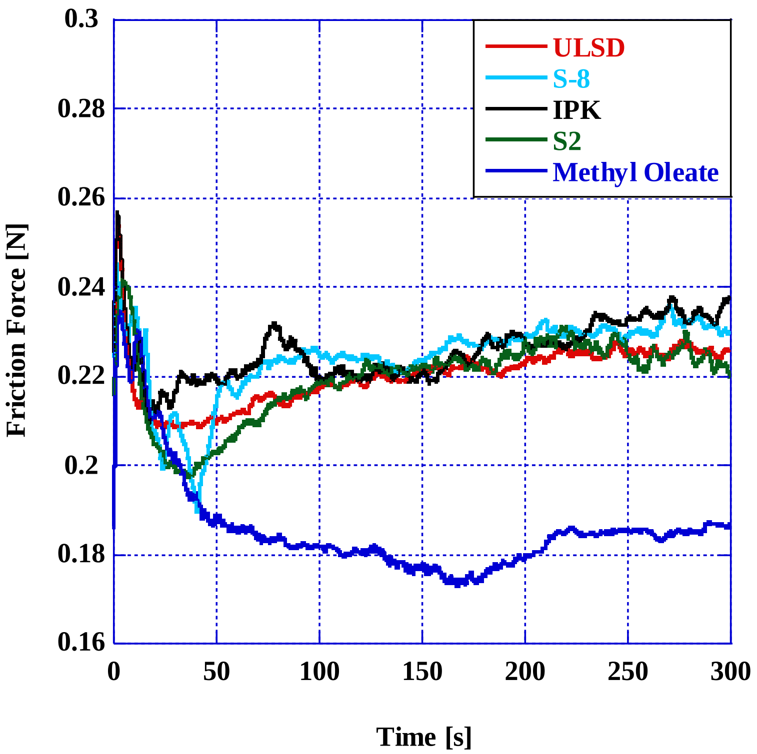

Figure 43: Friction Force for ULSD, S-8, IPK, S2, and Methyl Oleate

The average friction force was taken starting at 35 seconds to omit the initialization phase for each of the researched fuels and the results shown in Table 16 and graphed in Figure 43. Consistent with the results from the friction force over time, methyl oleate was shown to have the lowest average friction force of 0.1822 reflecting a 17.35% reduction in friction force when compared to ULSD. Both F-T fuels exhibited an increase in friction force of 2.19% and 2.58% for S-8 and IPK respectively. For the surrogate blend S2, there was found to be a slight reduction in friction force of 0.076%. The reduction, however, is within the tolerances of the instrument and it can therefore be considered that the S2 surrogate blend and ULSD are functionally equivalent in lubrication quality as determined by this experimentation.

Table 16: Average Friction Force and % Diff. from ULSD for ULSD, S-8, IPK, S2, and Methyl Oleate

Fuel	**Avg. Friction Force**	**% Diff. from ULSD**
ULSD	0.2205	-
S-8	0.2253	2.19
IPK	0.2262	2.58
S2	0.2203	-0.0907
Methyl Oleate	0.1822	-17.35

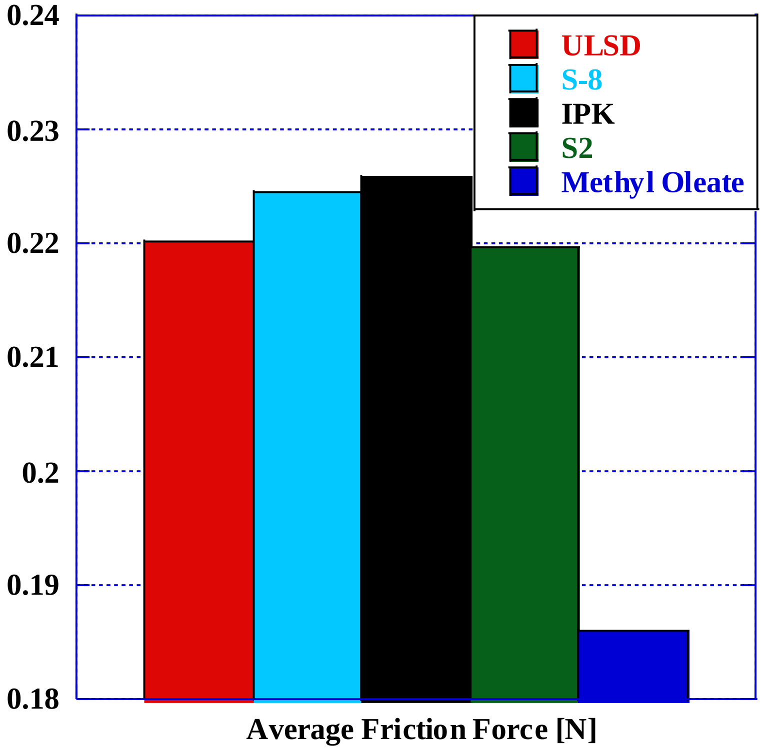

Figure 44: Total Average Friction Force for ULSD, S-8, IPK, S2, and Methyl Oleate

Further analysis of the wear scar depth was conducted using the procedures outlined in Section 3.3. Wear scar depth and profile investigations were conducted for each of the researched fuels where depth values can be found in Table 17 and profiles for ULSD and S2 shown in Figure 44 and Figure 45.

Table 17: Wear Scar Depths for ULSD, S-8, IPK, S2, and Methyl Oleate

Fuel	**Wear Scar Depth [μm]**	**%Difference from ULSD**
ULSD	9.69	-
S-8	10.51	-8.46
IPK	13.31	-37.36
S2	9.686	0.0413
Methyl Oleate	6.3	34.98

Wear scar profile images for the rest of the researched fuels can be found in the Appendix as Figures 117-119. It was found that both IPK and S-8 increased wear scar depth by 37% and 8% respectively when compared to ULSD. Methyl Oleate was found to reduce wear scar depth by

35% from that of ULSD and, when added in 3% concentration by mass to the DCN matched F-T blend, decreased wear scar depth. The final surrogate blend, S2, was found to have a wear scar depth 0.04% shallower than that of ULSD.

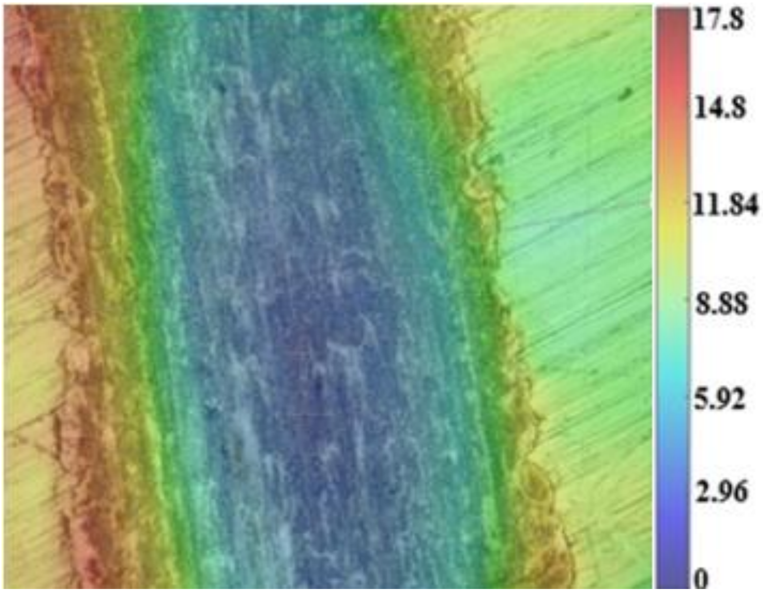

Figure 45: Wear Scar Depth Profile for ULSD

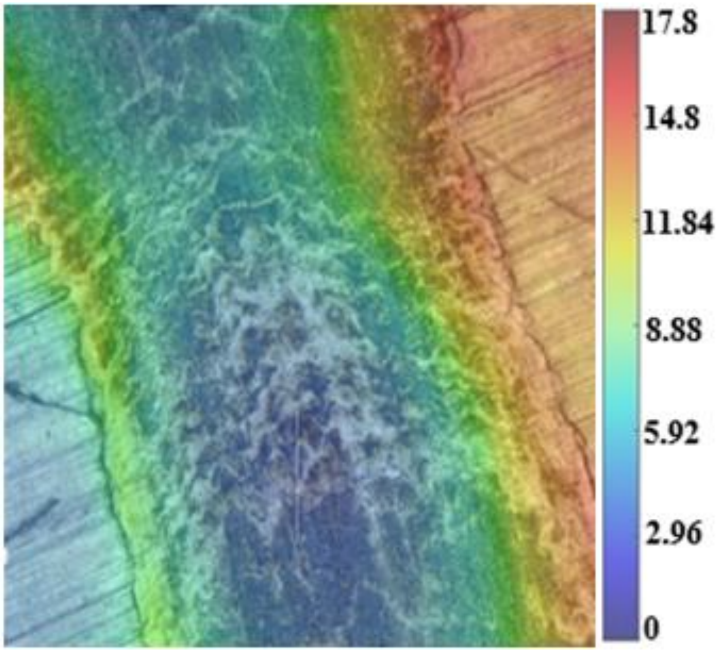

Figure 46: Wear Scar Depth Profile for S2

4.1.3 ENERGY CONTENT/HEAT OF COMBUSTION

A calorimetry study was performed for each synthetic F-T fuel, the S1 and S2 surrogate blends, and methyl oleate and the results compared those of ULSD as a baseline. Two heating values are determined for each fuel: Higher Heating Value and Lower Heating Value. Higher heating value includes the latent heat of vaporization of water as the cooling of the water formed from combustion condenses (Maleev 1954). The calorimetry analysis was used to determine the energy content of the fuel in terms of the lower heating value. The experiment was conducted using the procedure outlined in Section 3.2.1. The analysis results are displayed in Table 18.

Table 18: Lower Heating Value for S-8, IPK, and ULSD

Fuel	LHV (MJ/kg)	% Diff. from ULSD
ULSD	42.84	-
S-8	42.04	-1.87%
IPK	44.25	3.29%
S1	43.97	2.64%
S2	43.31	1.09%
Methyl Oleate	37.3	-12.93

It was found that the F-T fuels have Lower Heating Values (LHV's) which reside at the upper and lower extremes with IPK and S-8 having the largest and smallest LHV's respectively. Of the researched fuels, IPK was found to have the largest energy content with a lower heating value of 44.25 $\frac{MJ}{kg}$ and Methyl Oleate was found to have the smallest LHV at 37.3 $\frac{MJ}{kg}$ resulting in a 3.29% increase and a 12.93% decrease in energy content respectively when compared to ULSD's LHV of 42.84 $\frac{MJ}{kg}$. For the surrogate blends S1 and S2, both fuels were found to have an energy content between S-8 and IPK. Despite the small fraction, the addition of methyl oleate to the blend resulted in a reduction in the fuel's energy content of 0.66 $\frac{MJ}{kg}$ where S1 and S2 had an LHV of 43.97 $\frac{MJ}{kg}$ and 43.31 $\frac{MJ}{kg}$ respectively.

4.1.4 THERMAL STABILITY AND LOW TEMPERATURE OXIDATION

The TGA analysis was conducted as outlined in Section 3.2.2 on ULSD, S-8, IPK, S2, and methyl oleate to determine the thermal stability of each fuel through the measurement of vaporization rate as temperature increases from 20°C to 600°C. Rapid vaporization rate is favorable for IC engines as homogeneous air-fuel mixtures increase combustion efficiency by reducing variation in lambda within the cylinder (Ra et al. 2008). Additionally, fuels with low vaporization temperatures are more likely to maintain low viscosity at lower temperatures making it more favorable for cold weather conditions (Zhou et al. 2014). The graph of the non-vaporized mass in the crucible chamber as a function of increasing temperature is shown in Figure 46. It was found that IPK had the fastest vaporization rate followed in order of increasing vaporization rate by S2, S-8, and ULSD. Methyl oleate exhibited a slightly different rate profile where despite the increase in vaporization temperature, the slope of the curve was the steepest among the researched fuels. This can be attributed to the difference between single component and multi-component fuels. The fuels which contain several different compounds will have a rate profile which is dependent on the distribution of volatility among its component species (Menard 2014). As temperature increases, the chemicals will change state in order of increasing boiling point causing multi-component fuels to exhibit mass loss over a range of temperatures which corresponds to the boiling points of each chemical in its composition. Methyl oleate, however, is comprised of only one molecule meaning this fuel will experience mass loss due to vaporization over a much narrower temperature range.

The overall rate of vaporization of the fuel can then indicate the thermal stability of its chemical composition. Fuels which have a higher concentration of heavier hydrocarbons, high carbon number, have a slower vaporization rate and a higher boiling point and freezing point. IPK’s chemical composition favors unsaturated iso-alkanes of lower carbon number causing the faster rate of vaporization (Moses 2008). While also being a synthetic fuel, S-8 has a faster vaporization rate when compared to ULSD but slower when compared to IPK as it has a higher ratio of saturated normal paraffins. The surrogate blend, S2, being primarily composed of the lighter hydrocarbons found in the F-T fuels exhibits a vaporization rate between that of IPK and S-8.

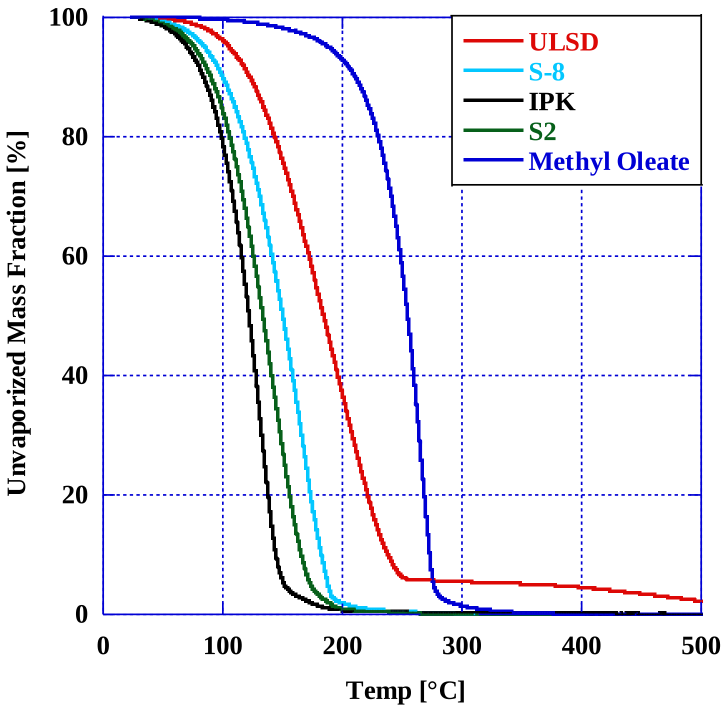

Figure 47: TGA for ULSD, S-8, IPK, S2, and Methyl Oleate

The vaporization rate is characterized by the 10% mass that is vaporized at specific points. These points are denoted as TA10, TA50, and TA90 and indicate the temperature for which 10%, 50%, and 90% of the fuel is vaporized. In accordance with the previous graphs, IPK has the lowest values for TA10, 50, and 90 and ULSD has the highest values. Each of these vaporization temperatures can be seen in Table 19.

Table 19: TA10, 50, and 90 for ULSD, S-8, IPK, S2, and Methyl Oleate

Fuel	TA10 [°C/K]	TA50 [°C/K]	TA90 [°C/K]
ULSD	122.68/395.83	184.42/457.56	238.09/511.25
S-8	100.24/373.39	150.34/423.49	183.59/455.74
IPK	84/357.14	122.06/395.21	144.56/417.71
S2	90.16/363.31	133.7/406.85	165.71/438.86
Methyl Oleate	210.88/484.03	254.68/527.83	273.08/546.23

The differential thermal analysis and thermogravimetric analysis were performed for each of the three researched fuel following the methods outlined in Section 3.2.2. The differential thermal analysis (DTA) measured the energy that is absorbed and released by the fuel while it is oxidizing. The results of this investigation are graphed in Figure 47. Energy absorption is indicated by a negative slope and represents an endothermic reaction while energy release is indicated by a positive slope and represents the exothermic reactions. The DTA curve for IPK, S-8, and ULSD is shown in figure 28. This curve represents the endothermic and exothermic reactions as the fuel is heated to 600°C. IPK has the fastest rate of energy absorption and release and ULSD has the slowest.

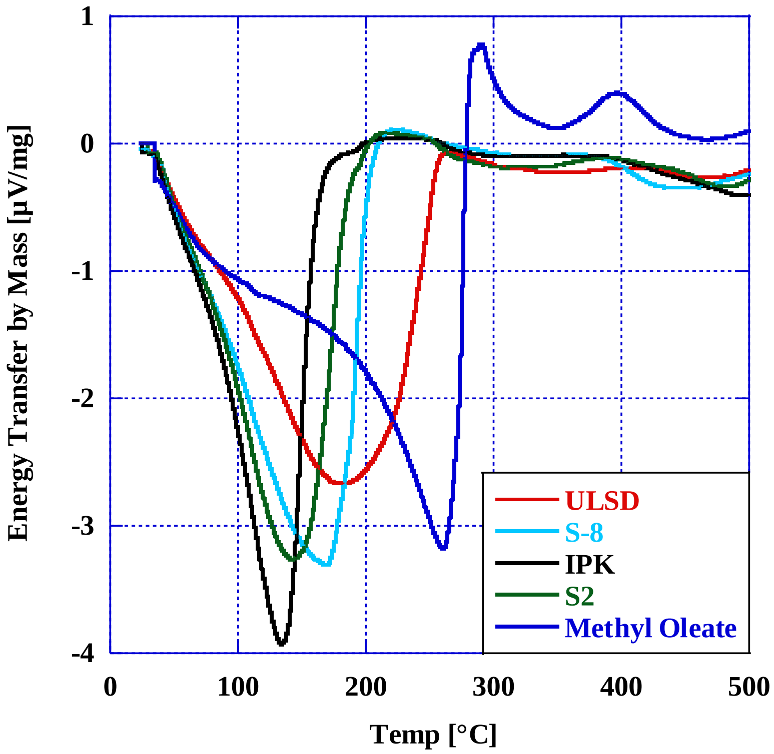

Figure 48: DTA for ULSD, S-8, IPK, S2, and Methyl Oleate

4.1.5 DROPLET FORMATION, SPRAY PROPAGATION, ATOMIZATION, AND MIXTURE FORMATION

Spray droplet distribution and Sauter Mean Diameter (SMD) of the spray over times for ULSD, S-8, IPK, S2, and Methyl Oleate were found using the procedures outlined in Section 3.2.5. The results of this determination are shown in Figure 48. Spray droplet size is an important parameter which affects in-cylinder combustion timing(III 1985), combustion efficiency (Cheng et al. 2023), and in-cylinder combustion dynamics. The graph in Figure 48 shows the SMD over time referencing the right hand y-axis and the top x-axis, and the spray volume frequency as a function of droplet diameter references the left hand y-axis and the bottom, logarithmic x-axis.

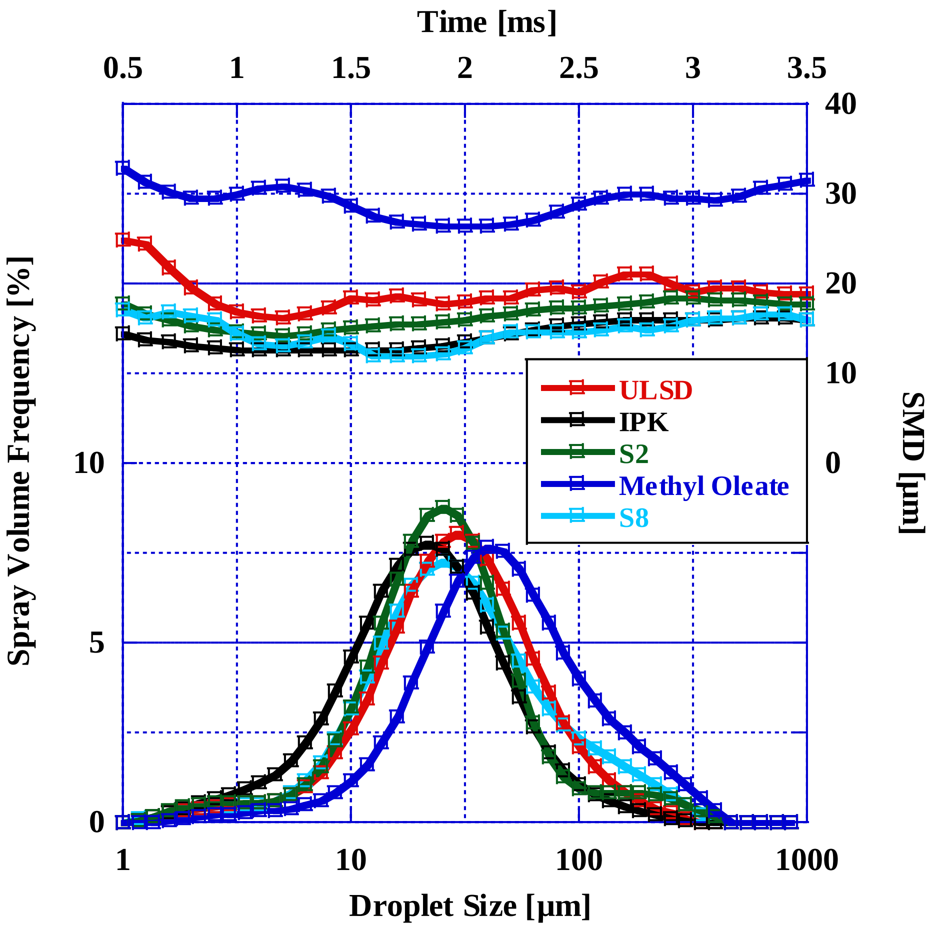

Figure 49: SMD and Droplet Size for S-8, ULSD, and IPK

Sauter Mean Diameter (SMD) for the entire fuel injection was calculated for each of the researched fuels in addition to the average droplet diameter for 10%, 50%, and 90% of the total spray denoted as Dv10, Dv50, and Dv90. These values are displayed in Table 20. Additionally, the Ohnesorge number was calculated for each of the researched fuels with those values listed in Table 21. It was found that methyl oleate had the largest SMD with a 10 µm increase when compared to ULSD with all other fuels falling below 20 µm. For S2, the addition of the methyl oleate additive was not found to significantly affect the SMD as it was found to lie between S-8 and IPK at 17.77 µm.

Table 20: SMD, Dv10, Dv50, and Dv90 for ULSD, S-8, IPK, S2, and Methyl Oleate

Fuel	SMD (μm)	Dv10 (μm)	Dv50 (μm)	Dv90 (μm)
ULSD	20.94	10.86	31.98	86.47
S-8	19.19	9.92	29.89	107.32
IPK	15.097	7.72	23.28	64.77
S2	17.77	10.29	27.33	78.92
Methyl Oleate	30.84	16.85	48.78	155.96

Spray propagation is indicated by the Dv10, 50, and 90 values as these represent the average droplet diameter when 10%, 50%, and 90% of the total spray has been injected. While Dv10 and Dv50 values are consistent with the SMD determination, Dv90 deviated from the trend with S-8 increasing in average spray droplet diameter to exceed that of ULSD. This indicates that as the spray develops, the S-8 droplets have a higher tendency to impact one another and increase in size. To further investigate the droplet behavior of each of the fuels, the Ohnesorge number was calculated using Equation 1 in Section 2.5.2 and the results displayed in Table 21. This parameter indicates the propensity of the fuel to break into a droplet relating internal fluidic forces to surface tension where a lower value indicates a higher tendency to form smaller droplets. From the evaluation of this dimensionless property, it was found that the results from the SMD calculation are consistent with each fuel's tendency to form droplets with methyl oleate having the highest value at 0.1682 and IPK at the lowest value at 0.0680.

Table 21: Ohnesorge Number Calculation for Each of the Researched Fuels

Research Fuel	Surface** Tension [N/m]	Viscosity* [cP]	SMD* [μm]	Density* [g/cm^3]	Oh
ULSD	28.02	2.44	22.36	0.850	0.1057
S-8	22.30	1.30	19.19	0.755	0.0723
IPK	20.30	1.02	15.097	0.740	0.0680
S2	21.68	1.41	17.77	0.748	0.0833
Methyl Oleate	27.40	4.54	30.84	0.862	0.1682

***Values determined from fuel testing using in-house equipment**
****Values obtained from literature (Edwards 2020) (Mousavi, Romero-Martínez, and Ramírez-Verduzco 2020)**

4.2 THERMODYNAMIC COMBUSTION ANALYSIS: CVCC

For the CVCC investigation and all further combustion analysis, the fuel blends will be referred to using the names listed in Table 22. Additionally, Table 22 lists the mass percentage of fuel in each of the analyzed fuel blends. Using the procedure outlined in Section 3.2.4, the three neat fuels (IPK, S-8, and ULSD) were investigated for Ignition Delay, Combustion Delay (CD), and Derived Cetane Number (DCN). Blends B1 through B3 were then created using IPK as a base and blending in S-8 with increasing even increments of 25% by mass to find the blends which most closely resembled the combustion profile of ULSD. Given the variability in both diesel fuel properties per batch as well as diesel fuel standards worldwide, a DCN of 50 was chosen as a target value. The target percentage was narrowed to lie between B2 and B3 allowing a final blend percentage to be calculated using the DCN equation. This fuel blend is denoted as S1 and with the lubricity analysis from Section 4.1.2 the lubricity improver was added to the blend and the final surrogate denoted as S2.

Table 22: Fuel Mass Percentage in Each Fuel Blend

Fuel Blend	IPK [%]	S-8[%]	Methyl Oleate [%]
B1	75	25	0
B2	50	50	0
B3	25	75	0
S1	40	60	0
S2	38.5	58.5	3

4.3.1 COMBUSTION CHAMBER PRESSURE: CVCC

The pressure trace for the CVCC analysis for each of the three neat, researched fuels is displayed in Figure 49. This is the primary measurement method for CVCC using the procedure outlined in Section 3.2.4. Other characteristics for defining the combustion of each fuel are calculated from the pressure-time data. For a baseline analysis, the neat fuels were run through the CVCC for assessment of ID, CD, and DCN with values for ID and CD given from calculations within the instrument. While traditionally, autoignition was defined by just the ID in a Cooperative Fuel Research (CFR) Variable Compression Ratio (VCR) Engine (Zahos-Siagos et al. 2017), DCN gives an accurate representation of the Cetane Number (CN) as found by ASTM standards while maintaining a high degree of repeatability (Knothe 2014; Prak et al. 2021; Seidenspinner et al. 2015).

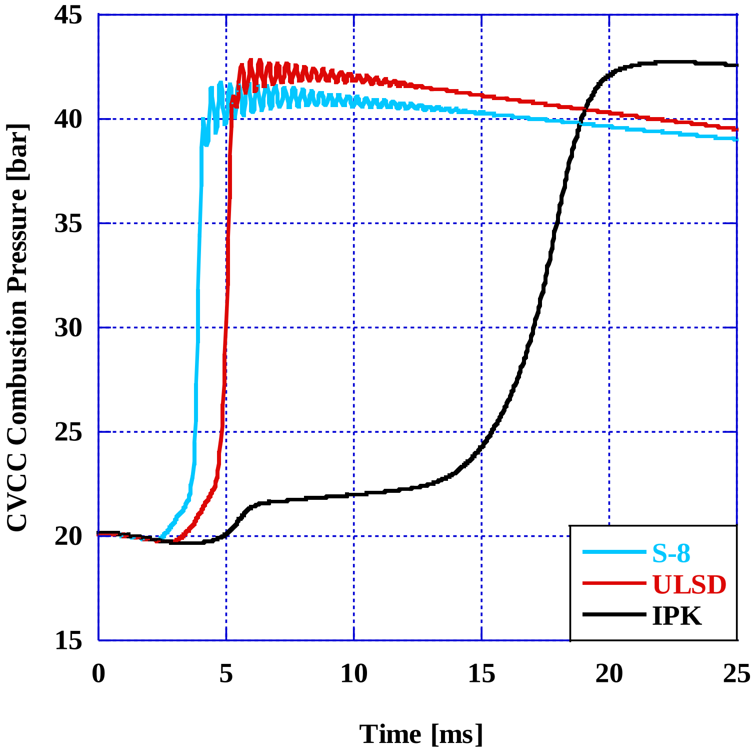

Figure 50: Pressure Trace for IPK, S-8, and ULSD

It can be seen from this graph that the peak pressure for IPK is the highest and lowest for S-8 with ULSD falling between the two. Consistent with the difference in DCN between IPK, S-8, and ULSD, S-8 exhibits the shortest combustion durations and the greatest magnitude oscillations around peak pressure. The combustion duration can be attributed to the ratio of iso-paraffins to normal paraffins as the double bonds found in the branch chain iso-paraffins require a higher activations energy than those found in the straight chain normal paraffins (Mayer 1967; Elmalik et al. 2013). The pressure trace of ULSD lies between S-8 and IPK with a DCN of 47.

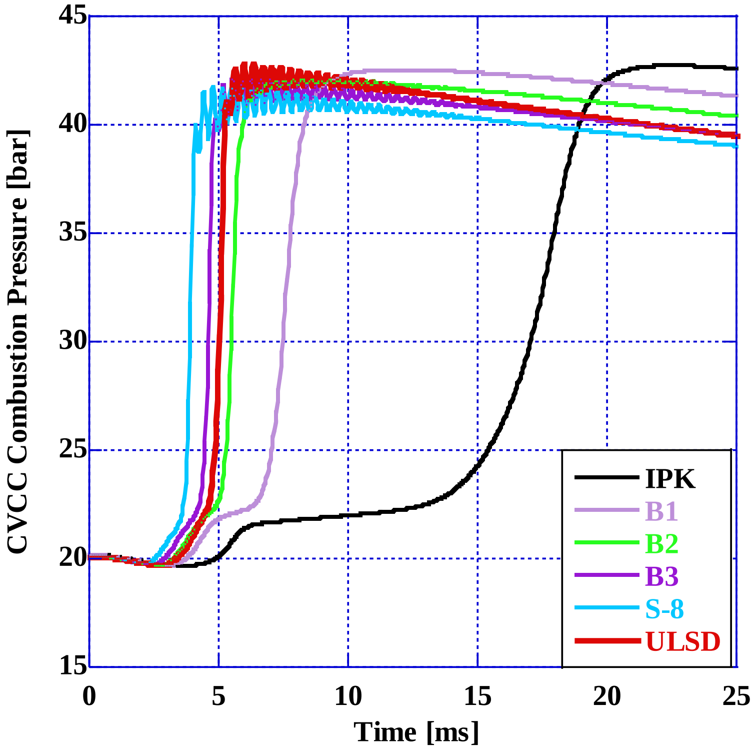

Figure 51: Pressure Trace for Neat IPK, S-8, and ULSD with B1, B2, and B3

To determine the blend percentage necessary to achieve the required DCN, a range of fuel blends between IPK and S-8 were analyzed with the pressure traces shown in Figure 51. These blends were denoted as B1, B2, and B3, and correspond to an increase percentage of S-8 in the blend with B1 at 25% by mass S-8 and increasing by 25% for each consecutive blend. The exact blend percentages are listed in Table 23. B2 is displayed with a dotted line as it is the closest match in DCN to neat ULSD. B2 and B3 were found to be almost equidistant from the required DCN indicating the ideal blend percentage lies between B2 and B3.

Table 23: Ignition Delay, Combustion Delay, and Derived Cetane Number for Neat ULSD, IPK and S-8 with blends B1, B2, and B3

Fuel	ID [ms]	CD [ms]	DCN
ULSD	3.5688	5.1523	47
IPK	5.3063	17.1718	25.88
S-8	2.7422	3.903	62.2
B1	3.6616	6.9959	38.55
B2	3.2313	5.2253	46.33
B3	2.9517	4.4058	53.97

Since DCN is a mathematical association between the ignition delay and the combustion delay, the equation can then be used to determine the ignition delay and combustion delay necessary to achieve the desired output DCN. Given the input data from each of 6 trials, the coefficients from the general DCN equation for ignition quality testing (IQT) at ASTM standard were changed to fit our specific instrument and its output values using a linear regression model. The standard DCN equation is written in Equation 10 as:

$$DCN = 13.028 + \left(-\frac{5.3378}{ID}\right) + \left(\frac{300.18}{CD}\right) + \left(-\frac{1256.8}{CD^2}\right) + \left(\frac{3415.32}{CD^3}\right) \qquad \text{Eq. 10}$$

This equation gives the general association between ID and CD for all IQT measurements following the ASTM standard D7668-14a listed in Table 2. The general equation has a less than 1% error and a standard deviation of 0.0018.

$$DCN = 13.161 - \left(\frac{6.6257}{ID}\right) + \left(\frac{302.46}{CD}\right) - \left(\frac{1274.6}{CD^2}\right) + \left(\frac{3426.5}{CD^3}\right) \qquad \text{Eq. 11}$$

Equation 11 was then used to create a graph of DCN as a function of ID and CD with surface graph of the function shown in Figure 52. The function was created using linear regression with the framework from the general DCN equation. Input values for ID, CD, and DCN were taken from the F-T fuel trials to fit the resulting equation to values specific to the alternative fuels.

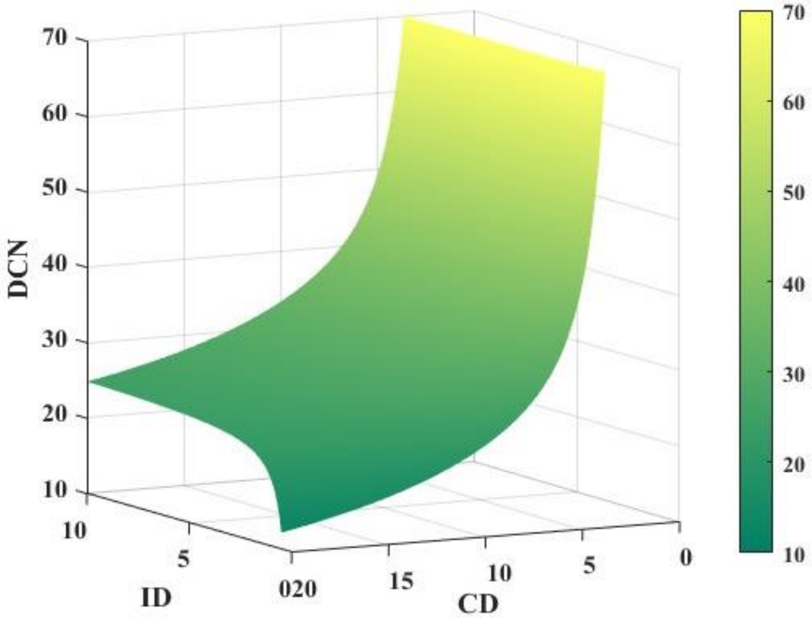

Figure 52: Surface Graph of the DCN Equation and a Function of ID and CD

The two blends which were found to be the closest in DCN to ULSD were B2 and B3. The pressure traces from the combustion of these fuels are shown in Figures 52 and 53. Between ULSD, B2, and B3, ULSD maintained the highest peak pressure contrary to the inverse correlation between DCN and peak pressure identified by comparing only the F-T blends. Given the results from B1, B2, and B3, a DCN of 50 was used as a target for the final fuel blend. The ideal blend percentage must exist between B2 and B3 limiting the range for IPK's and S-8's mass fraction to 0.5 through 0.25 and 0.5 through 0.75 respectively. Equation 11 was then used to calculate the target ID and CD values which were then correlated with fuel mass fraction and a final fuel blend of 60% S-8 and 40% IPK (S1) chosen for the surrogate.

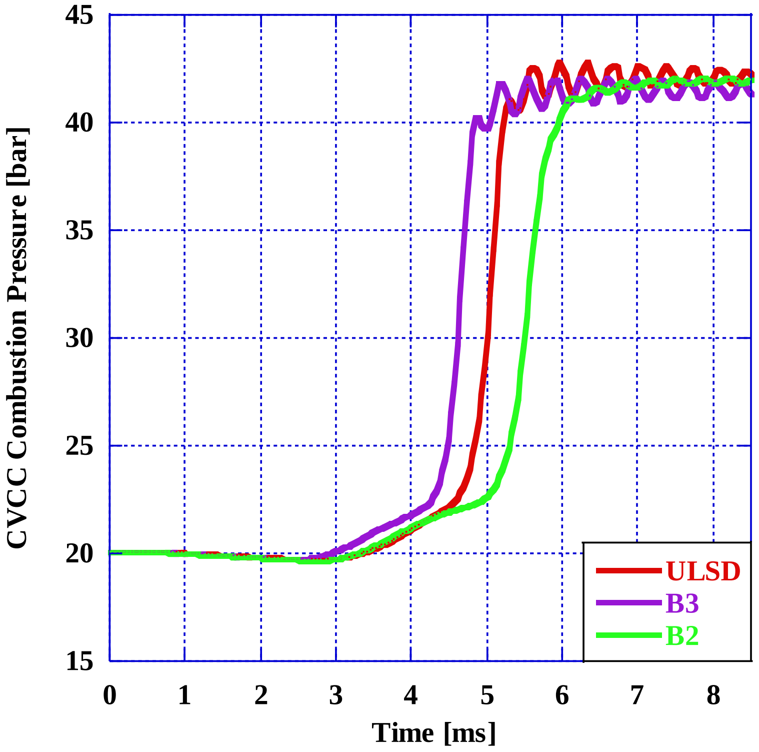

Figure 53: Pressure Trace for ULSD, B2, and B3

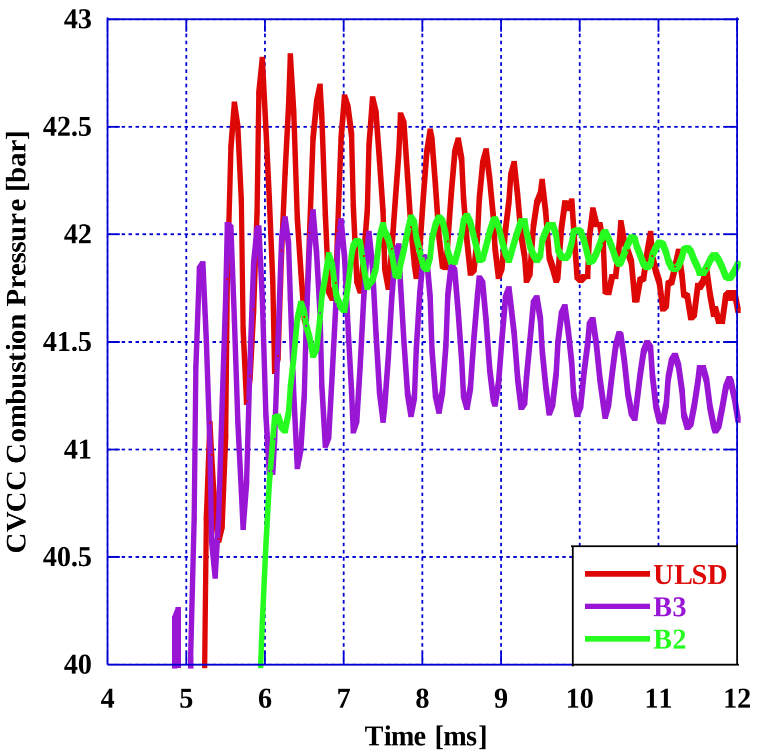

Figure 54: Peak Pressure Curves for ULSD, B2, and B3

With the blend percentage identified, two surrogate blends were investigated for combustion properties in the CVCC. From the lubricity analysis in Section 4.1.2, it was determined that an addition of 3% Methyl Oleate to the F-T fuels would increase the lubricity to comply with fuel standards. To determine if this addition had a significant impact on combustion, the surrogate blends S1 and S2 were compared to each other and to ULSD in the CVCC where S1 is 40% IPK and 60% S-8 while S2 is 38.5% IPK, 58.5% S-8, and 3% methyl oleate by mass. Figures 54 and 57 show the pressure trace over the entire combustion period and a zoom of the oscillations around peak pressure, respectively. Further analysis of the pressure trace of S2 was conducted and compared to ULSD.

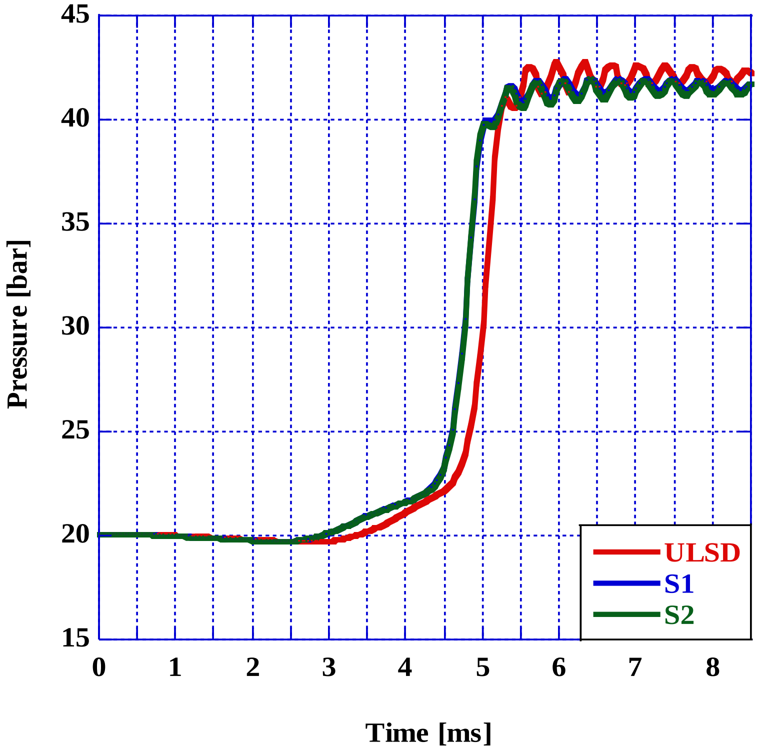

Figure 55: Pressure Trace for ULSD, S1, and S2

Table 24 displays the ID, CD, and DCN for ULSD , S1, and S2. Both of the blends exhibited an identical CD and DCN with a percent difference from ULSD at 7.4% decrease for CD and a 6.3% increase for DCN. For S1 and S2, ID was found to have the greatest percent difference at approximately -14% when compared to ULSD. From this analysis, it was concluded that the addition of 3% methyl oleate did not significantly affect the combustion characteristics of the blend and therefore did not require further analysis.

Table 24: ID, CD, and DCN for ULSD, S1, and S2 and the % Difference from ULSD

Fuel	ID [ms]/% diff	CD [ms]/% diff	DCN/ % diff
ULSD	3.5688	5.1523	47/-
S1	3.0725/-13.91	4.7714/-7.39	49.95/6.28
S2	3.0669/-14.06	4.7713/-7.39	49.95/6.28

For the pressure curves of S2 and ULSD, trendlines were taken for portions of the combustion pressure trace for further analysis. Figures 56 and 57 are the graphical representations of the trendlines for the pressure rise rate during combustion and the pressure drop after combustion. A linear representation was determined from the pressure values between start and end of combustion and the resulting graph is shown in Figure 55. This correlation was used to analyze the rate of combustion for each fuel as this can greatly affect ringing intensity (Soloiu, Weaver, Parker, Brant, et al. 2022). It was found through this determination that despite the increase in DCN, the surrogate does not burn at a significantly faster rate than ULSD. The slope of the trendline for ULSD and S2 show a percent difference of only 1%.

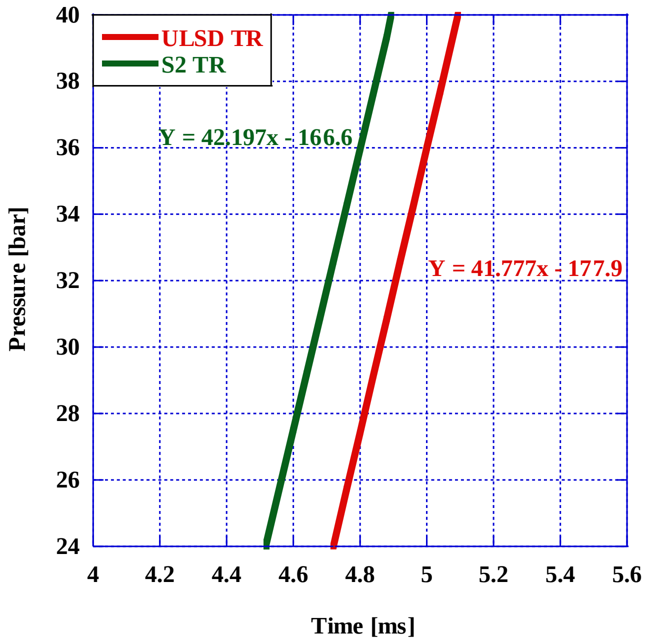

Figure 56: Trendlines for Pressure Rise Rate for ULSD and S2

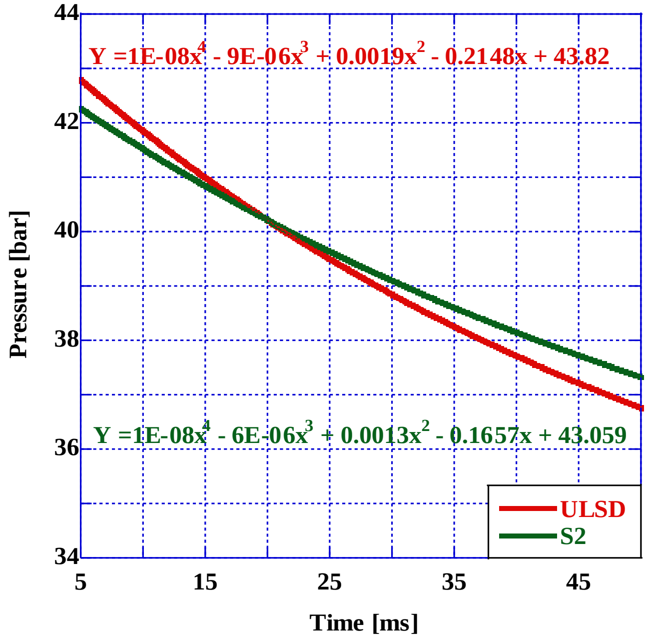

Figure 57: Trendlines of the Pressure Drop after Combustion for ULSD and S2

After the main combustion event, pressure begins to drop due to thermal losses through the walls of the combustion chamber. As the combustion chamber can be considered a closed system after fuel injection and the temperature outside the combustion chamber is constant, the rate at with the temperature and pressure drop can be attributed to the specific heat of the gas mixture.

Figure 57 shows the graph of trendlines created from the pressure values taken after end of combustion for ULSD and S2. From an analysis of each trendline, it was determined that despite the decrease in peak pressure and the reduction of ID and CD for the combustion of S2 when compared to ULSD, the end gas pressure dropped more slowly for S2. At 20 ms after start of injection, the pressure curves cross and the pressure for S2 is greater than that of ULSD. This indicates that the specific heat of the end gas mixture from the combustion of S2 is significantly greater than that of ULSD.

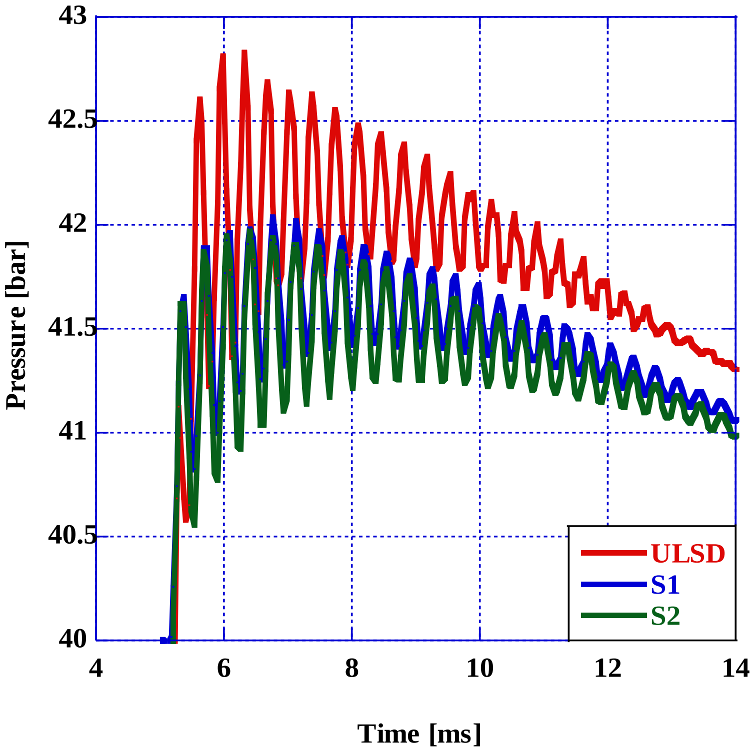

Figure 58: Peak Pressure Oscillations for ULSD, S1, and S2

The oscillations around peak pressure, ringing events, for ULSD, S1, and S2 are shown in Figure 58. Additionally, the peak pressures from the combustion of ULSD, S1, and S2 are listed in Table 25. It was found that for both S1 and S2, there was a reduction in peak pressure with a percent difference of -1.8% and -2% from ULSD respectively. Given the similarity between S1 and S2, it was further determined that the differences in combustion due to the addition of methyl oleate were negligible. Despite the similarity in pressure rise rate and the 2% difference in peak pressure, notable differences in both the magnitude and quantity of ringing events around peak pressure when comparing the combustion of S2 to that of ULSD. To analyze these ringing events, pressure data was taken between 4 and 16 ms and the maximum and minimum values recorded for each oscillation. Figures 59 and 60 show these values as two continuous curves representing the maximums and minimums for ULSD and S2.

Table 25: Peak Pressures for ULSD, S1, and S2

	Peak Pressure [bar]	% Difference
ULSD	42.83	-
S1	42.042	-1.83983
S2	41.97	-2.00794

Each circular point represents a point at which the pressure curve hits a maximum or minimum value. The magnitude of each ringing event was calculated as a difference between the maximum and minimum and the plot of magnitude with respect to time is shown in Figure 61. It was found that the average magnitude of the ringing events after the combustion of S2 was lower than that of ULSD indicating greater combustion stability.

Furthermore, the pressure oscillations for ULSD show inconsistencies in the pressure peaks as they begin to reduce in magnitude which is not present in the combustion of S2. The pressure oscillations after the combustion of S2, while smoother, persist until around 15 ms after SOI while those of ULSD stop before 13 ms after SOI.

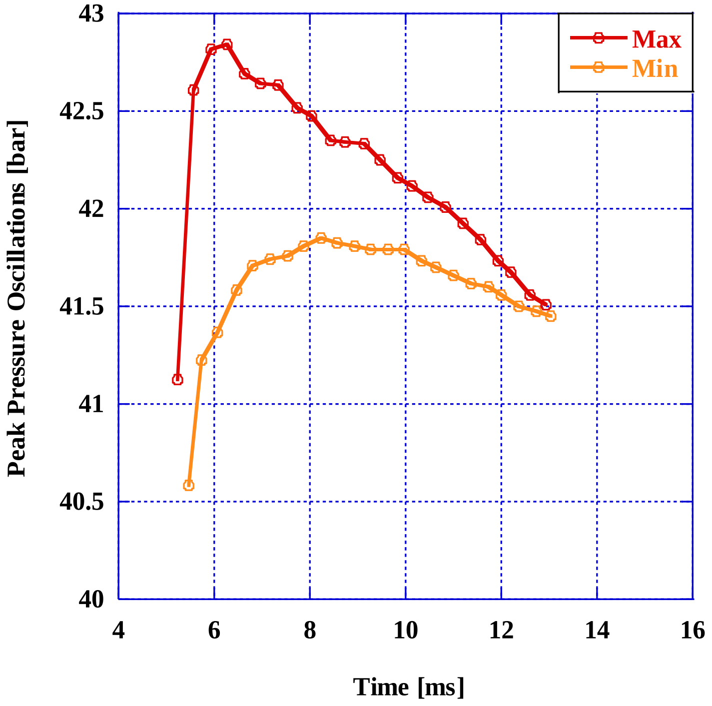

Figure 59: Ringing Intensity/Magnitude in the Pressure Trace for ULSD

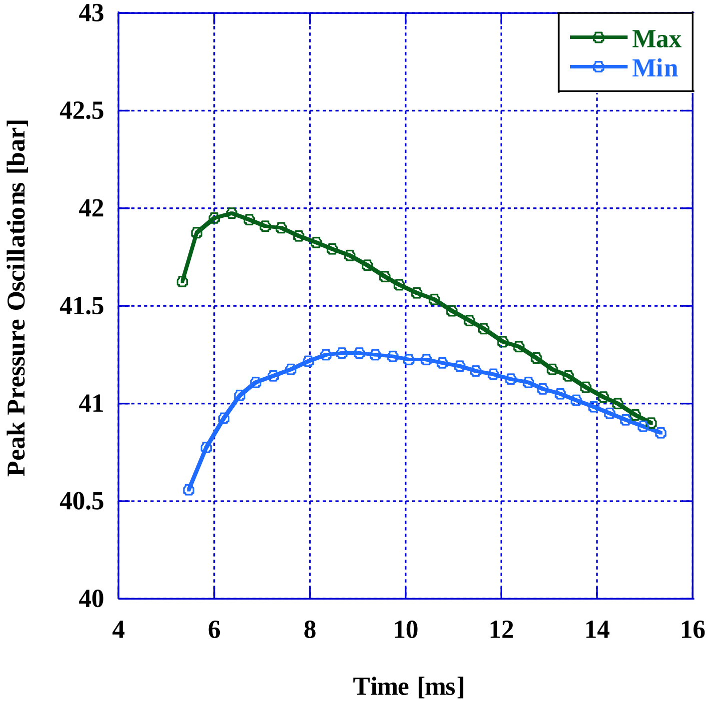

Figure 60: Ringing Intensity/Magnitude in the Pressure Trace for S2

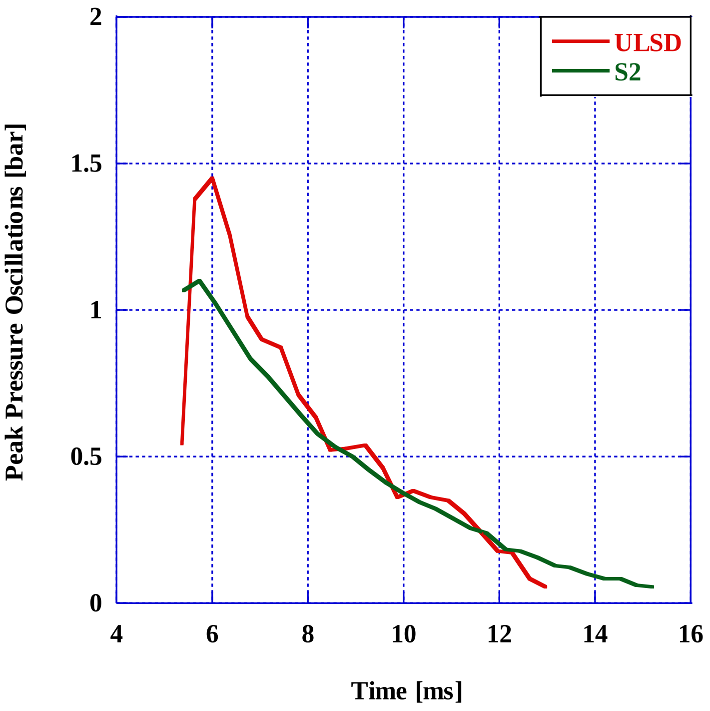

Figure 61: Magnitude of Ringing for ULSD and S2

Both fuels experienced an exponential reduction in the ringing amplitude after reaching peak pressure. An exponential trendline was used to quantify the difference in pressure oscillations between S2 and ULSD by comparing the coefficients b and k in Equation 12. These coefficients represent the rate at which the pressure oscillations drop in magnitude as shown in the graph in Figure 61.

$$y = be^{kx} \quad \text{Eq. 12}$$

It was found that the oscillations from the combustion of S2 begin at a lower intensity and converge at a slower rate. Consistent with the reduction in peak pressure from S2 compared to ULSD, the pressure oscillations begin at a reduced magnitude resulting in a b-value of 6.89 for S2 and 12.54 for ULSD. Additionally, the rate of oscillation convergence was found to be lower for S2 than ULSD with a k-value of -0.3 for S2 compared to -0.358 for ULSD. This reduction in convergence rate results in a greater quantity of ringing events for the combustion of S2 when compared to ULSD. This is an indication that S2 has a more stable combustion than that of ULSD.

$$\mathrm{y} = 12.54\mathrm{e}^{-0.358\mathrm{x}} \quad \text{Eq.13}$$

$$y = 6.89e^{-0.3x} \quad \text{Eq.14}$$

The equations of the trendline for ULSD and S2 can be seen in Equation 13 and Equation 14 respectively. The reduction in the pressure oscillations after combustion indicates that the combustion of S2 is more stable than that of ULSD. This correlated to the extended region of cool flame formation outlined in Section 4.2.2. Cool flames were found to have a significant impact on the ignition timing burn rate, burn limit, and engine knock (Guzman and Brezinsky 2021)

4.2.2 APPARENT HEAT RELEASE RATE: CVCC

The apparent heat release rate (AHRR) is a measurement of the amount of energy produced from combustion which affects the mixture. This is only part of the energy which is released from combustion as a portion of the heat released from the exothermic reaction is taken by the activation energy of the remaining reactants as well as the specific heat of the gas mixture.

AHRR is calculated using the first law of thermodynamics, and, in the CVCC, is variable only with the first derivative of pressure. Volume remains constant and is equal to the volume of the combustion chamber. The specific heat ratio, γ, is assumed to be that of air and is kept as a constant for this investigation. The equation for AHRR in the CVCC is listed in Equation 15. The AHRR for each of the neat research fuels is shown in Figure 62.

$$\frac{dQ}{dt} = \frac{1}{[\gamma - 1]} V \frac{dP}{dt} \quad \text{Eq.15}$$

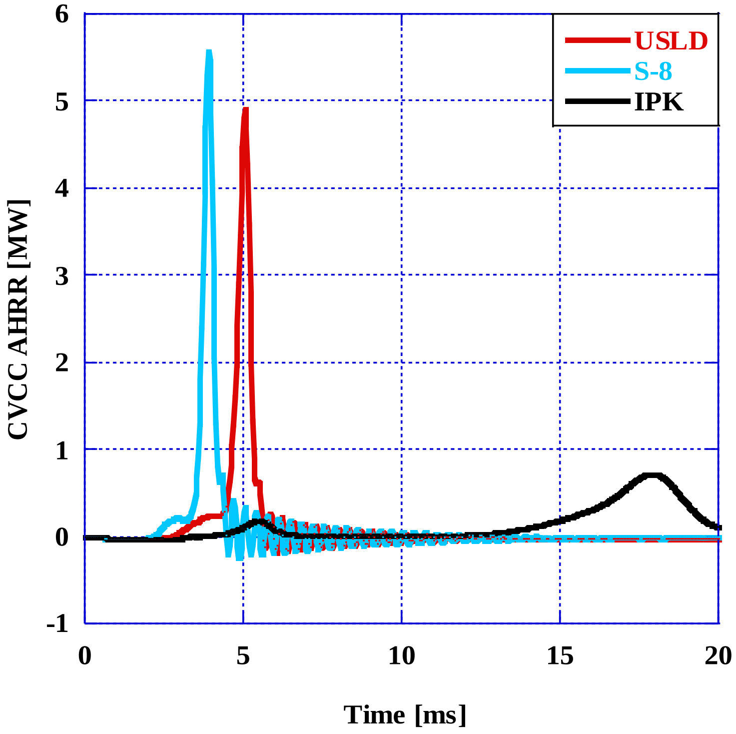

Figure 62: Apparent Heat Release Rate for IPK, S-8, and ULSD

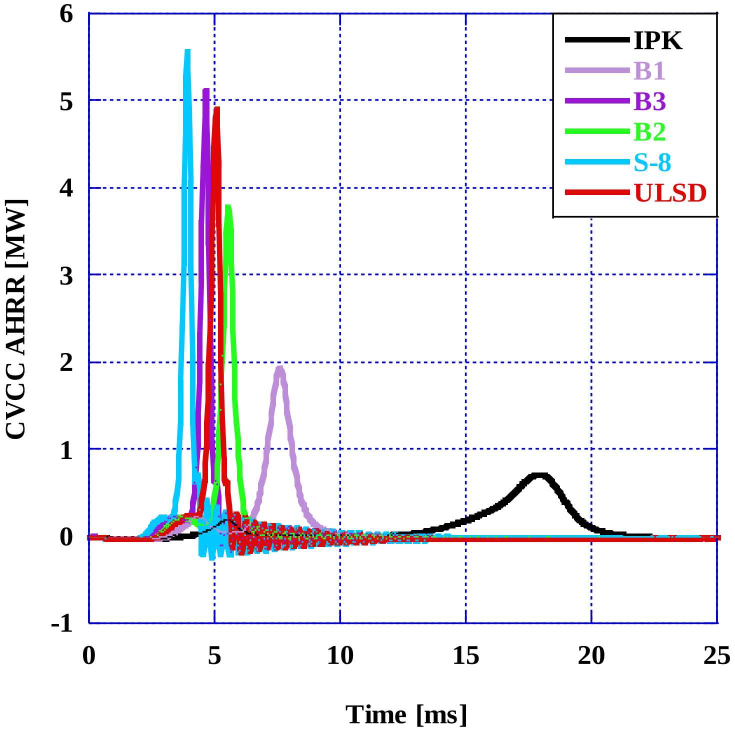

Figure 63: AHRR for IPK, S-8, ULSD, and blends B1, B2, andB3

The AHRR curves for each of the neat fuels are shown in Figure 62 and the neat fuels with the IPK and S-8 blends are shown in Figure 63. There can be seen an exponential correlation between the reduction in DCN and the reduction in peak AHRR. Additionally, with the B1 and IPK there are no oscillations after the main combustion event correlating to a reduction in pressure rise rate.

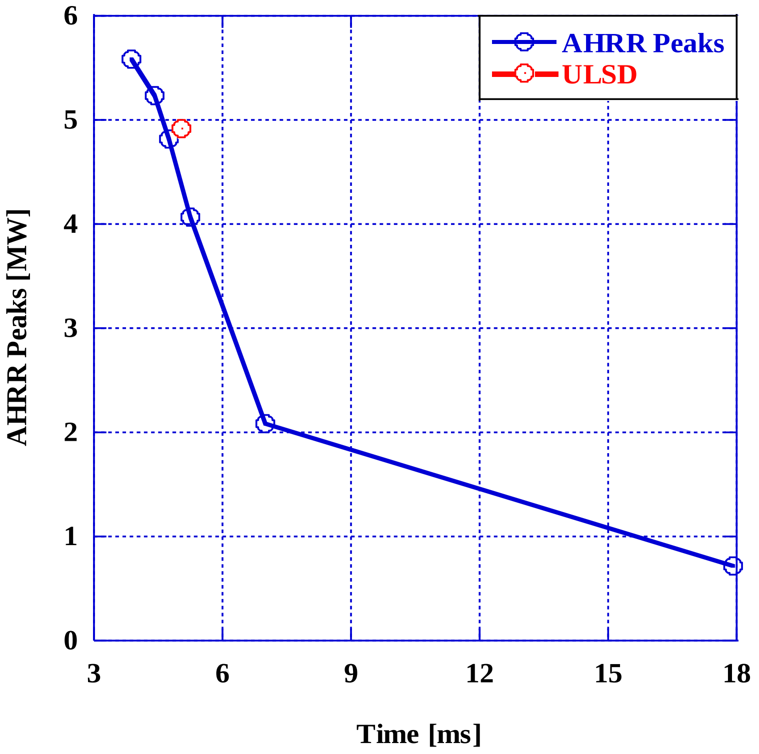

Figure 64: Curve of the Peaks in the AHRR Curve for Each of the Researched Fuels

Figure 64 is a graph of the peak AHRR as a single point whose x-value is the time at which AHRR hits its peak for each fuel. ULSD is marked on the graph with a point in black as it is not F-T fuel or blend and therefore falls outside the equivalence. The blue line connecting the AHRR points illustrates the exponential decrease in peak AHRR as the percentage of IPK in the blend increases. Listed in Table 26 are peak AHRR values and the precent differences from ULSD for ULSD, IPK, S-8 and Fuel Blends B1, 2, and 3 with the same values for S1 and S2 specifically listed in Table 27.

Table 26: Peak AHRR for ULSD, IPK, S-8 and Fuel Blends B1, 2, and 3

Fuel	Peak AHRR	% Diff.
ULSD	4.913	-
IPK	0.721	-85.325
S-8	5.778	17.606
B1	2.089	-57.480
B2	4.064	-17.281
B3	5.227	6.391

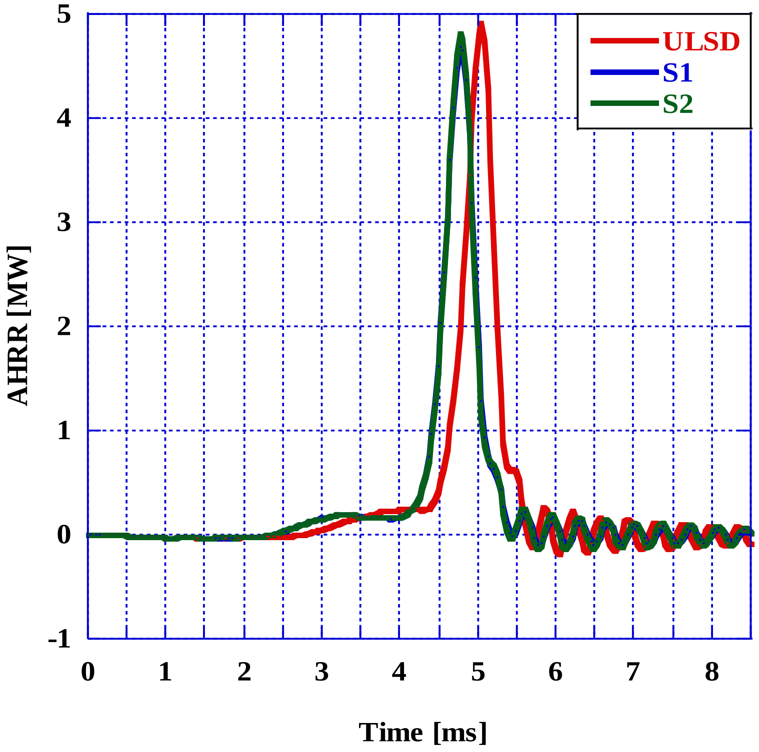

Figure 65: AHRR for ULSD and Surrogate Blends S1 and S2

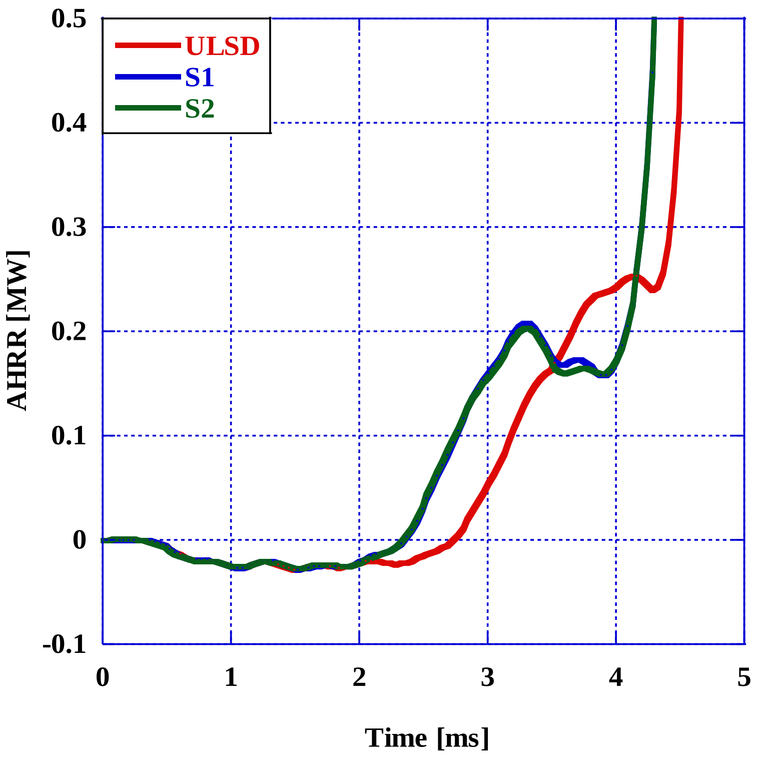

Figure 66: LTHR Region for ULSD and Surrogate Blends S1 and S2

Table 27: Peak AHRR for ULSD and Surrogate blends S1 and S2

Fuel	**Peak AHRR**	**% Diff. from ULSD**
ULSD	4.913	-
S1	4.68	-4.68
S2	4.81	-2.06

AHRR as derived from pressure, volume, and specific heat ratio can be analyzed for each region of combustion exhibited in the heat release curve. For each fuel, there are two peaks associated with the two primary regions of combustion, Low Temperature Heat Release (LTHR) and the High Temperature Heat Release (HTHR). These two regions become more defined as the DCN of the fuel decreases. Both the graphical representation of AHRR as well as the numerical data can be used to identify the various regions of combustion.

This study identifies the ignition delay (ID), combustion delay (CD), start of combustion (SOC), end of combustion (EOC), cool flame formation region, Negative Temperature Coefficient (NTC) region, LTHR, and HTHR. These regions are defined as follows:

- Start of injection initiates data recording and is therefore denoted on all graphs at 0 ms. This coincides with the beginning of ID with the peak Heat Release Rate (HRR) in LTHR marking the end of ID.
- LTHR begins the moment AHRR crosses zero and becomes positive indicating that the exothermic chemical reactions have reached an equivalence to the energy which is absorbed from the vaporization of the atomized fuel.
- Within LTHR, the region is defined by two main combustion events denoted as the cool flame formation region and the NTC region.
- Cool flame formation begins at the same time as the LTHR region and ends when LTHR reaches its peak and the slope of the AHRR curve becomes negative.
- From this point to the point at which AHRR exceeds its peak in LTHR is denoted as the NTC region. This point also marks the end of LTHR and the beginning of HTHR and defines Start of Combustion (SOC).
- The midpoint of the HTHR region where the pressure rise rate changes inflection or, in other terms, the second derivative of pressure changes from positive to negative is defined as the Combustion Delay (CD). This is the point at which the reaction rate is no longer governed by the increasing temperature but is controlled by the concentration of reactants to products as the reaction begins to slow despite the increase in temperature.
- End of Combustion (EOC) is defined as the moment at which the AHRR crosses zero and becomes negative for the first time after CD.
- Oscillations after EOC are identified as ringing events due to the initial shock of the rapidly increasing pressure from combustion.

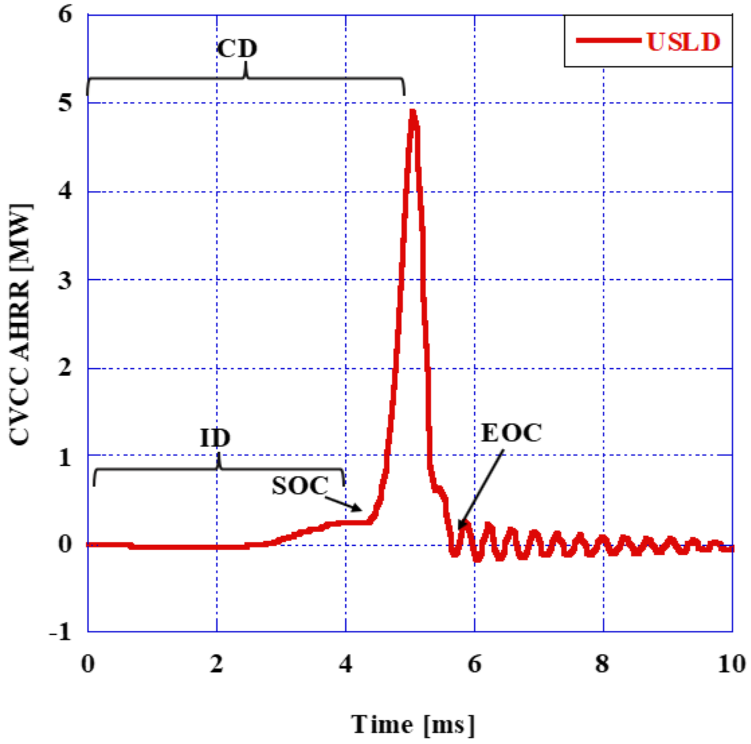

Figure 67: Points of Definition on the AHRR Curve for ULSD

Figure 67 shows the AHRR curve for ULSD with the points for ID, CD, SOC, and EOC marked on the graph. The graphs in Figures 68 and 69 show the regions in LTHR for ULSD and S2. The total duration for LTHR between the two fuels is very similar with S2 exhibiting a 10% increase in LTHR duration when compared to ULSD. The regions of combustion, however, show significant differences as the NTC region for the combustion of S2 is 3 times longer than that of ULSD. Additionally, Figures 68 and 69 illustrate the effect of fuel injection and vaporization as AHRR is negative between SOI and the start of LTHR. The injected fuel is at a much lower temperature than the chamber gas and therefore reduces the temperature due to an increase in the mass of the closed system. Additionally, the atomized fuel vaporizes and absorbs heat from the chamber gas further reducing the temperature and pressure and reflects as negative values in the AHRR.

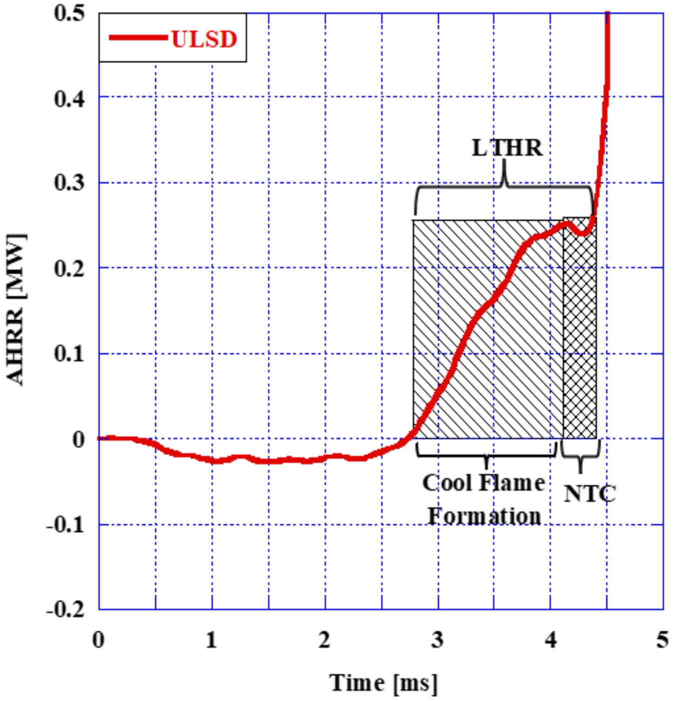

Figure 68: Regions of LTHR for the Combustion of ULSD in the CVCC

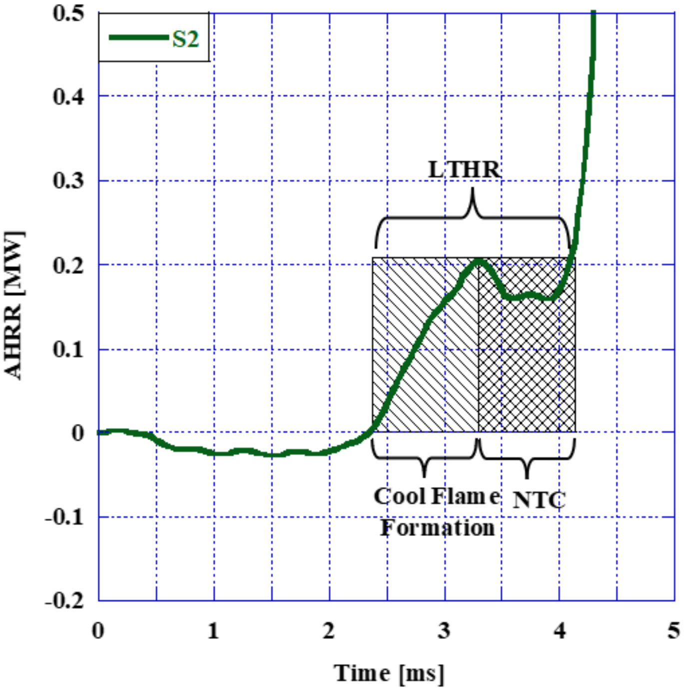

Figure 69: Regions of LTHR for the Combustion of S2 in the CVCC

The energy released for each combustion region as well as the duration of each combustion region are listed in Tables 28 and 29 and displayed as stacked column graphs in Figures 70 and 71. In terms of energy released, it is clear that HTHR is the region for which the majority of the energy from combustion is released. The divide in the regions of LTHR are what distinguish each fuel and blend. For the F-T fuels, the increase in the mass % of IPK in the blend increases the percentage of total energy release as well as the energy released in the NTC region.

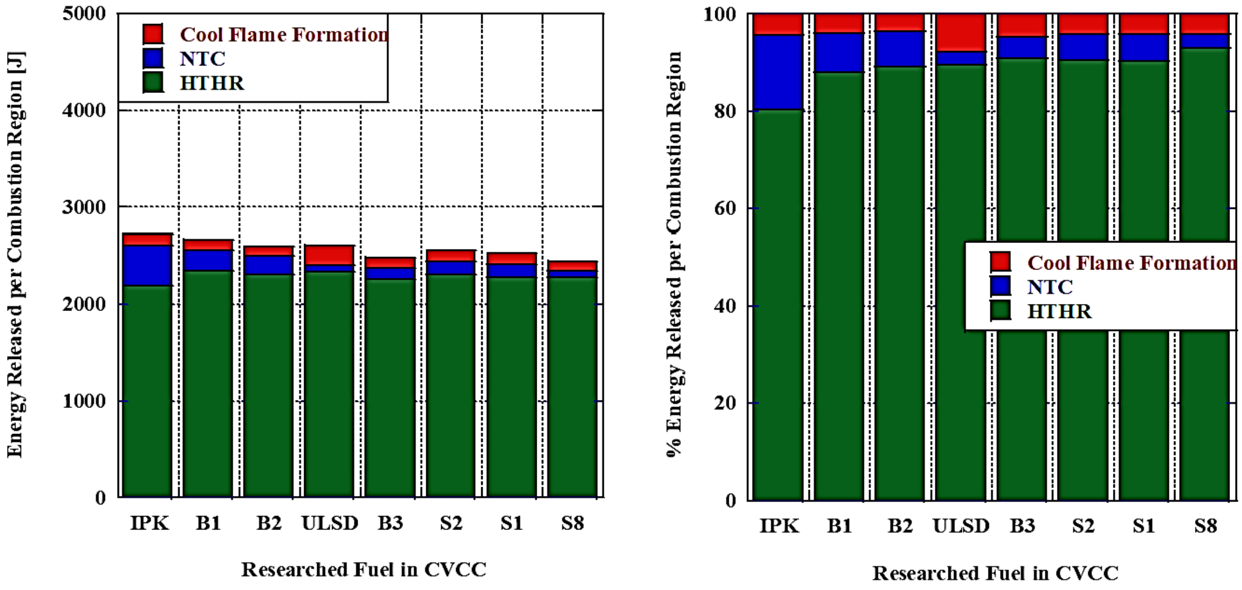

Figure 70: Regions of Combustion for Each Researched Fuel in Terms of Energy Released by Region and Percentage of Total Energy Released

The graphs in Figure 70 represent the energy released per combustion region and the percentage of total energy released per combustion region for all of the researched fuels arranged by DCN (lowest to highest). It was found that there was a general association between increasing DCN, and total energy released with S-8 releasing the lowest total energy at 2447.02 J and IPK releasing the most total energy at 2728.23 J. For each of the F-T fuels, the cool flame formation region released approximately the same amount of energy as a percentage of its total released energy at around 4%. Despite the increase in total released energy correlated with the decrease in fuel DCN of the F-T fuels, the energy released in the cool flame region of LTHR remained proportionally comparable. ULSD, on the other hand, has a relatively small NTC region favoring cool flame formation in LTHR and releasing around 8% of its total energy in this region.

Table 28: Regions of Combustion for Each Researched Fuel in Terms of Energy Released by Region and Percentage of Total Energy Released

	LTHR		NTC		HTHR		Total
	[J]	[%]	[J]	[%]	[J]	[%]	[J]
ULSD	273.07	10.45	70.22	2.67	2339.84	89.55	2612.91
IPK	535.03	19.61	411.91	15.09	2193.20	80.39	2728.23
S-8	171.93	7.03	72.90	2.98	2275.09	92.97	2447.02
B1	319.4	11.98	214.4	8.04	2346.49	88.02	2665.89
B2	283.52	10.9	189.86	7.31	2312.13	89.08	2595.65
B3	227.55	9.13	107.22	4.30	2265.0	90.87	2492.55
S1	246.52	9.75	141.65	5.60	2281.91	90.25	2528.43
S2	243.62	9.54	138.67	5.43	2311.71	90.46	2554.71

To further analyze the divide between the regions of combustion, the duration of each combustion region was considered. The time duration for each combustion region as well as the percentage of total combustion time was taken for each researched fuel and displayed as two stacked diagrams in Figure 71 with the data shown in Table 29. The graphs in Figure 71 show the fuels in order of increasing DCN like the graphs in Figure 69 for energy released.

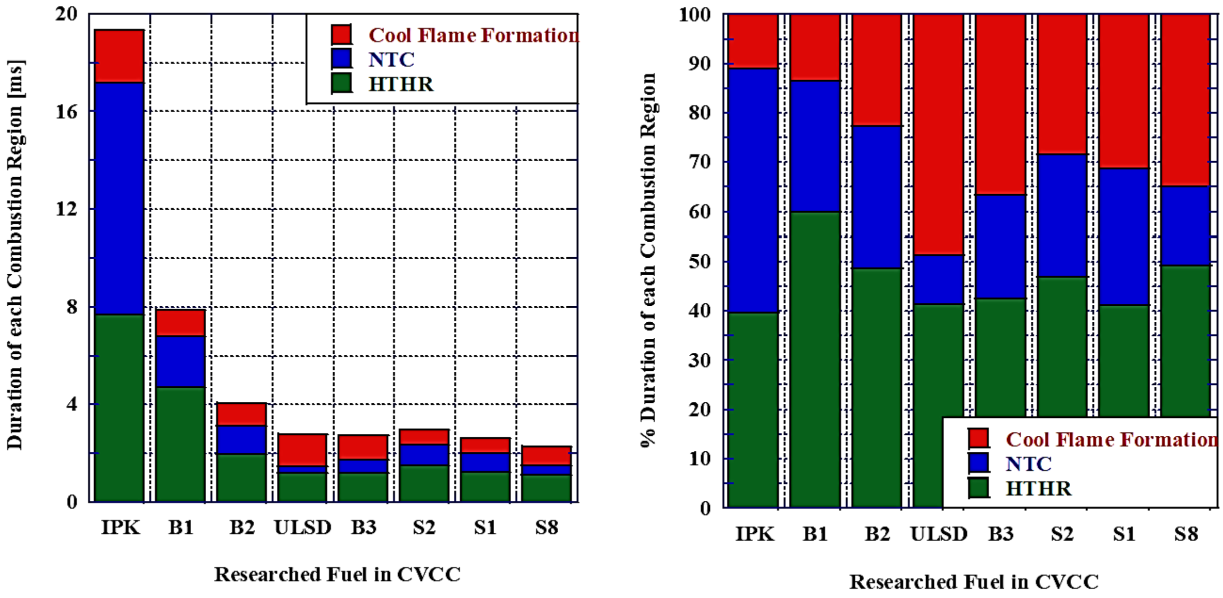

Figure 71: Duration of Each Combustion Region and Percentage of Total Combustion Duration for Each Researched Fuel

Here there can be seen a clear correlation between the increase in fuel DCN and total combustion duration. With the exception of S2, combustion duration decreases exponentially with the increase in fuel DCN. Furthermore, the analysis of combustion duration more clearly shows the changes in the NTC region with the increase in fuel DCN.

Table 29: Duration of Each Combustion Region and Percentage of Total Combustion Duration for Each Researched Fuel

	LTHR		**NTC**		**HTHR**		**Total**
	[ms]	**[%]**	**[ms]**	**[%]**	**[ms]**	**[%]**	**[ms]**
ULSD	1.64	58.57	0.28	10	1.16	41.43	2.8
IPK	11.64	60.25	9.48	49.07	7.68	39.75	19.32
S-8	1.16	50.88	0.36	15.79	1.12	49.12	2.28
B1	3.16	40.10	2.08	26.39	4.72	59.89	7.88
B2	2.08	51.48	1.16	28.71	1.96	48.51	4.04
B3	1.56	57.35	0.56	20.59	1.16	42.64	2.72
S1	1.72	58.90	0.8	27.39	1.2	41.09	2.92
S2	1.72	58.09	0.8	24.69	1.52	46.91	3.24

The length of these regions is important in understanding the combustion behavior and the LTHR region. The LTHR region is the period of combustion where heavy peroxides and radicals are rapidly formed and breakdown releasing small amounts of energy at temperatures below Auto Ignition Temperature (AIT) (Y. Ju et al. 2019; Y.G. Ju 2021). Fuels which have a larger quantity of complex hydrocarbons will experience an extended period of LTHR (Phuong X. Pham 2021; Heywood 2018). These complex hydrocarbons break down into radicals, peroxides, and aldehydes, and low luminosity cool flames are formed, decay, and quench in rapid succession in early combustion (Nayagam et al. 2012; Heywood 2018). After the region of cool flame formation, there is a period of increased peroxide formation of predominantly ketohydroperoxides. These compounds have a positive enthalpy of formation consuming more energy from their formation than is released from combustion(Y.G. Ju 2021; Steeger et al. 2022). This phenomenon is the driving factor behind the reduction in AHRR before HTHR and creates the NTC region. (Z. Wang et al. 2018), (Z. Wang and Sarathy 2016), (Yehia, Reuter, and Ju 2018)

4.2.3 COMBUSTION TEMPERATURE: CVCC

Combustion temperature was derived from the measured pressure data and the known constant volume of the combustion chamber with the reference gas mixture assumed to be air a 79% nitrogen-19% oxygen ratio. The temperature traces for ULSD and S2 are shown in Figure 72. Key points in the LTHR and the NTC regions are mapped in terms of temperature and shown in Table 30. The combustion of S2 resulted in a lower temperature at the end of LTHR when compared to ULSD correlating the larger quantity of energy released during this region for ULSD.

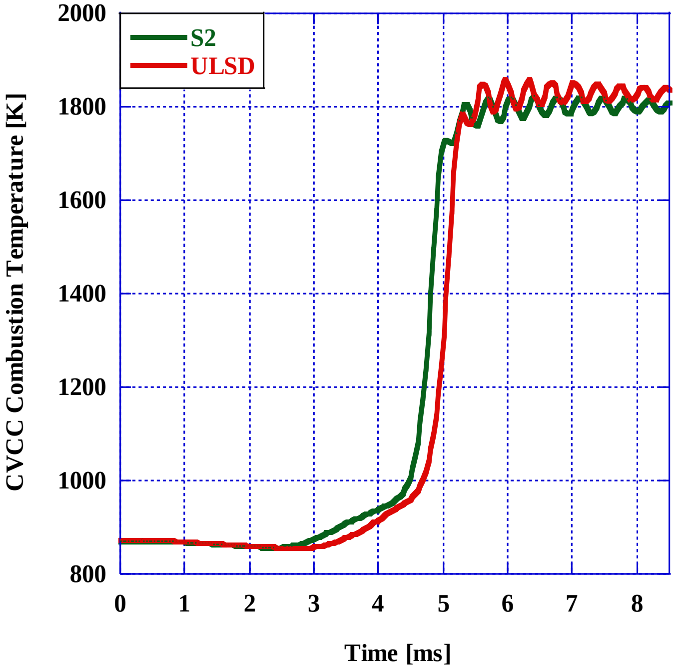

Figure 72: Combustion Chamber Temperature for ULSD and S2

Just as the low temperature combustion regions were mapped and determined for the AHRR curve, these regions are again mapped along the temperature curves for ULSD and S2 shown in Figures 73 and 74. With the increase in DCN, S2’s LTHR region begins at 2.4 ms compared to 2.76 ms for ULSD. Due to the decrease in time between start of injection and start of LTHR, the chamber temperature at the start of LTHR is higher for the combustion of S2 than that of ULSD. The time between the start of injection and start of LTHR, seen as negative AHRR values, determines the temperature at which LTHR begins. This can be attributed to the absorption of heat from the injected fuel which decreases the temperature the longer AHRR is negative. There can also be seen a slower increase in the temperature during LTHR for S2 than that of ULSD.

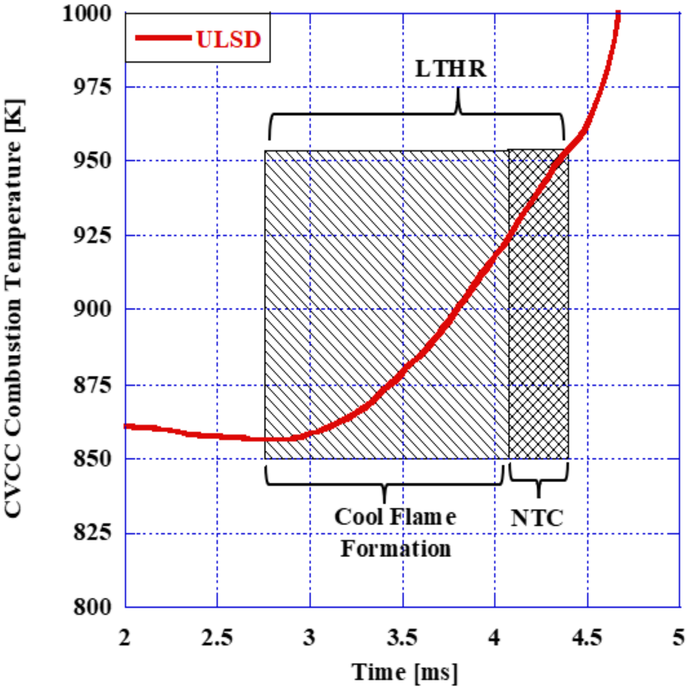

Figure 73: Combustion Regions by Temperature for ULSD

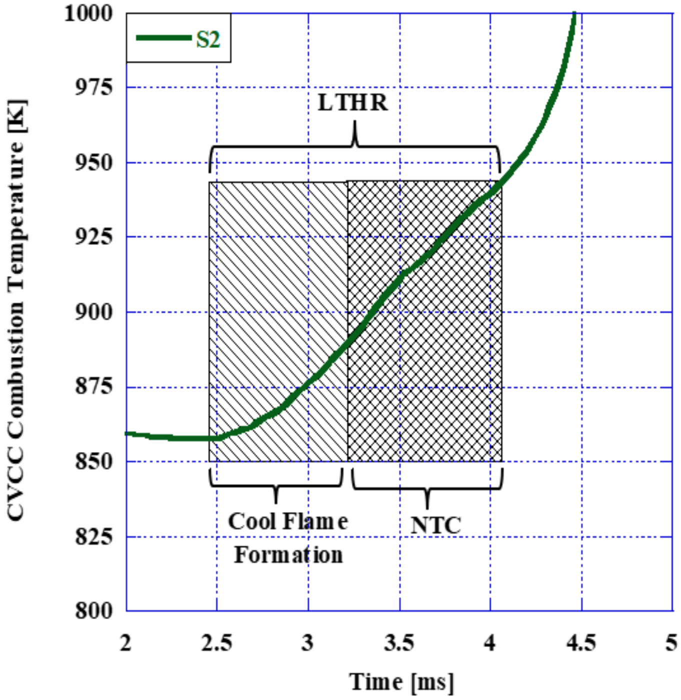

Figure 74: Combustion Regions by Temperature for S2

Figures 73 and 74 represent the temperature curves for the combustion of ULSD and S2 respectively. Specifically, these figures highlight the LTHR regions and identify the corresponding regions of cool flame formation and NTC regions. Temperature values were taken at the start of the LTHR region, the peak in LTHR, start of the NTC region, the lowest point (valley) in NTC, and at peak HTHR. These values are listed in Table 30.

Table 30: Temperatures [K] and Durations [ms] of LTHR and NTC for ULSD and S2

	LTHR Temp		**LTHR Peak**		**NTC Temp**		**NTC Valley**		**Peak HTHR**	
	Start	**End**	**Temp**	**Time**	**Start**	**End**	**Temp**	**Time**	**Temp**	**Time**
ULSD	856.77	957.51	933.29	4.16	913.4	957.51	944.85	4.28	1395.2	5.04
S2	857.65	945.21	898.03	3.28	898.03	947.98	914.68	3.56	1402.7	4.76

It was found that despite starting LTHR at approximately the same temperature, the combustion of S2 exhibits lower temperatures for all subsequent measured points in LTHR. The low temperature combustion behavior is apparent at temperatures below 1000K where ignition delay is outside of the temperature range for high temperature ignition (H.W. Wang and Oehlschlaeger 2012). This is consistent with the analysis of energy released per combustion region as discussed earlier in the section. The reduction in the duration of the cool flame formation region and extended NTC region for the combustion of S2 reduces the energy released in LTHR when compared to ULSD. This results in lower temperatures in LTHR. In HTHR, however, the shorter CD of S2 from rapid combustion after SOC when compared to ULSD is reflected in the increase in temperature at peak HTHR despite the notable disparity in temperature between ULSD and S2 at the end of LTHR.

Further analysis of temperature and AHRR for each fuel can be seen in Figure 75 where AHRR for ULSD and S2 is plotted as a function of temperature starting from the point at which AHRR becomes positive. This correlation shows the changes in AHRR normalized for its effect on increasing temperature. As temperature increases, the formation and quenching of cool flames can be seen as oscillations in AHRR where intermediate species are oxidized until temperature reaches sufficient levels to initiate autoignition or HTHR (Y. Ju et al. 2019). This is observed from approx. 850 °C to 945 °C as the fluctuations of slope as they reach their peak AHRR value during their respective LTHR phase.

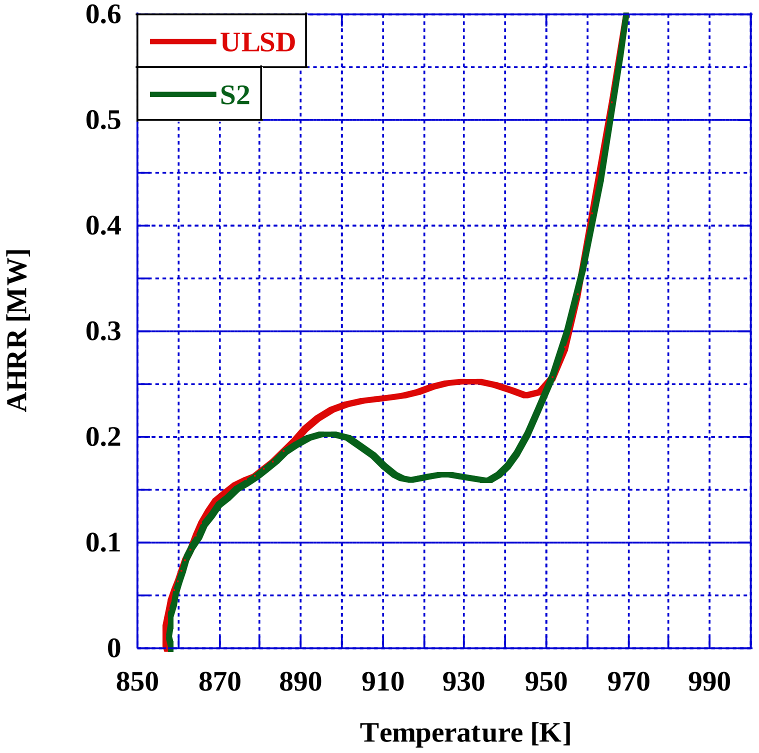

Figure 75: AHRR vs Temperature for ULSD and S2

In LTHR, both cool and warm flames are formed where in this paper the cool flame formation region references the initial low luminosity flames which occur in the preliminary combustion reactions where further distinction between cool and warm flames is dependent on temperature (Heywood 2018; Y. Ju et al. 2019). The following change in inflection of AHRR in intermediate temperatures (800K-1000K) begins the NTC region. This intermediate temperature region is where LTHR takes place for each researched fuel. In this study, the Low Temperature Ignition (LTI) and High Temperature Ignition (HTI) coincide with the start of LTHR and the start of HTHR respectively. The difference between these two ignition delay times is primarily governed by the kinetic interactions between the intermediate radicals which stem from the chemical composition of the fuel (Y. Ju et al. 2019). The concentration, species, and addition of radicals through the combustion, extinction, and reignition of flames in this region changes the influence of LTI on HTI (Y. Ju et al. 2019; Law and Zhao 2012; Nayagam et al. 2012).

The NTC region characterized by the reduction in AHRR is additionally defined by the non-monotonicity of the reactions within this region. Though temperature continues to increase, the intermediate reactions favor endothermic processes where chain-branching intermediaries absorb more energy during their formation than is released from their combustion. This region is vitally necessary for the formation of stable cool flames(Y. Ju et al. 2019; Heywood 2018).

4.2.4 MASS FRACTION BURNED: CVCC

For each of the researched fuels, the mass fraction burned was calculated using the integration of AHRR and the LHV for each fuel. The graph of the mass fraction burned for F-T fuel blends and ULSD is shown in Figure 75 where the x-axis is on a logarithmic scale to include the combustion of IPK. This graph more clearly illustrates burn rate as the ringing events are not factored into the calculation and only heat release values between start of LTHR and end of combustion are used to calculate fuel mass burned. It can be noted from the curves for B2 and ULSD, the F-T fuels exhibit different fractional burn rates than that of ULSD. Where B2 begins to combust sooner than ULSD in low temperature combustion, ULSD combusts more rapidly in HTHR leading to an overall faster burn rate.

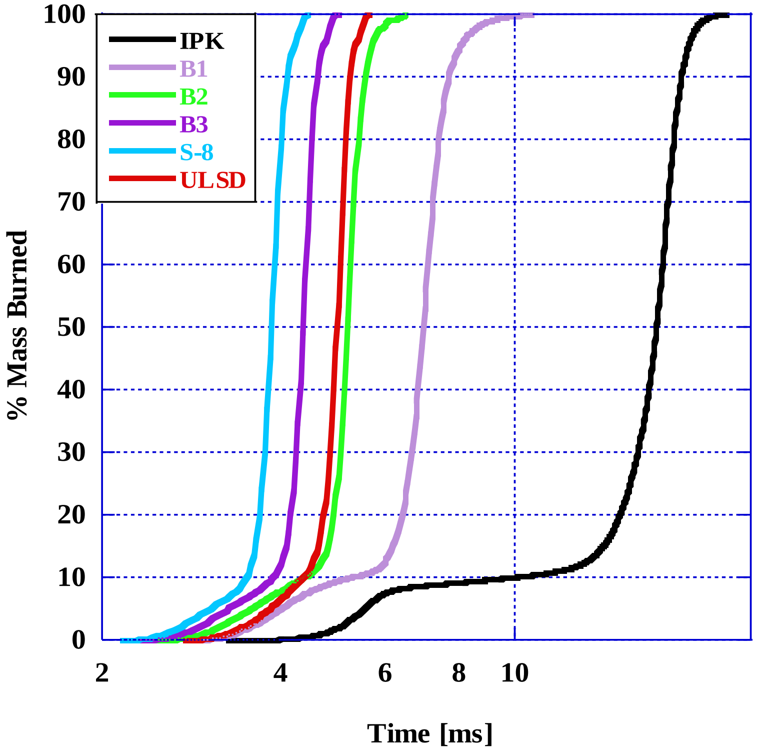

Figure 76: % Mass Burned in the CVCC for the F-T Synthetic neat Fuels and Fuel Blends

For each of the researched fuel blends, the time at which 10%, 50% and 90% mass burned are listed in Table 31 and denoted as t10, t50, and t90 respectively. With increasing DCN, the time necessary to hit 10%, 50%, and 90% mass burned increases exponentially following the trend established in previous sections.

Table 31: Time at which 10%, 50%, and 90% MFB for ULSD, S-8, IPK, B1, B2, and B2

Fuel	t10	t50	t90
IPK	9.76	17.28	19.04
B1	5.24	6.96	7.72
B2	4.36	5.2	5.56
ULSD	4.36	5	5.24
B3	3.88	4.36	4.6
S-8	3.48	3.84	4.12

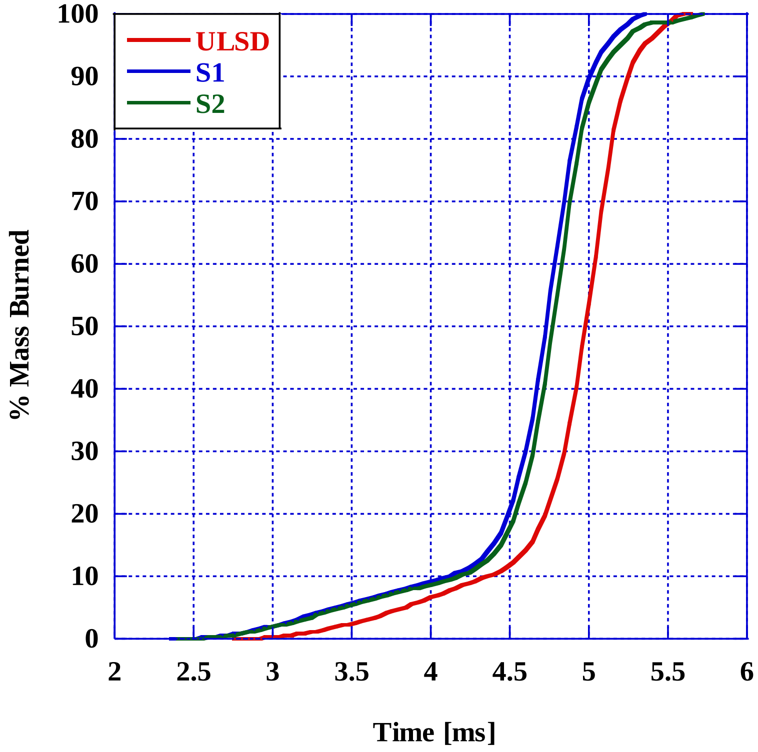

Figure 77: Mass Fraction Burned in CVCC for ULSD, S1, and S2

Figure 77 represents the mass fraction burned for ULSD, S1 and S2 with time demarcations for increasing percentage mass burned listed in Table 32. From this graph, slight differences can be found between the combustion of S1 and S2 where the mass fraction burned follows the same trace until they reach HTHR where they begin to deviate. At this point, the combustion of S2 is slower than that of S1 reaching 100% mass burned at 5.68 ms compared to 5.36 ms for S1. Despite having the lowest DCN, ULSD reaches 100% mass burned between the two surrogates at 5.64 ms making its total combustion duration the shortest out of the three fuels in Figure 77.

Table 32:Time at which 10%, 50%, and 90% MFB for ULSD, S1, and S2

Fuel	**t10**	**t50**	**t90**
ULSD	4.36	5	5.24
S1	4.12	4.72	5
S2	4.16	4.74	5.02

4.3 THERMODYNAMIC COMBUSTION ANALYSIS: IDI ENGINE

The initial investigations into the combustion and emissions characteristics of the surrogate fuel blend, S2, were conducted in a single cylinder IDI CI engine. Of the research fuels outlined in previous sections, three fuels were chosen for analysis in the fired engine. ULSD was used as the baseline fuel for Conventional Diesel Combustion (CDC) by the current industry standard. Neat IPK was chosen as a representative alternative fuel as it has a low DCN similar to other potential alternative fuels such as ethanol, methanol, etc. S2 was then compared to both conventional ULSD and neat IPK for performance and emissions characteristics. Measurement points were executed for each of the three selected fuels using the procedure outlined in Section 3.5 with data gathered from the sensors described in Section 4.3.1-4.3.5. The graph in Figure 78 shows the pressure vs volume for ULSD, IPK, and S2 with the valve timing marked as pink and blue points on the graph. Operational speed and load were kept at a constant 2400 rpm and 4 bar Break Mean Effective Pressure (BMEP) for all IDI measurement points.

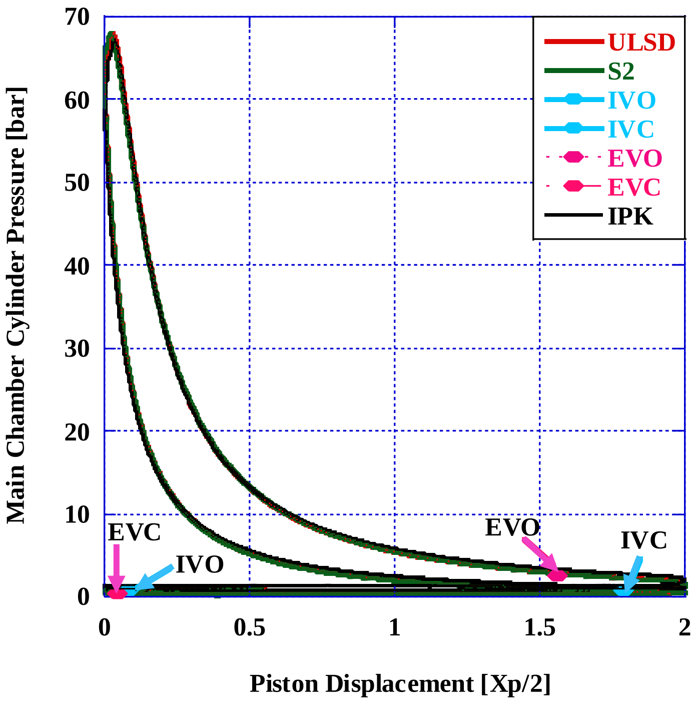

Figure 78: Pressure-Volume Diagram for ULSD, S2, and IPK with Mapped Valve Timing

4.3.1 COMBUSTION AND FUEL LINE PRESSURE IDI

For each of the researched fuels, the main chamber, pre-chamber, and fuel line pressure is measured from the Kistler pressure sensors described in Section 3.5.3. The graph in Figure 79 shows the pressure curves gathered from each pressure sensor in terms of CAD for ULSD. The y-axis on the left indicates the scale used to plot the in-cylinder pressure data while the y-axis on the right indicates the scale used to plot the fuel line pressure. Per manufacturer specifications, the SOI remains the same for each measurement point at 335° ATDC of the intake stroke or 25° BTDC of the expansion stroke. Motoring pressure was taken using an external electric motor to turn over the engine without fuel injection and is represented in the graph by a black dashed line. Combustion pressure in the main chamber and swirl chamber are shown in the graph with the blue and pink lines respectively. During compression, pre-chamber pressure is lower than main chamber pressure as the ports connecting the chambers restrict the flow of air while the speed of the engine limits the time for the pressure between the chambers to return to equilibrium.

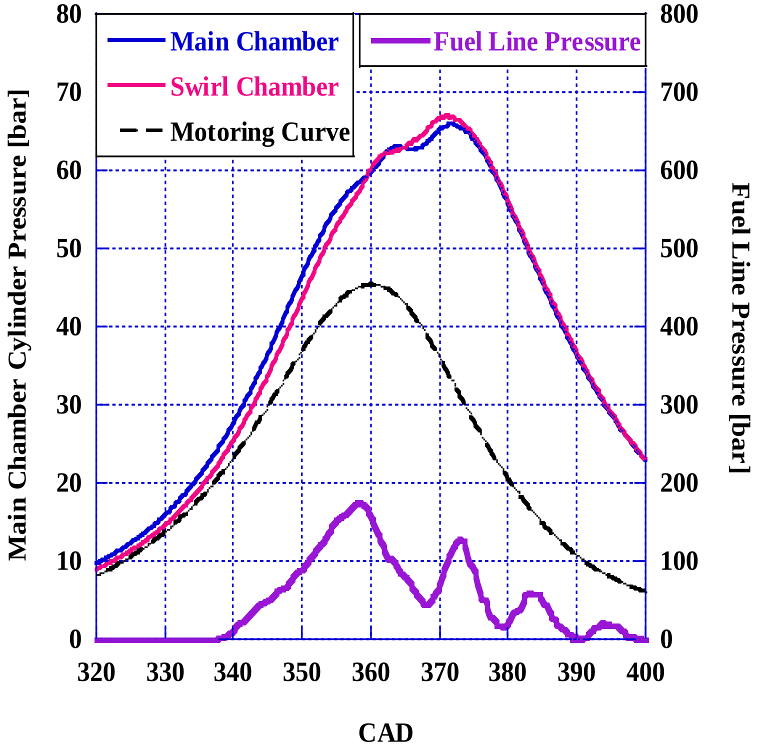

Figure 79: In-Cylinder Combustion Pressure and Fuel Rail Pressure

As this engine configuration is mechanically injected, the physical properties of the fuel have a much more significant impact on the injection system than with electronically actuated injection systems. Fuel line pressure is further investigated for each of the researched fuels using the graph shown in Figure 80. It is immediately apparent that there is a significant reduction in fuel line pressure when running S2 and IPK when compared to ULSD as well as an increase in intensity of oscillations in the fuel line pressure trace. This can be attributed to the reduction in both density and viscosity of S2 and IPK. As a result, these fuels do not build as much pressure in the fuel line as compared to ULSD indicating that sufficient fuel can be injected through a smaller orifice size. Additionally, it was found that, following SOI, the pressure traces for each of the researched fuels deviated not only in magnitude, but also in timing as the line pressure for S2 and IPK exhibits a slight delay when compared to ULSD.

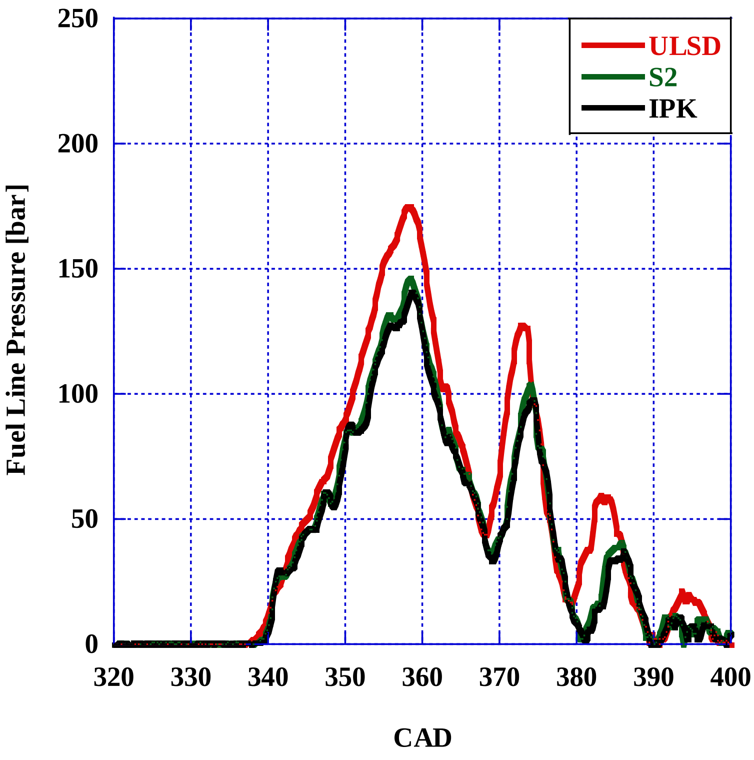

Figure 80: Fuel Line Pressure for ULSD, S2, and IPK

Maximum fuel line pressure was taken for each of the researched fuels as well as the crank angle degree for while that pressure was achieved with the results listed in Table 33. Consistent with the analysis of viscosity and density in Section 4.1, ULSD was found to have reached the highest fuel line pressure of 175 bar with neat IPK achieving the lowest pressure of 141.25 bar. As S2 is a blend of F-T fuels, it reached a similar pressure to that of IPK at 146.31 bar. All three researched fuels reached peak pressure at approximately 358° ATDC on intake with the F-T fuels reaching peak pressure slightly later than ULSD.

Table 33: Peak Fuel Line Pressure for ULSD, S2, and IPK

	Peak Fuel Line Pressure	
	[bar]	**[CAD]**
ULSD	175	358.2
S2	146.31	358.38
IPK	141.25	358.56

While there was no external adjustment of the mechanically actuated SOI, the physical properties of the alternative fuels which caused the reduction in peak fuel line pressure also had an effect on the SOI. The calculation of exact SOI began with an assessment of the pressure behavior around the point which is designated by the manufacturer to be SOI for the pressure trace of its intended fuel, ULSD. It was found that around 335° CAD, the fuel line pressure for ULSD begins to increase due to the actuation of the mechanical fuel pump from the crank driven cam lobe. This point at which the pressure begins to increase from zero is then assumed to be true SOI and will be used in later analysis of ID and CD. The graph in Figure 81 is a zoom of the fuel line pressure traces found in Figure 80 to highlight the difference in injection timing for each of the researched fuels. In this short 10° time increment, it can be seen that there is a notable delay in the increase in pressure for the F-T fuels when compared to ULSD despite no alteration to the fueling system.

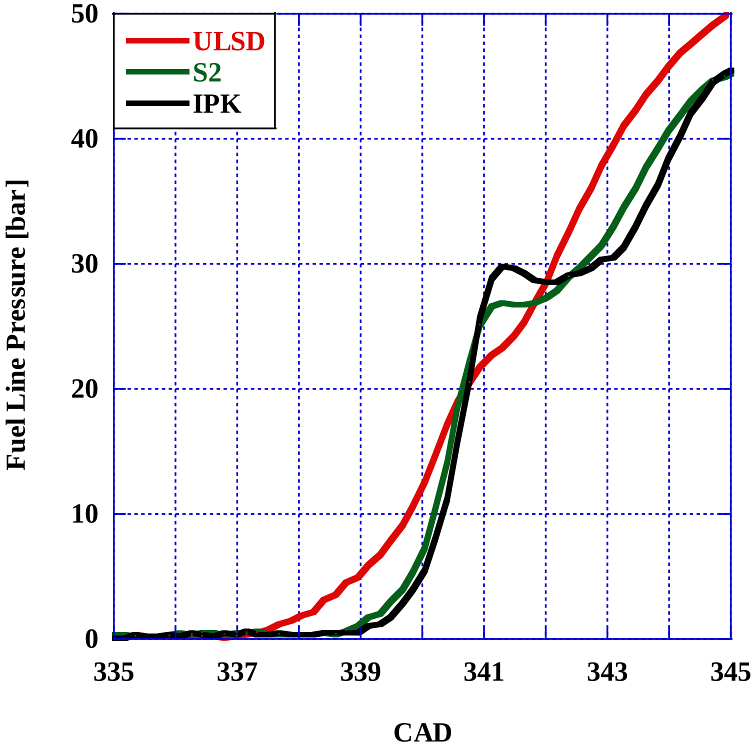

Figure 81: SOI and Fuel Line Pressure Rise for ULSD, S2, and IPK

For each fuel, the inflection point for the fuel line pressure was calculated with all the final values for SOI listed in Table 34. Based on these parameters for SOI, it was found that ULSD began to inject at 336.78° while the alternative fuels saw an approximate 2° delay in SOI at 338.58° and 338.94° for S2 and IPK respectively. These values for CAD at which the fuel line pressure begins to increase will be designated as SOI for each fuel for the duration of this study.

Table 34: Fuel Line Pressure Inflection Point for ULSD, S2, and IPK

Fuel	Pressure Inflection Point [CAD]	% Difference from ULSD
ULSD	336.78	-
S2	338.58	0.53
IPK	338.94	0.64

Additionally, further evaluation of the fuel line pressure around SOI revealed that, despite reduction in peak pressures associated with the F-T fuels, there is a point just after 341° where S2 and IPK achieve a greater line pressure when compared to ULSD. This follows the trend which can be seen more clearly in Figure 81 where the F-T fuels operate in the fuel system at a lower average pressure while simultaneously exaggerating the fluctuations in fuel line pressure.

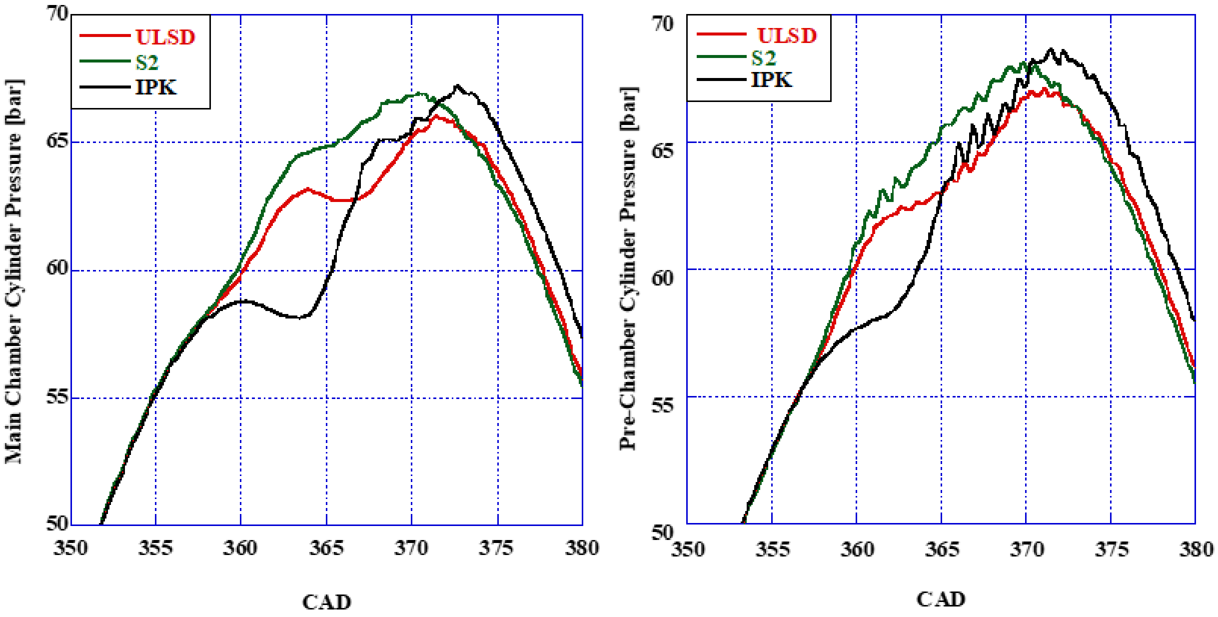

Figure 82: Pre-Chamber and Main Chamber Combustion Pressure for ULSD, S2, and IPK

Following the injection system analysis, the pressure from the main chamber and pre-chamber were taken for each of the researched fuels and the pressure traces graphed in terms of CAD and displayed in Figure 82. In this graph, the dotted lines represent pressure taken from the pre-chamber and the solid lines represent the main chamber pressure. As was initially determined from Figure 81, the pre-chamber pressure remains lower than the main chamber pressure while on the compression stroke. Once combustion is initiated, the pre-chamber pressure exceeds the main chamber pressure as ignition occurs in the highly turbulent environment induced by the pre-chamber geometry. This swirl can be seen in the oscillations around peak pressure of the pre-chamber pressure trace where the combustion gases form rotating pressure waves that pass across the pressure sensor.

Peak chamber pressure was taken for both the pre-chamber and the main chamber as well as the CAD for which they occur with the results listed in Table 35 with a calculation for the percent difference from ULSD. It was found that the F-T fuels exhibited a greater peak pressure in both the main chamber and the pre-chamber where S2 reached its peak pressures sooner than ULSD and IPK reached its peak pressures later than ULSD. Additionally, the F-T fuels showed a greater pre-chamber peak pressure relative to peak main chamber pressure with a 1.17 bar difference for S2 and a 1.44 bar difference for IPK, and, unlike ULSD, both IPK and S2 reached a maximum pre-chamber pressure prior to reaching maximum main chamber pressure. Due to its favorable thermophysical properties and higher DCN, S2 ignites readily in the pre-chamber causing the observed changes in combustion phasing and chamber pressure. IPK, however, resists autoignition allowing more time for homogeneous mixture formation causing an increase in flame speed after ignition resulting in the increase in chamber pressure and larger discrepancy between the pre-chamber and main chamber.

Table 35: Peak Pressure in Main Chamber and Pre-Chamber for ULSD, S2, and IPK

	Peak MC Pressure		**Peak PC Pressure**	
Unit	**[bar]**	**[CAD]**	**[bar]**	**[CAD]**
ULSD	66.06	371.52	67.08	371.88
S2	66.93	370.44	68.10	369.9
IPK	67.21	372.78	68.65	372.52

For further analysis on the interaction between the pre-chamber and the main chamber, the delta between the two chambers was taken and graphed in Figure 83. This delta was calculated by subtracting the main chamber pressure from pre-chamber pressure where the resulting negative values indicate a higher main chamber pressure and positive values indicate a higher pre-chamber pressure.

Consistent with the previous chamber pressure analysis, the main chamber pressure exceeds pre-chamber pressure during compression reaching a minimum at 350° where compression slows allowing the chamber pressures to trend toward equilibrium. Just before TDC in compression, ignition takes place in the pre-chamber as indicated by the first spike into positive values in the graph of the pressure difference. This first pressure spike then propagates to the main chamber before the main combustion event causes pressure to remain higher in the pre-chamber through 40° ATDC in the expansion stroke. The point at which pre-chamber pressure exceeds main chamber pressure can be directly correlated with the DCN where this point occurs earlier in the cycle for fuels with a higher DCN. As S2 and ULSD have a very similar DCN, this point occurs at 359.28° and 359.64° respectively. IPK's resistance to autoignition causes a delay in pre-chamber pressure rise where delta values become positive 1.98° ATDC at 361.98 CAD. Additionally, IPK showed the greatest difference between the pre-chamber and main chamber once combustion is initiated, and, unlike ULSD and S2, the combustion of IPK does not drop back to negative delta values after start of combustion.

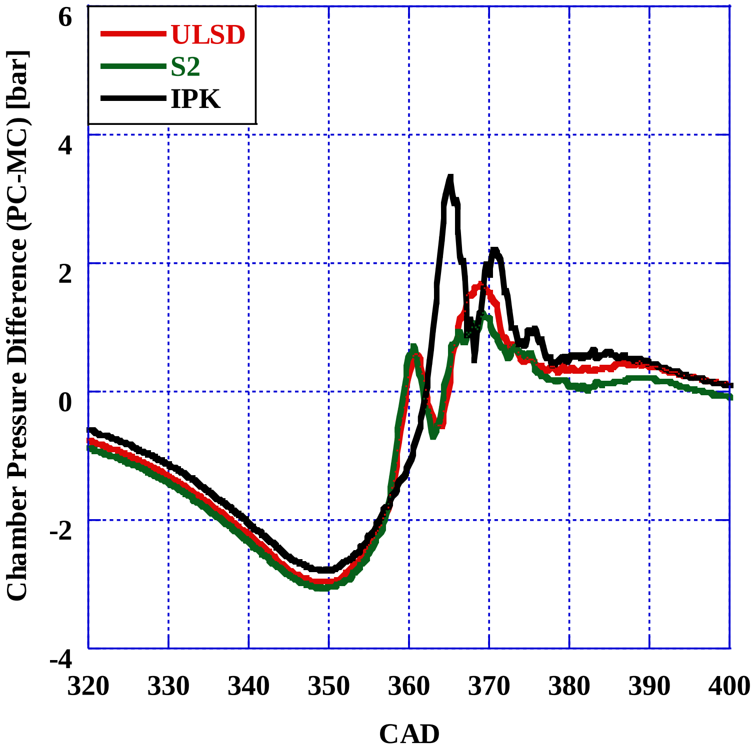

Figure 83: Chamber Pressure Difference between Pre-Chamber and Main Chamber for ULSD, S2, and IPK

To quantify the combustion stability and ignition timing, an analysis of Pressure Rise Rate (PRR) was conducted on each of the three researched fuels. The first derivative of the pressure curve from the main chamber was calculated with the graph shown in Figure 84. In the pressure rise rate analysis, for both S2 and ULSD, the inflection point, which indicates the increase in pressure due to combustion, occurs before TDC while IPK's resistance to autoignition delays this point until just after TDC. This results in negative pressure rise rate values as chamber pressure begins to drop due to the increase in volume before combustion takes place.

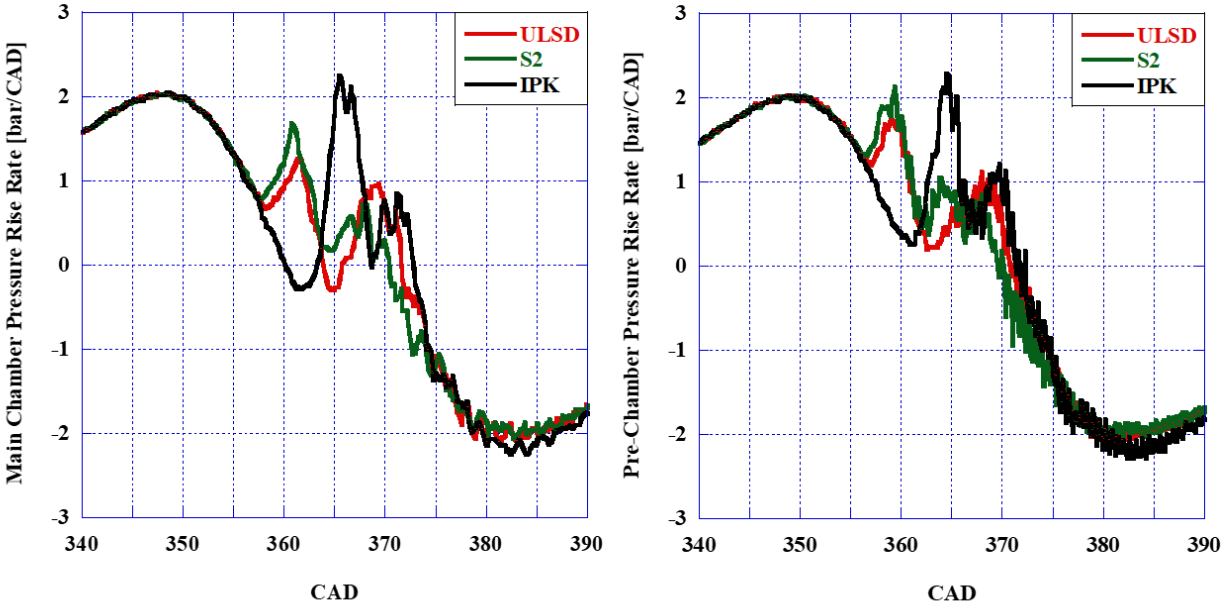

Figure 84: Pressure Rise Rate in Main Chamber and Pre-Chamber for ULSD, S2, and IPK

Peak Pressure Rise Rate (PPRR) was found for each of the three fuels within the range of values exclusive to combustion for the pre-chamber and the main chamber. This is done to exclude the PRR due to compression which exceeds PRR in combustion for ULSD and S2. PPRR for IPK was found to be the greatest among the researched fuels at 2.24 bar/CAD. All final values for PPRR and the CAD for which they occur are listed in Table 36.

Table 36: PPRR in Combustion for ULSD, S2, and IPK

	Peak Pressure Rise Rate in Combustion	
Unit	**[bar/CAD]**	**[CAD]**
ULSD	1.27	361.26
S2	1.68	360.72
IPK	2.24	366.3

The extended ignition delay for IPK due to its resistance to autoignition coupled with the very short physical ignition delay as determined in the analysis of thermophysical properties results in an increase in pressure rise rate from combustion. On the other hand, the combustion of S2 also exhibited a higher PPRR than that of ULSD at 1.68 bar/CAD. The increase in DCN of S2 shifts combustion phasing while the same thermophysical properties which induce rapid mixture formation for IPK create conditions which are more favorable for rapid flame propagation.

The PRR was then used to determine one of several key points in the combustion process which can been used in previous research to define ignition delay. As the ignition delay is a vital metric for characterizing in-cylinder combustion analysis, an investigation was conducted on the differences between each ID determination method. This complete analysis can be found in Appendix B following the calculation of ID using the 2nd derivative of pressure, 1st derivative of AHRR, CA5, and CA10.

Using the pressure analysis, the first metric for defining ID is the change in inflection of the PRR where the combustion reaction releases enough energy to positively influence the chamber pressure. This point was determined by taking the 2nd derivative of pressure in the main chamber. From SOI, the inflection point was calculated to be the point at which the 2nd derivative changes from positive to negative. Table 37 shows the inflection point, SOI, and ID in CAD for each of the researched fuels. By this calculation, ID aligns directly with DCN as an increase in DCN as found in the CVCC reflects in a shorter ID in the fired engine.

Table 37: Inflection Point in the PRR Curve due to Combustion for ULSD, S2, and IPK

Fuel	Inflection Point [CAD]	SOI [CAD]	ID [CAD]
ULSD	358.92	336.78	22.14
S2	358.38	338.58	19.8
IPK	362.16	338.94	23.22

4.3.2 APPARENT HEAT RELEASE RATE: IDI

Apparent Heat Release Rate (AHRR) was calculated in the IDI engine for all three researched fuels using Equation 16. In this analysis, change in CAD, pressure, volume, delta pressure, and delta volume, are the input parameters with pressure and delta pressure being the values which change for each fuel. The specific heat ratio γ was kept constant at 1.33. AHRR was determined for both pre-chamber and main chamber for ULSD, IPK, and S2.

$$\frac{dQ}{d\theta} = \frac{1}{(\gamma - 1)} V \frac{dP}{d\theta} + \frac{\gamma}{(\gamma - 1)} P \frac{dV}{d\theta} \qquad \text{Eq.16}$$

The graph in Figure 85 displayed the AHRR as calculated from the main chamber pressure. There was found to be two phases of combustion for all three fuels with two points to the AHRR curve. For the combustion of IPK, these two phases are the most prominent with the initial phase occurring just after 365° and the second phase occurring after 370°. For ULSD and S2, the two combustion phases have a much larger disparity in magnitude than that of IPK.

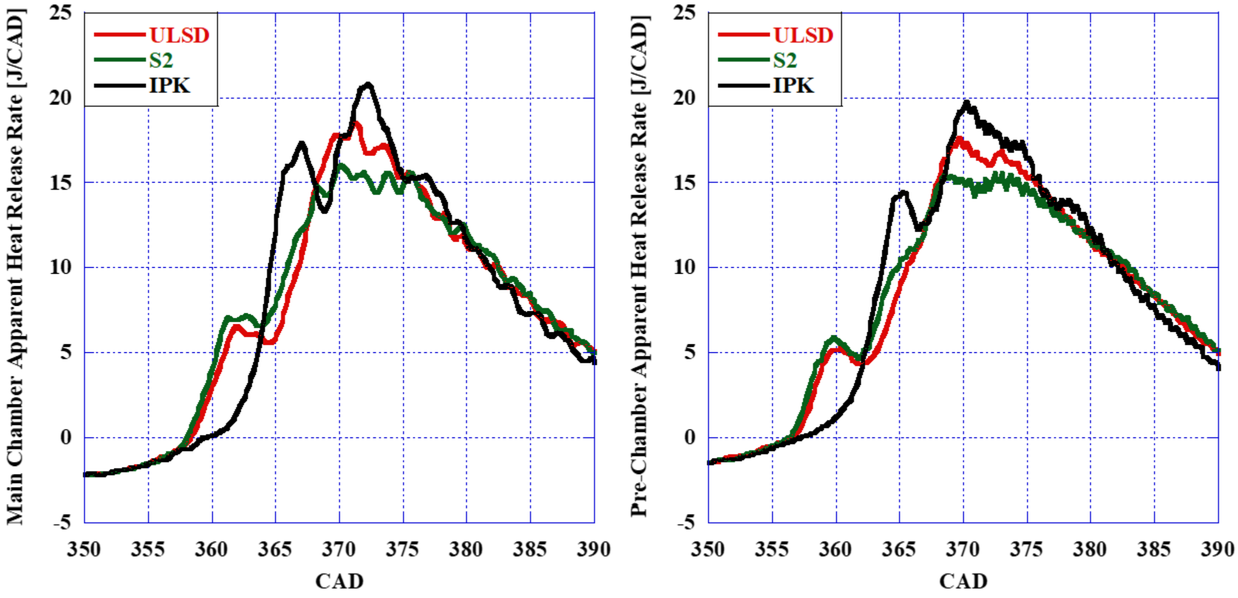

Figure 85: AHRR in Main Chamber and Pre-Chamber for ULSD, S2, and IPK

From an analysis of the AHRR for each of the researched fuels, it was found that S2 had the lowest peak AHRR at 16.05 J/CAD and began combusting earlier than ULSD. IPK was found to have the highest peak AHRR at 20.83 J/CAD consistent with the results from the PRR analysis.

These results indicate that, when compared to ULSD, the combustion of S2 had a slower flame front more consistent with diffusion flames while IPK exhibited a rapid flame front more akin to premixed flames.

Peak AHRR and the CAD for which they occur for each of the researched fuels in both the pre-chamber and the main chamber and the total combustion duration are listed in Table 38. Combustion duration was calculated for each of the fuels in both the pre-chamber and the main chamber where start of combustion was defined as the point at which AHRR becomes positive and end of combustion was defined as the point at which AHRR becomes negative for the first time. For both the pre-chamber and the main chamber calculations, it was found that S2 exhibited the longest combustion duration. Both IPK and S2 were found to have a significant increase of around 10 CAD from combustion duration in the main chamber to the pre-chamber. This is notable as ULSD was found to decrease in pre-chamber combustion duration when compared to its main chamber duration. As S2 and IPK have autoignition characteristics which exist on either side of ULSD, this anomaly must be associated with the thermophysical properties of the F-T fuels. While all three fuels reached peak AHRR within 5 CAD of each other, S2 reached peak AHRR in the main chamber the soonest with IPK reaching peak AHRR the latest and ULSD falling between the two consistent with the DCN of each fuel. Peak heat release in the pre-chamber was found that for all researched fuels peak heat release was lower in the pre-chamber than the main chamber.

Table 38: Peak AHRR and Combustion Duration for ULSD, S2, and IPK

	MC Peak AHRR		**Duration MC**	**PC Peak AHRR**		**Duration PC**
Unit	**[J/CAD]**	**[CAD]**	**[CAD]**	**[J/CAD]**	**[CAD]**	**[CAD]**
ULSD	18.62	371.16	53.36	17.67	369.72	52.74
S2	16.05	370.08	61.56	15.63	372.42	70.02
IPK	20.83	372.24	49.42	19.78	370.26	59.58

An analysis was conducted on the heat release in the pre-chamber and the main chamber and the difference between the two. The delta heat release between the chambers was calculated by taking the pre-chamber values and subtracting the main chamber values. Like the analysis in Section 4.3.1, this results in positive values indicating greater values in the pre-chamber and negative values indicating grater values in the main chamber. The graph in Figure 86 shows the results of this determination. It can be seen that heat release from the pre-chamber begins to increase at a greater rate than in the main chamber starting at SOI. This is due to the increase of mass in the pre-chamber as well as early combustion radical formation slowly releasing heat before the main combustion event. The main combustion event can be seen as a sharp increase in heat release in the main chamber just before TDC for ULSD and S2 or just after TDC for IPK. The subsequent drop in delta AHRR indicates the expulsion of flames from the pre-chamber to the main chamber. Following oscillations in the delta AHRR indicate the reverberation of the flame front between the two chambers. The magnitude of these oscillations increases with decreasing DCN.

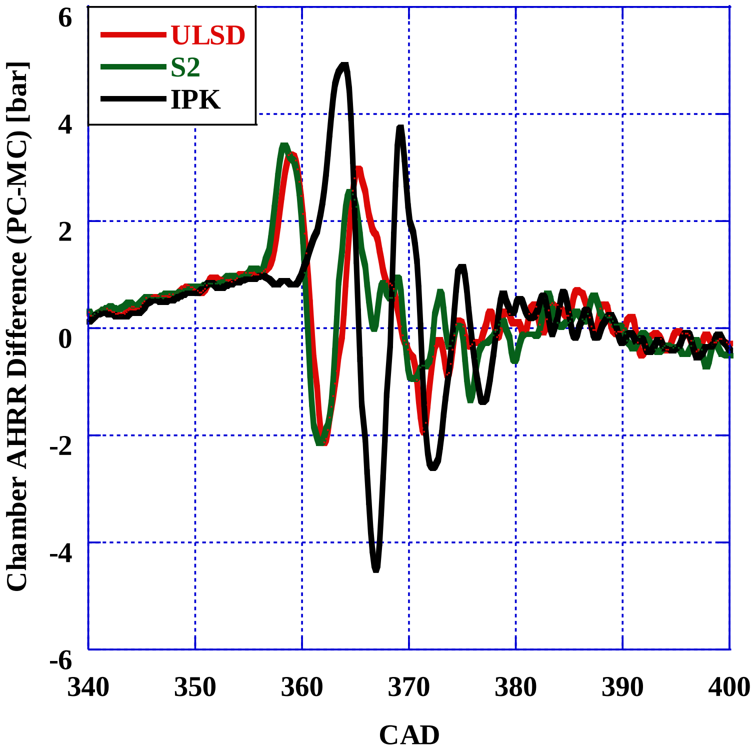

Figure 86: Difference in AHRR between the Pre-Chamber and the Main Chamber for ULSD, S2, and IPK

As SOI was determined for each of the researched fuels in the analysis of the fuel line pressure in Section 4.3.1, a graph of AHRR just before it becomes positive with SOI labeled for each fuel is shown in Figure 87. As seen in the analysis of the delta AHRR, the heat release in the pre-chamber increases more rapidly after SOI. Following the determination of ID from the inflection point of the PRR curve in the main chamber and the pre-chamber, the second method for characterizing ID uses AHRR. For this analysis, the point determined for SOI to the point at which AHRR becomes positive defines AHRR-based ID. As is the PRR ID determinations, ID was calculated for both pre-chamber and main chamber. The results of this investigation can be found in Table 39 and Table 40.

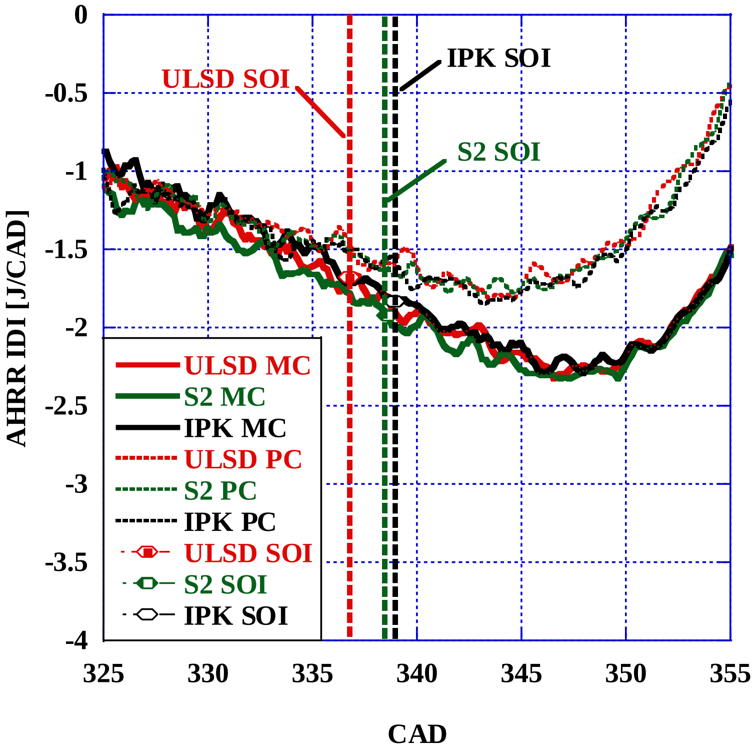

Figure 87: SOI and Early AHRR for ULSD, S2, and IPK

Table 39: Main Chamber Ignition Delay using Positive AHRR for ULSD, S2, and IPK

	SOI [CAD]	AHRR>0 [CAD]	ID [CAD]
ULSD	336.78	358.38	21.6
S2	338.58	358.02	19.44
IPK	338.94	359.46	20.52

Table 40: Pre-Chamber Ignition Delay using Positive AHRR for ULSD, S2, and IPK

	SOI [CAD]	AHRR>0 [CAD]	ID [CAD]
ULSD	336.78	356.4	19.62
S2	338.58	356.4	17.82
IPK	338.94	357.12	18.18

From the analysis of ID based on the point at which AHRR becomes positive, it was found that ULSD had the longest ID both in the main chamber and pre-chamber. This is due to the increase in physical ID for ULSD characterized by its slow vaporization rate and high Oh number when compared to the F-T fuels. Of the researched fuels, S2 was found to have the shorted ID due to its high affinity for autoignition coupled with its short physical ID. The pre-chamber ID investigation maintained the same trend for each of the researched fuels with a reduction in ID duration. This is due to fuel injection and combustion occurring first in the pre-chamber before propagating to the main chamber.

4.3.3 RINGING INTENSITY IDI

Ringing Intensity (RI) was calculated for each of the researched fuels as a measure of combustion stability and detonation associated with the combustion of each fuel. Equation 17 was used to calculate RI with β set to 0.05 and γ set to 1.33. Other factors which influence the equation are the PPRR, maximum cylinder pressure and maximum cylinder temperature. High RI is detrimental for the long-term operation of the engine and increases the noise and vibration produced from combustion.

$$RI = \frac{(\beta(\frac{dP}{dt})_{max})^2}{(2\gamma P_{max})}\sqrt{\gamma R T_{max}} \qquad \text{Eq. 17}$$

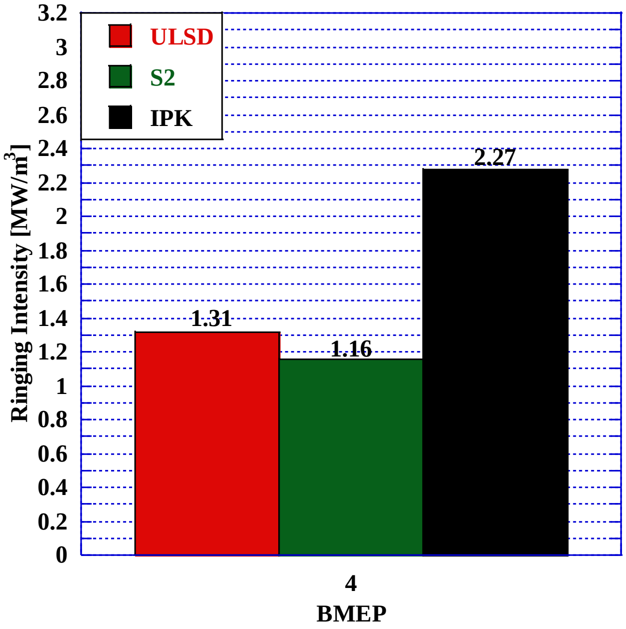

Figure 88: Ringing Intensity for ULSD, S2, B4, and IPK

The graph in Figure 88 shows the RI values for ULSD, S2, and IPK. It was found that IPK had the highest RI at 2.26 MW/m^3 consistent with the results for peak pressure and PPRR in Section 4.3.1. Between S2 and ULSD, the combustion of S2 showed a reduction in RI by 11.5% indicating that the fuel surrogate exhibits more combustion stability than ULSD. The reduction in RI with the combustion of S2 can be attributed to the reduction in ID as the fuel begins to combust in a short time after it first enters the chamber. This means that very little fuel will accumulate in the chamber before SOC. The reduces the burn rate favoring diffusion flame combustion behavior resulting in a smoother pressure increase and force exertion on the piston (P.W. Gill, Smith Jr., and Ziurys 1954).

4.3.4 PERCENT MASS BURNED IDI

Mass burned in the IDI engine was calculated using the integration of net heat release in combination with the LHV for each fuel in both the pre-chamber and the main chamber with the resulting graph shown in Figure 89 and Figure 90. In the main chamber before 10% mass burned, ULSD and S2 exhibit almost identical fractional burn rates while IPK shows a delay in mass burned consistent with its resistance to autoignition. At around 25% mass burned, however, the behavior changes with a decrease in burn rate with the increase in DCN of the researched fuel. The slower ID of IPK allows more fuel to accumulate in the chamber before SOC, increasing mass burn rate once ignition begins (P.W. Gill, Smith Jr., and Ziurys 1954). This results in the initial delay found the mass fraction burned followed by a rapid burn rate exceeding that of ULSD and S2.

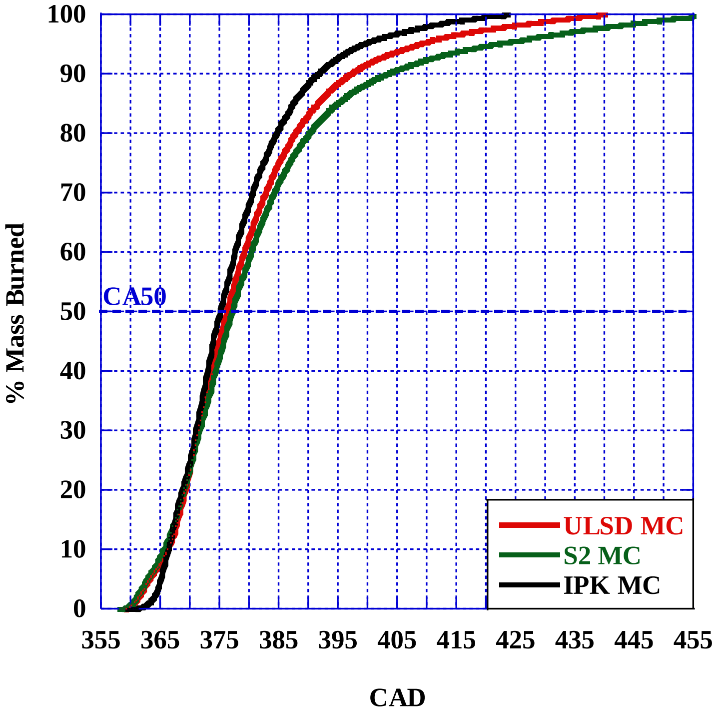

Figure 89: % Mass Burned Calculated from Net Heat Release in the Main Chamber for ULSD, S2, and IPK

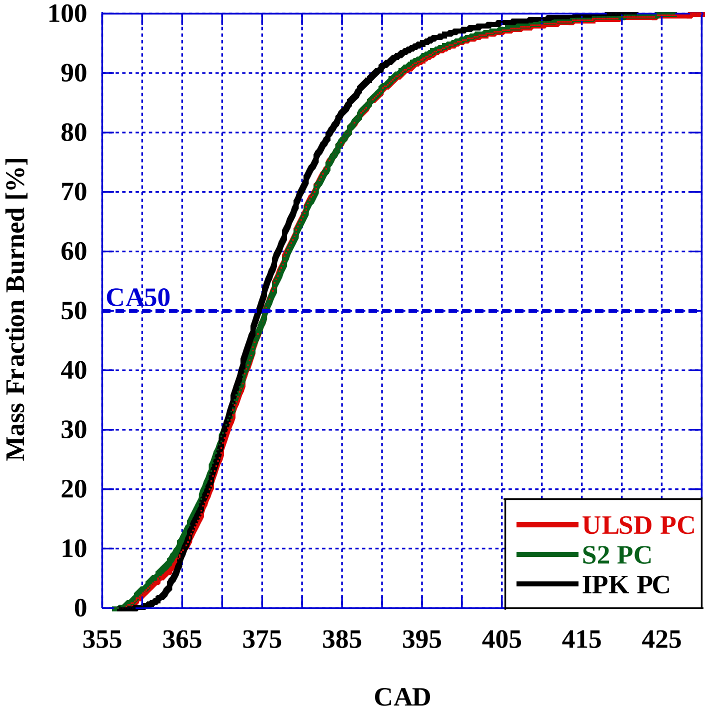

Figure 90: Mass Fraction Burned Calculated from Net Heat Release in the Pre-Chamber for ULSD, S2, and IPK

Table 41 and Table 42 are representations of the mass fraction burned and the CA5, CA10, 50, and 90 for ULSD, S2, and IPK. It was found that, when compared to ULSD, S2 had an extended region of combustion with an earlier CA10 and a later CA90. The opposite case was found for the combustion of IPK where, despite the delay in early combustion before 7° ATDC, its CA 90 occurs 6° sooner than that of ULSD.

Table 41: CA5, 10, 50, and 90 Calculated from Main Chamber Pressure for ULSD, S2, and IPK

Fuel	CA5	CA10	CA50	CA90
ULSD	363.15	366.21	376.2	397.08
S2	362.79	365.58	377.1	403.2
IPK	365	366.26	375.04	391.52

Table 42: CA5, 10, 50, and 90 Calculated from Pre-Chamber Pressure for ULSD, S2, and IPK

Fuel	CA5	CA10	CA50	CA90
ULSD	362.07	365.13	375.39	397.08
S2	361.35	365.58	375.39	391.95
IPK	363.72	365.16	374.45	388.98

4.3.5 IN-CYLINDER HEAT LOSS AND HEAT FLUX: IDI

Figures 91, 92, and 93 show the graph of the integrated heat loss for net heat, radiation, convection, and crevices. Radiation heat loss is shown in green, convection heat loss in red, and net heat released in purple for all three graphs. Convection heat loss was found to be the largest source of heat loss for all three fuels with influence both in early and late stages of combustion and expansion. Radiation heat loss does not appear until after 370 CAD when soot particles form and lose heat through absorption, emission, and scattering of radiation from combustion. Of the three fuels, the combustion of IPK resulted in the greatest heat loss due to radiation at 14.7% compared to S2 and ULSD at 13.98% and 13.9% respectively. For convective heat transfer, the combustion of S2 suffered the greatest losses at 41.04% which resulted in S2 having the lowest percentage of its gross mass contributing to pressure-volume expansion at 46.29% as compared to

50.94% for ULSD. This is due to the extended combustion duration for S2 increasing the amount of time for which the hot gas can transfer heat.

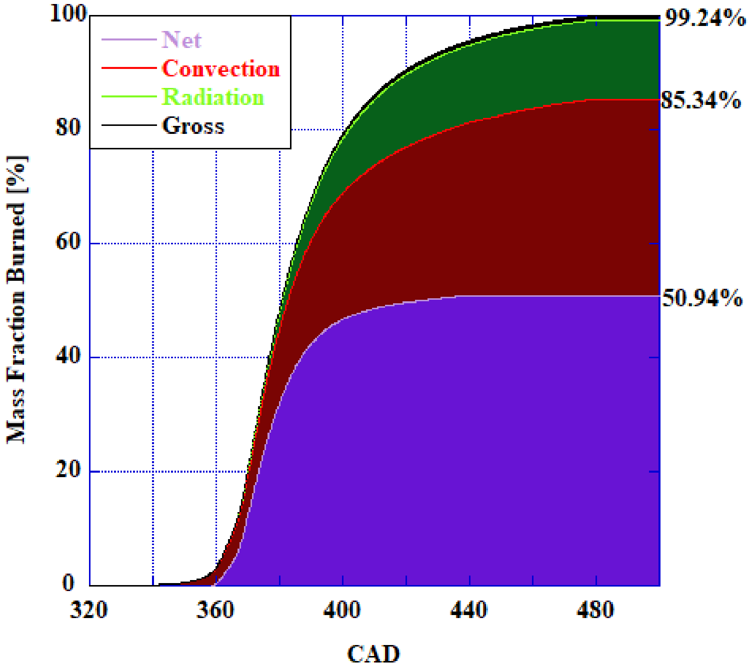

Figure 91: Heat Losses in Terms of Mass Fraction Burned for ULSD

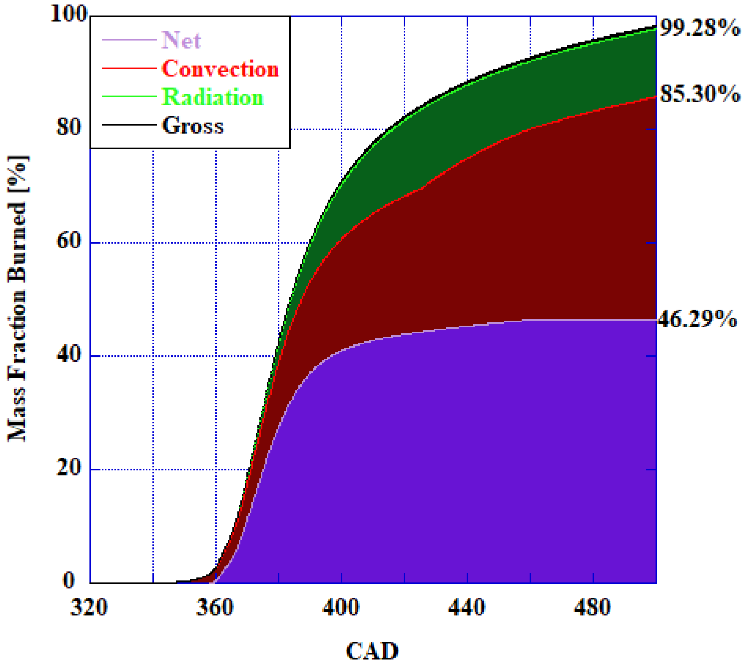

Figure 92: Heat Losses in Terms of Mass Fraction Burned for S2

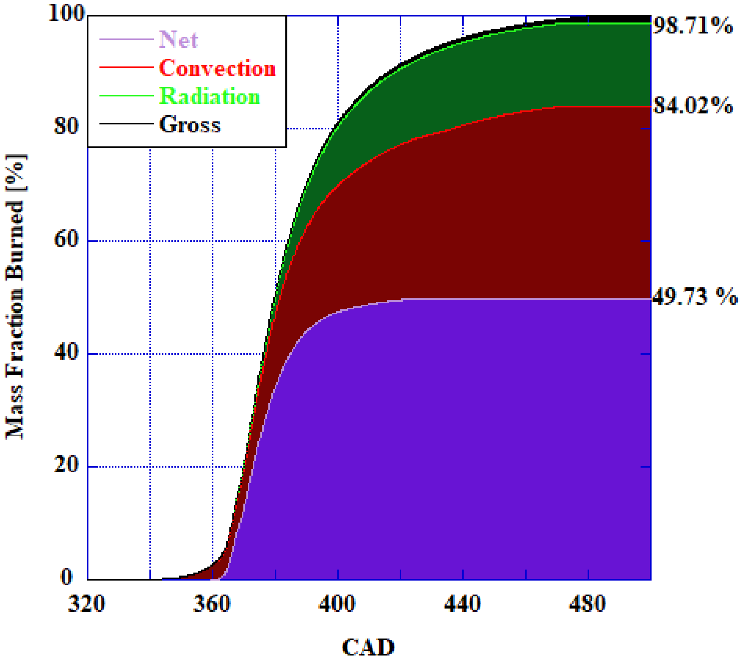

Figure 93: Heat Losses in Terms of Mass Fraction Burned for IPK

Heat fluxes based on thermodynamic loss region were calculated from heat release and piston and cylinder surface area. Radiation, convection, and total heat flux were calculated for ULSD, S2, and IPK using in-cylinder Reynold's number, air viscosity, and the thermal conductivity of air using Equations 18, 19, and 20 respectively. In Equation 18, S, N, and D represent stroke, engine speed, and bore respectively with $\rho(\alpha)$ representing gas density and $\mu(\alpha)$ representing gas viscosity.

$$Re(\alpha) = \rho(\alpha)\frac{S * N * D}{30 * \mu(\alpha)} \qquad \text{Eq. 18}$$

$$\mu(\alpha) = 4.94\left(\frac{1273.15 + 110.4}{T_A + 110.4}\right) * \left(\frac{T_A(\alpha)}{1273.5}\right)^{1.5} * 10^{-5} \qquad \text{Eq. 19}$$

$$\lambda_A(\alpha) = -1.2775 * 10^{-8} * T_A(\alpha)^2 + 7.66696 * 10^{-5} * T_A(\alpha) + 0.0044488 \qquad \text{Eq. 20}$$

Each of these values for in-cylinder gas dynamics was found as a curve based on temperature calculations and pressure for instantaneous volume averaged gas properties. The Borman-Nishiwaki thermodynamic model was then used to calculate the heat flux. The equation used for radiation and convection heat flux can be found in Equation 20.

$$\dot{q}(\alpha) = Ct * \frac{\lambda_A(\alpha)}{D} Re(\alpha)^{0.7}\left(T_{A(\alpha)} - T_W\right) + \sigma * \varepsilon(T_A^4(\alpha) - T_W^4) * A \qquad \text{Eq. 21}$$

Convection, radiation, and total heat flux are graphed for the combustion of ULSD, S2, and IPK from the main chamber pressure and displayed in Figure 94 with peak values listed in Table 43. For ULSD and S2, there was found to be a high degree of similarity between both the graphed heat flux curves and peak heat flux values with S2 exhibiting a reduction in peak total heat flux and a slight advancement in total heat flux. IPK, consistent with its late ignition and rapid combustion shows a delay in heat flux and a faster reduction in heat flux after combustion.

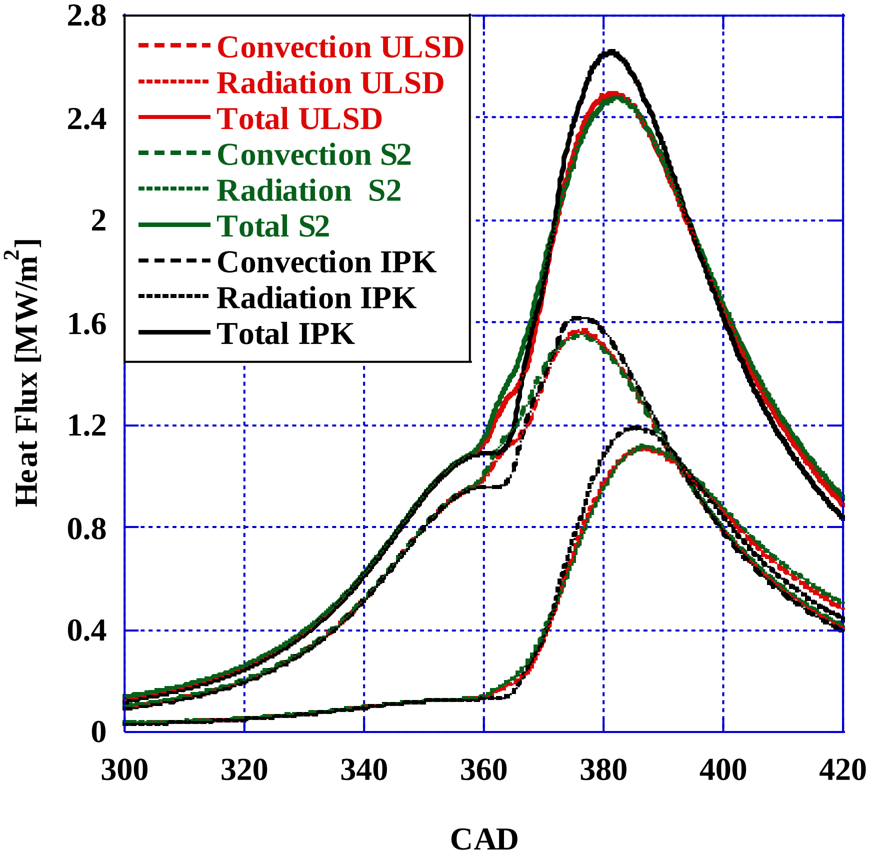

Figure 94: Heat Fluxes for ULSD, S2, and IPK in IDI

Peak heat flux for each fuel and calculated region are listed in Table 43 with calculations for the sum of the heat flux throughout the cycle listed in Table 44. The increase in peak heat flux for IPK indicates higher peak in-cylinder temperatures contributing to the formation of NOx. The rapid combustion of IPK, however, reduces the amount of time the in-cylinder gases are at high temperatures for the formation of thermal NOx. Further analysis of the NOx emissions for each of the researched fuels can be found in Section 4.5.2. On the other hand, the combustion of S2 reaches the lowest peak heat flux in both radiation and convection of the three researched fuels but has the largest summation values for heat flux. When compared to ULSD, IPK saw a reduction in convection heat flux by 2.66% while S2 exhibited an increase of 5.4%. The summation of radiation heat flux showed a similar trend with S2 increasing by 9.7% and IPK decreasing by 4.8% when compared to ULSD. The increase in total radiation heat flux from the combustion of S2 is an indication that there is an increase in soot formation as soot particles under high heat conditions emit luminescent radiation. Further analysis of the soot emissions can be found in Section 4.5.2.

Table 43: Peak Heat Flux Values for ULSD, S2, and IPK

Fuel	Peak Convection Flux [MW/m^2]	Peak Radiation Flux [MW/m^2]	Peak Total Flux [MW/m^2]
ULSD	1.57	1.11	2.49
S2	1.55	1.12	2.48
IPK	1.62	1.19	2.66

Table 44: Heat Flux Sum for ULSD, S2, and IPK

Fuel	Convection Flux Sum [MW/m^2]	Radiation Flux Sum [MW/m^2]	Total Flux Sum [MW/m^2]
ULSD	632.07	437.29	1069.36
S2	666.11	479.68	1145.78
IPK	615.22	416.44	1031.67

Peak cylinder temperatures and exhaust gas temperatures were determined and measured for each of the researched fuels and the results can be found in Table 45. Despite the reduction in heat flux for the combustion of IPK, it was found to have the highest peak cylinder temperature in addition to the lowest exhaust gas temperature congruent with its short combustion duration. While the combustion of S2 resulted in a slightly over 10° increase in peak cylinder temperature when compared to ULSD, this resulted in only a 1° increase in exhaust temperature.

Table 45: Cylinder Temperature and Exhaust Gas Temperature for ULSD, S2, and IPK

Fuel	Peak Cylinder Temperature [K]	Exhaust Gas Temperature [K]	Temperature Reduction [K]
ULSD	2070.03	575.05	1494.98
S2	2083.27	576.15	1507.12
IPK	2110.64	570.29	1540.34

4.4 THERMODYNAMIC COMBUSTION ANALYSIS: CRDI ENGINE

Further investigations were conducted in a Common Rail Direct Injection (CRDI) research engine for ULSD, S2, and IPK. Measurement points were taken at 1500 rpm and 4 bar BMEP. The common rail and electronic injection enabled control of both rail pressure and injection timing by the engine control software, Drivven. For all three researched fuels, the rail pressure was maintained at 800 bar with injection timing set to 15° BTDC of compression. With the instrumentation outlined in Section 3.5, real time monitoring and data collection was performed for the calculated values CA50, CoV, PRR, and IMEP. Pressure traces were taken for intake air, exhaust gas, and in-cylinder pressure. The graph in Figure 95 shows the P-v diagram for the CRDI engine with labels for valve timing and SOI.

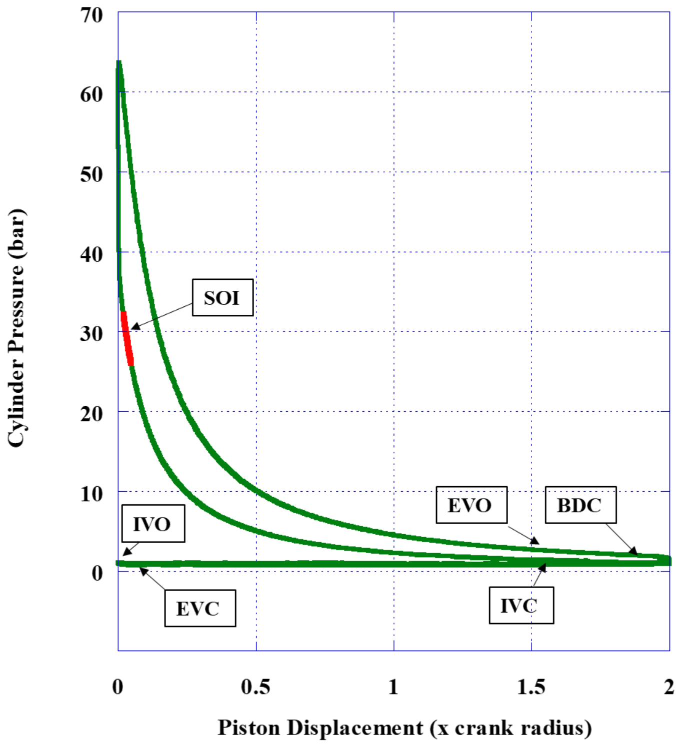

Figure 95: Pressure-Volume Diagram with Valve Timing and SOI for the CRDI Research Engine

4.5.1 IN-CYLINDER COMBUSTION PRESSURE: CRDI

Both intake and exhaust gas pressures were measured for the duration of the 4 stroke cycle under no boost conditions and no exhaust back pressure or exhaust gas recirculation with the graph for both shown in Figure 96. Each of the 4 cycles and valve timing can be seen in the pressure trace of the exhaust and intake air. Additionally, due to the pressure of the air column on the intake valve, there remains a small gap between the valve creating observable interactions between the air pressure within the cylinder and the intake pressure sensor as indicated by the increase in intake air pressure during the compression and expansion strokes from around 250 CAD to 450 CAD.

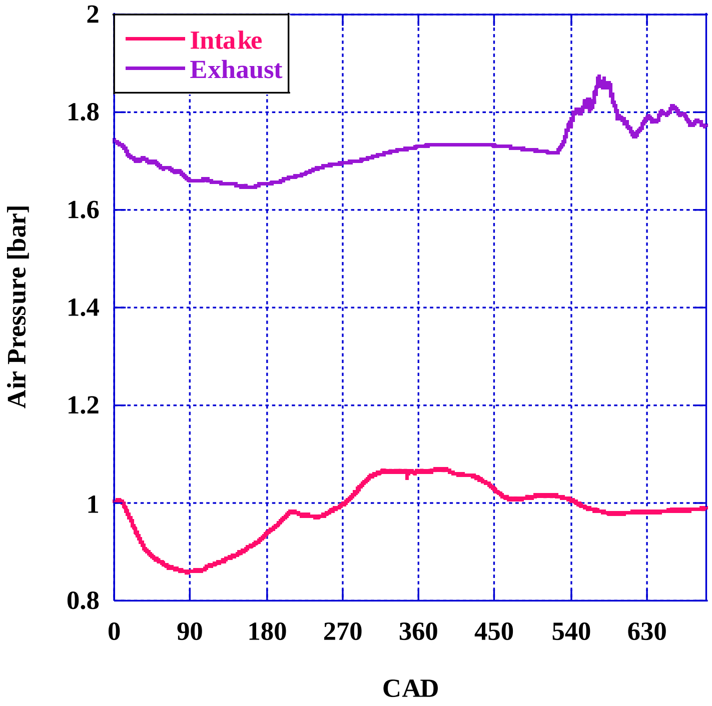

Figure 96: Intake and Exhaust Pressure for ULSD

Combustion chamber pressure for ULSD, S2, and IPK are illustrated in the graph in Figure 97 along with the motoring pressure trace. While the pressure traces for ULSD and S2 are almost identical, IPK exhibits a delay in combustion consistent with its reduced DCN. Unlike the IDI engine, IPK experiences a significant reduction in maximum pressure when compared to ULSD and S2. This delay in combustion greatly reduces efficiency as pressure rise and maximum pressure occur after TDC in the expansion stroke eliminating any time spent in isochoric combustion. Peak pressure and the crank angle at which it occurs for each of the researched fuels can be found in Table 46. It can be seen that the combustion of S2 reaches peak pressure slightly sooner than that of ULSD due to its higher DCN.

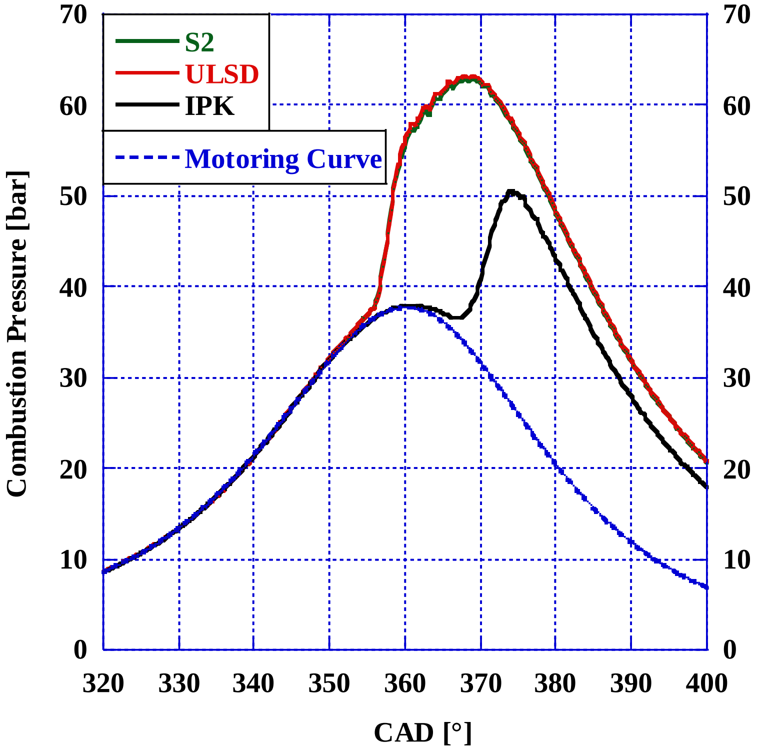

Figure 97: Motoring Pressure and Combustion Pressure for ULSD, S2, and IPK

Table 46: Peak Pressure and Crank Angle Location for ULSD, S2, and IPK

Fuel	Peak Pressure [bar]	CAD Location
ULSD	63.47	369.8
S2	63.09	368.97
IPK	50.78	373.91

Pressure rise was determined for each of the researched fuels and the graph of which is shown in Figure 98. Peak pressure rise rate, CAD for which each fuel hits PPRR, and the inflection point for pressure rise rate were also calculated and shown in Table 47. Consistent with the evaluation of the pressure, S2 was found to have a nearly identical pressure rise rate to that of ULSD. This high degree of similarity between S2 and ULSD indicates S2's viability as a drop-in fuel replacement for ULSD. IPK, however, shows a significant delay in combustion as well as a reduction in PPR. The reduction in PRR is a result of the delayed combustion causing the primary heat release region occurring during the power stroke where combustion takes place in a much larger volume.

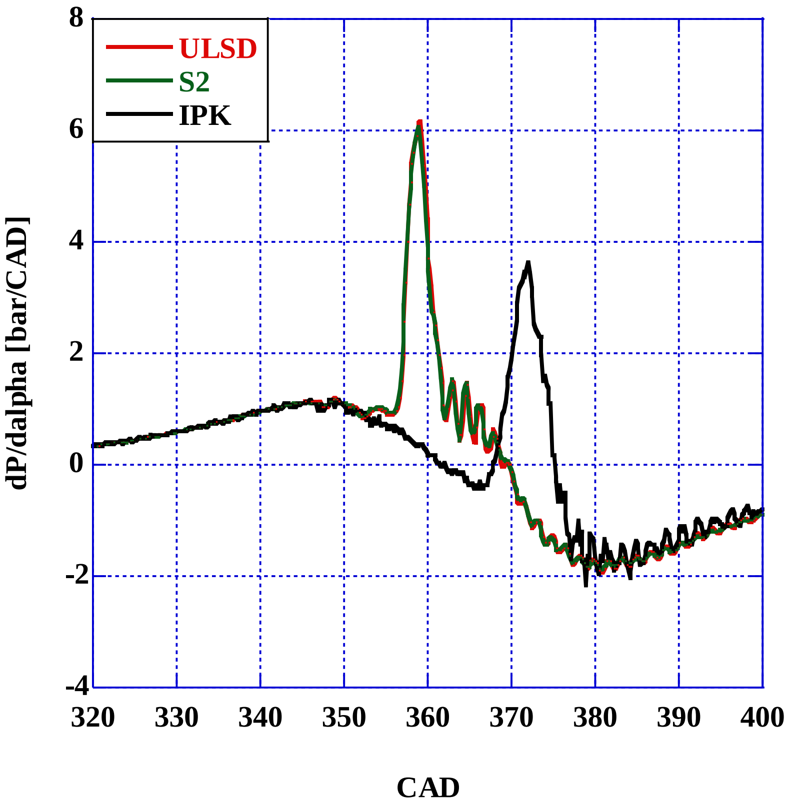

Figure 98: Pressure Rise Rate for ULSD, S2, and IPK

Table 47: PPRR, Crank Angle for PPRR, Pressure Inflection Point, and Ignition Delay for ULSD, S2, and IPK

Fuel	PPRR [bar/CAD]	CAD for PPRR [CAD]	Inflection Point [CAD]	Ignition Delay [CAD]
ULSD	6.15	359.18	355.93	10.93
S2	6.07	357.97	354.72	9.72
IPK	3.62	370.67	365.26	20.26

4.4.2 APPARENT HEAT RELEASE RATE: CRDI

The AHRR was calculated for each fuel using Equation 16 found in Section 4.3.2 for the AHRR in the IDI engine. In the heat release trace a similar trend is observed to the one found in the pressure analysis with the combustion of S2 falling in the same phase as that of ULSD with a slight reduction in measured values. IPK, however, has an extremely delayed combustion caused by its resistance to autoignition. Where a distinct difference can be determined between the premixed and diffusion flame regions for the combustion of S2 and ULSD, IPK's combustion is almost entirely in premixed flame regions. Relative to peak pressure, IPK has a much larger AHRR when compared to ULSD and S2. Additionally, the delay in combustion reduces overall combustion time for IPK with the inverse true for S2. Peak AHRR and the crank angle at which it occurs can be found in Table 48.

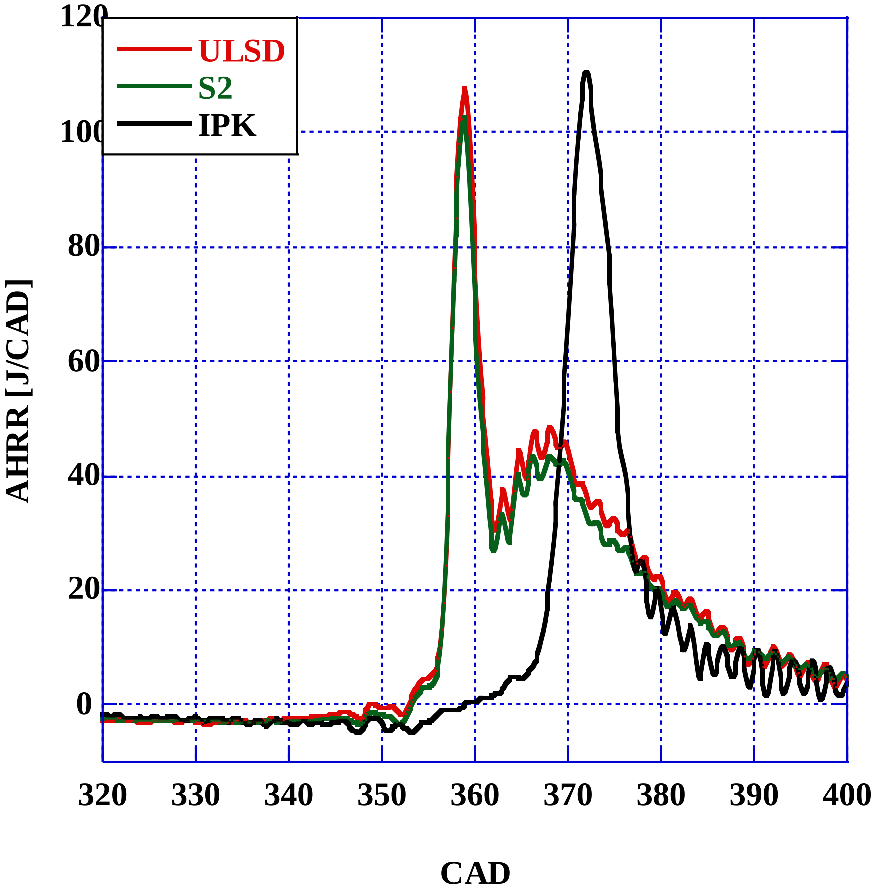

Figure 99: AHRR for ULSD, S2, and IPK in CRDI

From the results in Table 48 and Figure 99, it was found that with the reduction in DCN there was an increase in peak AHRR consistent with the results found from the IDI engine. Additionally, AHRR was seen to peak earlier in the combustion phase with increasing DCN. These two factors resulted in S2 having the lowest peak AHRR occurring before TDC while IPK had the highest peak AHRR occurring slightly over 10° ATDC. IPK combusts primarily in the expansion stroke outside of the ideal range for quasi isochoric combustion likely contributing to a significant reduction in thermal efficiency despite the shorter combustion duration and higher peak AHRR. On the other hand, S2 has an earlier combustion phase due to its increased DCN and a longer combustion duration indicating a favorable combustion profile for increased overall efficiency.

Table 48: Peak AHRR and CAD at which it Occurs for ULSD, S2, and IPK

Fuel	Peak AHRR [J/CAD]	CAD for AHRR Peak	Total Combustion Duration [CAD]
ULSD	107.65	359	72.84
S2	102.59	357.97	83.5
IPK	110.58	370.66	41.8

The graph in Figure 100 shows the LTHR and SOI for each of the researched fuels. After SOI, there is an initial drop in AHRR associated with the heat absorption from the vaporizing fuel. As AHRR increases, further oscillations indicate regions of early peroxide and cool flame formation. It was found that the initial reduction in heat release is phase consistent with all three fuels but changes in magnitude with the change in fuel composition. IPK was found to have the highest magnitude of heat absorbed after SOI consistent with the results for the volatility analysis in Section 4.1.4. Before SOI, each fuel exhibits a different heat release with ULSD having the highest heat release at SOI with S2 and IPK falling after in order of decreasing AHRR. This can be attributed to higher cylinder temperatures from combustion which carries more thermal energy through to the intake air when compared to the F-T fuels.

After the initial drop in AHRR, all fuels experience a short period of more rapid heat release associated with the initial stages of LTHR and low luminosity cool flames where temperatures are between 500° and 900° K (Y.G. Ju 2021). End of Injection (EOI) is at 350 CAD as injection pulse width was maintained at 5 CAD, and at this location, all fuels are in a section of negatively sloped AHRR. This can be attributed both to the continuing absorption of heat from the vaporizing fuel and the formation of endothermic peroxides associated with the NTC region of combustion. For S2 and ULSD, AHRR changes inflection at around 352 CAD and transitions to HTHR around 353 CAD. IPK exhibits a different behavior where, despite AHRR changing inflection at 353 CAD, there is an extended region of LTHR delaying the transition to HTHR to just after 365 CAD.

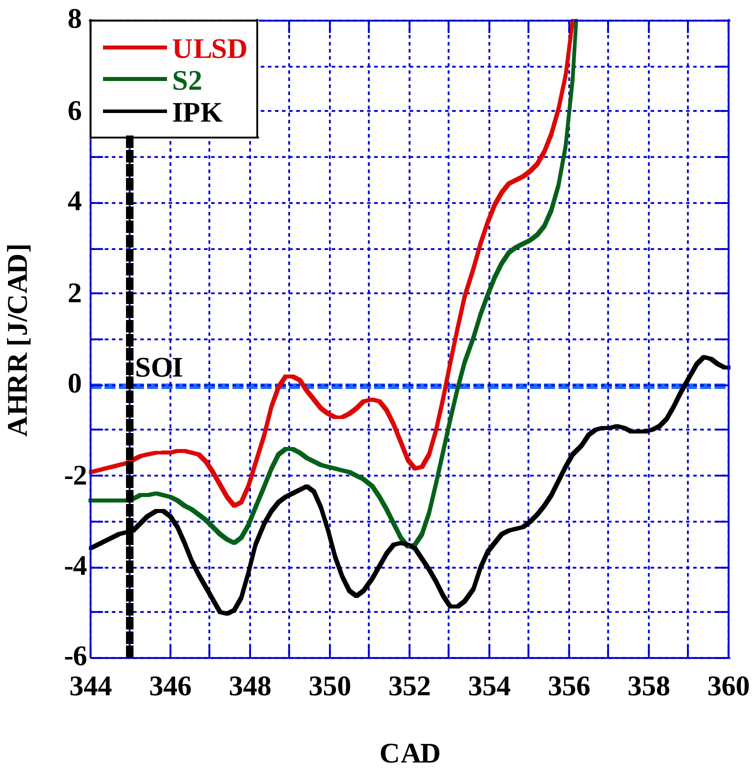

Figure 100: Low Temperature Heat Release with Injection Timing for ULSD, S2, and IPK

Continuing the investigation of ignition delay calculations, the point at which AHRR becomes positive after SOI was determined for each of the researched fuels and displayed in Table 49 along with the resulting determination of ID. From this evaluation, it can be seen that the delay in combustion due to IPK's low DCN has a much more significant impact on ignition delay in the CRDI engine when compared to the combustion of neat IPK in the IDI engine. Additionally, despite S2's higher volatility and DCN, it has a longer ID when compared to ULSD. This is likely due to higher in-cylinder temperatures prior to fuel injection, increasing vaporization rate and reducing ignition delay for ULSD.

Table 49: Point at which AHRR becomes Positive and Ignition Delay for ULSD, S2, and IPK

Fuel	Positive AHRR [CAD]	Ignition Delay [CAD]
ULSD	353.04	8.04
S2	353.4	8.4
IPK	357.69	12.9

4.4.3 RINGING INTENSITY: CRDI

The Ringing Intensity was calculated for each of the researched fuels using Equation 17 found in Section 4.3.3. This calculation is based on the maximum cylinder pressure, maximum temperature, and temperature rise rate in relation to pressure rise rate and is a measure of the degree of detonation associated with the combustion of the fuel. This factor is also an indicator of the effect of combustion on the longevity of the engine. A reduction in RI is beneficial for the engine as there is less wear and component degradation associated with high temperatures, pressure rise rates, and combustion instability. The results for the RI calculations can be found in the graph in Figure 101.

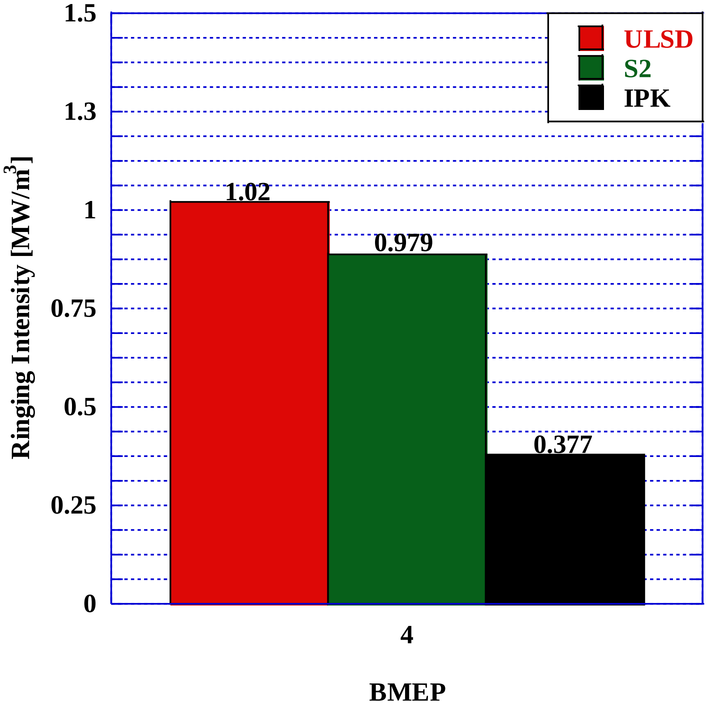

Figure 101: Ringing Intensity for ULSD, S2, and IPK

There was found to be a decrease in ringing intensity for both S2 and IPK when compared to ULSD. Since this reduction in ringing intensity is consistent with both F-T fuels, it is not directly related to the ignition timing or the DCN of the fuel. Higher combustion stability is consistent with the results from the CVCC investigation as S2 had a reduction in the magnitude of ringing events when compared to ULSD, and the combustion of IPK resulted in zero ringing events after EOC.

Additionally, the CVCC investigation showed that the F-T fuels have a significantly longer NTC region than that of ULSD further contributing to the reduction in RI.

4.4.4 PERCENT MASS BURNED: CRDI

The percentage of mass burned as a function of crank angle degree was calculated for each of the researched fuels with the results displayed in the graph in Figure 102. This calculation was conducted using the integration of AHRR as calculated in Section 4.4.2 and multiplying the resulting integration curve with LHV.

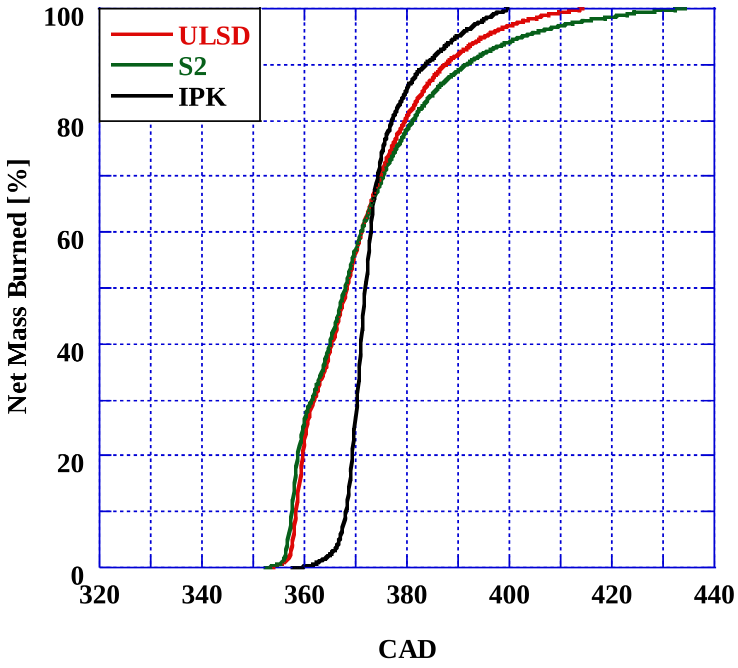

Figure 102: Percent Mass Burned in CRDI for ULSD, S2, and IPK

Table 50: CA5, 10, 50, and 90 for ULSD, S2, and IPK

Fuel	**CA5**	**CA10**	**CA50**	**CA90**
ULSD	357.74	358.46	368.22	387.56
S2	356.89	357.61	367.89	391.51
IPK	366.79	367.99	371.85	383.64

4.4.10 HEAT LOSSES AND HEAT FLUXES: CRDI

In the CRDI engine, heat loss regions were calculated using Equations 18-21 found in Section 4.5.3 for the determination of heat loss and heat flux in the IDI engine with modifications for the change in internal geometry. Heat loss by region, as in the IDI section, is quantified as a percentage mass burned which can be attributed to heat losses to convection, radiation, crevices, and emissions. The percent mass burned in terms of CAD for each fuel can be seen in the graphs in Figures 103-105.

It was found that IPK had the highest percentage of its combusted mass contributing to pressure-volume work when compared to ULSD and S2 as represented by the integration of net heat release shown in purple on each of the graphs. This can be attributed to the reduction in overall combustion duration reducing the amount of time for radiation and convection heat transfer to take place during the combustion process. Between S2 and ULSD, S2 had a reduction in radiation heat transfer contributing to a slight decrease in heat loss where 66.56% of S2’s combusted mass contributed to net heat release compared to 66.31% for ULSD.

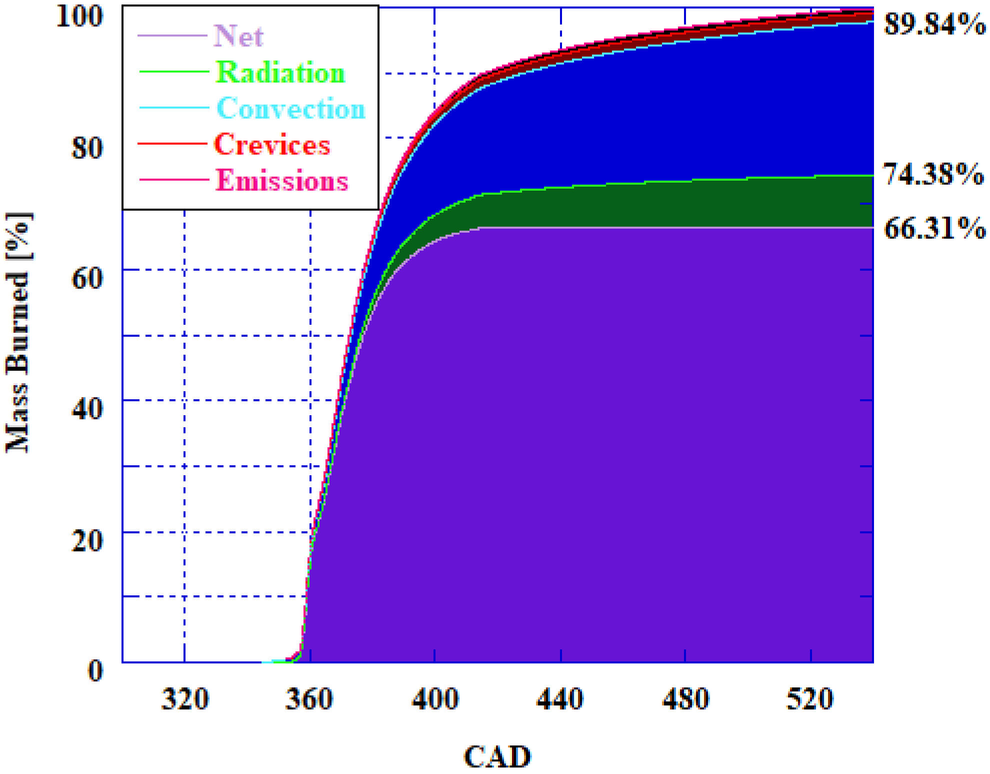

Figure 103: Mass Burned by Heat Loss Region for ULSD in CRDI

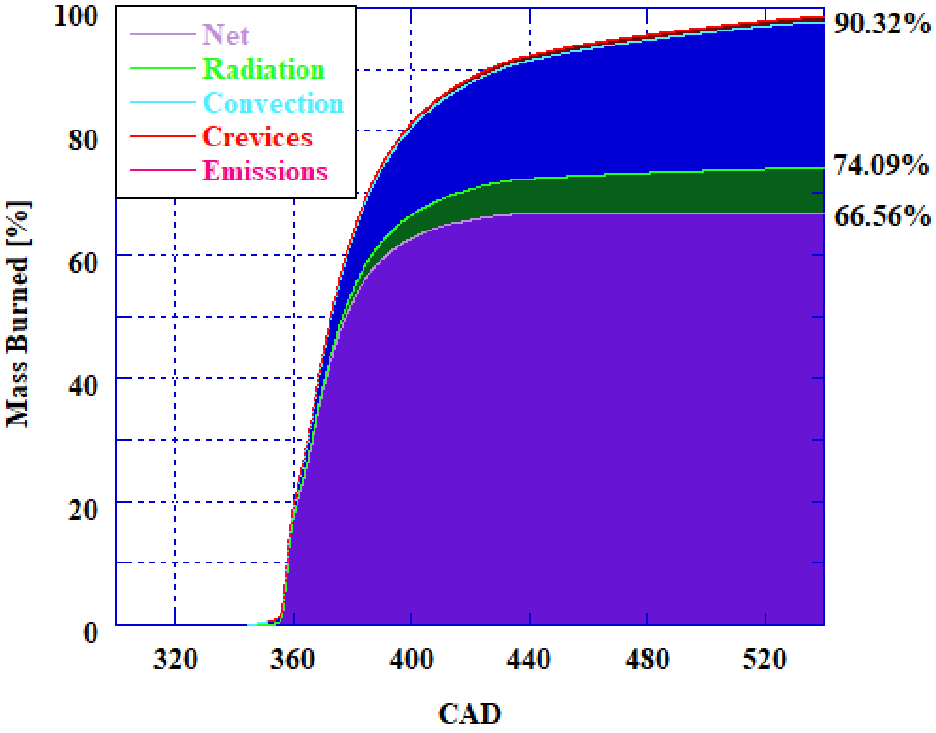

Figure 104: Mass Burned by Heat Loss Region for S2 in CRDI

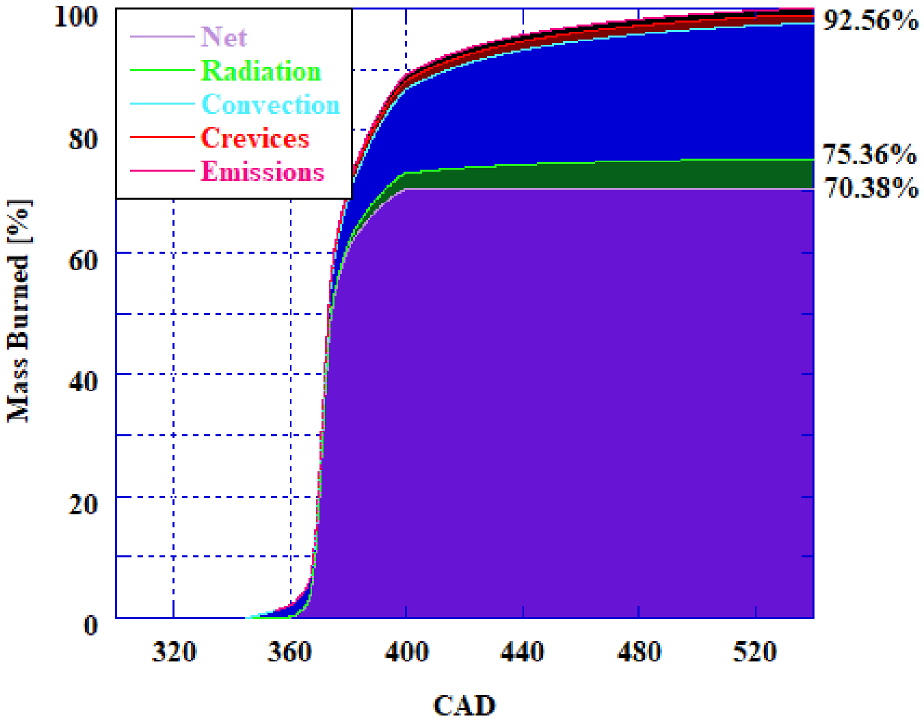

Figure 105: Mass Burned by Heat Loss Region for IPK in CRDI

Heat flux in the CRDI was calculated from the heat release calculated for convection and radiation heat loss in addition to piston area and cylinder area versus crank angle degree. The results from this calculation are displayed in the graph in Figure 106 for ULSD, S2, and IPK. It was found that consistent with the reduction in heat loss found from the combustion of IPK, there is a significant reduction in heat flux for all three calculated loss regions for IPK when compared to ULSD and S2.

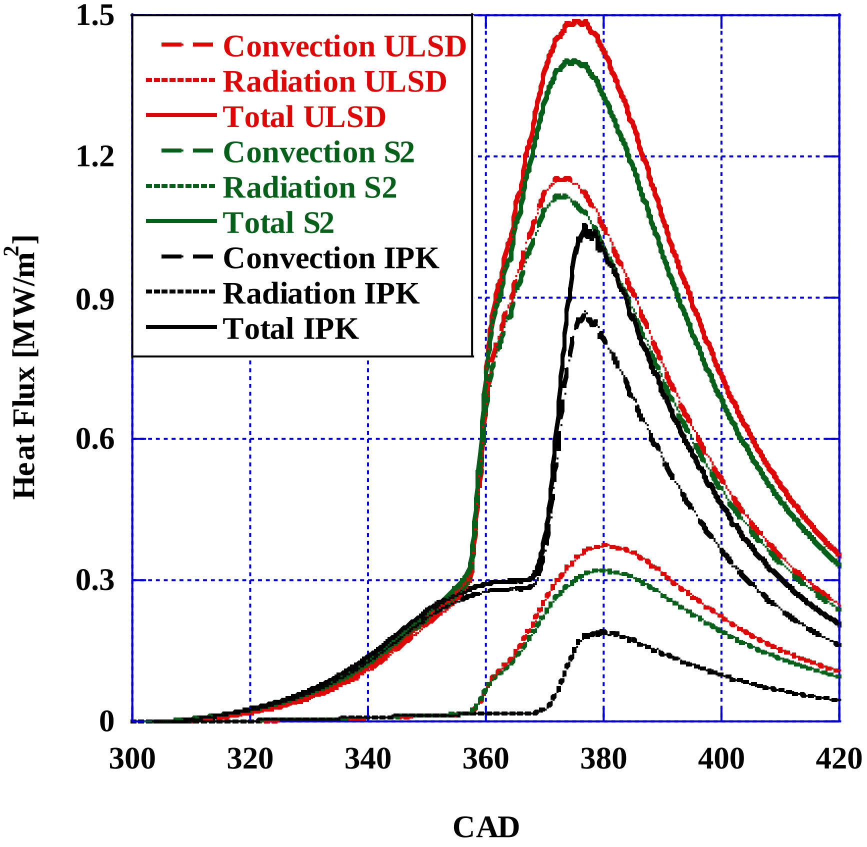

Figure 106: Heat Fluxes by Loss Region for ULSD, S2, and IPK

For ULSD and S2, there was found to be a reduction in heat flux for both radiation and convection heat flux for the combustion of S2 when compared to ULSD. This decrease in heat flux indicates a reduction in cylinder gas temperatures and in-cylinder turbulence for the combustion of S2. Peak cylinder heat fluxes and a summation of each heat flux are displayed in Table 51. For both S2 and IPK, there was found to be a reduction in both maximum and summed heat flux for all calculated values when compared to those of ULSD. When evaluated as a sum of the entire cycle, it was found that, for the combustion of IPK, the directionality of total convection heat flux shifted where more heat was transferred from the chamber walls to the chamber gases through convection.

Table 51: Peak and Summed Heat Fluxes for ULSD, S2, and IPK in CRDI

	ULSD	**S2**	**ULSD % Diff.**	**IPK**	**ULSD % Diff.**
Peak Rad. Flux [MW/m^2]	0.37	0.321	-13.24	0.221	-40.27
Peak Con. Flux [MW/m^2]	1.15	1.12	-2.61	0.904	-21.39
Peak Total Flux [MW/m^2]	1.49	1.404	-5.77	1.12	-24.83
Sum Rad. Flux [MW/m^2]	95.82	84.47	-11.845	41.36	-101.59
Sum Con. Flux [MW/m^2]	84.17	80.94	-3.837	-1.52	-50.86
Sum Total Flux [MW/m^2]	179.99	165.41	-8.1	39.84	-77.86

Table 52: Cylinder Temperature and Exhaust Gas Temperature for ULSD, S2, and IPK in CRDI

	Peak Cylinder Temp. [K]	**Exhaust Gas Temp. [K]**	**Temp. Drop [K]**
ULSD	1880.5	655.48	1225.02
S2	1819.89	650.95	1168.94
IPK	1684.28	570.75	1113.53

Peak cylinder temperatures and exhaust gas temperatures for each researched fuel are listed in Table 52. From the analysis of cylinder and exhaust temperature in combination with the heat loss and heat flux calculations, it can be seen that the reduction in cylinder temperatures for the combustion of S2 results in a reduction in thermal loss associated with its combustion. IPK also shows a significant decrease in cylinder and exhaust temperature when compared to ULSD, however, this is due to its much shorter combustion duration caused by its late ignition and short physical ignition delay. S2 was found to have a beneficial reduction in thermal loss and cylinder and exhaust temperatures without a significant shift in combustion phasing as found from the previous sections.

4.5 EMISSIONS AND EFFICIENCIES INVESTIGATION: IDI AND CRDI

4.5.1 EMISSIONS ANALYSIS

An analysis of the emissions produced from each fuel was conducted using the test methods outlined in Section 3.5.8 with the 20 species FTIR used to measure gaseous emissions and the MSS used to measure soot emissions. The emissions analyzed in this section include water, CO_2, CO, NOx, soot, and Unburned Hydrocarbons (UHC). These emissions species are indicators of the in-cylinder combustion properties such as stoichiometric combustion, hydrocarbon ratio, gas temperatures, and combustion efficiency.

Figures 107 and 108 represent the water and carbon dioxide emissions for each of the researched fuels at 4 bar BMEP for both IDI and CRDI with IDI consistently on the right-hand y-axis and CRDI on the left-hand y-axis. As these two species are products of stoichiometric hydrocarbon combustion, the comparative levels of the two emissions can give an indication of initial fuel and combustion properties.

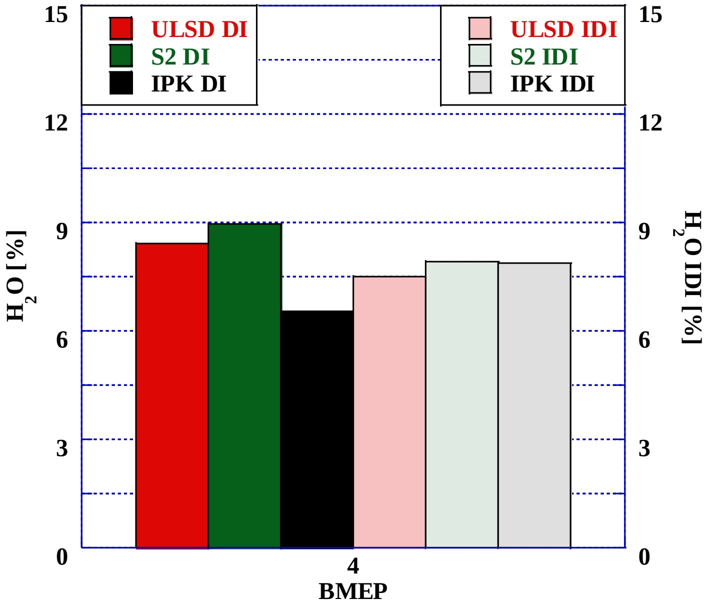

Figure 107: Percent Water Content in IDI and CRDI for ULSD, S2, and IPK

From the graph in Figure 107, it can be seen that the combustion of S2 produces a higher water content when compared to ULSD. This is an indication of the higher hydrocarbon (H/C) ratio of S2 consistent with the H/C ratio of F-T as found from literature when compared to ULSD. For the combustion of IPK, however there was found to be a decrease in exhaust water despite its increase in hydrocarbon ratio. From the analysis of the combustion phasing of IPK when compared to ULSD, this drop in percent water is likely due to a decrease in combustion efficiency. This property is emphasized in the CRDI engine as the reduction in both compression ratio and in-cylinder turbulence does not combust the low reactivity fuel as efficiently as in the IDI engine.

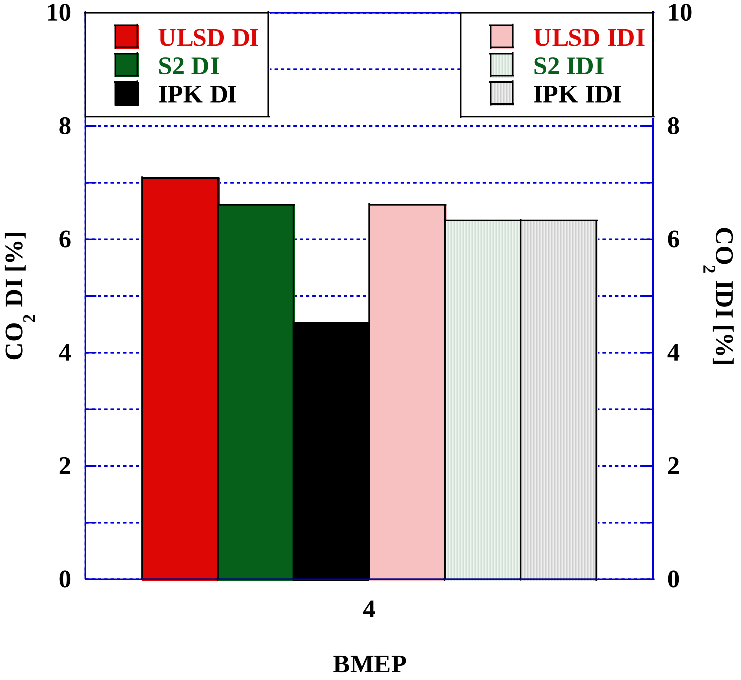

Figure 108: CO_2 Emissions for ULSD, S2, and in IDI and CRDI

As was the case with the water concentration, CO_2 is formed as a stoichiometric product in hydrocarbon combustion and is dependent on the carbon content of the fuel in conjunction with carbon monoxide (CO). The ratio of CO to CO_2 depends on the local air fuel ratio where the increase in this ratio indicates more areas of rich combustion low in free oxygen. The trends found in the CO_2 emissions reflect the H/C ratio of the fuel with an observed reduction in CO_2 with the increase in H/C ratio. Consistent with the results for water content, IPK exhibits a reduction in carbon dioxide more consistent with a decrease in combustion efficiency in CRDI as its H/C ratio is similar to that of S2 which has almost identical CO_2 emissions in IDI.

Combustion efficiency was determined for each researched fuel based on the CO and the UHC emissions with the results for these emissions species in CRDI and IDI for ULSD, S2, and IPK in Figures 109 and 110. The formation of CO is primarily linked to the local relative air-fuel ratio. In CI engines, most operation is under fuel lean conditions significantly reducing the CO emissions. As a result, the CO emissions from a CI engine are controlled by the mixture formation rate where despite the lean global equivalence ratio, there are areas of local fuel rich conditions. When compared to ULSD, S2 performed similarly in CRDI and saw a slight reduction in CO emissions in IDI while IPK exhibited a reduction in CO in CRDI and an increase in IDI. This indicates that the combustion of IPK in IDI burned under more localized areas of fuel rich mixtures while S2's mixture formation and global lambda was much more similar to that of ULSD.

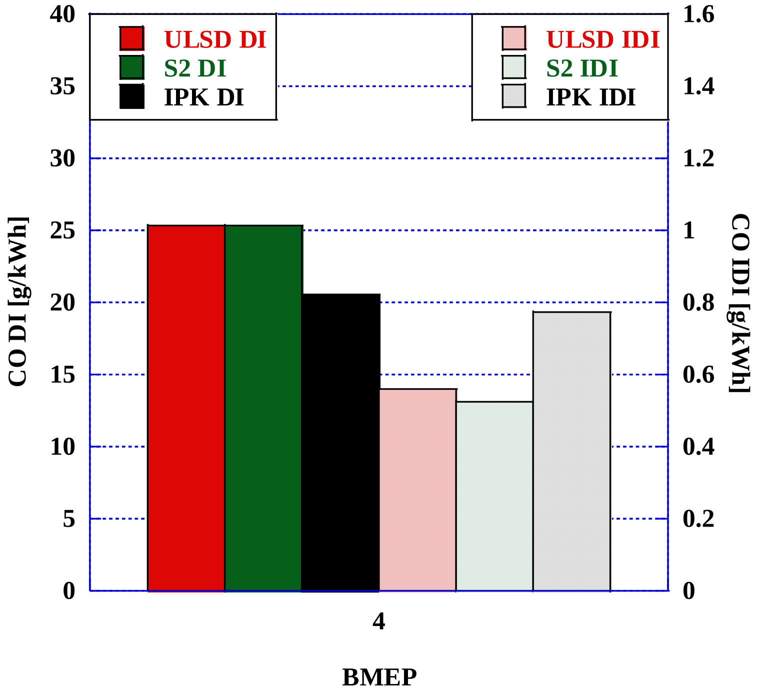

Figure 109: CO Emissions for ULSD and S2 in IDI and CRDI

The measurement of UHC indicates the quantity of fuel which does not combust in the chamber, but instead leaves through tailpipe emissions. The molecular weight of the UHC used to calculate g/kWh was modified to fit the average molecular formula for each researched fuel. It was found that in both CRDI and IDI, the F-T fuels produced more UHC during combustion when compared to ULSD. Of the three fuels, IPK had the highest level of UHC in both IDI and CRDI indicating that due to the delay in ignition, there was a high level of wall wetting leading to an increase in unburned fuel in the exhaust. Since peak temperatures were low for the combustion of IPK, areas round the boundary layer between the bulk gas and the chamber accumulate fuel which remains unburned and is instead expelled through the exhaust gas (Westbrook 2000).

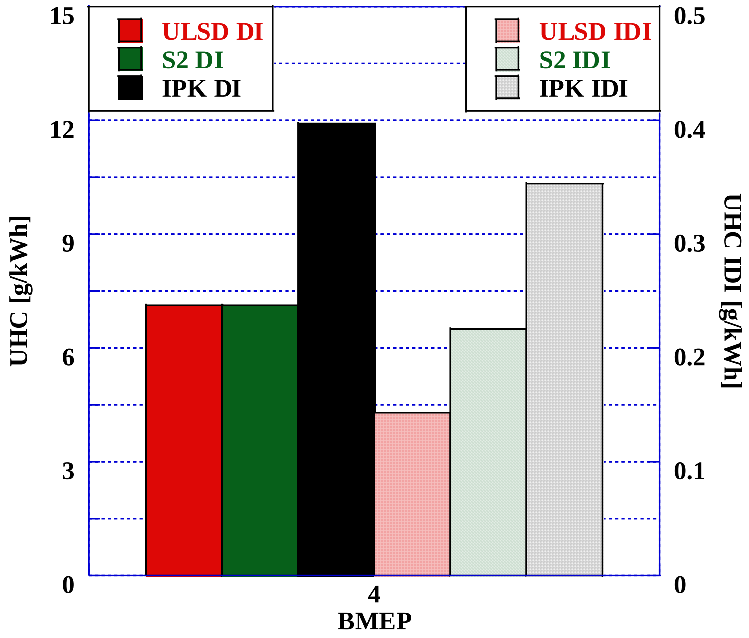

Figure 110: Unburned Hydrocarbon Emissions for ULSD, S2, and IPK in CRDI and IDI

Both the incomplete oxidation of CO and the unburned hydrocarbons contribute to the losses in the engine. This value is defined as the combustion efficiency where the products of incomplete combustion were calculated in terms of energy content and compared to the energy content in the fuel flow rate. The results of this evaluation are listed in Figure 114 and can be found with the other efficiency calculations in Section 4.5.2.

Soot and NOx form as a trade-off during combustion which is dependent on the temperature of combustion. Nitrogen reacts with oxygen to form nitric oxide (NO), nitrogen dioxide (NO_2), and nitrous oxide. These NO and NO_2 are most commonly grouped together and referred to as NOx. NOx is formed during the combustion process from 3 sources: fuel NOx, prompt NOx, and thermal NOx. Fuel NOx is formed out of the nitrogen contained within the chemical composition of the fuel. This is highly dependent on the chemical composition of the fuel and is removed during the desulfurization of diesel fuel. After desulfurization, ULSD contains less than 10 ppm of bound nitrogen contributing to less than 1 ppm of exhaust NOx. Prompt or Fenimore NOx is formed from the reaction of atmospheric nitrogen with early combustion radicals created during LTHR. Prompt NOx is heavily reliant on air-fuel stoichiometry and, for diesel, can be attributed to approximately 5% of the tailpipe NOx emissions. Thermal NOx refers to the formation of NOx at peak cylinder temperatures through the Zeldovich mechanisms. These reactions require very high temperatures as they are highly endothermic with a high activation energy making the minimum temperature required for thermal NOx 1400 K. For combustion analysis, the focus is on thermal NOx as this is the formation regime which is most easily controlled through modulation of peak in-cylinder temperatures (Heywood 2018).

$$N_2 + O = NO + N \qquad \text{Eq. 22}$$

$$N + O_2 = NO + O \qquad \text{Eq. 23}$$

$$N + OH = NO + H \qquad \text{Eq. 24}$$

The Zeldovich mechanisms model the formation of NOx in terms of the formation of NO and subsequent formation of NO_2. While NO can form in both the flame front and the post flame gases, formation in the post flame gases far exceeds the formation in the flame front. This is due to the increasing pressure and temperature of an IC engine during the combustion process as well as the very thin flame reaction zone and short residence time. This leaves very few areas for flame front formation and more opportunity for post flame gas formation as these gases continue to increase in both temperature and pressure. The reaction rate of NO is highly dependent on the oxygen and temperature and can therefore be modeled as a function of local equivalence ratio in post flame gases and gas temperature. The formation of NO_2 is a byproduct of NO formation rapidly after the flame front. It’s formed in higher quantities in CI engines when compared to SI engines where it can attribute to up to 30% of the total NOx in light load, CI conditions (Heywood 2018).

For this study, it is assumed that the NOx as measured from the FTIR is due to thermal NOx as fuel NOx and prompt NOx have a relatively low contribution to the overall exhaust gas concentration. The soot and NOx emissions are displayed in the graphs in Figures 111 and 112 respectively. It was found that the F-T fuels produced lower levels of NOx when compared to ULSD in both CRDI and IDI. Between the two F-T fuels, the results for NOx formation are consistent with peak cylinder pressure. In DI, IPK’s late ignition was reflected in lower peak cylinder pressure when compared to S2 and ULSD resulting in the reduction in formation of NOx. This was not the case in IDI where IPK exhibited the highest peak cylinder pressure where the formation of NOx was limited by the short combustion duration.

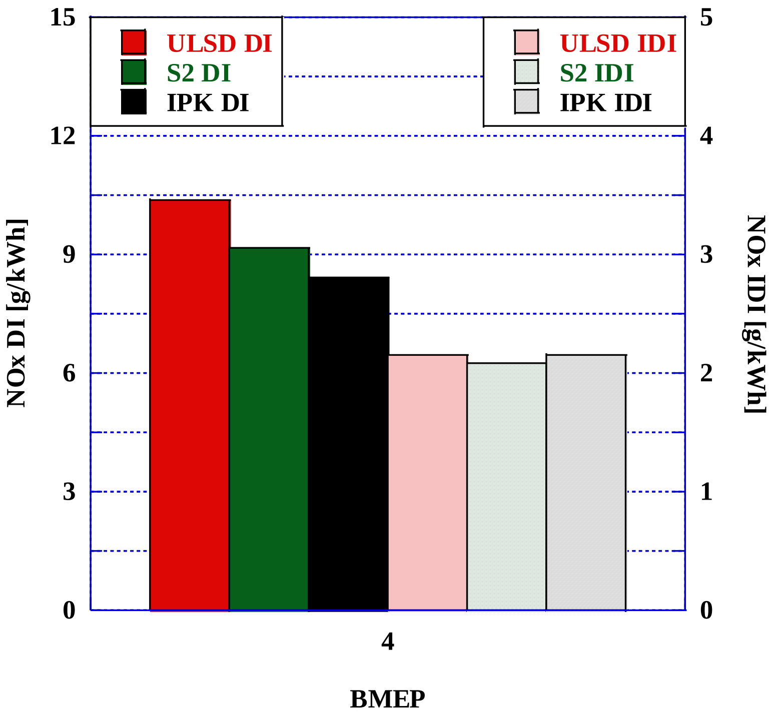

Figure 111: NOx Emissions for ULSD, S2, IPK in IDI and CRDI

In the engine, soot is formed within the evolving spray where most of the soot is burned up in the combustion chamber. The particles which are left create nucleation points for other Particulate Matter (PM) and unburned hydrocarbon molecules in the exhaust adhere and condense to the nucleation particle. Categories of particle sizes, or accumulation modes, describe the nature of the PM in the exhaust.

As soot and NOx are both temperature dependent with NOx forming at high temperature and soot forming at low temperatures, an increase in soot indicates a decrease in NOx and vice versa. Looking at the results for the soot and NOx emissions from both engines and all three fuels, it can be seen that this correlation is very apparent in the CRDI engine with a decrease in NOx correlating with an increase in soot. In this injection strategy, ULSD was found to have the highest NOx emissions followed by S2 and IPK, in order of decreasing NOx. This was found to correlate with the soot emissions as IPK was found to have the highest soot emissions followed by S2 and ULSD with the lowest soot. As NOx is heavily temperature dependent, the peak pressure can be used to predict NOx (Tesfa et al. 2014) with the results for NOx consistent with the peak pressures determined in both IDI and CRDI found in Sections 4.3.1 and 4.4.1.

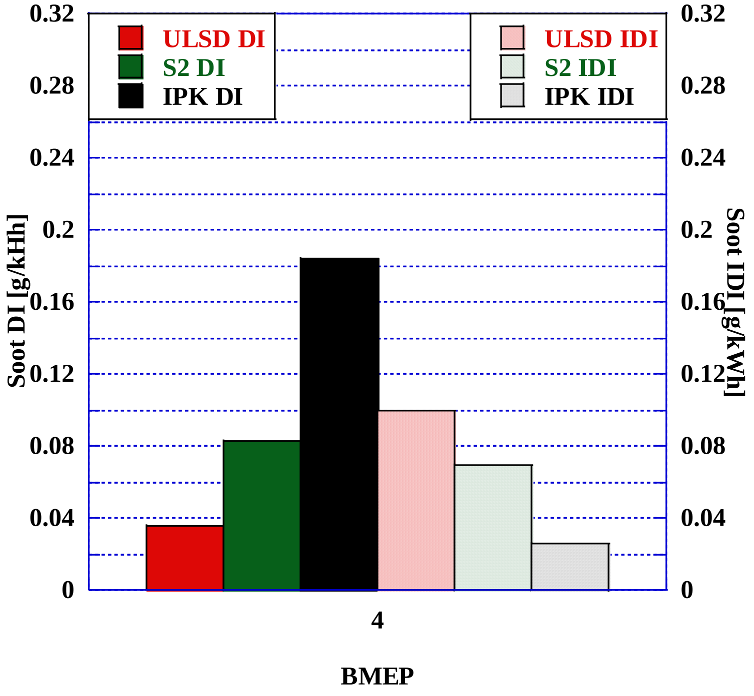

Figure 112: Soot Emissions for ULSD, S2, and IPK in IDI and CRDI

4.5.2 Efficiencies and Specific Fuel Consumption

Analyzed in this section are the metrics for determining the efficiency of the engine. These metrics include the Brake Specific Fuel Consumption (BSFC) in addition to effective thermal, indicated thermal, combustion, and mechanical efficiency. Each is a cumulative result of the combustion characteristics analyzed in previous sections. Figure 113 is the graph of the results of the calculation for effective thermal efficiency using Equation 25.

$$\frac{P_{eff}}{Fuel\ Flow\ \left[\frac{kg}{hr}\right] * 3600 * LHV\ \left[\frac{kJ}{kg}\right]} = Effective\ Thermal\ Efficiency \qquad \text{Eq. 25}$$

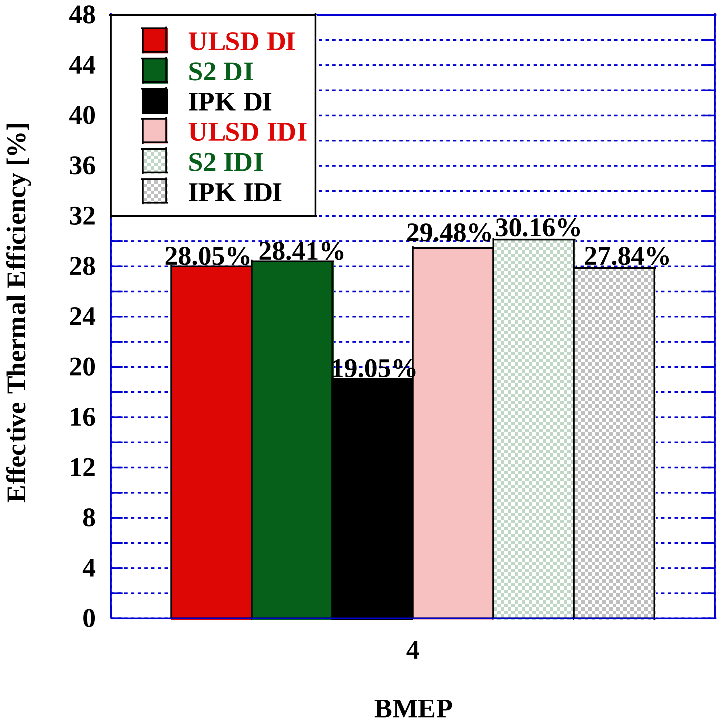

Figure 113: Effective Thermal Efficiency for ULSD, S2, and IPK in IDI and CRDI

Effective thermal efficiency represents the total efficiency of the engine from the quantity of fuel injected to the power output at the shaft. For diesel engines, effective thermal efficiency values do not exceed 40% except in rare cases. For these engines, effective thermal efficiency is expected to stay at or below 30%. It was found that in both the CRDI and the IDI engines, S2 saw an increase in effective thermal efficiency when compared to ULSD and IPK. This is consistent with the analysis of heat loss and heat flux in Sections 4.3.5 and 4.4.5 for IDI and CRDI as there was found to be a reduction in heat flux and heat loss for the combustion of S2 indicating an increase in thermal efficiency. Of the three fuels, IPK was found to be the least efficient. Between the two engines, the IDI engine was found to increase efficiency for each of the three fuels with the change in platform having the greatest influence on the efficiency of IPK. This is due to the increase in compression ratio for the IDI engine in addition to the use of a highly turbulent pre-chamber to aid in ignition.

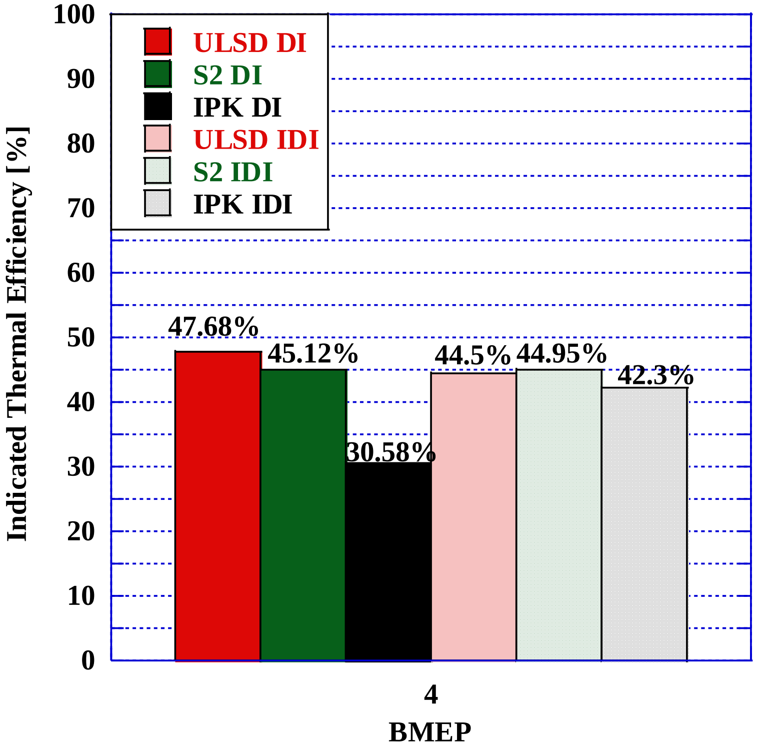

Figure 114: Indicated Thermal Efficiency for ULSD, S2, and IPK in IDI and CRDI

Figure 114 represents the results of the calculation for indicated thermal efficiency wherein the power variable in Equation 25 was exchanged for the indicated power as calculated from the P-V diagram for the combustion of each fuel. For this calculation, it was found that the combustion of S2 resulted in a reduction in efficiency when compared to ULSD in the CRDI engine and only a slight increase in efficiency in the IDI engine. The trend for IPK between the two engine platforms was consistent with an increase in efficiency when run in the IDI engine as compared to the CRDI engine. Contrary to the evaluation for the effective thermal efficiency, the CRDI was found to perform better than the IDI engine for the combustion of S2 and ULSD with IPK being the exception.

As mentioned in Section 4.5.1 for the analysis of emissions, the combustion efficiency for each fuel in both engine platforms was calculated using the BSFC, power specific emissions for UHC and CO, and the LHV for both the fuel and the oxidation of CO. The results of this determination are shown in the graph in Figure 115. It was found that there was a significant increase in combustion efficiency for the IDI engine when compared to the CRDI engine reaffirming the effectiveness of increased compression ratio and cylinder turbulence on combustion efficiency. For the researched fuels, S2 was found to have the lowest combustion efficiency in the CRDI engine and a slight reduction in combustion efficiency when compared to ULSD in the IDI engine. For this investigation, rail pressure and injection timing were kept constant for equivalent evaluation, however, given the findings from the combustion efficiency analysis, the drop in efficiency for the combustion of S2 could likely be adjusted for with calibration of injection timing and rail pressure without changing the engine platform.

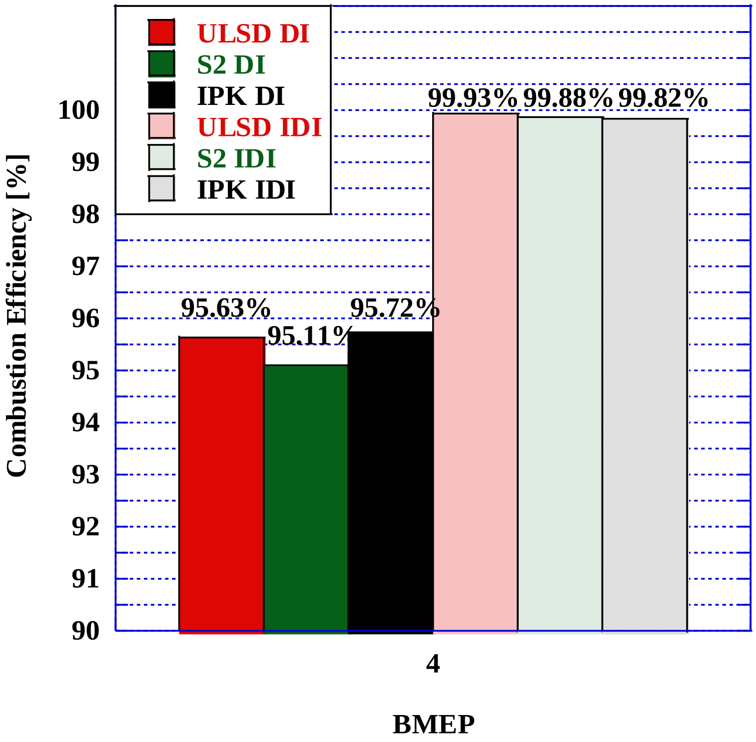

Figure 115: Combustion Efficiency for ULSD, S2, and IPK in IDI and CRDI

Mechanical efficiency was calculated for each test point by comparing the indicated power as calculated from IMEP to the effective power as calculated from the BMEP measured from the torque sensor on the dynamometer with the results displayed in Figure 116. This metric represents the percentage of engine power which is consumed to overcome friction forces and auxiliary engine systems and is defined in Equation 26. While many of the factors affecting mechanical efficiency are inherent to the engine, transient parameters such as temperature can affect this value as well. As shown in Section 4.1.1 in the analysis of the viscosity of each fuel, an increase in temperature causes a reduction in viscosity. Coupled with the results from the lubricity investigation in Section 4.1.2, it can be assumed that as temperature of the lubrication oil increases it loses lubricity causing an increase in friction force reducing mechanical efficiency.

$$\eta_m = \frac{\dot{W}_b}{\dot{W}_{i,g}} = \frac{\dot{W}_{i,g} - \dot{W}_f}{\dot{W}_{i,g}} = 1 - \frac{\dot{W}_f}{\dot{W}_{i,g}} \qquad \text{Eq. 26}$$

It was found that mechanical efficiency for both engines remained between 60 and 70% with a slight increase found for the IDI engine. For all test points, the combustion of S2 resulted in an increase in the mechanical efficiency when compared to ULSD and IPK. This can be traced back to the analysis of cylinder temperatures and exhaust temperatures in the IDI and CRDI engines found in Sections 4.3.5 and 4.4.5. Peak cylinder temperatures were found to be approximately 200° higher in the IDI engine with exhaust gases around 70-80° lower when compared to the CRDI engine. This indicates a higher average in-cylinder gas temperature for the CRDI engine when compared to the IDI engine. Mechanical efficiency is related to engine temperatures with friction forces increasing as the fuel and the oil decrease viscosity with increasing temperature.

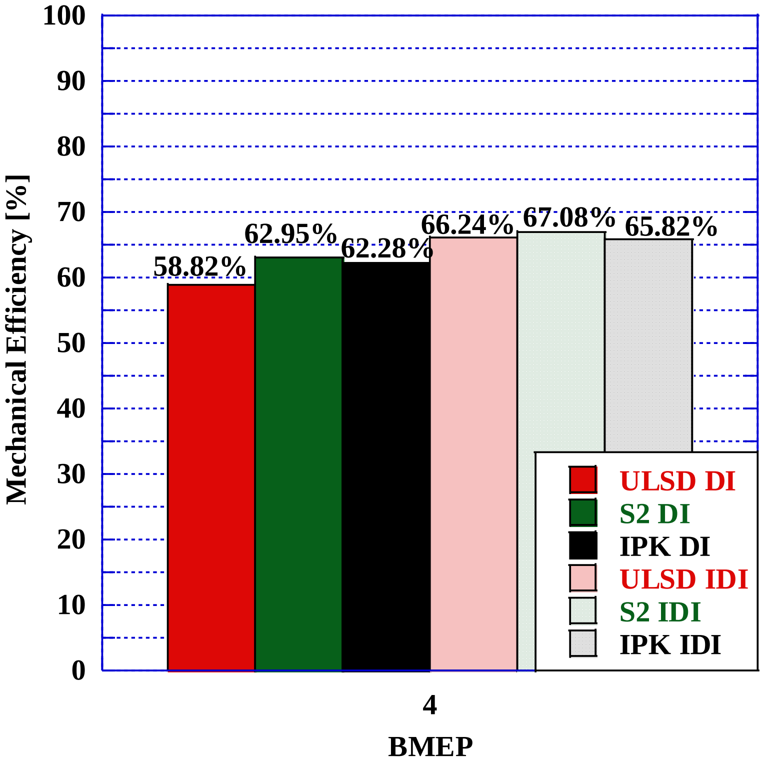

Figure 116: Mechanical Efficiency for ULSD, S2, and IPK in IDI and CRDI

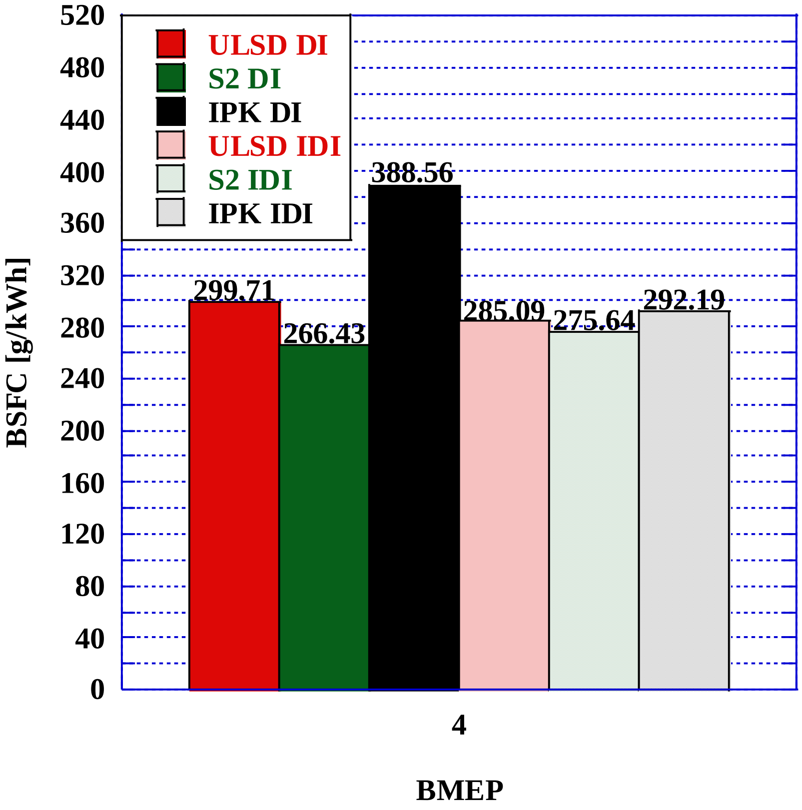

Figure 117: BSFC for ULSD, S2, and IPK in IDI and CRDI

For each of the researched fuels in both IDI and CRDI, Brake Specific Fuel Consumption (BSFC) was calculated using the LHV of the fuel, fuel flow rate, and effective power output of the engine. The results of this calculation can be found in the graph in Figure 117. For both engines, there is a reduction in BSFC when running S2 when compared to ULSD. IPK, however, saw a significant increase in BSFC when compared to ULSD and S2 with a much greater relative increase in BSFC in the CRDI engine than the IDI engine. This is consistent with the emissions results as there was found to be an increase in UHC emissions for the combustion of IPK when compared to the other researched fuels. S2, on the other hand, shows a decrease in BSFC despite its similarity to ULSD in UHC emissions due to the fuel’s decrease in density and increase in calorific content (Rahim et al. 2012).

CHAPTER 5:

CONCLUSIONS AND FUTURE WORKS

5.1 CONCLUSION

A study was conducted on the combustion and emissions characteristics of neat Fischer-Tropsch synthetic aviation fuel, Iso-Paraffinic Kerosene (IPK) and a drop-in fuel surrogate for CI engines, S2, with ULSD used as a baseline. The fuel surrogate, S2, was created using a blend of other neat alternative fuels (IPK (CTL), S-8 (GTL), and methyl oleate) to match the autoignition quality and the lubrication characteristics of ULSD. For autoignition quality, F-T fuels S-8 and IPK were blended in 25% increments as S-8 was found to have a very high DCN of 62 and IPK was found to have a very low DCN of 26.

Investigations in the CVCC revealed the correlation between blend percentage and DCN for fuel blends of IPK and S-8. Using the data collected from the neat F-T fuels and the blends between them, labeled as B1, B2, and B3, a linear regression calculation was conducted for the determination of a DCN equation whose coefficients accurately represent the relationship between ID, CD, and DCN specific to the F-T fuels. It was found that when using the two variable equation for DCN, not only does CD have a much more significant effect on DCN, but also, for CD values exceeding 10 ms, a reduction in ID exponentially reduces DCN despite short ignition delays associated with higher DCNs. This represents the importance of overall combustion duration on DCN as calculated by the two variable DCN equation.

A DCN of 50 was chosen as the target for the autoignition criteria for the surrogate fuel as this value adheres to a wider range of global standards for diesel fuels in addition to the association between shorter ignition delays and smoother combustion. The determined F-T blend percentage was 40% IPK to 60% S-8 by mass. This fuel blend is labeled as S1.

Lubricity testing was then conducted on the neat F-T fuels, ULSD, and methyl oleate to determine the percentage of lubricity improver necessary to match the lubricity of ULSD using methyl oleate and F-T fuel. Friction force analysis revealed a 2.2% and 2.5% increase from ULSD for S-8 and IPK respectively, and wear scar analysis showed an 8.5% and a 37% increase depth for S-8 and IPK compared to ULSD. With the addition of 3% methyl oleate by mass to S1 both wear scar depth and average friction force were found to be within 1% of ULSD. This blend is labeled as S2 and represents the final surrogate blend.

As there was found to be very little difference in viscosity and DCN between S1 and S2, further fuel analysis focused on S2 as compared to the other neat fuels. Spray analysis, TGA, and DTA were conducted to determine spray characteristics, volatility, and low temperature oxidation. It was found that S2 exhibited property values between IPK and S-8 indicating more favorable thermophysical characteristics for rapid air-fuel mixing in-cylinder when compared to ULSD.

In the CVCC, S2 was found to have a DCN of 49.95 with a more rapid pressure rise rate. An analysis of ringing events around peak pressure showed a decrease in magnitude coupled with an increase in quantity of pressure oscillations for the combustion of S2 when compared to ULSD. Despite an increase in peak pressure and temperature, cylinder pressure after EOC reduced in magnitude more slowly for S2 indicating that its exhaust gas mixture had a higher specific heat than that of ULSD. Low temperature combustion characteristics were found to have significant differences as the ratio of the cool flame formation region and the negative temperature coefficient region favored the former for the combustion of ULSD where S2 exhibited ratio closer to 50/50.

For the analysis of the fuel surrogate in an ICE, two platforms were selected as the combustion behavior could be studied in different compression ratios, displacements, and injection systems. S2 was compared against ULSD in both platforms in addition to neat IPK for a reference to the combustion performance of neat F-T fuel.

From the combustion and emissions analysis of IPK in both IDI and CRDI it was found that the high resistance to autoignition as indicated by the low DCN coupled with a rapid vaporization rate, fine spray atomization, low viscosity, and low density causes late ignition followed by high pressure rise rates and rapid combustion. The long ignition delay allows time more time for the fuel and air to form a more homogeneous mixture such that once ignition occurs the flames exhibit premixed combustion behavior. From the emissions analysis, it was determined that there was a significant reduction in combustion efficiency for IPK as indicated by the increase in UHC and BSFC. Complete homogeneity fuel/air mixture is not achievable in this time frame leaving a significant fraction of the fuel in liquid droplets as well as fuel rich regions in the combustion chamber. The low DCN coupled with the late combustion phasing caused a short combustion duration as the decrease in pressure on the expansion stroke extinguished the flame before all the injected fuel was burned.

In both IDI and CRDI, S2 was found to have a longer combustion duration when compared to ULSD though no there were no significant differences between peak combustion pressure, PPRR, or combustion phasing for ULSD and S2. The reduction in magnitude for the ringing events around peak pressure as found in the CVCC was found to be consistent in the two engines as well with a reduction in RI found for the combustion of S2 as compared to ULSD. In the emissions analysis, S2 produced a greater percentage of H_2O coupled with a reduction in CO_2 consistent with its greater hydrogen to carbon ratio. CO and UHC were functionally equivalent in the CRDI engine with a notable increase in UHC for the combustion of S2 in IDI when compared to ULSD. In CRDI, the soot/NOx tradeoff is apparent with a reduction in NOx and an increase in soot for the combustion of S2 compared to ULSD with further reduction in NOx and increase in soot found for IPK. This was not the case in IDI, however, as there was a reduction in both soot and NOx found for S2. Effective thermal efficiency increased for S2 in both CRDI and IDI with a decrease in indicated thermal efficiency found for the combustion of S2 in CRDI. Despite a reduction in combustion efficiency, there was a reduction in BSFC found for the combustion of S2 in both IDI and CRDI.

From the investigations into the thermophysical properties of the alternative drop-in fuel blend, S2, in addition to the combustion analysis in both IDI and CRDI engines configurations, it can be concluded, based on the criteria for success as described in Section 1.7 of this work, that S2 is a functional surrogate whose properties accurately emulate those of ULSD.

5.2 FUTURE WORKS

Further development on this project would involve investigation into the performance of this surrogate blend in various diesel combustion strategies such as forced induction and Exhaust Gas Recirculation (EGR) as well as in dual fuel strategies such as RCCI and PCCI. As a few challenging areas in terms of performance were discovered for the combustion of S2, there is an opportunity for further investigation into optimization of injection timing and injection pressure as well as the implementation of multiple injections. Additionally, since this study focuses on one load and one speed, future projects would be required to analyze the performance and emissions of the surrogate fuel blend across multiple speeds and loads. The effect of fuel properties could also be investigated where the blend percentages of the component fuels are changed as well as investigating the effect of changing the base fuels used for blending. Optimization of lubricity with an alternative fuel additive could also be compared back to commercially produced lubricity improvers. Furthermore, this blend optimization strategy can be applied to spark ignition engines and the key properties for their ideal function.

The primary purpose of this work is to demonstrate the capabilities and prospects for alternative fuels. Where the vast majority of current studies and implementation of alternative fuels focuses on non-blended fuels which require significant changes to the engine platform, there is no backwards compatibility with previous IC engines. Given the wide variety of feedstocks available for alternative fuel development, there is tremendous opportunity to create fuels to fit specific requirements for thermophysical and combustion characteristics through blending. Front end research would require thorough investigation and characterization of all fuel properties and the effects of those properties for rapid determination of ideal blend percentage. With further development of alternative fuels using feedstocks of recently sequestered carbon, the possibility opens for the establishment of a carbon cycle wherein the carbon emissions created from combustion comes from carbon sequestered from the atmosphere within recent years.

APPENDIX A

MATERIALS AND EQUIPMENT

Table 53. Fuel Types used During Experimentation

Fuel Type	
Fuel Sample	**Manufacturer/Provider**
ULSD	Standard on-road diesel fuel
IPK	Air Force Research Laboratory
S-8	Air Force Research Laboratory
Methyl Oleate	Thermo Scientific

Table 54. Multigas FTIR Gas Analysis System Equipment (MKS 2023)

Emissions Analysis Equipment			
Equipment Name	**Manufacturer/Provider**	**Model Type/Version**	**Quantity**
MultiGas^{TM} FTIR Continuous Gas Analyzer	MKS Instruments, Inc.	MKS 2030DBG2FZK13T	**1**
Heated Sampling Pump	MKS Instruments, Inc.	2380KS-5-10	**1**
Heated Line	MKS Instruments, Inc.	2385S	**1**
Dual-Channel Temperature Controller	MKS Instruments, Inc.	2384-2	**1**
liquid Nitrogen	Logan Hagan Welding Supply, Inc.	206689	**≈ 800 mL**
UHP Nitrogen Gas	Logan Hagan Welding Supply, Inc.	55-401806525-1	**≈ 120 psi**
EGHTP	Georgia Southern University	N/A	**1**
Computer	Lenovo	ThinkCentre 10A8	**1**
MG200 Quantitative Anlysis Software	MKS Instruments, Inc.	10.1	**1**

Table 55. Parr Calorimeter Equipment List (Parr 2023)

Calorimeter			
Equipment Name	**Manufacturer/Provider**	**Model Type/Version**	**Quantity**
Oxygen Calorimeter with a Plain Insulted jacket	Parr Instrument Company	1341	**1**
Calorimetric Thermometer	Parr Instrument Company	6772	**1**
Ni-alloy Fuse Wire	Parr Instrument Company	45C10	**10 cm**
Measuring Scale	Shimadzu Corporation	AUW120D	**1**
Compressed O^2	Logan Hagan Welding Supply, Inc.	UN1072	**25 atm**
Deionized Water	Georgia Southern University	N/A	**2000 mL**

Table 56. Bookfield DV II Pro Rotational Viscometer Equipment List (Brookfield 2015)

Viscometer			
Equipment Name	**Manufactuerer/Provider**	**Model Type/Version**	**Quantity**
Brookfield DV II Pro Rotational Viscometer	Brookfield Engineering Laboratoriesm, Inc.	LVDV-II + Pro	**1**
Brookfield Spindle	Brookfield Engineering Laboratoriesm, Inc.	SC-18	**1**
Brookfield Fuel Sample Adapter	Brookfield Engineering Laboratoriesm, Inc.	13RP	**1**
PID Temperature Controller	Omega Engineering, Inc.	N/A	**1**
Heating Chamber	N/A	N/A	**1**
Single Phase ODP Motor	N/A	CPSS-IN-1	**1**
10 mL Graduate Cylinder	N/A	N/A	**1**
Computer	Gateway, Inc.	AK MFATXPMT MDP E4100	**1**
Rheocalc Software	Brookfield Engineering Laboratoriesm, Inc.	3.2	**1**

Table 57. Malvern Spraytec Equipment List (Malvern 2023)

Spraytec			
Equipment Name	**Manufacturer/Provider**	**Model Type/Version**	**Quantity**
He-Ne Laser Receiver & Transmitter Assembly	Malvern Instruments, Inc.	STP2000	**1**
Wall Mounted airflow control system	Malvern Instruments, Inc.	STP2502	**1**
Nozzle Tester Assembly	Robert Bosch Tool Corporation	681200502	**1**
Bosch Fuel Pump	Robert Bosch Tool Corporation	Bestell-Nr	**1**
Bosch Fuel Injector	Robert Bosch Tool Corporation	Pintle	**1**
NCG Round Body Cylinder	SMC Corporation	NCDGBN32-0300	**1**
Air Regulator & Filter	SPEEDAIRE	4ZK76A	**1**
Air Filter	Kobalt	SGY-AIR9JH	**1**
11-gal compressed air tank	Torin Jacks, Inc.	T88011	**1**
Compressed air	Georgia Southern University	N/A	**≈ 0.3 Mpa**
Computer	Lenovo	ThinkCentre 7484	**1**
Spraytec software	Malvern Instruments, Inc.	N/A	**1**

Table 58: T-11 Pin-on-Disk Tribometer (IST 2008)

T-11 Pin-on-Disk Tribometer			
Equipment Name	Manufacturer/Provider	Model Type/Version	Quantity
Pin-on-Disk Tribometer	Institute for Sustainable Technologies	T-11	1
DAQ	National Instruments	9205	1
Force Transducer	Hottinger Baldwin Messtechnik	U1A	1

Table 59. DTG-60 Equipment List (Shimadzu 2018)

DTG			
Equipment Name	**Manufacturer/Provider**	**Model Type/Version**	**Quantity**
Thermo Gravimetric and Differential thermal Analysis Device	Shimadzu Corporation	DTG-60	**1**
Thermal Analyzer	Shimadzu Corporation	TA-60WS	**1**
Purge Box	Shimadzu Corporation	FC-60A	**1**
Aluminum Crimp Pans	Shimadzu Corporation	S201-52943	**2**
Alumina Powder	Shimadzu Corporation	DJNA	**≈ 20 mg**
Compressed Air	Air Gas, Inc.	AI UZ300	**30 psig**
Flow Meter	Key Instruments, Inc.	N/A	**1**
Computer	Gateway, Inc.	E-4500D	**1**
TA-60WS Collection Monitor software	Shimadzu Corporation	N/A	**1**
TA60 Software	Shimadzu Corporation	N/A	**1**

Table 60. PAC CID510 CVCC Equipment List (PAC 2021)

PAC			
Equipment Name	**Manufacturer/Provider**	**Model Type/Version**	**Quantity**
Constant Volume Combustion Chamber	PAC, LP	CID510	**1**
Cooling Thermstat	LAUDA	RA 8	**1**
UHP Compressed N^2	Logan Hagan Welding Supply, Inc.	NI UHP200C	**≈ 8-10 Bar**
Compressed Gas, N.O.S	Air Gas, Inc.	X02NI80P300CLS0	**≈ 23-25 Bar**

APPENDIX B:

ADDITIONAL EXPERIMENTAL RESULTS

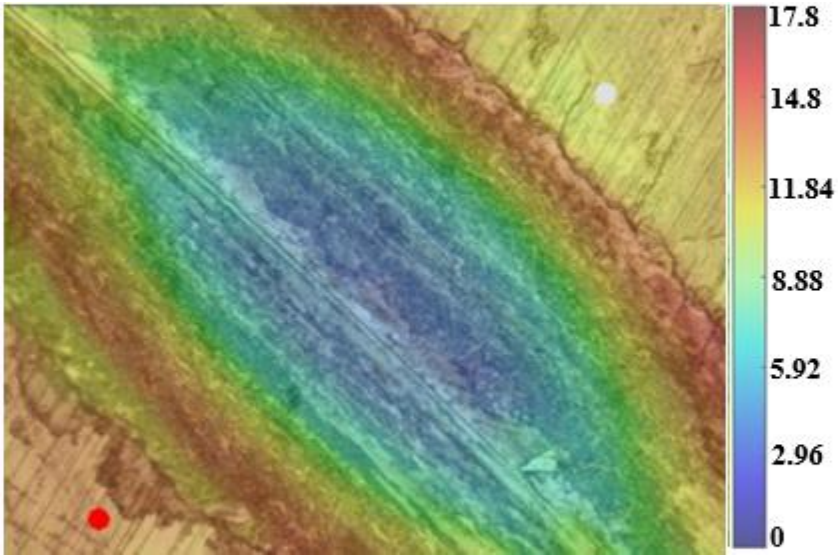

Figure 118:Wear Scar Image for S-8

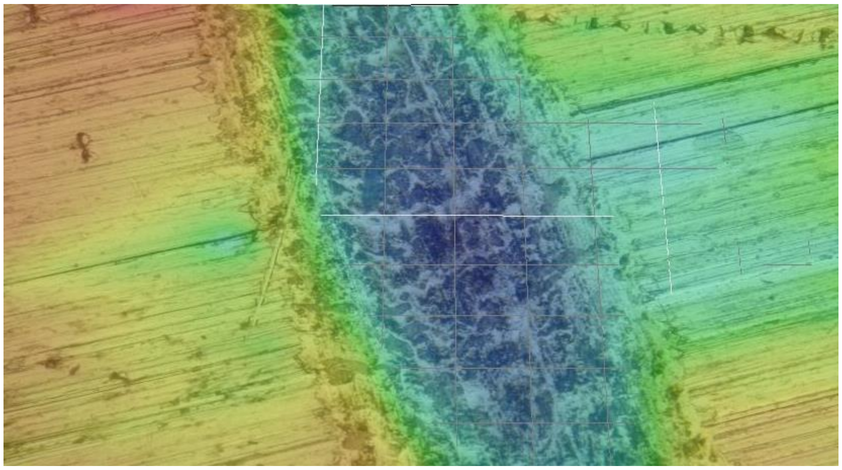

Figure 119: Wear Scar Profile for Methyl Oleate

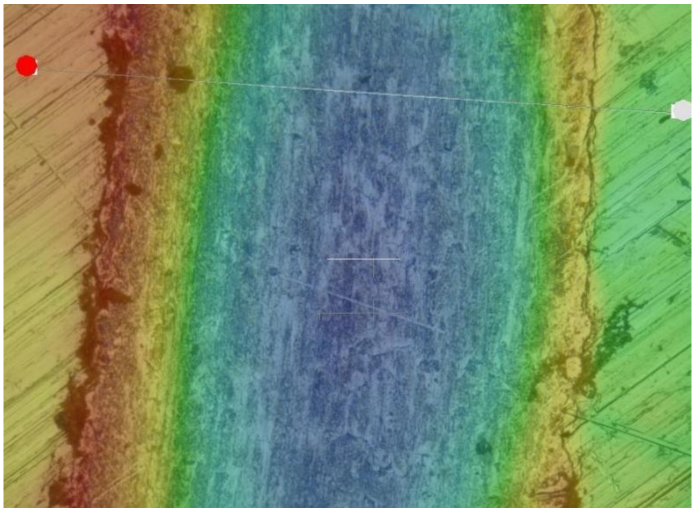

Figure 120: Wear Scar Profile for IPK

Table 61: Ignition Delay Calculation Method Index Numbers

ID Determination Method	Reference Number
CA5	1
CA10	2
AHRR +	3
$(d^2P)/(dt^2)$ +	4

Table 62: Calculated IDs for each Method in the CVCC in Milliseconds

Method	IPK	B1	B2	B3	S-8	S1	S2	ULSD
CA5	5.51	3.99	3.55	3.26	3.03	3.39	3.4	3.82
CA10	9.75	5.23	4.36	3.82	3.47	4.1	4.13	4.38
AHRR +	3.6	2.8	2.48	2.28	2.16	2.36	2.32	2.72
$(d^2P)/(dt^2)$ +	8.24	5.6	4.44	3.52	3.16	3.96	3.96	4.36

Table 63: Compendium of Calculated Ignition Delays and Combustion Delays in the IDI Engine

Fuel	Inflection Point [CAD]	SOI [CAD]	ID [CAD]
ULSD-4	358.92	336.78	22.14
S2-4	358.38	338.58	19.8
IPK-4	362.16	338.94	23.22
Fuel	**CA5 [CAD]**	**ID**	
ULSD-1	363.15	26.37	
S2-1	362.79	24.21	
IPK-1	365	26.06	
Fuel	**CA10 [CAD]**	**ID**	
ULSD-2	366.21	29.43	

S2-2	365.58	27	
IPK-2	366.26	27.32	
Fuel	**SOI [CAD]**	**AHRR>0 [CAD]-MC**	**ID [CAD]**
ULSD-3	336.78	358.38	21.6
S2-3	338.58	358.02	19.44
IPK-3	338.94	359.46	20.52
Fuel	**SOI [CAD]**	**AHRR>0 [CAD]-PC**	**ID [CAD]**
ULSD-3	336.78	356.4	19.62
S2-3	338.58	356.4	17.82
IPK-3	338.94	357.12	18.18

Table 64: Compendium of Calculated Ignition Delays and Combustion Delays in the CRDI Engine

Fuel	PPRR [bar/CAD]	CAD for PPRR [CAD]	Inflection Point [CAD]	Ignition Delay [CAD]
ULSD-4	6.15	359.18	355.93	10.93
S2-4	6.07	357.97	354.72	9.72
IPK-4	3.62	370.67	365.26	20.26
Fuel	**Peak AHRR [J/CAD]**	**CAD for AHRR Peak**	**CD based on Peak AHRR**	
ULSD	107.65	359	14	
S2	102.59	357.97	12.97	
IPK	110.58	370.66	25.66	
Fuel	**Positive AHRR [CAD]**	**Ignition Delay [CAD]**		
ULSD-3	353.04	8.04		
S2-3	353.4	8.4		
IPK-3	357.69	12.9		
Fuel	**CA5 [CAD]**	**ID [CAD]**		
ULSD-1	357.46	12.74		
S2-1	356.89	11.89		
IPK-1	366.79	21.79		
Fuel	**CA10 [CAD]**	**ID [CAD]**		
ULSD-2	358.46	13.46		
S2-2	357.61	12.61		
IPK-2	367.99	22.61		

REFERENCES

AFDC. 2023a. "Batteries for Electric Vehicles ". U.S. Department of Energy https://afdc.energy.gov/vehicles/electric_batteries.html.

---. 2023b. "Biodiesel Fuel Basics." Fuels and Vehicles Energy, Efficiency, and Renewable Energy. https://afdc.energy.gov/fuels/biodiesel_basics.html.

---. 2023c. "Developing Infrastructure to Charge Electric Vehicles ". U.S. Department of Energy https://afdc.energy.gov/fuels/electricity_infrastructure.html.

---. 2023d. "How do All-Electric Vehicles Work?". Energy, Efficiency, and Renewable Energy U.S. Department of Energy https://afdc.energy.gov/vehicles/how-do-all-electric-cars-work.

Alleman, Teresa L., Christopher J. Tennant, R. Robert Hayes, Matt Miyasato, Adewale Oshinuga, Greg Barton, Marc Rumminger, Vinod Duggal, Christopher Nelson, Mike May, and Ralph A. Cherrillo. 2005. "Achievement of Low Emissions by Engine Modification to Utilize Gas-to-Liquid Fuel and Advanced Emission Controls on a Class 8 Truck." SAE Technical Paper Series. https://doi.org/10.4271/2005-01-3766.

Alptekin, Ertan, and Mustafa Canakci. 2008. "Determination of the density and the viscosities of biodiesel–diesel fuel blends." *Renewable Energy* 33 (12): 2623-2630. https://doi.org/10.1016/j.renene.2008.02.020.

Anandan, Vikram. 2023. "The Effects of Internal Combustion Engines on the Environment." Industry News. Last Modified May 16, 2023.

Arnott, W. Patrick, John W. Walker, Hans Moosmüller, Robert A. Elleman, Haflidi H. Jonsson, Gintautas Buzorius, William C. Conant, Richard C. Flagan, and John H. Seinfeld. 2006. "Photoacoustic insight for aerosol light absorption aloft from meteorological aircraft and comparison with particle soot absorption photometer measurements: DOE Southern Great Plains climate research facility and the coastal stratocumulus imposed perturbation experiments." *Journal of Geophysical Research: Atmospheres* 111 (D5). https://doi.org/10.1029/2005jd005964.

Aste, Niccolò, R. S. Adhikari, Junia Compostella, and Claudio Del Pero. 2013. "Energy and environmental impact of domestic heating in Italy: Evaluation of national NOx emissions." *Energy Policy* 53: 353-360. https://doi.org/10.1016/j.enpol.2012.10.064.

ASTM. 2022. *Standard Test Method for Determination of Ignition Delay and Derived Cetane Number (DCN) of Diesel Fuel Oils by Combustion in a Constant Volume Chamber*. D6890 − 18. Danvers, MA: ASTM.

AVL. 2008. Online Soot Measurement - AVL Microsoot Sensor.

Barbour, R. H., D. J. Rickeard, and N. G. Elliott. 2000. "Understanding Diesel Lubricity." SAE Technical Paper Series.

Bastawrose, Hannah. 2023. "Average Energy Consumption Per Household." EnergyBot. Last Modified June 2023. https://www.energybot.com/blog/average-energy-consumption.html.

Birkl, Christoph R., Matthew R. Roberts, Euan McTurk, Peter G. Bruce, and David A. Howey. 2017. "Degradation diagnostics for lithium ion cells." *Journal of Power Sources* 341: 373-386. https://doi.org/10.1016/j.jpowsour.2016.12.011.

BOSMAL. 2018. "Title." Exhaust Emissions and Fuel Consumption Tests, Poland.

Brookfield. 2015. BROOKFIELD DV-II+Pro. In *Viscometers*, edited by Inc. Brookfield Engineering Laboratories. USA.

Charitha, V., S. Thirumalini, M. Prasad, and S. Srihari. 2019. "Investigation on performance and emissions of RCCI dual fuel combustion on diesel - bio diesel in a light duty engine." *Renewable Energy* 134: 1081-1088. https://doi.org/10.1016/j.renene.2018.09.048. https://www.sciencedirect.com/science/article/pii/S096014811831111X?via%3Dihub.

Cheng, Chong, Rasmus Faurskov Cordtz, Troels Dyhr Pedersen, Kim Winther, Niels Langballe Førby, and Jesper Schramm. 2023. "Investigation of combustion characteristics, physical and chemical ignition delay of methanol fuel in a heavy-duty turbo-charged compression ignition engine." *Fuel* 348 (2023): 128536. https://doi.org/https://doi.org/10.1016/j.fuel.2023.128536. https://www.sciencedirect.com/science/article/pii/S0016236123011493.

Colket, Meredith, Steve Zeppieri, Zhongtao Dai, and Don Hautman. 2012. "Fuel Research at UTRC." 5th Annual Fuel Research Meeting, Sandia National Laboratories, Livermore, CA.

Crocker, Mark. 2010. *Thermochemical Conversion of Biomass to Liquid Fuels and Chemicals*. Edited by Royal Society of Chemistry. Cambridge, UK: Royal Society of Chemistry.

Dalla Chiara, Bruno, Francesco Deflorio, and Marco Eid. 2019. "Analysis of real driving data to explore travelling needs in relation to hybrid–electric vehicle solutions." *Transport Policy* 80: 97-116. https://doi.org/10.1016/j.tranpol.2018.04.009.

Dawes, Chester. 1956. *Industrial Electricity*. Edited by McGraw-Hill. Third ed. Vol. 1. McGraw-Hill Book Company, Inc. .

de Lorenzi, Otto. 1957. *Combustion Engineering*. edited by Otto de Lorenzi. New York, NY: Combustion Engineering, Inc. .

Dimitriou, Pavlos, and Taku Tsujimura. 2017. "A review of hydrogen as a compression ignition engine fuel." *International Journal of Hydrogen Energy* 42 (38): 24470-24486. https://doi.org/10.1016/j.ijhydene.2017.07.232.

Dooley, Stephen, Sang Hee Won, Saeed Jahangirian, Yiguang Ju, Frederick L. Dryer, Haowei Wang, and Matthew A. Oehlschlaeger. 2012. "The combustion kinetics of a synthetic paraffinic jet aviation fuel and a fundamentally formulated, experimentally validated surrogate fuel." *Combustion and Flame* 159 (10): 3014-3020. https://doi.org/10.1016/j.combustflame.2012.04.010.

Duynslaegher, Catherine, Francesco Contino, Jacques Vandooren, and Hervé Jeanmart. 2012. "Modeling of ammonia combustion at low pressure." *Combustion and Flame* 159 (9): 2799-2805. https://doi.org/10.1016/j.combustflame.2012.06.003.

Edwards, James T. 01/28/2020 2020. *JET FUEL PROPERTIES*. Fuels and Energy Branch Turbine Engine Division, (Wright-Patterson Air Force Base, OH: AIR FORCE RESEARCH LABORATORY).

EIA. 2022. "Coal and the Environment." U.S. Energy Information Administration. Last Modified November 16, 2022.

---. 2023. "Renewable Energy Explained ". Monthly Energy Review. U.S. Energy and Information Administration Last Modified June 9, 2023. https://www.eia.gov/energyexplained/renewable-sources/.

Ejim, C. E., B. A. Fleck, and A. Amirfazli. 2007. "Analytical study for atomization of biodiesels and their blends in a typical injector: Surface tension and viscosity effects." *Fuel* 86 (10-11): 1534-1544. https://doi.org/10.1016/j.fuel.2006.11.006.

Elmalik, Elfatih E., Bilal Raza, Samah Warrag, Haider Ramadhan, Ehsan Alborzi, and Nimir O. Elbashir. 2013. "Role of Hydrocarbon Building Blocks on Gas-to-Liquid Derived

Synthetic Jet Fuel Characteristics." *Industrial & Engineering Chemistry Research* 53 (5): 1856-1865. https://doi.org/10.1021/ie402486c.

EPA. 2023. "Global Greenhouse Gas Emissions Data." United States Environmental Protection Agency. Last Modified February 15, 2023.

EVBox. 2022. "How much electricity does an electric car use?". https://evbox.com/en/ev-home-charger-electricity-usage#:~:text=Average%20driving%20distance%20in%20the%20US&text=Using%20the%20average%20EV's%20energy,and%204%2C310.65%20kWh%20per%20year.

Gainey, Brian, Ziming Yan, John Gandolfo, and Benjamin Lawler. 2022. "High Load Compression Ignition of Wet Ethanol Using a Triple Injection Strategy." *Energies* 15 (10). https://doi.org/10.3390/en15103507.

Gilfillan, Dennis, Greg Marland, Tom Boden, and Tom Andres. 2020. Global, Regional, and National Fossil-Fuel CO2 Emissions: 1751-2017. In *Global, Regional, and National Fossil-Fuel CO2 Emissions*, edited by Environmental System Science Data Infrastructure for a Virtual Ecosystem (ESS-DIVE). United States: U.S. Department of Energy.

Gill, Paul W., James H. Smith Jr., and Eugene J. Ziurys. 1954. *Fundamentals of Internal Combustion Engines as applied to Reciprocating, Gas Turbine, and Jet Propulsion Power Plants*. Third ed. 1 vols. Vol. 1. Annapolis, Maryland: United States Naval Institute

Gill, S. S., A. Tsolakis, K. D. Dearn, and J. Rodriguez-Fernandez. 2011. "Combustion characteristics and emissions of Fischer-Tropsch diesel fuels in IC engines." *Progress in Energy and Combustion Science* 37 (4): 503-523. https://doi.org/10.1016/j.pecs.2010.09.001. <Go to ISI>://WOS:000291510300004.

Gokalp, B., E. Buyukkaya, and H. S. Soyhan. 2011. "Performance and emissions of a diesel tractor engine fueled with marine diesel and soybean methyl ester." *Biomass and Bioenergy* 35 (8): 3575-3583. https://doi.org/10.1016/j.biombioe.2011.05.015.

Grantz, D. A., J. H. Garner, and D. W. Johnson. 2003. "Ecological effects of particulate matter." *Environ Int* 29 (2-3): 213-39. https://doi.org/10.1016/S0160-4120(02)00181-2. https://www.ncbi.nlm.nih.gov/pubmed/12676209.

Grigoratos, Theodoros, Georgios Fontaras, Giorgio Martini, and Cesare Peletto. 2016. "A study of regulated and green house gas emissions from a prototype heavy-duty compressed natural gas engine under transient and real life conditions." *Energy* 103: 340-355. https://doi.org/10.1016/j.energy.2016.02.157.

Guzman, Juan, and Kenneth Brezinsky. 2021. "Experimental and modeling study of the oxidation of F-24 jet fuel, and its mixture with an iso-paraffinic synthetic jet fuel, ATJ." *Combustion and Flame* 224: 108-125. https://doi.org/10.1016/j.combustflame.2020.12.008.

Hamid R. Rahai, Ehsan Shamloo, Jeremy Ralph Bonifacio. 2011. "Investigation of the Effect of a Humid Air System on Diesel NOx and PM Emissions of a Small Diesel Engine." SAE World Congress & Exhibition, Detroit, MI, 04/12/2011. https://www.sae.org/publications/technical-papers/content/2011-01-0692/#:~:text=Results%20showed%20approximately%203.7%25%20and,75%25%20and%2095%25%20respectively.

Harto, Chris. 2023. "Blog: Can the grid Handle EVs? Yes!". Consumer Reports. Advocacy. Last Modified May 10, 2023. https://advocacy.consumerreports.org/research/blog-can-the-grid-handle-evs-yes/#:~:text=A%20question%20that%20frequently%20comes,a%20little%20bit%20of%20math.

HBM. 2005. U1A Force Transducer. In *Data Sheet*, edited by Hottinger Baldwin Messtechnik GmbH.

Heywood, John B. 2018. *Internal Combustion Engine Fundamentals*. Edited by McGraw-Hill Education. London.

Honecker, Christian, Bastian Lehrheuer, Stefan Pischinger, and Karl Alexander Heufer. 2023. "Molecularly-controlled high swirl combustion system for ethanol/1-octanol dual fuel combustion." *Fuel* 345. https://doi.org/10.1016/j.fuel.2023.128184.

IER. 2023. "Environmental Impacts of Lithium-Ion Batteries ". Commentary Institute for Energy Research. Last Modified May 11, 2023. https://www.instituteforenergyresearch.org/renewable/environmental-impacts-of-lithium-ion-batteries/.

III, Thomas W. Ryan. 1985. "Correlation of Physical and Chemical Ignition Delay to Cetane Number." *SAE International Journal of Fuels and Lubricants* 94 (7): 12. https://doi.org/https://doi.org/10.4271/852103. https://saemobilus.sae.org/content/852103/.

Ikegami, M., K. Miwa, and M. Shioji. 1982. "A study of hydrogen fuelled compression ignition engines." *International Journal of Hydrogen Energy* 7 (4): 341-353. https://doi.org/10.1016/0360-3199(82)90127-6.

İnci, Mustafa, Mehmet Büyük, Mehmet Hakan Demir, and Göktürk İlbey. 2021. "A review and research on fuel cell electric vehicles: Topologies, power electronic converters, energy management methods, technical challenges, marketing and future aspects." *Renewable and Sustainable Energy Reviews* 137. https://doi.org/10.1016/j.rser.2020.110648.

Iodice, Paolo, and Massimo Cardone. 2021. "Ethanol/Gasoline Blends as Alternative Fuel in Last Generation Spark-Ignition Engines: A Review on CO and HC Engine Out Emissions." *Energies* 14 (13). https://doi.org/10.3390/en14134034.

IST. 2008. T-11 Elevated Temperature Pin-on-Disk Tribometer edited by Institute for Sustainable Technologies. Radom.

Jain, Akshay, Bhaskor Jyoti Bora, and Rakesh Kumar. 2023. "Production, performance, and emission analysis of new generation biodiesel in an unmodified engine." In *Advancement in Oxygenated Fuels for Sustainable Development*, 199-220.

Jelles, Sytse 1999. "Diesel Exhaust Aftertreatment- Development of catalytic systems for diesel particulate oxidation." PhD, Applied Sciences, Technical University of Delft. https://repository.tudelft.nl/islandora/object/uuid%3Aafc2d44f-a92b-47bd-80d3-5c8a20233cc5.

Jozwik, J., K. Dziedzic, M. Barszcz, and M. Pashechko. 2019. "Analysis and Comparative Assessment of Basic Tribological Properties of Selected Polymer Composites." *Materials (Basel)* 13 (1). https://doi.org/10.3390/ma13010075. https://www.ncbi.nlm.nih.gov/pubmed/31877867.

Ju, Y. G. 2021. "Understanding cool flames and warm flames Yiguang Ju." *Proceedings of the Combustion Institute* 38 (1): 83-119. https://doi.org/10.1016/j.proci.2020.09.019. <Go to ISI>://WOS:000668883100003.

Ju, Yiguang, Christopher B. Reuter, Omar R. Yehia, Tanvir I. Farouk, and Sang Hee Won. 2019. "Dynamics of cool flames." *Progress in Energy and Combustion Science* 75. https://doi.org/10.1016/j.pecs.2019.100787.

Keyence. 2012. Digital Microscope VHX-1000E. In *User's Manual*: Keyence.

Kistler. 2009. Dual Mode Charge Amplifier with Piezotron Operating Mode. edited by Kistler Instrument Corporation.

---. 2011a. Amplifier for Measuring Pressure and Temperature. edited by Kistler Group. Winterthur Switzerland.

---. 2011b. Type 6053CC Mini Measuring Probe. edited by Kistler Group. Winterthur, Switzerland: Kistler.

---. 2020a. Glow Plug Adapter. edited by Kistler Group. Winterthur, Switzerland.

---. 2020b. Type 6056A High Temperature Pressure Transducer. edited by Kistler Group. Winterthur, Switzerland.

Knothe, Gerhard. 2014. "A comprehensive evaluation of the cetane numbers of fatty acid methyl esters." *Fuel* 119 (2014): 6-13. https://doi.org/https://doi.org/10.1016/j.fuel.2013.11.020.

Kobayashi, Hideaki, Akihiro Hayakawa, K. D. Kunkuma A Somarathne, and Ekenechukwu C Okafor. 2019. "Science and technology of ammonia combustion." *Proceedings of the Combustion Institute* 37 (1): 109-133. https://doi.org/10.1016/j.proci.2018.09.029.

Kodavanti, U. P., R. Thomas, A. D. Ledbetter, M. C. Schladweiler, J. H. Shannahan, J. G. Wallenborn, A. K. Lund, M. J. Campen, E. O. Butler, R. R. Gottipolu, A. Nyska, J. E. Richards, D. Andrews, R. H. Jaskot, J. McKee, S. R. Kotha, R. B. Patel, and N. L. Parinandi. 2011. "Vascular and cardiac impairments in rats inhaling ozone and diesel exhaust particles." *Environ Health Perspect* 119 (3): 312-8. https://doi.org/10.1289/ehp.1002386. https://www.ncbi.nlm.nih.gov/pubmed/20980218.

Lacey, P. I., and S. A. Howell. 1998. "Fuel Lubricity Reviewed." SAE Technical Paper Series.

Law, Chung King, and Peng Zhao. 2012. "NTC-affected ignition in nonpremixed counterflow." *Combustion and Flame* 159 (2012): 1044-1054. https://doi.org/https://doi.org/10.1016/j.combustflame.2011.10.012.

Lefebvre, Arthur H., and Vincet G. McDonnell. 2017. *Atomization and Sprays*. Edited by CRC Press. Boca Raton.

Lyu, Y., E. Bergseth, and U. Olofsson. 2016. "Open System Tribology and Influence of Weather Condition." *Sci Rep* 6: 32455. https://doi.org/10.1038/srep32455. https://www.ncbi.nlm.nih.gov/pubmed/27573973.

Maleev, V. L. 1954. *Diesel Engine Operation and Maintainence*. Edited by McGraw-Hill. York, PA: The Maple Press Company.

Malvern. 2023. Spraytec. edited by Malvern Panalytical. Worcestershire, UK: Malvern Instruments Ltd.

Marchese, Marco, Emanuele Giglio, Massimo Santarelli, and Andrea Lanzini. 2020. "Energy performance of Power-to-Liquid applications integrating biogas upgrading, reverse water gas shift, solid oxide electrolysis and Fischer-Tropsch technologies." *Energy Conversion and Management: X* 6. https://doi.org/10.1016/j.ecmx.2020.100041.

Marcotte, Florence, and Stéphane Zaleski. 2019. "Density contrast matters for drop fragmentation thresholds at low Ohnesorge number." *Physical Review Fluids* 4 (10). https://doi.org/10.1103/PhysRevFluids.4.103604.

Marmiroli, Benedetta, Maarten Messagie, Giovanni Dotelli, and Joeri Van Mierlo. 2018. "Electricity Generation in LCA of Electric Vehicles: A Review." *Applied Sciences* 8 (8). https://doi.org/10.3390/app8081384.

Mayer, S.W. 02/21/1968 1967. *Computed Activation Energies for Reactions*

of 02, N2, NO, N20, NO2, CO, and CO2. Laboratory Operations, Aerodynamics and Propulsion Aesearch Laboratory (Los Angeles, CA: Space and Missile Systems Organization). https://apps.dtic.mil/sti/tr/pdf/AD0665473.pdf.

McCormick, Robert, and Kristi Moriarty. 2023. *Biodiesel Handling and Use Guide.* Office of Energy Efficiency and Renewable Energy, Alliance for Sustainable Energy, LLC. (Denver, CO: National Renewable Energy Laboratory).

Menard, Kevin P. 2014. The Benefits of Thermogravimetric Gas Chromatography–Mass Spectrometry. *The Column* 10 (13): 31.

Mi, Chris, and M. Abdul Masrur. 2018. *Hybrid Electric Vehicles Principles and Applications with Practical Perspectives* Second ed., edited by John Wiley & Sons Ltd.: John Wiley & Sons Ltd. .

Mitutoyo. 2016. *Portable Surface Roughness Tester Surftest SJ-210 Series.* Aurora IL: Mitutoyo America Corporation. www.mitutoyo.com.

MKS. 2023. MultiGas FTIR Gas Analyzer. edited by MKS.

Mohan, Shankar, Jason B. Siegel, Anna G. Stefanopoulou, and Ram Vasudevan. 2019. "An Energy-Optimal Warm-Up Strategy for Li-Ion Batteries and Its Approximations." *IEEE Transactions on Control Systems Technology* 27 (3): 1165-1180. https://doi.org/10.1109/tcst.2017.2785833.

Morita, Akiyoshi, and Gen Sugiyama. 2003. "Influence of Density and Viscosity of Diesel Fuel on Exhaust Emissions." SAE Technical Paper Series.

Moses, Clifford A. September 2008 2008. *Comparative Analysis of Semi-Sythetic Jet Fuels.* Universal Technology Corporation.

Mousavi, Nayereh Sadat, Ascención Romero-Martínez, and Luis Felipe Ramírez-Verduzco. 2020. "Predicting the surface tension of mixtures of fatty acid ethyl esters and biodiesel fuels using UNIFAC activity coefficients." *Fluid Phase Equilibria* 507. https://doi.org/10.1016/j.fluid.2019.112430.

Mueller, Charles J., William J. Cannella, Thomas J. Bruno, Bruce Bunting, Heather D. Dettman, James A. Franz, Marcia L. Huber, Mani Natarajan, William J. Pitz, Matthew A. Ratcliff, and Ken Wright. 2012. "Methodology for Formulating Diesel Surrogate Fuels with Accurate Compositional, Ignition-Quality, and Volatility Characteristics." *Energy & Fuels* 26 (6): 3284-3303. https://doi.org/10.1021/ef300303e.

Nabi, Md Nurun, Johan Einar Hustad, and Md Arman Arefin. 2020. "The influence of Fischer–Tropsch-biodiesel–diesel blends on energy and exergy parameters in a six-cylinder turbocharged diesel engine." *Energy Reports* 6: 832-840. https://doi.org/10.1016/j.egyr.2020.04.011.

Nayagam, Vedha, Daniel L. Dietrich, Paul V. Ferkul, Michael C. Hicks, and Forman A. Williams. 2012. "Can cool flames support quasi-steady alkane droplet burning?" *Combustion and Flame* 159 (12): 3583-3588. https://doi.org/10.1016/j.combustflame.2012.07.012.

Nayak, Satyabrata , Madhumita Das, Binpani Pradhan, and Sandeep Kundu. 2019. "Environmental Impacts of Fossil Fuels." In *Sustainable Energy and Environment*, 245-260. Apple Academic Press.

Newell, A. B. . 1953. *Diesel Engineering Handbook*. 8th ed., edited by A. B. Newell. New York, NY: Diesel Publications, Inc.

NI. 2023. "NI-9205 Specifications." Last Modified August 8, 2023. https://www.ni.com/docs/en-US/bundle/ni-9205-specs/page/specs.html.

Nicholas, Michael. 2019. "Estimating electric vehicle charging infrastructure costs across major U.S. metropolitan areas." August 2019. https://theicct.org/wp-content/uploads/2021/06/ICCT_EV_Charging_Cost_20190813.pdf.

Nordelöf, Anders, Maarten Messagie, Anne-Marie Tillman, Maria Ljunggren Söderman, and Joeri Van Mierlo. 2014. "Environmental impacts of hybrid, plug-in hybrid, and battery electric vehicles—what can we learn from life cycle assessment?" *The International Journal of Life Cycle Assessment* 19 (11): 1866-1890. https://doi.org/10.1007/s11367-014-0788-0.

OHPI. 2022. "Average Annual Miles per Driver by Age Group." U.S. Department of Transporation. https://www.fhwa.dot.gov/ohim/onh00/bar8.htm.

Onorati, A., R. Payri, B. M. Vaglieco, A. K. Agarwal, C. Bae, G. Bruneaux, M. Canakci, M. Gavaises, M. Günthner, C. Hasse, S. Kokjohn, S. C. Kong, Y. Moriyoshi, R. Novella, A. Pesyridis, R. Reitz, T. Ryan, R. Wagner, and H. Zhao. 2022. "The role of hydrogen for future internal combustion engines." *International Journal of Engine Research* 23 (4): 529-540. https://doi.org/10.1177/14680874221081947.

PAC. 2021. *Cetane ID 510 Fully Automated Derived Cetane Number Analyzer.*

Pani, Abinash. 2020. "Formation, Kinetics and Control Strategies of Nox Emission in Hydrogen Fueled IC Engine." *International Journal of Engineering Research & Technology (JERT)* 9 (1). https://doi.org/10.17577/IJERTV9IS010081.

Parr. 2023. "1341 Plain Jacket Bomb Calorimeter ". Parr Instrument Company https://www.parrinst.com/products/oxygen-bomb-calorimeters/1341-plain-jacket-bomb-calorimeter/.

Peters, Jens F., Manuel Baumann, Benedikt Zimmermann, Jessica Braun, and Marcel Weil. 2017. "The environmental impact of Li-Ion batteries and the role of key parameters – A review." *Renewable and Sustainable Energy Reviews* 67: 491-506. https://doi.org/10.1016/j.rser.2016.08.039.

Phuong X. Pham, Nam V.T. Pham, Thin V. Pham, Vu H. Nguyen, Kien T. Nguyen. 2021. "Ignition delays of biodiesel-diesel blends: Investigations into the role of physical and chemical processes." *Fuel* 303 (2021): 121251. https://doi.org/https://doi.org/10.1016/j.fuel.2021.121251. https://www.sciencedirect.com/science/article/pii/S0016236121011303.

Prak, Dianne L. , Jay Cooke, Terrence Dickerson, Andy McDaniel, and Jim Cowart. 2021. "Cetane number, derived cetane number, and cetane index: When correlations fail to predict combustibility." *Fuel* 289 (2021): 119963. https://doi.org/https://doi.org/10.1016/j.fuel.2020.119963.

Ra, Youngchul, Rolf D. Reitz, Joanna McFarlane, and C. Stuart Daw. 2008. "Effects of Fuel Physical Properties on Diesel Engine Combustion using Diesel and Bio-diesel Fuels." *SAE International Journal of Fuels and Lubricants* 1 (1): 16. https://doi.org/https://doi.org/10.4271/2008-01-1379.

Radhakrishna, Vishnu, Weixiao Shang, Longchao Yao, Jun Chen, and Paul E. Sojka. 2021. "Experimental characterization of secondary atomization at high Ohnesorge numbers." *International Journal of Multiphase Flow* 138. https://doi.org/10.1016/j.ijmultiphaseflow.2021.103591.

Rahim, Rafidah, Rizalman Mamat, Mohd Yusof Taib, and Abdul Adam Abdullah. 2012. "Influence of Fuel Temperature on a Diesel Engine Performance Operating with Biodiesel Blended." *Journal of Mechanical Engineering and Sciences* 2: 226-236. https://doi.org/10.15282/jmes.2.2012.10.0021.

Rahman, M., S. Upadhyay, K. Ganguly, M. Introna, J. Ji, C. Boman, A. Muala, A. Blomberg, T. Sandstrom, and L. Palmberg. 2023. "Comparable Response Following Exposure to Biodiesel and Diesel Exhaust Particles in Advanced Multicellular Human Lung Models." *Toxics* 11 (6). https://doi.org/10.3390/toxics11060532. https://www.ncbi.nlm.nih.gov/pubmed/37368632.

Ryder, R, Robert C. Hendricks, M. L. Huber, and D.T. Shouse. 2010. "Computational Analysis of Dynamic SPK(S8)-JP8 Fueled Combustor-Sector Performance." International Symposium on Transport Phenomena and Dynamics of Rotating Machinery, Honalulu, HI, USA, April 4-9, 2010.

Santos, Ronaldo Gonçalves dos, and Andre Cardoso Alencar. 2020. "Biomass-derived syngas production via gasification process and its catalytic conversion into fuels by Fischer Tropsch synthesis: A review." *International Journal of Hydrogen Energy* 45 (36): 18114-18132. https://doi.org/10.1016/j.ijhydene.2019.07.133.

Seidenspinner, Philipp , Martin Härtl, Thomas Wilharm, and Georg Wachtmeister. 2015. "Cetane Number Determination by Advanced Fuel Ignition Delay Analysis in a New Constant Volume Combustion Chamber." SAE 2015 World Congress & Exhibition, Detroit, MI, 04/14/2015. https://www.sae.org/publications/technical-papers/content/2015-01-0798/.

Selim, Osama M., and Ryoichi S. Amano. 2021. "Co-Pyrolysis of Chicken and Cow Manure." *Journal of Energy Resources Technology* 143 (1). https://doi.org/10.1115/1.4047597.

Semin, Rosli A. B. . 2008. "A Technical Review of Compressed Natural Gas as an Alternative Fuel for Internal Combustion Engines." *American Journal of Engineering and Applied Sciences* 1 (4): 302-311. https://doi.org/10.3844/ajeassp.2008.302.311.

Shah, Pinkesh R., and Anuradda Ganesh. 2018. "Study the influence of pre-heating on atomization of straight vegetable oil through Ohnesorge number and Sauter mean diameter." *Journal of the Energy Institute* 91 (6): 828-834. https://doi.org/10.1016/j.joei.2017.10.006.

Shimadzu. 2018. DTG-60 Series. In *Simultaneous TG/DTA*, edited by Shimadzu Corporation.

Singh, Narendra, and Jin Hui Li. 2014. "Environmental Impacts of Lead Ore Mining and Smelting." *Advanced Materials Research* 878: 338-347. https://doi.org/10.4028/www.scientific.net/AMR.878.338.

Soloiu, V., C. Carapia, R. Smith III, A. Weaver, L. McKinney, D. Mothershed, D. Grall, M. Ilie, and M. Rahman. 2020. "RCCI With High Reactivity S8-ULSD Blend and Low Reactivity N-Butanol." ASME 2020 Internal Combustion Engine Division Fall Technical Conference.

Soloiu, V., R. Smith III, A. Weaver, L. Parker, D. Brock, A. Rowell, and M. Ilie. 2022. "Combustion characteristics of F24 compared to Jet A in a Common Rail Direct Injection Research Compression Ignition Engine." ASME 2022 ICE Forward Conference.

Soloiu, V., A. Weaver, L. Parker, A. Brant, R. Smith III, M. Ilie, G. Molina, and C. Carapia. 2022. "Constant volume combustion chamber (CVCC) investigations of aerospace F-24 and Jet-A in low-temperature heat release and negative temperature coefficient regions." *Energy Conversion and Management* 263. https://doi.org/10.1016/j.enconman.2022.115687.

Soloiu, V., A. Weaver, L. Parker, R. Smith III, A. Brant, D. Brock, and M. Ilie. 2022. "Investigations Into the Performance and Emissions Characteristics of FT Synthetic Aviation Fuel, Isoparaffinic Kerosene (IPK), in a Single-Cylinder Indirect Injection (IDI) Engine." ICE Forward Conference, Indianapolis, IN.

Soloiu, V., A. Weaver, J. Willis, A. Rowell, and N. Dillon. 2023. "Combustion Research in Wide DCN Range Synthetic Aviation Fuels in a High Compression Ratio Engine." ICE Forward Conference, Pittsburgh, PA.

Steeger, F., T. Raffius, C. Schulz, F. Ratz, B. Morcinkowski, B. Lehrheuer, G. Gruenefeld, and S. Pischinger. 2022. "Investigation of the chemical effect of pilot injection on main combustion in a gasoline controlled auto-ignition engine by in-cylinder measurements and numerical simulation of H2O2, HO2, and OH radicals." *Combustion and Flame* 244. https://doi.org/ARTN 112283

10.1016/j.combustflame.2022.112283. <Go to ISI>://WOS:000838326800002.

Sukjit, Ekarong, Karl D. Dearn, and Athanasios Tsolakis. 2011. "Interrogating the surface: the effect of blended diesel fuels on lubricity." *SAE International Journal of Fuels and Lubricants* 5 (1): 154-162. https://doi.org/10.4271/2011-01-1940.

Sydbom, A., A. Blomberg, S. Parnia, N. Stenfors, T. Sandstrom, and S. E. Dahlen. 2001. "Health effects of diesel exhaust emissions." *Eur Respir J* 17 (4): 733-46. https://doi.org/10.1183/09031936.01.17407330. https://www.ncbi.nlm.nih.gov/pubmed/11401072.

Sympatec. 2023. "Laser Differaction." Sympatec GmbH. https://www.sympatec.com/en/particle-measurement/glossary/laser-diffraction/.

Tesfa, Belachew Chekene, R. Mishra, F. Gu, and A. D. Ball. 2014. "NOx Emission prediction based on measurement of in-cylinder pressure for CI engine running with diesel and biodiesel." *International Journal of Automotive Engineering and Technologies* 3 (2). https://doi.org/10.18245/ijaet.42717.

TriboNet. 2022. "Pin-on-Disk Test." Last Modified December 27, 2022. https://www.tribonet.org/wiki/pin-on-disk-test/.

Upadhyay, Abhishek, Mihir Dalal, Naman Sanghvi, Vaibhav Singh, Sheeja Nair, Ionut Scurtu, and Christian Dragan. 2021. "Electric Vehicles over Contemporary Combustion Engines." IOP Conference Series: Earth and Environmental Science.

USGS. 2022. *Mineral Commodity Summaries 2022.* (Reston, VA: U.S. Geologial Survey).

Valco, D., G. Gentz, C. Allen, M. Colket, T. Edwards, S. Gowdagiri, M. A. Oehlschlaeger, E. Toulson, and T. Lee. 2015. "Autoignition behavior of synthetic alternative jet fuels: An examination of chemical composition effects on ignition delays at low to intermediate temperatures." *Proceedings of the Combustion Institute* 35 (3): 2983-2991. https://doi.org/10.1016/j.proci.2014.05.145. <Go to ISI>://WOS:000348049500058.

Wang, Bin, Anren Yao, Chunde Yao, Chao Chen, Han Lu, and Jun Feng. 2019. "Experimental investigation on methanol auto-ignition in a compression ignition engine under DMDF mode." *Fuel* 237: 133-141. https://doi.org/10.1016/j.fuel.2018.09.154.

Wang, H. W., and M. A. Oehlschlaeger. 2012. "Autoignition studies of conventional and Fischer-Tropsch jet fuels." *Fuel* 98: 249-258. https://doi.org/10.1016/j.fuel.2012.03.041. <Go to ISI>://WOS:000305150300031.

Wang, Xiaoyu, Tinghao Jia, Lun Pan, Qing Liu, Yunming Fang, Ji-Jun Zou, and Xiangwen Zhang. 2020. "Review on the Relationship Between Liquid Aerospace Fuel Composition and Their Physicochemical Properties." *Transactions of Tianjin University* 27 (2): 87-109. https://doi.org/10.1007/s12209-020-00273-5.

Wang, Zhandong, Bingjie Chen, Kai Moshammer, Denisia M. Popolan-Vaida, Salim Sioud, Vijai Shankar Bhavani Shankar, David Vuilleumier, Tao Tao, Lena Ruwe, Eike Bräuer, Nils Hansen, Philippe Dagaut, Katharina Kohse-Höinghaus, Misjudeen A. Raji, and S. Mani Sarathy. 2018. "n-Heptane cool flame chemistry: Unraveling intermediate species measured in a stirred reactor and motored engine." *Combustion and Flame* 187: 199-216. https://doi.org/10.1016/j.combustflame.2017.09.003.

Wang, Zhandong, and S. Mani Sarathy. 2016. "Third O2 addition reactions promote the low-temperature auto-ignition of n-alkanes." *Combustion and Flame* 165: 364-372. https://doi.org/10.1016/j.combustflame.2015.12.020.

Werpy, M. R. , K. Bertram, and A. Burnham. February 16, 2011 2010. *Propane Vehicles: Status, Challenges, and Opportunities.* Energy Efficiency and Renewable Energy Energy, Argonne National Laboratory (USA: U. S. Department of Energy). http://www.transportation.anl.gov/pdfs/AF/633.PDF.

Westbrook, Charles K. 2000. "Chemical kinetics of hydrocarbon ignition in practical combustion systems." Preceedings of the Combustion Institute, Edinburgh, Scotland, 08/04/2000.

Yehia, Omar R., Christopher B. Reuter, and Yiguang Ju. 2018. "Low-temperature multistage warm diffusion flames." *Combustion and Flame* 195: 63-74. https://doi.org/10.1016/j.combustflame.2018.03.013.

Zahos-Siagos, Iraklis, Theodoros Mourtidis, Dimitrios Karonis, and Maria Kamaterou. 2017. "A Comparison of Ignition Quality of Ultra Low Sulfur Diesel Fuels Measured by Different Constant Volume Chamber Methods." International Colloquium Fuels, Stuttgart, Germany. https://www.researchgate.net/profile/Iraklis-Zahos-Siagos/publication/320780214_A_Comparison_of_Ignition_Quality_of_Ultra_Low_Sulfur_Diesel_Fuels_Measured_by_Different_Constant_Volume_Chamber_Methods/links/5 a8561940f7e9b2c3f50b89a/A-Comparison-of-Ignition-Quality-of-Ultra-Low-Sulfur-Diesel-Fuels-Measured-by-Different-Constant-Volume-Chamber-Methods.pdf.

Zhang, Chi, Xin Hui, Yuzhen Lin, and Chih-Jen Sung. 2016. "Recent development in studies of alternative jet fuel combustion: Progress, challenges, and opportunities." *Renewable and Sustainable Energy Reviews* 54: 120-138. https://doi.org/10.1016/j.rser.2015.09.056.

Zhou, G. C., S. Roby, T. Wei, and N. Yee. 2014. "Fuel Heat of Vaporization Values Measured with Vacuum Thermogravimetric Analysis Method." *Energy & Fuels* 28 (5): 3138-3142. https://doi.org/10.1021/ef402491p. <Go to ISI>://WOS:000336199300031.